A Thesis Submitted for the Degree of PhD at the University of Warwick

Permanent WRAP URL:
http://wrap.warwick.ac.uk/107576/

Copyright and reuse:
This thesis is made available online and is protected by original copyright.
Please scroll down to view the document itself.
Please refer to the repository record for this item for information to help you to cite it.
Our policy information is available from the repository home page.

For more information, please contact the WRAP Team at: wrap@warwick.ac.uk

warwick.ac.uk/lib-publications

Novel Silicate Matrix Composites.

by

A.Chamberlain, BSc (Hons).

For submission
to the degree of
Doctor of Philosophy.

University of Warwick
Department of Physics
July 1994.

To my wife,
Una.

Contents.

Chapter 1. Engineering Ceramics.

1.1. Ceramic Materials. 1.

1.2. Current Gas Turbine Materials and Structural Composites. 2.

1.3. Monolithic Ceramics. 5.

  1.3.1. Examples of Monolithic Ceramics for Engineering Applications. 10.

1.4. Composite Ceramics. 14.

1.5. Fibre Reinforced Ceramics. 16.

1.6. Glass Ceramics. 19.

Chapter 2. Continuous Fibre Reinforced Ceramic Matrix Composites.

2.1. Composite Theory. 22.

  2.1.1. Introduction, Matrix Microcracking and Residual Stress. 22.

  2.1.2. Composite Ultimate Strength. 27.

  2.1.3. Measurement of the In-situ Materials Properties. 29.

  2.1.4. The Behaviour of 2D Composites. 31.

2.2. Ceramic Matrix Composites : Fabrication and Properties. 32.

  2.2.1. Fibre and Matrix Properties. 32.

  2.2.2. Methods of CMC Fabrication. 36.

2.3. Glass Ceramic Matrix Composites. 43.

2.4. Selection of Fibre and Matrix. 47.

2.5. Research Program Objectives. 52.

Chapter 3. Experimental Techniques.

3.1. Scanning Electron Microscopy. 53.
  3.1.1. Specimen Preparation. 53.
  3.1.2. SEM Imaging. 54.
3.2. Transmission Electron Microscopy. 55.
  3.2.1. Specimen Preparation. 55.
  3.2.2. TEM Imaging. 56.
3.3. X - Ray Diffraction. 57.
3.4. Differential Thermal Analysis (DTA). 57.
3.5. Mechanical Testing. 58.
  3.5.1. Room Temperature Mechanical Testing. 60.
  3.5.2. Elevated Temperature Mechanical Testing. 63.
  3.5.3. Creep Deformation Testing. 65.
3.6. Micromechanical Measurement. 65.
3.7. Miscellaneous Characterisation Techniques. 67.

Chapter 4. Composition Selection and Composite Fabrication.

4.1. Composition Selection. 69.
  4.1.1. Silicate Ceramic Phases and the Glass Ceramic Process. 69.
  4.1.2. Glass Preparation and Crystallisation. 76.
4.2. Composite Fabrication. 83.
  4.2.1. Chopped Fibre Systems. 83.
  4.2.2. Pre - Impregnation of the Fibre Tow. 89.
  4.2.3. Unidirectional Composite Fabrication. 93.

Chapter 5. Microstructure and Interfacial Properties of MAS Matrix Composites.

5.1. Chopped Fibre Materials. 97.

5.2. Unidirectional Composite Materials. 106.

  5.2.1. Microstructural Investigation. 106.

  5.2.2. Interfacial Structure and Micromechanical Behaviour. 115.

5.3. Discussion of the Microstructure and Interfacial Properties of the Composites. 120.

  5.3.1. Matrix Densification and Crystallisation. 120.

  5.3.2. Composite Interface, Microstructure and Properties. 122.

Chapter 6. Mechanical Behaviour of MAS Matrix Composites.

6.1. Mechanical Response of Monolithic Glass Ceramics. 136.

6.2. Thermal Expansion Characterisation. 137.

6.3. The Mechanical Behaviour of Composite Materials. 140.

  6.3.1. Room Temperature Testing in Flexure. 141.

  6.3.2. Room Temperature Tests in Tension. 150.

  6.3.3. The Mechanical Behaviour of Composite Materials at Elevated Temperature. 153.

  6.3.4. The Mechanical Behaviour of Composite Materials Subjected to Thermal Aging Treatments in Air. 155.

  6.3.5. The Creep Deformation of Composite Materials in Air. 163.

6.4. Summary. 165.

Chapter 7. Comparative Studies on CAS Matrix Composites.

7.1. Composition Selection and Composite Fabrication. 169.
7.2. Mechanical Properties of CAS Composite Materials. 172.
7.3. Conclusion from the Comparative Study. 173.

Chapter 8. Overview, Conclusions and Future Work.

8.1. Overview. 175.
8.2. Conclusions. 179.
8.3. Future Work. 181.

References.

List of Figures and Tables.

Figures.

Chapter 1.

Figure 1.1. Schematic diagram of the gas turbine engine, showing the possible areas for the implementation of ceramic components.

Figure 1.2. Effect of the overall pressure ratio and the turbine entry temperature on the thermal efficiency of the gas turbine engine (4).

Figure 1.3. Stress intensity factor notation for the different loading configurations.

Figure 1.4. Idealised mechanical behaviour of a fibre reinforced composite.

Chapter 2.

Figure 2.1. Evolution of matrix cracks in a CMC system. As the applied stress increases, failure occurs at the defect sites.

Figure 2.2. The ACK model schematically depicting the transition from single to multiple fracture dependence on fibre volume fraction.

Figure 2.3. Composite ultimate strength dependence on Weibull 'm' value. From Curtin (65).

Figure 2.4. Schematic illustration of materials parameters used for the determination of the in-situ composite properties.

Figure 2.5. Schematic stress / strain curve for a 0° / 90° composite.

Figure 2.6. Schematic of the interface formation in silicate matrix composites showing the direction of ionic or molecular diffusion.

Figure 2.7. Processing compromises in the fabrication of GCMCs.

Chapter 3.

Figure 3.1. Schematic DTA trace illustrating the type of features obtained.
Figure 3.2. Tensile gripping arrangement and specimen geometry.
Figure 3.3. Schematic of the four point high temperature flexure rig.
Figure 3.4. Schematic of the SEM based indenter system.

Chapter 4.

Figure 4.1. Part of the MAS ternary diagram.
Figure 4.2. Nucleation and growth for a glass ceramic system.
Figure 4.3. Predicted thermal expansion coefficient for the matrix with the percentage of enstatite present.
Figure 4.4. DTA traces for the powders studied.
Figure 4.5. Schematic of the hot press system.
Figure 4.6. Schematic process routes for Window I and Window II schedules.
Figure 4.7. XRD trace for CF1.
Figure 4.8. Schematic of the pre - preg apparatus developed in this program.
Figure 4.9. Schematic of the optimised process route for composite fabrication.

Chapter 5.

Figure 5.1. SEM backscattered micrograph of CF1.
Figure 5.2. SEM backscattered micrograph of CF3.
Figure 5.3. SEM backscattered micrograph of CF7.
Figure 5.4. SEM backscattered micrograph of CF10.
Figure 5.5. SEM backscattered micrograph of CF15.

Figure 5.6. SEM backscattered micrograph of CF14.

Figure 5.7. SEM backscattered micrograph of the BGMC glass ceramic.

Figure 5.8. SEM backscattered micrograph of the CDM glass ceramic.

Figure 5.9. TEM micrograph showing the fibre / matrix interface in CF2.

Figure 5.10. SEM backscattered micrograph indicating the structure of UDM2.

Figure 5.11a. Low magnification SEM backscattered micrograph of CUDM5.

Figure 5.11b. Higher magnification SEM backscattered micrograph of CUDM5.

Figure 5.12a. Lower magnification SEM secondary electron micrograph of CUDM17.

Figure 5.12b. Higher magnification SEM backscattered micrograph of CUDM17.

Figure 5.13a. Lower magnification SEM backscattered micrograph of CUDM18 unidirectional.

Figure 5.13b. Higher magnification SEM backscattered micrograph of CUDM18 unidirectional.

Figure 5.14a. Lower magnification SEM backscattered micrograph of CUDM19 unidirectional.

Figure 5.14b Higher magnification SEM backscattered micrograph of CUDM19 unidirectional.

FIgure 5.15. High magnification SEM secondary electron micrograph of CUDM19 cross-ply.

Figure 5.16. SEM backscattered micrograph for 450°C aging.

Figure 5.17. SEM backscattered micrograph for 1000°C aging of CUDM12.

Figure 5.18. TEM micrograph and light element analysis results for UDM4.

Figure 5.19. TEM micrograph and light element analysis results for CUDM7.

Figure 5.20. TEM micrograph and light element analysis results for CUDM7 after aging at 700°C for 100hrs.

Figure 5.21. SEM micrograph showing indented fibre.

Figure 5.22. Load versus tip displacement plots for the NL-201 and NL-607 fibres.

Figure 5.23. Graphical plot of the interfacial micromechanical properties 2Γ and τ, compared to thermal aging temperature.

Figure 5.24. Schematic diagram indicating the degradation of the composite at intermediate and high temperatures by 'pipe-line' oxidation.

Chapter 6.

Figure 6.1. Thermal expansion coefficients for composites with $V_f = 0.5$ versus the percentage of enstatite.

Figure 6.2. Stress / deflection curve for CUDM7, with a backscattered SEM micrograph of the tensile face of a composite specimen.

Figure 6.3. Stress / deflection curve for CUDM11.

Figure 6.4. Plot of modelling strength verses V_f. The models used are the simple bundle failure, TSSE (67) and Curtin (65). Also plotted are literature values for comparison with the materials fabricated in this study.

Figure 6.5. A typical tensile test curve for cross ply CUDM18 sample at room temperature is shown in a). and a hysteresis curve in b).

Figure 6.6. Stress / deflection curve for CUDM15 tested in four point flexure at 450°C during a short term exposure.

Figure 6.7. Stress / deflection curve for CUDM19 tested in four point flexure at 1000°C during a short term exposure.

Figure 6.8. Summary plot for the aged 3hr isotherm composites indicating the trends in σ_{mm} and σ_{UBS}.
Figure 6.9. Stress / deflection curve for CUDM12 aged at 450°C.
Figure 6.10. Stress / deflection curve for CUDM11 aged at 700°C.
Figure 6.11. Stress / deflection curve for CUDM14 aged at 1000°C.
Figure 6.12. Stress / deflection curve for CUDM14 aged at 1200°C.
Figure 6.13. Summary plots for the Rolls-Royce fabricated composites indicating the trends in σ_{mm} and σ_{UBS}.
Figure 6.14. Typical creep deformation curves.

Chapter 7.

Figure 7.1. Part of the CAS ternary system.
Figure 7.2. DTA traces for the CAS glasses.
Figure 7.3. Typical stress / deflection curve for a CAS / NL - 607 composite.

Tables.

Chapter 1.

Table 1.1. Development and future requirements of the gas turbine engine.
Table 1.2. Mechanical property data for some monolithic engineering ceramics.
Table 1.3. Mechanical property data for some whisker and platelet reinforced ceramic matrix composites.
Table 1.4. Mechanical property data for some glass ceramics.
Table 1.5. Thermal expansion data for some commonly used crystalline phases in glass ceramics (All data taken from (51) and (52)).

Chapter 2.

Table 2.1. Properties of fibre reinforcements.

Table 2.2. Process routes available for CMC fabrication.

Table 2.3. Properties of CMC fabricated systems.

Table 2.4. Possible maximum use temperatures of some glass ceramic and glass systems (from (39)). § denotes a Corning Glass Works designation.

Table 2.5. Measured interfacial properties for some GCMCs.

Chapter 4.

Table 4.1. Compositions of the glasses studied.

Table 4.2. Particle size analysis results for the glasses studied.

Table 4.3. Chopped fibre pressings, the pressure used was 10MPa in all cases.

Table 4.4. Identification of the composite samples fabricated.

Chapter 5.

Table 5.1. Micromechanical property measurements for composites in this study.

Chapter 6.

Table 6.1. Flexural test data for the glass ceramics fabricated in this study.

Table 6.2. Thermal expansion coefficients for the materials fabricated in this study.

Table 6.3. Summary of the mechanical test data for the UDM series of composites.

Table 6.4. Summary of the mechanical test data for the CUDM series of unidirectional composites.

Table 6.5. Tensile test data for room and higher temperature tests.

Table 6.6. Summary of the creep experimental conditions and the creep rates observed.

ACKNOWLEDGEMENTS.

I would like to thank a number of people for their help, patience, guidance and encouragement during the course of this work. To begin, I would like to thank my supervisor, Professor Mike Lewis for his help and guidance. Both Rolls-Royce and the SERC are gratefully acknowledged for financial support during the three year duration of this work.

Over the three years, I have had the privilege and pleasure of working with many people within the Physics Department at the University of Warwick all of whom have helped and encouraged me during this work. Gerry Smith and Steve York have shown both considerable expertise as well as patience. Thanks also to Steve 'Flash' Carpenter, Dave Hammond, Bob Lamb, Pat Beecraft, Rebecca Cain, and Keith Briggs. Past and present members of the Centre for Advanced Materials have given valuable time and insight over a wide variety of topics and so I have been fortunate to work with Markys Cain, John Lumby, Mark Pharaoh, Tony Razzell, Stuart Sutherland, Adrian Daniel, Hong Feng, Olwen Pullum, Czaba and Marianna Rappensberger, Stefan Bjorkert and Hywell Jones. Notably, I must thank Adrian Daniel for the use of his indenter system, Tony Razzell for the loan of a computer, and Martin Lockyer for particle size analysis.

Within Rolls-Royce, help and encouragement was also to be found, and I would like to thank Colin Beesley, Andy Bennet, Bob Minor, Paul Doleman, Ted Butler and all of the ceramics team for their help.

Away from the world of ceramics, I would like to thank a number of people. Thanks goes to good friends Squash and Mickey, all the gym goers at Warwick, Arts Fed and the Ballingham Boys.

Thanks must go to my parents for belief in me, help, support and encouragement. Finally, a considerable thank you to my wife Una. Her love, support, encouragement and patience is astounding and without her, this thesis would never have been finished.

Declaration.

This thesis is submitted to the University of Warwick in support of my application for the admission to the degree of Doctor of Philosophy. It is an account of my work carried out in the Department of Physics, University of Warwick during the period October 1990-July 1994, and except where specifically acknowledged in the text, is a result of my own independent research. No part of this thesis has been submitted in respect of a degree to this or any other University.

Part of this work has been presented previously at conferences, appearing in the proceedings as follows :-

1. Lewis M.H., Daniel A.M., Chamberlain A., Pharaoh M.W. and Cain M.G., J. Microsc. 169, 109 (1993).
2. Chamberlain A. and Lewis M.H., Ceram. Eng. Sci. Proc. 14[9-10], 939 (1993).
3. Chamberlain A., Daniel A.M., Pharaoh M.W. and Lewis M.H., HTCMC 1, 321. Ed. Naslain R., Lamon J. and Doumiengts D. ECCM-6 Bordeaux 1993. Woodhead Publishing.
4. Lewis M.H., Chamberlain A., Daniel A.M., Pharaoh M.W., Razzell A.G. and Sutherland S. Ref 10. AGARD - R - 795. "Introduction of Ceramics into Aerospace Structural Composites.". Antalya Turkey 1993.

A. Chamberlain July 1994.

Abstract.

Within this study, a novel matrix selection principle, within the MAS glass ceramic system, has been developed with emphasis placed on the use of this matrix in a ceramic fibre reinforced composite. Matrix selection was applied in order to develop a diphasic microstructure to allow tailoring of the matrix thermal expansion coefficient via a phase mixture. The phases selected were α-cordierite and enstatite, with a Nicalon fibre reinforcement. Initial studies centred on the use of chopped fibre systems in order to develop a processing methodology giving the correct phase structure, microstructure and interface development between the matrix and the fibre. It was found that variations in process route including the use of window I and window II pressing regimes (below and above the maximum crystallisation rate) caused large differences in the matrix microstructure. During this part of the study the effects of added nucleants were investigated (P_2O_5 at 2wt%, and TiO_2 at 10wt%), the results indicating that, with the use of glass frit, the added nucleant was not necessary. Initial studies upon composite fabrication indicated the criticality of pressure application during processing indicated by a fall in the elastic modulus of the composite from the rule of mixtures calculation.

A pre-preg methodology was developed to produce high quality green state composite, including a T-piece traverse head arrangement for the fibre tow infill, 'walls' on the winding cage and rollering the pre-preg sheets. Following this, a refined process route for hot pressing was developed with application of pressure during heating in a 'process-window' identified using DTA. Composites were fabricated using the NL-607 fibre type with optimised properties reaching a matrix microcracking stress of σ_{mm} = 665±75MPa, ultimate flexure strength of σ_{UBS} = 1168±41MPa and E = 157±12GPa (within the rule of mixtures calculation). TEM analysis indicated an interface width of 25-70nm, with carbon enrichment occurring. Measurement of the micromechanical properties of the interface used an indentation technique giving the interfacial debond energy 2Γ = 12.4±5.4Jm^{-2}, and shear sliding resistance τ = 48±15MPa. Tensile studies indicated that two regions could be identified associated with microcracking in the 90° and 0° plies by a modulus drop and acoustic emission.

Thermal aging in air (100hrs) indicated that channelled oxidation via fibre / matrix interfaces was occurring at intermediate temperatures (450° - 700°C) and partial silica bridging of the interface at higher temperatures in this interval. Micromechanical property measurements indicated that for 450°C aging 2Γ = 13.6±4.4Jm^{-2} with τ = 108±54 MPa, whereas for 700°C aging 2Γ = 35.6±29.2Jm^{-2} with τ = 248±120MPa. At higher temperatures (1000°C), rapid silica bridging of the interface caused plugging to occur and the retention of as-fabricated mechanical properties for the bulk material. Fibres in the bulk of the composite had micromechanical properties similar to as fabricated materials, whereas fibres ~ 30µm from the edge of the sample had very high micromechanical properties indicative of fully silica bridged interfaces. Above 1000°C microstructural degradation was observed with the formation of a surface layer on the composites (60-80µm at 1000°C, 80-140µm at 1200°C).

Tensile creep studies indicated, for the conditions utilised within this work (1000°-1150°C and 50-90MPa), that fibre creep properties dominated, with the observed creep rate being ~ $1.6 \times 10^{-8}s^{-1}$. For all the creep studies conducted, non-steady state creep was observed, with a continuously decreasing creep rate with time.

Chapter 1. Engineering Ceramics.

1.1. Ceramic Materials.

Ceramics form a group of materials offering a diverse and sometimes unique set of properties. They are inorganic, non-metallic materials, usually consisting of more than one elemental species, processed at an elevated temperature. The applications of ceramics are numerous, particularly with respect to the more traditional roles of whiteware and earthenware. However, more recently, ceramics are being used for their unique properties.

This increase in the use of ceramics has been realised through the refinements in processing technology that have allowed a controlled synthesis with consistent reproduction of microstructure and properties. An excellent introduction to ceramics can be found in Kingery, Bowen and Uhlmann (1). There are now specialist areas developing, and broadly ceramics may be divided into 5 classes; traditional, electronic, magnetic, optical and engineering. This thesis is concerned with the engineering applications of ceramics, a broad review of which is given in Richerson (2), with the current status reviewed by French (3).

The reason that there is a considerable interest in ceramics for engineering applications is that they can offer, in comparison to more conventional metallic systems, the following properties :-

i). High specific strength.
ii). High specific stiffness.
iii). Higher temperature capability (refractoriness).
iv). Lower thermal expansions.
v). Lower density.
vi). Greater resistance to chemical attack (higher durability).
vii). Improved hardness.
viii). Improved wear resistance.
ix). Lower thermal conductivity.

Because of these properties, engineering ceramics have already found uses as high speed machining parts, wire drawing dies and application in energy conversion systems. The driving force for use in energy conversion is the ability to operate at a higher temperature which allows higher thermal efficiency and less forced (parasitic) cooling of engine parts. One of the ultimate goals, and part of the driving force behind this research, is to evaluate the suitability of ceramics for use in the advanced gas turbine environment, where the payoffs would be substantial, but the service conditions severe.

1.2. Current Gas Turbine Materials and Structural Composites.

The gas turbine environment presents interesting challenges to the materials scientist. Components within the gas stream are subjected to a variety of conditions which can include high temperatures, high mechanical loadings and large thermal shocks. A simplified diagram of a gas turbine is shown in Fig 1.1. The principle of operation is as follows; air is compressed on the inlet side of the engine before being mixed with fuel. This mix is then ignited and allowed to expand through a turbine that is connected to the compressor at the front of the engine. For aircraft propulsion this exhaust can be used to propel the aircraft or, by the addition of an extra turbine, the engine can be used in electrical power generation and marine propulsion.

Since the introduction of the gas turbine over 50 years ago, the increase in performance of the engine has been considerable, as summarised in Table 1.1., along with the future requirements for the engine (4) (5). Increases in performance have been achieved both by improved aerothermal design and by enhanced materials performance. The Ni-based superalloys currently employed in the hot areas of the gas turbine engine operate at a higher proportion of their melting temperature than any other alloy system (6) (up to 80% T_m (7)). However, these alloys are nearing the end of their development, the composition (including trace elements), heat treatments for fabricated parts and the manufacturing processes (both directionally solidified and single crystal) have all been refined (6).

To remain competitive, increases in engine performance must occur, and

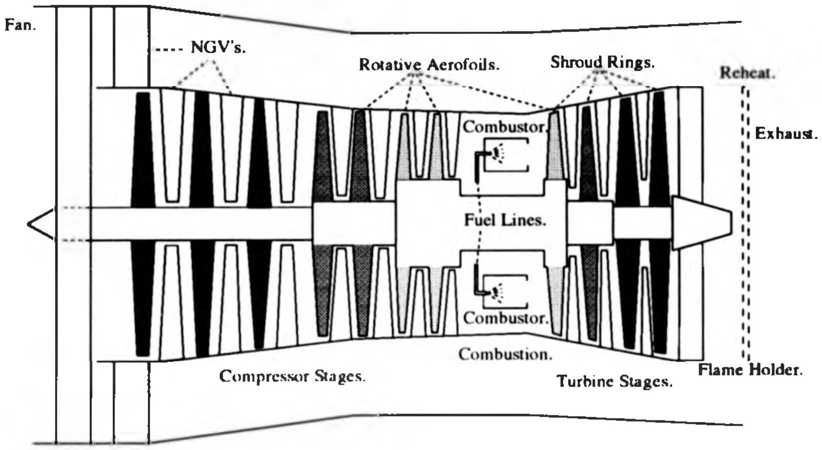

High Bypass Ratio Gas Turbine Engine.

Fan.
NGV's.
Rotative Aerofoils.
Shroud Rings.
Reheat.
Exhaust.
Combustor.
Fuel Lines.
Combustor.
Combustion.
Compressor Stages.
Turbine Stages.
Flame Holder.

Figure 1.1. Schematic diagram of the Gas Turbine Engine, showing the possible areas for the implementation of ceramic components.

Development of the Gas Turbine Engine in the Aero Market.

	Year. 1940.	1987	2000+.
Thrust / Weight Ratio.	3:1	10:1	20:1
Compression Ratio.	4:1	30:1	40:1
Turbine Entry Temperature (TET).	800°C	1400°C	2000°C

Future Military Engine Requirements.

. Fuel burn reduced by 25%.
. Cost reduced by 25%.
. Maintenance cost reduced by 25%.
. Life to 5000 cycles.

This is to be achieved 50% by design and 50% by improved materials.

Table 1.1. Development and future requirements of the gas turbine engine.

since the scope for improving the aerodynamic efficiency of the engine is limited, other ways to improve the efficiency need to be found. One of the ways in which significant gains can be made is to increase both the operating temperature and the pressure of the engine, as shown in Fig 1.2. (4). Full potential in thermal efficiency is only realised with high pressure ratios and turbine entry temperatures (TETs) >1800K. Currently superalloys have a temperature limit ~1050°C and require a considerable amount of forced air (parasitic) cooling at up to 20% to operate in the current conditions (4) (8). As a 1% drop in cooling air is equal to a 1% increase in power, large gains can be made if cooling can be reduced whilst thermal efficiency is increased (4). Further to this, considerable weight savings can be found since the density of ceramic components would be approximately one third (0.30x-0.38x) that of the equivalent metallic superalloy component for direct replacement, with reductions in the weight of the discs these components are attached to also.

However, the materials that are suitable candidates for replacement of the currently used Ni-based superalloys must exhibit improved specific strength and stiffness, an increased temperature capability and predictable behaviour with economic cost levels (4). Ceramic materials can meet the these requirements, but also need to possess overstrain tolerance, thermal shock and impact resistance.

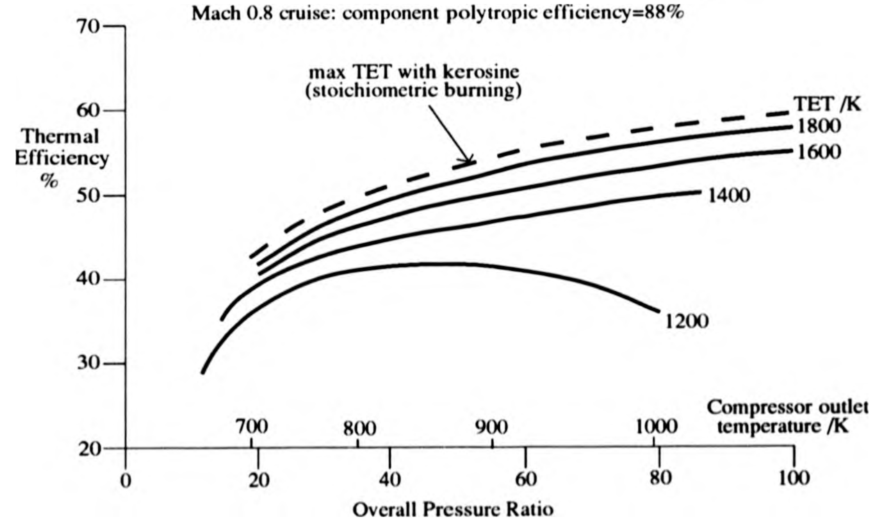

Figure 1.2. Effect of the overall pressure ratio and turbine entry temperature on the thermal efficiency of the gas turbine engine (4).

The potential areas for application of ceramics within the gas turbine are indicated on Fig 1.1., and are rotative and static aerofoils, shroud rings, reheat, exhaust and combustor components. These components depending on application need to possess high mechanical strength, tolerate transient overstress, have good creep, fatigue and erosion / corrosion resistance and be able to withstand thermal shock, impact, high frequency vibration and fretting / abrasion.

As can be realised from the above list there are many potential application areas for ceramics within the gas turbine engine both in structural and non-structural areas. Primarily, within this study, the structural requirements are of most interest. Ceramics offer a number of advantages over their metal alloy counterparts, not only in materials performance areas, but also in the abundance of raw materials and in some cases their non-strategic compositions. The typical in-service stress values for components are in the range 100-300MPa, which is readily achieved by monolithic ceramics as shown in Section 1.3. (4). A small amount of work has been carried out on the integration of ceramics into gas turbines with limited success (8). However, ceramics can suffer from brittle fracture behaviour, which means that direct replacement of metal alloys can be difficult in high integrity parts. This is where the development of structural ceramic matrix composites may allow the wider introduction of ceramics into the gas turbine environment.

1.3. Monolithic Ceramics.

Monolithic ceramics can possess outstanding mechanical and other properties, but suffer from one significant problem in that they fail in a brittle and hence catastrophic manner. This is because dislocation motion does not occur, or occurs to such a limited extent that the crack tip remains atomically sharp (at higher temperatures, the diffusion of point defects can be important and it is possible for both rock salt and fluorite structures to deform plastically when carefully prepared) (2).

The theoretical strength of a solid can be calculated from the tensile stress required to break the atomic bonds within the material and form new fracture surfaces (2):-

$$\sigma_{Th} = \sqrt{\left(\frac{E\gamma}{a_0}\right)} \qquad (1.1).$$

where E = Young's Modulus of the material (E= (σ/ε)).

γ = Fracture Surface Energy.

a_0 = Interatomic Spacing.

Near theoretical strength materials can be produced, such as 'E' glass fibres or even bulk glass, however most ceramic materials do not possess strengths near that of their theoretical limit (usually, the experimentally determined strength is ~0.001x-0.002x E) (9). The reason for this is the presence of flaws within the material which act as stress concentrators. Flaws may be introduced into ceramics during processing (intrinsic), or during the service life of the ceramic. Intrinsic flaws can arise from porosity, foreign or impurity particles, inclusions, agglomerates, and large grains. During service, flaws can be introduced by machining damage, impurity ingress, and the growth of voids at grain boundaries due to stress. Improved processing has led to a reduction in the flaw population, but removal of flaws is impossible.

The first evaluation of a theoretical relationship between the actual strength of ceramics and the flaws contained within them was carried out by Inglis (10) and Griffith (11) in the early 1900s. The Inglis approach was to use the stress distribution around an elliptical hole (when the ellipse is infinitely narrow, this can be a crack) to give :-

$$\sigma_m = 2\sigma\sqrt{\left(\frac{c}{\rho}\right)} \qquad (1.2).$$

where σ_m = Stress at the crack tip.

σ = Applied stress.

2c = Length of the major axis of the crack.

ρ = Crack tip radius.

The Griffith approach uses the different conditions of energy balance (11). Here the calculation was for the surface energy to create the new fracture faces compared with the change in elastic strain energy of the material and the external work carried out on the material. The result is :-

$$\sigma_f = A\sqrt{\left(\frac{E\gamma}{c}\right)} \qquad (1.3).$$

where σ_f = Fracture stress.

c = Flaw size.

A = Constant dependant on the specimen and flaw geometries.

Both Inglis and Griffith found that $\sigma_f \propto (1/c)^{½}$ by different approaches, and these early studies have now been extended through the developments of the 1950s into the area of Linear Elastic Fracture Mechanics (LEFM). Here the stress intensity at the crack tip, and the crack surface displacement are used. The stress intensities at the crack tip are denoted by K_I, K_{II} and K_{III}, depending on the direction of load application as shown in Fig 1.3. For ceramics, the intensity factor is usually written in the form of K_{IC}, the critical stress intensity required for the crack to propagate and hence cause material failure. This property of the material is also known as the fracture toughness for the ceramic and can be related to the previously used parameters assuming perfectly brittle conditions by (2) :-

$$\begin{aligned} K_{IC} &= (2\gamma E)^{½} \\ &= \sigma_a Y c^{½} \qquad (1.4). \end{aligned}$$

Toughness is an important material parameter, since it gives a measure of the material's resistance to damage and hence the material's reliability (12). The

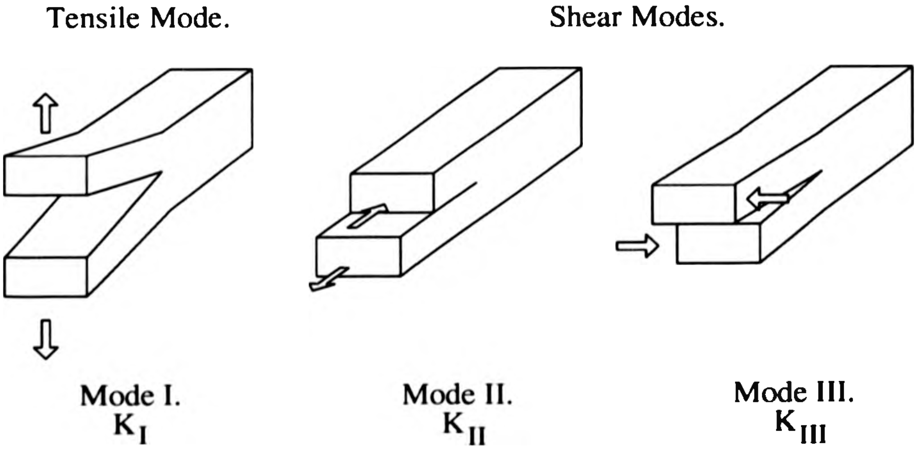

Figure 1.3. Stress intensity factor notation for the different loading configurations.

resistance to fracture can also be characterised by the work of fracture (WOF). This considers the fracture process from an energetic viewpoint and, in this case, fracture only becomes possible if the release of elastic energy per unit area of crack advance (G_c) equals the work of fracture. It can be found that, for a homogeneous material :-

$$K_{IC} = EG_c \qquad (1.5).$$

The above discussion has related the material failure stress or the stress intensity to the various parameters and, in particular, the flaw size within the ceramic. The strength of a ceramic not only varies because of inaccuracies in the test method, but because of actual variations in the material's strength. Strength depends on test methodology and the volume of material under stress. This information, coupled with the existence of a flaw size distribution in the ceramic, means that failure can occur over a wide range of applied stress.

Thus, for the design of a ceramic component, a number of approaches can be used. The most straight forward is the empirical or trial and error approach. Alternatively the deterministic approach may be employed, where analysis (i.e. Finite Element Methods (FEM)) is used but no account of the variation of the stress with volume, or area, or the flaw distribution is made.

For a ceramic component, the probability of failure at a particular stress level is required. Hence, much design work is carried out using the probabilistic approach, where the flaw size and stress distribution within the component are taken into account. The Weibull distribution proposed by a Swedish engineer of the same name has been found to be applicable in many cases. However, some specific cases require other statistical distributions. The Weibull function in its simplest form is based on the 'weakest-link' theory, where the volume of material under stress will fail at the most severe flaw. The probability of failure can be expressed as a function of the applied stress and the volume and area under this stress. Weibull proposed that, for ceramics, the function has the following form :-

$$f(\sigma) = \left(\frac{\sigma - \sigma_u}{\sigma_0}\right)^m \qquad (1.6).$$

where σ = Applied stress.

σ_u = Threshold stress (the stress below which the probability of failure is zero).

σ_o = Normalising parameter.

m = Weibull modulus, which gives an indication of the scatter in the data and hence the flaw size distribution.

The Weibull function with the stressed volume taken into account can now be written :-

$$F = 1 - \exp\left[-\int_V \left(\frac{\sigma - \sigma_u}{\sigma_0} \right)^m dV \right] \qquad (1.7).$$

For practical application of this theory, it is usual to plot lnln [1/ (1 - F)] vs lnσ to give a straight line whose gradient gives m. For ceramics, the above 3-parameter Weibull function is not used, as σ_u, the threshold stress, is set to zero. It is important to point out that the test configuration used alters the volume under consideration. For instance, uniaxial tension puts the whole volume under investigation, with a decrease in volume stressed for 4-point bending and a further decrease for 3-point bending.

For actual component design, the stress distribution within the component needs to be taken into account, as the above analysis only gives the failure probability for an applied stress. The analysis does however allow for trade off between high strengths and low scatters, but suffers from problems in defining the peak stresses, stress distributions and the strength-flaw size distribution. For an actual component the stress distribution is complicated by thermal and mechanical loadings and, unlike metals, ceramics do not redistribute stress via ductility. It is difficult to identify accurately the strength-flaw size distribution since there can be a large scatter in the results, requiring large numbers of specimens to be tested, and care must be taken to ensure that the strength-flaw distribution is unimodal for the above analysis and not multimodal.

Finally, LEFM is a design approach that uses probabilistic design considerations but does account for fast and slow fracture data which may affect the component life. Given that currently, for monolithic ceramics, m ranges typically from 5-20, failure probabilities are too high for gas turbine applications except for the case of very small components which operate at low stresses (4) (9).

1.3.1. Examples of Monolithic Ceramics for Engineering Applications.

Although, from the above data, it may seem that monolithic ceramics cannot satisfy the requirements for use in applications such as the advanced gas turbine, monolithic ceramics still have many useful structural properties. Work on composite ceramics using carbon fibres began in the late 1960s and the properties achieved were very good (13). However, in the early and mid 1970s considerable promise was being shown by monolithic ceramics and in particular SiC, Si_3N_4 (14) and the SiAlON systems (15) - (18). Refinements in processing led to improved properties that, at the time, were believed to be suitable for application in heat engines if the Weibull modulus could be improved sufficiently. In combination with this improvement in the properties of monolithic ceramics, the development of composite ceramics was hindered by the lack of availability of thermally stable and low cost reinforcements. Hence monolithic ceramics received considerable research . and development expenditure; the properties of some engineering monolithics are given in Table 1.2.

As can be seen from Table 1.2., the toughness of monolithic ceramics can be high, and this is one of the reasons that their use has increased. The toughness of a monolithic ceramic can be increased by several mechanisms, with detailed reviews found in Mah et al (28), with more mathematical approaches in Evans (29) and Weiderhorn (30). Toughening of monolithics occurs by modification of the microstructure so that stresses near the crack tip are reduced, and can be summarised as below :-

i). **Crack Deflection.** Here, the crack path is made more tortuous by deflection along grain boundaries or second phases within the ceramic. Because the crack is moved from the optimal plane of stress concentration, there is a reduction in the driving force for crack extension. Two different components act in the deflection process, a twisting and

Material.	Flexural Strength (MPa).	K_{IC} ($MPam^{½}$).	Comments & Reference.
Glass		0.7	(2).
Si_3N_4	700 - 1000	6 - 7	(19).
SiC	400 - 700	3 - 5	(19).
Al_2O_3	300 - 450	2 - 3	(19).
ZrO_2	700 - 1200	8 - 15	(19).
AlN	466		La_2O_3 added (20).
$3Al_2O_3$ - $2SiO_2$	400	4.5	(2).
Sialon - 0	935	3.6	no α (21).
Sialon - 30	717	4.3	30% α (21).
Sialon - 60	702	5.0	60% α (21).
Sialon - 100	552	4.9	100% α (21).
RBSN		2.5	Polycrystalline (2).
Si_3N_4	1020	7.4	$6Y_2O_3$ - 4MgO - $0.5ZrO_2$ (2).
Si_3N_4	900	10 - 14	Hot pressed Y_2O_3 - MgO - ZrO_2 (2).
Si_3N_4 - ZrO_2	950	8.5	(2).
Al_2O_3 - ZrO_2	1200	15	(2).
Mullite - ZrO_2	250±10	4.2	(22).
Mg - PSZ		9 - 12	(2).
Ce - TZP		10 - 16	(2).
Y - TZP	700	6.4	(2).
Y - TZP	1134±28	6.04	(23).
Y - TZP	1530	15.6	(24).
ZTA	1590	14.4	(24).
SiC / TiC		6	25Vol% (25).
SiC / TiC	~ 500		(26).
SiC / $MoSi_2$	310	8	(16).
SiC - ZrO_2		5.9	(2).
Al_2O_3 / TiB_2	~ 300		40Vol%(26).
Al_2O_3 / TiC	800		20Vol%(26).
Al_2O_3 / TiC		4.2 - 4.5	(2).
Al_2O_3 / YAG	373	4	(16).
Al_2O_3 / TiN / AlN	229	10.2	40/30/30(27).

Table 1.2. Mechanical property data for some monolithic engineering ceramics.

a tilting component, with the twisting component giving the largest contribution. The mechanism depends on the density of the deflecting particles and their shape. Rod-like particles or grains can enhance the K_{IC} value by up to 4x, then lower for disc shaped particles, followed by spherical particles (31).

ii). **Microcracking.** The ceramic microstructure may possess areas with large residual stress concentrations which are susceptible to microcracking. These areas may arise from thermoelastic mismatch or from a second phase. The effect is size dependent, with a critical size of particle being required for microcracking to occur within a limited zone of stress concentration near a large crack tip. Two crack tip shielding processes occur, firstly the local elastic modulus of the material is reduced and secondly there is a dilation induced by the microcracking. Dilation provides the largest toughening component, displaying an R-curve type behaviour, with enhancements in K_{IC} up to 2x.

iii). **Crack Pinning.** The crack can be pinned by the microstructure or by added second phases. The pinning retards the motion of the crack, the main part bowing around the pinned sections. Two theories have been developed to explain the toughening mechanisms, the first by Lange and the second by Evans (29). For particulate composites K_{IC} can be enhanced by 2x-6x (29).

iv). **Crack Bridging.** Experiments carried out with large-grain alumina showed that events could occur at large distances from the crack tip, which can have a substantial effect on the toughness (28). The toughening effect depends on the mechanical interlocking of grains protruding from rough surfaces causing closure forces on the crack surfaces. It has been found that glass ceramics can exhibit crack bridging as can whisker toughened ceramics.

v). **Transformation Toughening.** Toughening is achieved via the martensitic transformation of a particulate in a matrix. Usually, the martensitic transformation of t-ZrO_2 to m-ZrO_2 is utilised, with an associated volume increase of ~ 4% and a shear distortion of ~ 7%. The effect is critically dependent on microstructure size and uniformity, with the dilatational component contributing far more to the crack tip shielding process. The t-ZrO_2 particles which are hydrostatically constrained by the matrix can transform around a limited zone of stress concentration near the crack tip. Toughening can be modelled via two approaches, a thermodynamics and a mechanics calculation, both giving equivalent results. The ZrO_2 is usually stabilised using MgO, CaO, CeO_2 or Y_2O_3, with the usual matrix material being c-ZrO_2 or Al_2O_3. A trade-off in material properties between strength and toughness appears to occur, very high strength materials (σ> 2GPa) have lower toughness (K_{IC} ~ 5-8 $MPam^{1/2}$) in Al_2O_3 / ZrO_2 and t-ZrO_2 systems, whereas higher toughness materials (K_{IC} ~ 15 $MPam^{1/2}$)

exhibit lower strengths ($\sigma \sim 600MPa$).

Other effects may also contribute to enhanced toughness in monolithic ceramics, such as residual stresses, however, it is probable that more than one toughening mechanism will operate. It has been demonstrated that a doubling of K_{IC} is possible in Si_3N_4 by use of an elongated, fibrous-grain structure (28). This grain structure can be formed by a high volume fraction of liquid phase present at the sintering temperature and hence mechanical properties at higher temperatures are degraded by the presence of residual glass at the grain boundaries (maximum use temperature ~ 1200°C) (2) (7) (32). Elongated grains are produced during liquid phase sintering via a solution-precipitation mechanism, giving a matrix of predominantly β-Si_3N_4 from an initial powder mixture of mainly α-Si_3N_4 crystals (33) (34). For a material with an average grain size <1μm, a toughness of $10.5MPam^{1/2}$ has been achieved.

However, the largest enhancements of fracture toughness occur in transformation toughened ceramics. These materials have received significant attention because of their damage-tolerance potential; an introduction to this field is given by Stevens (35). Unfortunately, for high temperature applications, the use of ZrO_2 toughened ceramics is limited as the transformation temperature is approached. Other monolithic ceramics, although possessing good room temperature properties, as in the case of ZrO_2 toughened ceramics, can possess much degraded higher temperature properties. This is usually because the additions of sintering aids in the ceramic (Si_3N_4 uses MgO, CaO and Y_2O_3, and SiC uses B, C or Al_2O_3) can leave a glassy residual grain boundary phase which will cause a deterioration in the high temperature mechanical behaviour both in the short and long term. Studies have been carried out to try to eliminate these residual glassy phases with some success (7).

1.4. Composite Ceramics.

If composite ceramics were taken to be ceramics with more than one phase, then most high performance engineering ceramics would be classified as composites. However, we can distinguish between multiphase ceramics and composites, since, in the case of a composite, a second phase reinforcement such as particulates, platelets, whiskers or fibres is added. Since there is a second phase addition, a number of factors must to be taken into consideration :-

. Chemical compatibility between the reinforcement and the matrix.

. The thermal expansion mismatch between the reinforcement and the matrix.

. The interface formed between the reinforcement and the matrix.

. Refractoriness of the system.

. Fabrication route and degradation of the reinforcement during processing.

A number of different types of composite can be fabricated when using a ceramic matrix, which include ductile particle or fibre, ceramic platelet, whisker, short and long fibre reinforced composites. As this research project is concerned with the high temperature application of composites within the gas turbine environment, this review will be concerned only with ceramic reinforcements within ceramic matrices. A number of review articles concerned with ceramic matrix composites are available and can be found in references (36) - (39). More detailed reviews of ceramic fibre reinforced composites can be found in Sections1.5 and 2.2.

For whisker and platelet toughened systems, properties are isotropic, but do not in general reach the strength levels of fibre reinforced ceramics. Reviews of these systems can be found in references (40) (41). Properties for some composites are given in Table 1.3., where it can be seen that the K_{IC} values can be improved considerably by addition of these types of reinforcement. The most studied systems tend to be those where the reinforcement is a SiC whisker. The whisker is usually a β-SiC single crystal with a diameter in the range 0.5-10μm, and a length in the range microns to millimetres. Fabrication is usually by a vapour-liquid-solid (VLS) or vapour-solid (VS) route which produces a very small defect size (0.1-0.4μm). The

Material.	Flexural Strength (MPa).	K_{IC} ($MPam^{½}$).	Reference.
Si_3N_4 / SiC_w	454	15.6	HP (37).
Si_3N_4 / SiC_w	900		RB (37).
Si_3N_4 / SiC_w	620±50	7.8±0.3	HPRBSN(42).
Si_3N_4 / SiC_w	850±42	7.7±0.3	HPSN (42).
Al_2O_3 / SiC_w	800	8.7	HP (37).
Al_2O_3 / SiC_w		6 - 9	(2).
Al_2O_3 / SiC_w	650 - 800	8 - 9	22°C (39).
Al_2O_3 / SiC_w	575 - 775	8	1000°C (39).
Al_2O_3 / SiC_w	475 - 550	10	1200°C (39).
Al_2O_3 / Glass / SiC_w	463±58	3.3±0.5	15Vol%(41).
Al_2O_3 / Glass / Si_3N_{4w}	296±43	3.4±0.3	20Vol%(41).
Zircon / SiC_w	342		(43).
Sodalime glass / SiC_w		0.7	20Vol%(38).
Aluminosilicate / SiC_w		0.8	20Vol%(38).
Mullite / SiC_w		2.0	20Vol%(38).
Mullite / Al_2O_{3w}	~ 180		(44).
HfB_2 / SiC_p	380		(44).
HfB_2 = SiC / SiC_p	1000	~ 8	(44).
ZrC (Zr) / $ZrB_{2\ pl}$	1800 - 1900	18	(44).

Table 1.3. Mechanical property data for some whisker and platelet reinforced ceramic matrix composites.

VLS whiskers contain a small amount of α-SiC and can have properties attaining a strength of 15.9GPa, a Young's Modulus of 580GPa and a toughness of $3.2MPam^{½}$ (45). Many of the toughening mechanisms associated with whiskers and platelets have been dealt with in Section 1.3., with crack deflection being of great importance as well as crack-tip shielding, whisker bridging and whisker pullout. The interface between the reinforcement and the matrix plays a role in the determination of the mechanical behaviour of the composite, since, for bridging to occur, there needs to be load transfer from the matrix to the reinforcement (36). It is important to note that the toughness of the composite depends not only on the volume fraction of the dispersed particles, but also their shape. Finally, the effects of pullout of whiskers can be analysed as though the whiskers are short fibres. Detailed reviews of the whisker toughening process and analysis of these processes can be found in Becher et al (41), Becher (25), Lui et al (46) and Faber and Evans (31).

From Table 1.3., it can be seen that a considerable amount of research effort has been expended on the development of Al_2O_3 / SiC_w composites with K_{IC}

doubled and a 50% increase in strength retained to 1000°C for a 30vol% whisker content (46) (47). Also from Table 1.3., Si_3N_4 has been used both as a reinforcement and a matrix. Whiskers of Si_3N_4 have been produced by Los Alomos and Ube Industries Ltd (2), but when incorporated into a Si_3N_4 matrix have had only limited success, with improvements being similar to those achieved by a Si_3N_4 self-toughened microstructure. For the cases of Si_3N_4 matrices reinforced with SiC_w, both crack deflection and whisker pullout contribute to enhanced toughness, but some effect of elongated β-Si_3N_4 grains may have also enhanced toughness (48).

1.5. Fibre Reinforced Ceramics.

Although development work on ceramic fibre reinforced ceramic matrix composites began in the late 1960s, there has been a resurgence in research into these materials over the last decade (13). Monolithic ceramics have yet been unable to meet the toughness requirements for application in high stress, high integrity environments such as the gas turbine, whereas continuous fibre reinforced ceramic matrix composites (CMCs) may fulfil these requirements. During the 1970s, more refractory reinforcements became available in the form of whiskers and also the invention by Yajima et al (49), of a polycarbosilane resin that can be spun and then pyrolysed to produce a high strength silicon-oxy-carbide fibre (marketed under the name Nicalon). Properties of CMCs are non-isotropic, but they can exhibit extremely high strengths in the fibre direction and show non-brittle failure. Because of this non-catastrophic failure mode under loading, a considerable amount of research effort has been expended on the development of CMCs. The possibility of tolerating transient overstress, without the failure of a component, in a high integrity environment with the benefits offered by ceramic materials (see Sections 1. and 1.1.) clearly is a large benefit.

A typical stress versus strain curve for a CMC exhibiting tough behaviour, is shown in Fig 1.4., and can be described by several distinct regions. In region I, the composite shows linear elastic behaviour, with the Young's modulus of the unidirectionally reinforced material given by the rule of mixtures :-

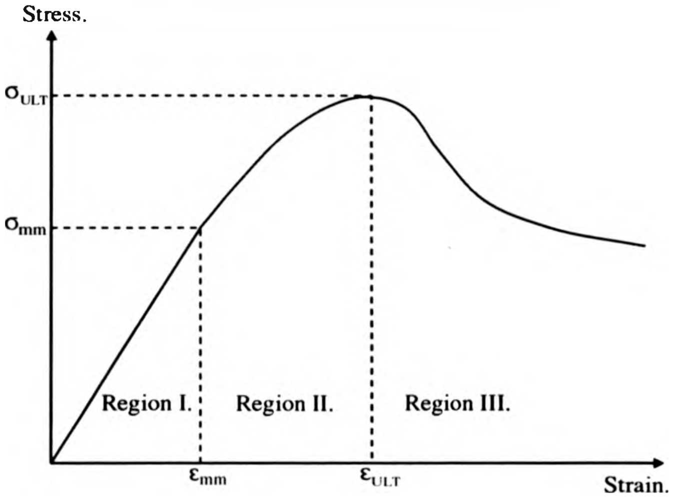

Figure 1.4. Idealised mechanical behaviour of a fibre reinforced composite.

$$E_C = E_f V_f + E_m V_m \qquad (1.8).$$

where, E_C, E_f, E_m = The composite, fibre and matrix elastic moduli.

V_f, V_m = Are the fibre and matrix volume fractions ($V_m = 1 - V_f$).

However, the composite material does not fail at its elastic limit as a monolithic material. As the stress is increased beyond the elastic limit (σ_{mm} and ε_{mm} in Fig 1.4.), there is a reduction in the composite elastic modulus, and the stress / strain curve becomes non-linear (region II in Fig 1.4.) and, in this region, the composite matrix forms a series of microcracks perpendicular to the fibre direction. The microcracks originate from pre-existing flaws within the matrix, but are bridged by intact fibres. As further stress is applied, the stress builds in the matrix via load transfer by the fibre / matrix interface away from the existing microcracks until it reaches a value where another matrix microcrack can form from a pre-existing flaw within the matrix. By this process a series of microcracks are introduced into the composite that eventually reach a saturation spacing when the microcrack stress fields overlap. Although the matrix blocks are bridged by intact fibres, some of the fibres will break at weakest sites away from the microcrack planes. Further stress transfer via the interface to the fibres causes fibre bundle failure, indicated in Fig 1.4. by σ_{ULT}, ε_{ULT}. This is the maximum load that can be sustained by the composite. However, failure after this point is still not catastrophic, as the broken fibres within the matrix blocks carry load and dissipate energy via frictional means as they pull out of the matrix.

The interface between the fibre and the matrix is critical to mechanical properties in CMCs. It must allow load transfer to occur from the weaker matrix to the high modulus fibres for the beneficial mechanical response indicated. However, the interface must not strongly bond the two components together, since then there would be no load transfer and the composite would fail in a brittle manner as a monolithic with no toughening effect.

It should be pointed out that for these composite materials, σ_{mm} and σ_{ULT}, are independent of the flaw size distribution and hence the component size, unlike the case for monolithic ceramics. The fracture toughness, K_{IC}, is no longer a valid parameter and, for these materials, more typical design parameters would be σ_{mm}, σ_{ULT}, and WOF (12). For the evaluation of these properties care has to be taken with the test methodology used, σ_{mm} can be measured in tension and flexure, but σ_{ULT} only in tension (12) (50). For design purposes, the matrix microcracking stress, σ_{mm}, is probably the parameter for use, as, once this stress has been reached within the component, the environment has direct access to the fibre / matrix interface and hence can degrade the material property appreciably.

Potential composite matrices need to show a number of properties in comparison to that of the fibre. For the application being discussed in this work, the ultimate temperature capability of both the fibre and the matrix needs to be considered, as well as the creep behaviour of both. The fabrication temperature of the composite must also be considered, and how this affects the properties of the reinforcement. Since high strength and high modulus are necessary properties of the reinforcing phase, care must be taken at all stages to ensure that the reinforcing fibres are not degraded in any way.

1.6. Glass Ceramics.

Glass ceramics are ceramic materials that are formed by the controlled crystallisation of glasses. The final material properties are a combination of those of the crystalline phases present in the glass ceramic and those of the small amount of the residual glassy phase. Because the final material is a ceramic it can possess all of the desirable properties shown in Section 1.1., and can be formed via standard glass preparation procedures. A considerable amount of research work has been conducted on glass ceramics and reviews of these and other aspects of glass ceramics can be found in McMillan (51) and Strnad (52). Following glass preparation by conventional means, carefully controlled heat treatments are used to produce fully dense polycrystalline multiphase ceramics. The devitrification of the glass and the formation of a fine grained microstructure can be aided by the addition of a nucleating agent to the glass composition (i.e. TiO_2, ZrO_2, P_2O_5, Cr_2O_3, Ag, Au etc).

The resultant properties of the glass ceramic are mainly dependent on the major crystalline phase present, but can also have a large dependency on the residual glass phase. The mechanical strengths of glass ceramics can be very high as shown in Table 1.4. However at higher temperatures, the residual glassy ·phase can play an important role in the determination of the strength. The thermal expansion of the final glass ceramic can have a wide range of values, from large positive values for

Material.	Flexural Strength (MPa).	K_{IC} ($MPam^{½}$).	Comments & Reference.
Zircon	281		(40).
Cordierite	210		(53).
LAS	50 - 250	2.0	(54).
MAS	150 - 300		TiO_2 nucleated (52).
CAS	70 - 130		Anorthite (52).
ZAS	60 - 130		Gehnite,β Quartz (52).
MAS - K_2O - F	80 - 105		Flurophlogopite (51).
Li_2O - SiO_2	30 - 398		none, P_2O_5 (51).
LZS	176 - 340		P_2O_5 nucleated (51).
BAS	55 - 64		TiO_2 nucleated (51).
ZMAS	69 - 103		ZrO_2 nucleated (51).
NAS	84		TiO_2 nucleated (51).
NBAS	89 - 114		TiO_2 nucleated (51).

Table 1.4. Mechanical property data for some glass ceramics.

Crystalline Phase.		Thermal Expansion Coefficient α (x 10^{6} K^{-1}).
β - Eucryptite	(LAS 1:1:2)	- 6.4 (20 - 1000°C).
Al_2O_3 - TiO_2		- 1.9 (20 - 1000°C).
β - Spodumene	(LAS 1:1:4)	0.9 (20 - 1000°C).
Cordierite	(MAS 2:2:5)	2.6 (25 - 700°C).
Celsian	(BAS 1:1:2)	2.7 (20 - 100°C).
Willemite	(ZS 2:1)	3.2 (20 - 1000°C).
Anorthite	(CAS 1:1:2)	4.5 (20 - 100°C).
ZrO_2 : Al_2O_3	(ZA 1:1)	7.2 (20 - 1300°C).
Clinoenstatite	(MS 1:1)	7.8 (100 - 200°C).
Magnesium Titanate	(MT 1:1)	7.9 (25 - 1000°C).
Corundum	(α - Al_2O_3)	8.7 (25 - 900°C).
Wollastonite	(CS 1:1)	9.4 (100 - 200°C).
Fosterite	(MS 2:1)	9.4 (100 - 200°C).
Lithium Disilicate	(LS 1:2)	11.0 (20 - 600°C).
Quartz	(SiO_2)	23.7 (20 - 600°C).
Cristobalite	(SiO_2)	27.1 (20 - 600°C).
Tridymite	(SiO_2)	14.4 (20 - 600°C).

Table 1.5. Thermal expansion data for some commonly used crystalline phases in glass ceramics (All data taken from (51) and (52)).

cristobalite to large negative values for β-eucryptite. In general, the crystalline phases can be selected to give low thermal expansion values as shown in Table 1.5., and hence glass ceramics have very good thermal shock properties. The refractoriness of the final glass ceramic can be made very good by selecting refractory crystalline phases. However, problems can be caused by the presence of a residual glassy phase which melts at a lower temperature. Chemical durability is another property which can be very good and can be affected by the presence of a minor residual glassy phase. The heat treatment used during the fabrication of the glass ceramic can not only influence the phases present in the final ceramic, including the residual glass content, but can also affect the volume fractions of these phases, and hence it is possible to affect the thermal expansion coefficient of the glass ceramic during processing.

As it can be seen from the above, glass ceramics offer many of the properties of the more conventionally processed ceramics but with the possibility of using lower processing temperatures. This allows the composite fabrication temperature to be lowered and may be beneficial in matrix / reinforcement reactions and degradation.

Within this chapter the necessity for improved materials performance in the gas turbine engine has been described, as has the behaviour of monolithic and composite ceramics. The objective of this research has been to develop a novel compositional selection principle and to fabricate and evaluate the composites produced using this principle. The approach used has been to select a glass ceramic ternary system and, by movement away from stoichiometry, produce a diphasic matrix with the possibility of tailoring matrix thermal expansion coefficient and enable the use of lower processing temperatures. In order to fabricate composites the development of a method for pre-impregnation of the fibre tow and subsequent tow winding was required as well as hot press consolidation schedules. Composite evaluation has attempted to encompass mechanical property measurement in the as-fabricated, thermally aged and crept conditions to test the applicability of this class of materials to the gas turbine environment.

Chapter 2. Continuous Fibre Reinforced Ceramic Matrix Composites.

This chapter reviews, in more detail, long fibre reinforced CMCs. Aspects of composite modelling are covered initially, starting with the work carried out by Aveston, Cooper and Kelly (A.C.K.) in the early 1970s (55). Their model was based around an energy balance criterion. More modern theories have also used this approach, as well as the matrix cracking strain criterion, with incorporation of Weibull statistics into the fibre failure process within the composite.

Following this review of composite modelling a review is presented of currently available fibre and matrix systems and their fabrication routes, before a more detailed review of the glass ceramic composite field. Section 2.4. details the selection criteria for the fibre and matrix used in this study, and Section 2.5., states the objectives of this research program.

2.1. Composite Theory.

2.1.1. Introduction, Matrix Microcracking and Residual Stress.

Composite modelling for CMC systems began with the application of the currently available theories based on polymer composite systems. This allowed prediction of the longitudinal composite modulus using equation 1.8. For CMC systems, models are required that predict the onset of microcracking (σ_{mm}), the composite ultimate strength (σ_{ult}), and the contributions to the work of fracture from the fibre matrix debonding and the fibre pullout from the matrix.

The first quantitative description of CMC behaviour was carried out by Aveston, Cooper and Kelly (A.C.K.) (55) using an energy balance criterion and frictional coupling between the fibre and the matrix at the interface. Since this first modelling description many authors have utilised the A.C.K. approach, as well as the matrix cracking strain approach and have included further sophistication by the incorporation of Weibull effects in the fibre failure process. The assumptions made within the models as well as the material parameters used can have a large effect on the predicted results as discussed by Yang and Knowles (56) and Cao et al (57).

For the A.C.K. model both the fibre failure and the matrix cracking stress are defined by unique stress levels. However, within the analysis the theory does account for the work done in applying the stress to the CMC, the work to fracture the matrix, the work for debonding the fibre from the matrix, the work done due to frictional sliding, the decrease in the strain energy of the matrix, and the increase in the strain energy of the fibres. For high strength fibres in a lower strength matrix the condition for multiple matrix cracking to occur is :-

$$\sigma_{fu} V_f > \sigma_{mu} V_m + \sigma_f' V_f \qquad (2.1).$$

where σ_{fu} = The fibre ultimate stress.

σ_f' = The stress in the fibre required to exceed the strain to failure of the matrix.

σ_{mu} = The matrix ultimate strength.

If this condition is not true, then σ is greater than σ_{fu} and so brittle failure occurs. As stated in Chapter 1., microcracking occurs in composites by load transfer from the matrix to the fibres via the fibre / matrix interface. The A.C.K. theory allows calculation of the crack spacing by a force balance approach at the interface, the analysis indicating that the crack spacing is dependent on the fibre radius and inversely dependent on both the fibre volume fraction and shear sliding stress of the interface.

More sophisticated models using the LEFM approach have been proposed (58) (59) (62) (63) (68) (69). However, care must be taken when using these models as assumptions are contained in them to simplify the analysis. The fibre / matrix interface is critical to the material response, and crack deflection at the interface has been analysed in detail by He and Hutchinson (70). The interfacial debond energy needs to be low for crack deflection and many models assume that it is small enough to be neglected. Models also assume that the shear sliding stress at the interface can be regarded as a constant. However, the steady state matrix microcracking stress can be evaluated for a unidirectional composite (63):-

$$\sigma_{mm} = \sigma - \frac{qE_c}{E_m} \qquad (2.2).$$

where $\sigma = \left[\frac{6\tau\Gamma_m V_f^2 E_f E^2}{(1 - V_f) E_m^2 r} \right]^{1/3}$

q = The axial residual stress in the matrix (positive q is tension).

τ = The interfacial shear sliding stress.

Γ_m = The matrix fracture energy.

r = The fibre radius.

At the matrix crack, for all applied stress σ, the matrix carries none of the applied load and hence the bridging fibres carry the entire load. By assuming that no fibres are broken and that global load sharing applies, the approximate stress in each fibre can be evaluated (65) :-

$$\sigma_{appf} \sim \frac{1}{V_f} \sigma_{app} \qquad (2.3).$$

Since the fibre matrix interface facilitates load transfer from the fibre to the matrix, in a linear manner, the stress in the matrix can build to the precracked value ($\sigma_m = \sigma E_m / E_c$) by this mechanism. This transfer length can be evaluated by use of a force balance equation :-

$$l_s = \left(\frac{1 - V_f}{V_f} \right) \frac{r\sigma_m}{2\tau} \qquad (2.4).$$

where σ_m = Pre-cracked stress level in the matrix.

Hence for distances $\pm l_s$ from the matrix crack, another matrix crack may be formed. By this mechanism multiple matrix cracking may occur as the stress applied to the composite is increased, as indicated in Fig 2.1. Note that saturation of cracks occurs when the slip lengths of the neighbouring cracks overlap, this is at approximately $2l_s$, with the average crack spacing $1.337l_s$ (65). Also from equation 2.3., it can be seen that there is a critical value for V_f when the equality in equation 2.1. is used. For a value of V_f there is a change over from a brittle type of fracture to a 'tough' multiple fracture mode as shown in Fig 2.2.

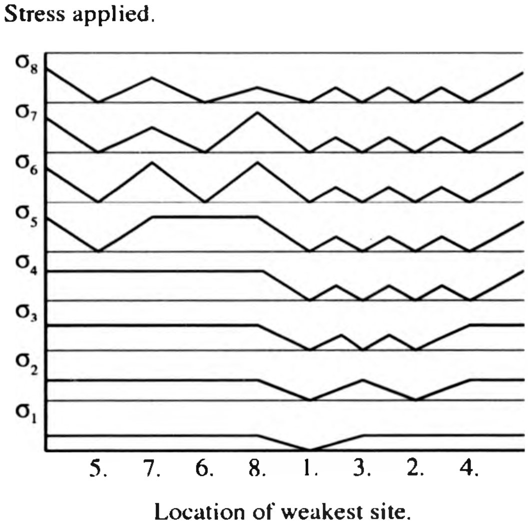
Stress applied.
σ_8
σ_7
σ_6
σ_5
σ_4
σ_3
σ_2
σ_1
5.
7.
6.
8.
1.
3.
2.
4.
Location of weakest site.

Figure 2.1. Evolution of matrix cracks in a CMC system. As the applied stress increases, failure occurs at the defect sites.

By referring to equation 2.2., it can be seen that σ_{mm} is proportional to τ, and so to increase the design stress σ_{mm} the interfacial sliding resistance can be increased. However, there is a point at which the composite will behave in a brittle manner for a value of τ. Studies have indicated that for composite behaviour to be realised three criteria need to be satisfied (57) (61) (62). These conditions indicate that for fibres to fail at a substantial distance from the matrix crack plane then 2 <= τ

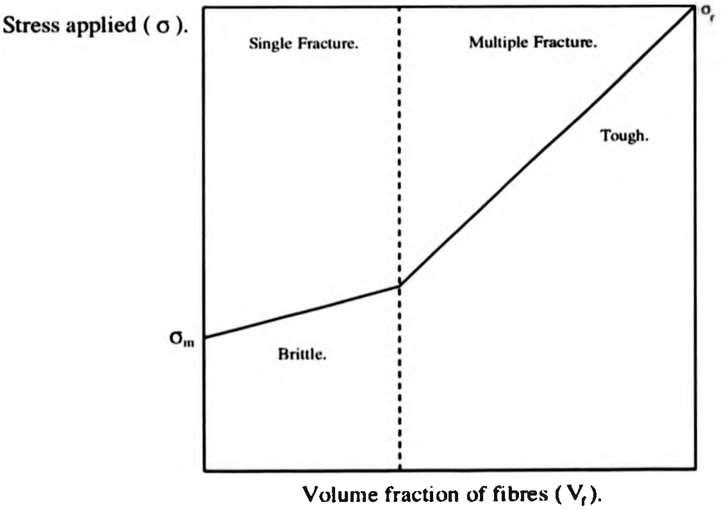

Figure 2.2. The ACK model schematically depicting the transition from single to multiple matrix fracture dependence on fibre volume fraction.

<=40MPa, for debonding at the fibre / matrix interface to occur Γ_i / Γ_f <¼ and that to avoid thermal cracking of the matrix the thermal mismatch ε_{THER} ~< 3 x 10^{-3}. If these conditions are met then the mechanical properties of the composite can be improved with higher fibre strengths σ_f, higher matrix fracture energies Γ_m, and higher volume fraction of fibres V_f.

From equation 2.2., it can be realised that residual strain can influence the composite behaviour. This issue has been dealt with in a number of models in addition to the ACK approach. Residual stresses usually arise since fabrication occurs at elevated temperatures. The situation is complicated by plasticity of the matrix, creep effects and the possibility of phase transformations. These effects produce an initial matrix stress as well as an interfacial pressure, and it can be noted that generally a positive interfacial pressure (tension) is associated with a positive initial matrix stress. If the strain mismatch is caused by thermal effects only, then :-

$$\Omega = \varepsilon_f - \varepsilon_m$$

$$\Omega = (\alpha_f - \alpha_m) \Delta T \qquad (2.5).$$

where ε_f = The fibre strain.

ε_m = The matrix strain.

α_f = The fibre linear thermal expansion coefficient over ΔT.

α_m = The matrix linear thermal expansion coefficient over ΔT.

ΔT = The temperature difference between the residual stress measurement temperature and the glass transition temperature, T_g.

Authors (57) (63) (64) have shown that the residual stresses can affect τ, and through this affect σ_{mm}. If the strain is due to thermal effects only then calculations can give the stress :-

$$q = \frac{\lambda_2 E_m E_f V_f \Omega}{\lambda_1 E (1 - \nu)} \qquad (2.6).$$

where ν = the Poisson's ration of the matrix.

$$\lambda_1 = 1 - \frac{(1 - 2\nu)}{2(1 - \nu)} \left(1 - \frac{E}{E_f} \right)$$

$$\lambda_2 = \frac{\left(1 + \frac{E}{E_f} \right)}{2}$$

This is illustrated by the results of Curtin (65) for a LAS GCMC where compressive radial residual stress increases τ. The stress q can be difficult to calculate as ΔT is difficult to quantify.

2.1.2. Composite Ultimate Strength.

Many modern theories use weakest link statistics for the prediction of fibre failure within the composite (64) (65) - (67) (71). Most of the theories assume that both Γ_i and τ are small and that the fibres are non-interacting with multiple matrix fracture occurring before composite failure. If global load sharing is being applied (65) :-

$$\sigma_{UTS} = V_f \sigma_c \left[\frac{2}{(m+2)} \right]^{1/(m+1)} \left[\frac{m+1}{m+2} \right] \qquad (2.7).$$

where σ_c = the characteristic strength for the fibres (a characteristic length can be defined $\delta_c = (r\sigma_c / \tau)$.

and the mean fibre pull-out length is given by h :-

$$h = \frac{\lambda(m) r \sigma_c}{4\tau} \qquad (2.8).$$

where $\lambda(m)$ is close to unity for m>3 (63).

Other analysis uses the notion of tractions acting on the matrix crack surface by the fibre bridging and pull out (57) (61) (64) (67). Again here weakest link statistics apply, also interactions between surrounding fibres are small therefore the ultimate tensile stress of the composite may be represented by :-

$$\sigma_{UTS} = V_f \hat{S} \exp\left\{ - \frac{\left[1 - \left(1 - \frac{\tau d}{rS} \right)^{m+1} \right]}{(m + 1) \left[1 - \left(1 - \frac{\tau d}{rS} \right)^{m} \right]} \right\} \qquad (2.9).$$

with

$$\left(\frac{rS}{\tau d} \right)^{m+1} = \left(\frac{A_0}{2\pi r H} \right) \left(\frac{rS_0}{\tau d} \right) \left[1 - \left(1 - \frac{\tau d}{rS} \right)^{m} \right]^{-1}$$

where d = the slip length.

S = the elastic compliance associated with matrix cracks.

A_0 = reference area of 1m^2.

H = Specimen gauge length.

$\hat{S}$ = Fibre strength.

S_0 = scale parameter associated with the stress distribution.

Load carrying does not cease at this point, as successive fibres break and then pullout from the matrix. This efficient way of increasing the WOF has been modelled by a number of authors, the contribution to the WOF from the work of pullout has been modelled by Curtin (65) :-

$$w_p = \frac{1}{12}\frac{\lambda_3(m)}{\lambda_1(m)} V_f \sigma_c \delta_c \qquad (2.10).$$

where $\lambda_3(m) / \lambda_1(m)$ is the ration of a dimensionless third moment to that of a dimensionless first moment.

This is similar to the Sutcu (71) result except for the prefactor. From Evans and Marshall (61), if τ is large, then the linear decrease in fibre stress away from the matrix is steep (see equation 2.5.) and hence the volume of fibre under stress is small. This suggests that fibre failure will occur nearer the crack plane and so contributions to the work of fracture (WOF) will be small. In comparison to this, for the case of a small τ, the length is increased and hence longer pullout lengths are expected, especially with decreasing Weibull shape parameter 'm'.

The value of the Weibull shape parameter 'm', also clearly has an influence on σ_{UTS}. This dependence was modelled by Curtin and the results schematically indicated in Figure 2.3. (65). Because of this it is important to be able to evaluate the Weibull parameter 'm' for fibres within the composite so that τ may be optimised (61) (64).

The currently available models do predict with reasonable accuracy the properties attained by experimental studies. The key parameters are the intrinsic fibre strength S_o, the Weibull modulus m, and the interfacial sliding resistance τ within the composite. Evaluation of these in-situ properties can be difficult and so can lead to inaccuracies in the model predictions. The ultimate tensile stress, σ_{UTS}, seems to scale by bundle effects with the modification of stress reduction in the fibres by frictional

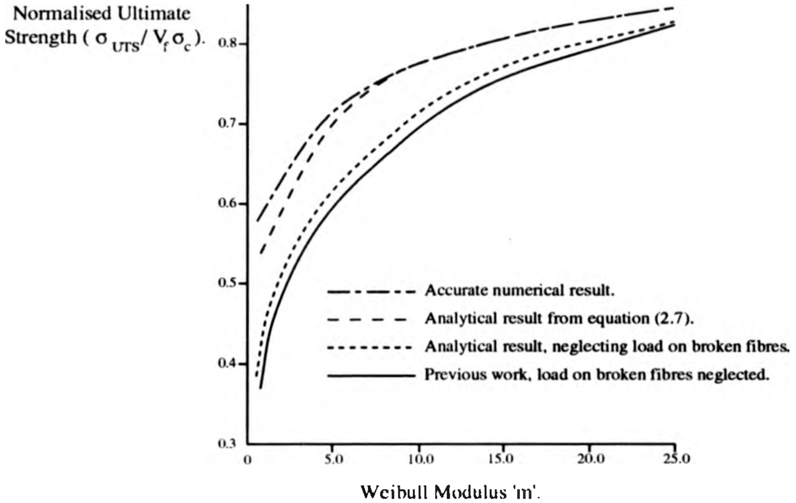

Figure 2.3. Composite ultimate strength dependence on Weibull 'm' value. From Curtin (65).

sliding at the interface. Hence, the composite strength scales with the strength of the fibres within the composite, so it is necessary to avoid fibre damage during composite processing. The values found for σ_{UTS} experimentally deviate from the theoretical predictions as the fibre can be damaged during fabrication and may fail in the crack wake or the strain localisation caused by a crack plane and hence, from modelling, σ_{UTS} is an upper bound (65). Further limitations of models are discussed by Yang and Knowles (56) who show that simplifying assumptions used can lead to predictions near that of the simple 'equal load sharing' bundle model.

2.1.3. Measurement of the In-situ Materials Properties.

From the above discussion many authors have indicated the necessity to evaluate the material properties in-situ in the composite (65) (72) (73) (63) (67). The parameters that need to be found are τ, Γ_m, Γ_i, Ω, S_0, and m. A number of methods exist to evaluate these parameters as summarised below (for more detail see (72)). The fibre characteristic strength and shape parameter can be determined from the ultimate strength of the composite (65) or by the use of fracture mirror radii on broken fibres after composite testing (72). The interfacial sliding stress τ can be measured by several techniques, with the materials properties schematically illustrated in Fig 2.4. (72) :-

i). Modulus of unloading ($\overline{E}$).

ii). Saturation crack spacing.

iii). Hysteresis loop ($\delta\varepsilon$).

iv). Pullout lengths (64) (65).

v). Indentation.

The interfacial debond energy Γ_i, can be calculated from indentation measurements as well as the composite permanent strain, ε_p (see Fig 2.4.), and the residual crack spacing within the composite after tensile testing (72). The matrix fracture energy, Γ_m, can be evaluated from a monolithic piece of matrix material, the saturation crack spacing, or the matrix cracking stress, σ_{mc}. Finally, a parameter of interest is the misfit strain Ω, which is the residual strain, usually caused by cooling from the fabrication temperature. Again, in order to evaluate this as for Γ_i, the permanent strain, ε_p, and the residual crack spacing can be used, as well as bilayer distortion (72).

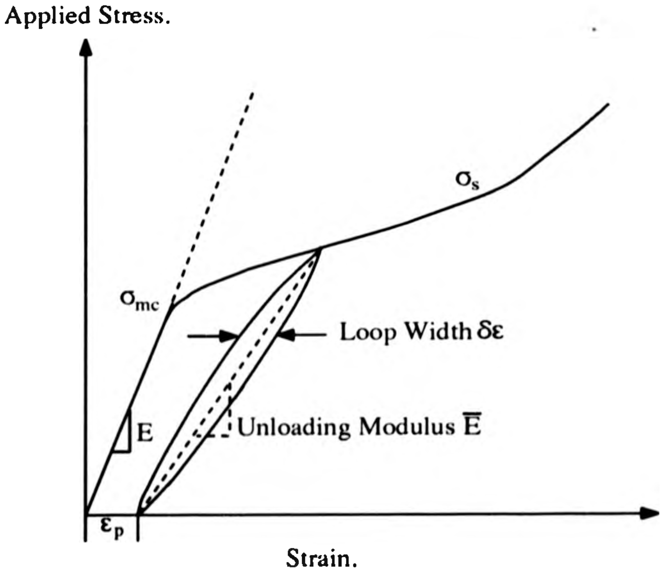

Figure 2.4. Schematic illustration of materials parameters used for the determination of the in-situ composite properties.

2.1.4. The Behaviour of 2D Composites.

Even the above analysis and theories cannot predict fully the behaviour of CMCs and most of the above relates specifically to 1D CMCs. Very recent theoretical developments have indicated that the theories require the incorporation of continuum damage mechanics (72) (74). Work is now beginning to predict the failure in 2D CMCs using existing theories and by devising mechanism maps, utilising non-dimensional parameters (72). It has been found that for 2D materials, σ_{UTS} can be predicted reasonably accurately by taking the results / analysis for 1D materials and dividing by two, which is appropriate for the decrease in V_f. Hence the 0° plies are the dominant load carriers, but 2D effects do occur at the initial deviation from linearity in the stress / strain curve as illustrated in Fig 2.5. It has been shown that cracks can evolve in the 90° plies or matrix rich areas in a 2D CMC at stresses much lower than those associated with those in the 1D case, i.e. at σ_t. These effects are slight in comparison to the overall non-linear behaviour of the material (63) (72). The cracking stress for the 90° plies usually occurs by a tunnelling mechanism with an associated stress (72):-

$$\sigma^t = \left[\frac{\Gamma_m E}{gt} \right]^{1/2} - \sigma_R \left(\frac{E_L + E_T}{2E_T} \right) \qquad (2.11).$$

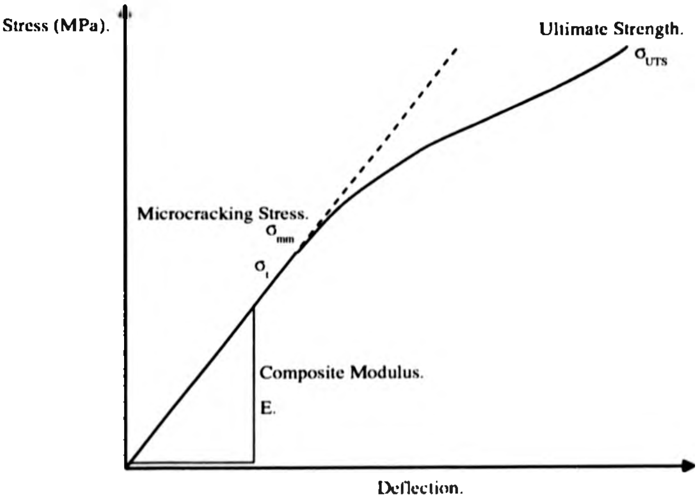

Figure 2.5. Schematic stress / strain curve for a 0° / 90° composite.

where g = a function ranging between 1/3 and 2/3

σ_R = residual stress in the 0° / 90° composite along the fibre axis.

These tunnel cracks can then extend into the 0° plies and, if the stress on the 0° plies is known, then the 1D solution can be used, otherwise it must be estimated. Stress concentration around the bridging fibres in the 0° plies can be significant and would drop the σ_{UTS} below the ($\sigma_{UTS}/2$) expected result. Stress concentrations are relieved by small τ, (E_T/E_L), and mean crack spacing in the 90° plies.

Work on modelling and understanding the behaviour of CMCs when stress concentrators such as holes or notches are introduced is also being carried out. Results indicate three types of behaviour, Class I being a mode I crack with fibre failure as crack extension occurs, Class II being mode I multiple matrix cracking, and Mode III being shear damage (72). Mechanism transitions have been evaluated for these types of behaviour but will not be discussed here.

As can be seen from the above a considerable amount of modelling has been attempted on CMC materials particularly in relation to the properties of 1D (unidirectional) fibre architectures. Within this chapter the next section details some of the CMC systems studied, their properties and methods of fabrication.

2.2. Ceramic Matrix Composites : Fabrication and Properties.

2.2.1. Fibre and Matrix Properties.

Fibre reinforced composites for high temperature applications in oxidising environments became a possibility with the invention of the Nicalon silicon-oxy-carbide fibre by Yajima et al in 1976 (49). Up to this point a fibre stable in air was not available for temperatures where ceramic matrices would provide obvious temperature benefits in oxidising conditions.

Common reinforcements available to research establishments are shown in Table 2.1. Carbon fibres have been available for a considerable amount of time, their development being driven by usage in polymer composite systems. Several routes exist

Reinforcement		Composition (wt%)	Tensile stength (MPa)	Tensile modulus (GPa)	Diameter (um)	Maximum temperature (°C)	Thermal expansion (x10^{-6}/°C)	Reference
Name	Manufact							
C - Yarn	BASF	C	1400-1500	200-500	7-10			(2)
300S	Thornel	C	2650	228				(2)
HMS	Hercules	C	2700	350				(2)
HTS	Hercules	C	2830	257				(2)
DG102	Celanese	C	1725	530				(2)
T300R	Amoco	Graphite		276	10	>1648		(75)
T40R	Amoco	Graphite		276	10	>1648		(75)
Nicalon	Nippon Carbon	59 Si,31 C,10 O	2520-3290	182-210	10-20	1204	3.1	(28)(75)(76)
Tyranno	UBE	48 Si,28 C,18 O	>2970	>200	8-10	1300	3.1	(28)(75)(77)
MPS	Dow / Celanese	69 Si,30 C,1 O	1050-1400	175-210	10-15			(2)
	Tonen	60 Si,37 C,3 N, O	2500	250	10			(80)
SCS-6	AVCO	SiC on carbon	3920	406	143	1299	4.4	(28)(75)(78)
	AVCO	Si,C	>2800	280-315	6-10			(28)
Sigma	BP	Si,C monofil		410	100	1259		(75)
MPDZ	Dow Corning	49 Si,30 C,15 N 8 O	1750-2100	175-210	10-15			(28)
HPZ	Dow Corning	59 Si,10 C,28 N 3 O	2100-2450	140-175	10	1400		(28)
Fiberamic	Rhone Poulenc	57 Si,22 N,13 C, O	2000	200	15			(80)
TNSN	TNK	Si_3N_4		296	10	1204		(75)
Nextel312	3M	62 Al_2O_3,14 B_2O_3 24 SiO_2	1750	154	143	1204		(2)(28)(75)(76)
Nextel440	3M	70 Al_2O_3,28 SiO_2 2 B_2O_3	2100	189	10-12	1426		(2)(28)(75)
Nextel480	3M	Same as 440	2275	224	10-12			(2)(28)
PRD-166	Du Pont	Al_2O_3,15-25 ZrO_2	2100-2450	385	20	1400		(2)(28)(75)
Sumitomo		85 Al_2O_3,15 SiO_2	1800-2600	210-250	9-17	1249		(28)(75)
FP	Du Pont	>99% α-Al_2O_3	>1400	385	20	1316	5.7	(28)(75)(76)
Saphikon	Saphikon Inc	Al_2O_3	2100-3400	414	120			(80)
Saffimax	ICI	96δ-Al_2O_3,4SiO_2	2000	300	3			(79)
Astroquartz		Pure fused silica		69	9	993		(75)
Boron Monofilament		Boron	2750	400	100-200		4.7	(75)

Table 2.1. Properties of fibre reinforcements.

for fibre fabrication, beginning with Rayon, pitch or PAN polymer precursors. These are drawn and pyrolysed, giving an oriented microstructure with layers of hexagonal carbon rings parallel to the fibre axis, and have anisotropic fibre properties.

For ceramic matrix composites much of the work has been carried out using SiC fibres because of the superior strength retention, at temperature, in oxidising environments. The Nicalon SiC fibre from Nippon has been used extensively as a fibre reinforcement. The fibre is based around the thermal decomposition of organometallic polymers which contain silicon. Dimethyldichlorosilane { $(CH_3)_2SiCl_2$ } is converted by de-chlorination to polydimethylsilane which is then pyrolysed in an inert atmosphere at 300 - 400°C to give polycarbosilane similar in structure to β-SiC (81) - (84) :-

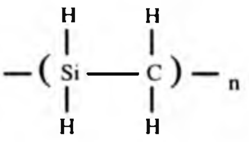

$$-(\mathrm{SiH_2}-\mathrm{CH_2})-_n$$

The hydrogen is then driven off by further pyrolysis at 300°C in air which leaves a residue of free carbon, introduces some oxygen into the structure and produces cross linking. The fibre is then subjected to further heat treatments to produce the predominantly nanocrystalline β-SiC fibre with some free carbon and oxygen. A low oxygen content Nicalon fibre is available for experimentation called Hi-Nicalon, commercial quantities however are not available. Another small diameter SiC fibre which is commercially available is Tyranno (UBE). As with Nicalon, fabrication of Tyranno begins with a polydimethylsilane $\{ \mathrm{Si}\,(\mathrm{CH_3})_2 \}_n$, with a subsequent mixture of titaniumalkoxide which gives a polytitanocarbosilane. The Tyranno fibre has a lower residual carbon content but a higher oxygen level, and exhibits less long-range order than Nicalon (85). The MPS Dow Corning and Celanese SiC fibre contains 50-80% crystalline SiC.

Large diameter SiC fibres are also available as monofilaments. The Textron SCS-6 fibre is used for metal matrix composites (MMCs) predominantly, but has found use in some CMC systems due to a higher temperature capability. Its larger diameter can preclude its use in complex shapes as its maximum bend radius is ~ 20mm. The fibre is fabricated by the deposition of silanes (to give SiC) onto a resistively heated 33µm carbon core (86). The microstructure of the fibre is complex, as an intentional variation of the SiC stoichiometry within the fibre core gives two layers and there is a three layer outer coating (32). Ceramic fibres utilising the properties of Si_3N_4 ceramics as well as those of SiC are being studied on a smaller and more experimental basis. The fibres are based on polycarbosilazane precursors. Fiberamic from Rhone Poulenc, which is not commercially available, uses the pyrolysis of polysilazanes to give a 95% amorphous phase fibre of Si-C-N-O with 5% free carbon (79). The Dow Corning and Celanese approach for the fabrication of Si-C-N-O fibres has been to utilise melt spinning of amorphous thermoplastic polymers, with a cross-linking step for the gelation of the spun fibre. For Si-C-N fibre a hydropolydisilazane (HPZ) is used, whereas for a Si-C-N-O fibre a methylpolydisilazane (MPDZ) is used (79).

It can be seen from Table 2.1., that a number of oxide and particularly Al_2O_3 fibres exist. These are designed to give higher oxidation resistance for application of CMCs, but have an increased tendency to react and bond to the matrix and hence require interface coating for application in CMCs. The first commercially available small diameter fibre was Du Pont's FP fibre, this is an α-Al_2O_3 fibre which by virtue of its fabrication has a SiO_2 outer layer (79). Du Pont's second Al_2O_3 fibre is PRD-166, designed for glass and ceramic matrix reinforcement, again based on α-Al_2O_3 but has the addition of 20% Y-PSZ, which improves the strength and the toughness of the fibre whilst stabilising the structure. The final pure Al_2O_3 fibre in Table 2.1., is Saphikon. It is a single crystal melt grown fibre with the c-axis of the hexagonal crystal preferentially grown in the fibre direction. This gives the fibre excellent properties due to a low flaw population and small flaw size, and a low resolved shear stress on the active glide planes for an axially applied stress. However, the fibre has a large diameter and so cannot be woven, and the fibre surface has a roughness asperity amplitude of ~ 0.3μm with a wavelength of 8-10μm (87).

The next group of fibres are Al_2O_3-SiO_2 fibres which include Sumitomo, Saffimax, and the Nextel 312, 440 and 480 series. The Sumitomo fibre is fabricated by the polymerisation of an organo-aluminium compound which is then spun before heat treatments to give a fine grained γ-Al_2O_3 fibre stabilised by SiO_2. Saffimax is solution spun from an aluminium salt followed by heating. The Nextel fibre series are based on mullite with varying additions of B_2O_3. They are elliptical fibres with an average diameter of 11μm and, whilst 440 and 480 are mullite only, the extra B_2O_3 oxide content in 312 gives a diphasic structure of mullite and γ-Al_2O_3.

For all the oxide fibres illustrated here, apart from the single crystal Saphikon, plasticity of the fibres at high temperature is their limiting factor for application, which requires that operating temperatures need to be <1000°C. This, coupled with the necessity of interfacial coating for a reaction barrier as well as debond and sliding, makes the application of these fibres in CMCs difficult.

The above is a brief overview of the potential reinforcements that are available for CMCs. Information in Chapter 1., Section 1.3.1., reviewed some of the monolithic ceramics available for matrix materials for CMC use. By referring to Table 1.2., it can be seen that there are a considerable number of high strength and toughness matrix materials available, giving very good high temperature properties for creep and oxidation / corrosion resistance. Glass ceramic matrices, although not exhibiting the same levels of strength as some of the monolithic ceramics indicated in Table 1.4., can satisfy many of the compatibility issues associated with composite fabrication, with the possibility of lower fabrication temperatures and the ease of processing offered by a glass (and hence liquid) matrix precursor.

2.2.2. Methods of CMC Fabrication.

A number of different methodologies exist for the fabrication of CMCs which depend on the matrix employed, the architecture of the fibre preform and the complexity of the shape to be produced. A summary of some of the methods is given in Table 2.2. For current CMC types, the matrices used can be grouped under four headings (80) :-

i). Glass ceramics.

ii). Oxides.

iii). SiC or Si_3N_4.

iv). Carbon.

For the fabrication of CMCs any technique utilised needs to consider two points; the thermal stability of the reinforcement and matrix cracking caused by thermal expansion mismatch of the constituents (80). Fabrication routes can be broadly divided by the techniques used for matrix infiltration of the fibres :-

i). Glassy phase infiltration.

ii). Liquid phase infiltration.

iii). Gas phase infiltration.

iv). Pyrolysis of a transferred liquid phase.

To begin the overview of fabrication techniques slurry infiltration of the fibre tow or preform is reviewed since this was one of the first techniques utilised to produce CMCs. The technique is confined to the production of 1D or 2D shapes but can be used for glass ceramic, oxide or covalent (SiC or Si_3N_4) matrices. Usually a matrix powder is mixed with an organic binder and carrier before winding the infilled fibre tow onto a drum, resulting in sheets of 'pre-preg'. Once wound, the green composite is consolidated usually by hot pressing (HP), after binder burnout, although solid state or liquid state sintering can be used.

The HP technique was developed both in the U.K. and the U.S. in the mid-1960s giving composites with unidirectional or laminate architectures, with residual porosity between 2-3% (80). Initial studies utilised borosilicate glass and carbon fibres, with a small amount of glass ceramic work, whereas later studies have used SiC fibres (Nicalon) (55) (75) (76) (78). Hot press conditions are usually 1000-1400°C and 3.5-15MPa, and now this technique is used mainly in the study of glass ceramic matrix composites (aluminosilicates such as LAS, LMAS, YMAS, MAS, BAS, CAS, BMAS) which have the capability of operating at temperatures of >1100°C (80).

Liquid processing routes may also be utilised in the CMC fabrication

Processing Route.	Matrices.
Viscous Phase Hot Pressing (2D).	glasses, glass ceramics.
Hot Pressing (2D).	oxides.
Sol - Gel Routes (2D and 3D).	oxides.
Pre - Preg curing and Pyrolysis.	SiC, Si_3N_4.
Solid State Hot Pressing.	SiC, Si_3N_4.
Polymer Precursor (3D).	SiC, Si_xN_y, $Si_xC_yN_z$.
Chemical Vapour Infiltration.	carbides, nitrides, carbon, oxides, borides.
Liquid Metal Infiltration.	(Si) -> SiC.
Gas Metal Reaction.	oxide (Al), nitrides (Al, Zn, Ti).

Table 2.2. Process routes available for CMC fabrication.

process. Two routes are available, one being by sol-gel processing and the other being via polymeric precursors. Both theses routes allow 3D preform architectures to be used. The **sol-gel route** to matrix fabrication can offer advantages of greater compositional homogeneity for a single phase matrix, formation of unique matrices, enhanced infiltration with the possible use of injection moulding technology, and the lowering of processing temperatures. There are a large number of potential matrix materials that can be prepared via sol-gel routes using hydrolysis and polycondensation reactions (i.e. SiO_2, $TiO_2.SiO_2$, $GeO_2.SiO_2$, $B_2O_3.SiO_2$, $Al_2O_3.SiO_2$, Al_2O_3, $ZrO_2.SiO_2$, MAS, LMAS, BAS etc). To fabricate dense composites a number of infiltration stages need to be carried out and this is one major disadvantage, coupled with matrix shrinkage. However, the possibility of using lower processing temperatures allows for minimal fibre degradation although the necessity, in some instances, for a conventional HP step for final composite fabrication, can lead to a reduction in the shape capability of the process and fibre damage.

The second liquid processing technique is that of **polymeric precursor infiltration**, which can use established techniques from polymer and carbon composite systems. However, there is a large difference in yield for ceramic matrices (SiC or Si_3N_4 is ~1:2.5) compared to carbon matrices (~1:1.8). This means that matrix shrinkage becomes important (~78% compared to ~35%) and hence, to achieve reasonable porosity levels of ~8-20%, a large number of infill and pyrolysis cycles must be carried out. To combat this a two stage process has been developed by ONERA France, which gives ~10-15% porosity for polymeric matrices from a normal infill followed by an injection step.

The final liquid process route reviewed here is that of **melt infiltration**. For CMCs the process has not been extensively used, but allows for complex shape capability and can offer the following advantages of fully dense matrices in a single process step, small dimensional changes from preform to CMC, and the processing of any fibre geometry (40). However, although this technique can be used for oxide and glass ceramic matrices there are disadvantages associated with it (40). Fibre damage may occur via chemical reactions due to the high melting temperatures associated with ceramics, and low infiltration rates occur due to the high viscosity of ceramics. Finally, wetting of the fibre preform becomes critical as the fibre dimension decreases and the fibre packing density increases.

Using this route liquid metal infiltration has been utilised on a small scale. A matrix such as SiC can be formed by use of a porous C preform infiltrated with liquid Si (usually by capillary action). Monolithic ceramics such as GE's silcomp and T&N's Refel (previously UKAEA) are formed by this route. GE are presently using carbon fibre to produce silcomp composites (80).

Gas phase infiltration is normally accompanied by reactive deposition such as **chemical vapour infiltration** (CVI) which offers one of the most flexible means of CMC fabrication; complex shapes and fibre architectures can be utilised using this technique and a variety of matrices can be deposited (i.e. carbon, SiC, Boron, Si_3N_4, TiC, ZrC, TiB_2, BN, ZrB_2, Al_2O_3, ZrO_2). Most of the matrices studied by this fabrication technique have been C / SiC or SiC / SiC. Within the CVI process two processes govern the matrix growth rate, the mass transfer of both the reactant species and reaction products which occurs by diffusion and chemically limited reaction kinetics. For good quality CMCs it is the 'chemically-rate-limited' reaction kinetics regime which is desired. This forces the fabrication process to operate at low pressures and temperatures and hence causes long infiltration times. This is the isothermal CVI case and attempts have been made to reduce the deposition time. Two methodologies have been developed, forced CVI and cyclic CVI. Forced CVI was pioneered by ORNL (USA) and uses a thermal and pressure gradient approach to cut infill times by ~ 50% , whilst density is maintained at 85-90% (80) (88). The cyclic or 'pulsed' CVI technique was pioneered by Kawasaki Heavy Industries (KHI) and uses cycles of a few seconds for infiltration.

A second gaseous fabrication technique that can be used is the reaction of molten metal with a gas. This fabrication method was used in the 1980s by LANXIDE for the fabrication of Al_2O_3 matrix ceramics. Composites have been fabricated using the process, and although complex shapes can be produced the process needs optimisation to remove Al metal from the matrix (80). Lanxide have also extended the process to nitride matrices.

Finally, solid state HP can be used, where laminates of alternate layers of fibres and matrix powders (usually with sintering aids) are consolidated. Temperatures are usually 1800-2100°C for Si_3N_4 and SiC matrices which precludes the use of many of the fibres, Textron SCS-6 being the only one that has survived processing for RBSN matrices (32) (80).

As can be realised from the large number of fabrication routes indicated above a considerable number of different CMCs have been studied. These composites can be loosely grouped via the matrix type as indicated in Table 2.3. This table is not exhaustive but gives an indication of the scope of CMC research.

A considerable amount of research has been directed toward glass and glass ceramic matrix composites. Early composites research was directed at glass / carbon fibre systems, but it should be noted that even in the early 1970s Aveston was fabricating SiC fibre reinforced cordierite matrix composites and achieving flexural strengths of ~600MPa (89). The LAS series of composites has developed from the early 1980s for a glass LAS matrix through to the LAS - III matrix composites in both a glassy and ceramed state (90) (91). A considerable amount of work has been carried out on cordierite based glass ceramics also and the reasons for this will be given in Sections 2.3., and 2.4.

Glass matrix composites were studied originally because of the ease of fabrication in relation to thermal stability of the fibres. Borosilicate matrices have been used extensively since these offer intermediate temperature capabilities (~600°C) and, when cristobalite crystallisation is suppressed, very high strengths (101).

For oxide matrix composites work involving the effects of deposited interfaces has been carried out on Nicalon fibre reinforced $ZrSiO_4$ matrix composites. These studies have also evaluated the effects of hot press atmosphere, ramp rate and calcination temperature, but, as indicated in Table 2.3., the fibre coating can have a

Material / Fabrication Route.	Flexural Strength. (MPa).	Tensile Strength. (MPa).	Fracture Toughness (MPam^{½}).	Reference / Comment.
Glass Ceramics.				
LAS/SiC		680		(39) unidirectional
LAS/SiC	830		17	(39)
SiO$_2$/C/SiC Sol gel	950			(39)
Al$_2$O$_3$/C/SiC Sol gel			10.5	(39)
LAS/Nicalon		700-800	10-20	(91)
LAS/Nicalon	800	500		(92)
LAS/Nicalon		690	16	(13)
LAS/Nicalon	359	393		(75) 3D braid
BMAS/Nicalon	250			(93) compressive
CAS/Nicalon	1000	400		(93) not Corning
BAS/Nicalon	670			(53) room temp
	270			(53) 1200°C
MAS/Nicalon	650			(53) room temp
	400			(53) 1300°C
MAS/SiC	600			(89)
MAS/SCS-6		620		(78)
LAS/SiC	900			(94) room temp
	1000			(94) 1150°C
	500			(94) 1250°C
LASIII/Nicalon	480	216		(80) 0°/90°
LAS/Tyranno	480			(80) 0°/90°
LAS/SiC	350	200		(80) woven
MAS-L/SiC	460	290		(80) 0°/90°
BMAS/Tyranno	476			(80) 0°/90°
BMAS/Nicalon	428			(80) 0°/90°
CAS/Nicalon		200		(80) 0°/90°
LAS/Nicalon	600		17	(95) UD
	800			(95) 800°C
	850			(95) 1000°C
	380		10	(95) 0°/90°
	410			(95) 800°C
	480			(95) 1000°C
BMS/Nicalon	703	416		(96) UD 4pt
LASI/Nicalon		455		(78) V$_f$ 46%
LASII/Nicalon		758		(76) V$_f$ 46%
LASII/Nicalon		664		(78) Ceramed
MAS/Nicalon	310			(97) UD V$_f$ 42%
BMAS/Nicalon	386			(97) UD V$_f$ 45%
NMAS/Nicalon	289			(97) UD V$_f$ 47%
ZMAS/Nicalon	379			(97) UD V$_f$ 44%
LMAS/Niclaon	386			(97) UD V$_f$ 45%
LZN/Nicalon	690			(97) UD V$_f$ 45%
Oxides.				
ZrSiO$_4$/Nicalon		210	7.5	(13) No fibre coat
		405	13	(13) BN fibre coat
ZrTiO$_4$/Nicalon		120	2	(13) No fibre coat
		470	15	(13) BN fibre coat
Zircon/SCS-6	287	217		(43) No fibre coat
Mullite/SCS-6	708			(98)
Glass				
Borosilicate/SiC	830		18.9	(39)
7740/SCS-6	930			(99) 350°C V$_f$ 65%
	1240			(99) 600°C V$_f$ 65%
7740/Nicalon	800			(90) V$_f$ 50%
	900			(90) 600°C V$_f$ 50%
7740/Nicalon	470			(100)
	611			(100) 600°C
	651			(100) 700°C

Table 2.3. Properties of CMC fabricated systems.

Material / Fabrication Route.	Flexural Strength. (MPa).	Tensile Strength. (MPa).	Fracture Toughness (MPam$^{\frac{1}{2}}$).	Reference / Comment.
Glass contd.				
7930/Nicalon	506			(100)
	691			(100) 950°C
	705			(100) 1050°C
Borosilicate/Nicalon	1293			(101)
Carbides.				
SiC/SiC CVI	345-415			(75) 3D braid
SiC/SiC		230		(102) 0°/90°
SiC/Nicalon CVI	470			(88)
SiC/Tyranno CVI	390			(88)
SiC/SiC	300	200	30	(80) room temp
	400	200	30	(80) 1000°C 2D
	250	150	30	(80) 1400°C 2D
C/SiC	500	350	32	(80) room temp 2D
	700	350	32	(80) 1000°C
	700	350	32	(80) 1400°C 2D
SiC/C/SiC	390			(103) plain weave
SiC/SiC CVI	500-600	300-400		(104) 0°/90°
SiC/C CVI CVI	450-500	270-330		(104) 0°/90°
C/SiC Si polymer	190-210	250-300		(105) V_f 45-55%
SiC/SiC Si polymer	280-300	180-200		(105) 0°/90°
	280-300			(105) 1000°C 0°/90°
Nitrides.				
RBSN/SCS-6	682		13	(106) V_f 30%
HPSN/SCS-6			7	(107)
HPSN/SCS-6	600		13	(108) V_f 15%
SRBSN/SCS-6	713			(32) room temp
	554			(32) 1200°C
	486			(32) 1400°C
		413		(32) room temp

Table 2.3. contd. Properties of CMC fabricated systems.

considerable effect on the composite properties.

For SiC matrix composites it has been found that, although good composite properties can be attained, care must be taken to ensure that the fibre / matrix interface has controlled composition. Experiments using both the isothermal and forced CVI techniques have shown that uncoated fibres can exhibit brittle composite behaviour (88) (109) (110). For nitride matrix composites, all examples shown in Table 2.3. utilise the SiC SCS-6 monofilament. This is due to the high processing temperatures required during conventional RBSN / HP of composites. The monofilaments retain stability to higher temperatures and can be processed at 1400°C for the considerable times necessary for RBSN. However matrix porosity can lead to degradation of the pre-coated carbon interface (32).

2.3. Glass Ceramic Matrix Composites.

In Chapter 1., Section 1.6. reviewed some of the desirable properties of glass ceramics such as high strength, tailoring of phase structure either by composition or heat treatment, tailoring of thermal expansion, and the possibility of forming refractory crystalline ceramics from a conventional glass and hence using a relatively low temperature processing route. The possible use temperatures for some glass ceramic systems are indicated in Table 2.4., along with some glass systems for comparison. From Table 2.4., it can be realised that glass ceramics and polymer - precursor fibres have similar maximum use temperatures and hence the final composite is not compromised in ultimate temperature use by either constituent.

From Section 2.1. of this chapter a number of criteria were given to indicate compatibility between fibre and matrix and predict whether a good composite could be formed by a particular fibre and matrix. These suggested that $\Gamma_i / \Gamma_f < 1/4$, which for a weak interface can be satisfied (see below), $2 < \tau < 40$MPa, and ε_{THER} ~<

Matrix System.		Maximum Use Temperature (°C).
Glass Ceramics.		
LAS - I	(β - Spodumene).	1000
LAS - II	(β - Spodumene).	1100
LAS - III	(β - Spodumene).	1200
MAS	(Cordierite).	1200
BMAS	(Barium Osumilite).	1250
Mullite	(Mullite).	~ 1500
Hexacelsian	(Hexacelsian).	~ 1700
Glasses.§		
7740 Borosilicate	(Pyrex).	600
1723 Aluminosilicate	(CMAS).	700
7930 High Silica.		1150

Table 2.4. Possible maximum use temperatures of some glass ceramic and glass systems (from (39)). § denotes a Corning Glass Works designation.

3×10^{-3}. Most glass ceramic matrix composites use small diameter SiC fibres (Nicalon or Tyranno) whose thermal expansions are ~ 3×10^{-6}°C^{-1}. Hence, in order to satisfy the final condition of ε_{THER} mismatch, the thermal expansion of the fibre and the matrix need to be reasonably close. Table 1.5. of Chapter 1. shows this can be reasonably easily achieved by a number of crystalline phases.

Hence, the condition to satisfy is the sliding resistance of the fibre / matrix interface. For glass ceramic silicate systems there is a fortuitous chemical reaction at the interface which promotes a low shear sliding resistance between the fibre and the matrix. Systems shown to have this reaction are LAS, CAS, MAS, BMAS, and MAS for the Nicalon / Tyranno fibre (42) (77) (91). A carbon-rich interface is formed in-situ between the fibre and the matrix due to chemical reaction at the elevated processing temperature. A number of authors have identified this type of interface and reviewed its mechanism of formation (39) (76) (77) (78) (91) (95) (111) (112). Detailed reviews of interface role and formation, as shown schematically in Fig 2.6., can be found in (67) (91) (112) (113). The basic reaction that causes the formation of the C-rich interfacial layer is that of the oxidation of the SiC at the fibre surface :-

$$SiC + O_2 \rightarrow SiO_2 + C \qquad (2.12).$$

The carbon formed can be amorphous or graphitic dependent on the composite processing temperature, and can act as a diffusion barrier for gaseous

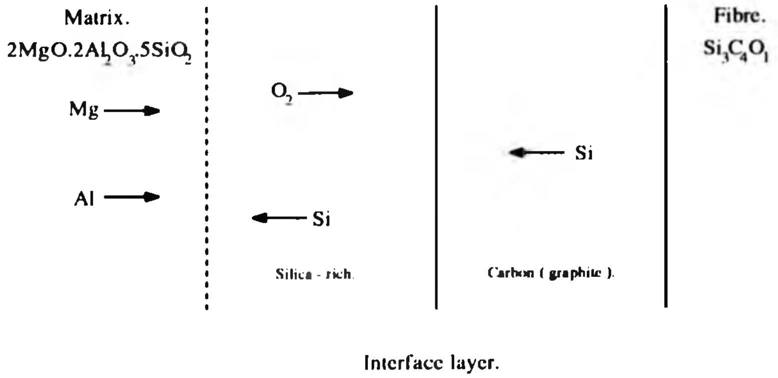

Figure 2.6. Schematic of the interface formation in silicate matrix composites showing direction of ionic or molecular diffusion.

oxygen, if the oxygen is derived from oxygen dissolved in the matrix, or for both the silicon and the oxygen down the activity gradient from the fibre to the matrix. It can be noted that the interface model developed by Cooper and Chyung (91) links SiO_2 activity in the composite matrix to the matrix 'basicity' and hence allows explanations of differences in interface reaction kinetics for different matrices. For silicates basicity is related to the degree of structural polymerisation. By the addition of network modifying oxides (Li_2O, CaO), the degree of ionic bonding is increased and hence the number of 'non-bridging' oxygens in the glass increases and results in a decrease of SiO_2 activity. This means that for matrices with a higher content of modifying oxide increased interface reaction kinetics should occur and, in comparison matrices with alkali ions, should have even greater reaction kinetics than the less basic magnesium or calcium silicates. This model proposed by Cooper and Chyung (91) does assume that carbon diffusion into the matrix is slow and this is consistent with the presence of a sharp matrix to fibre interface. This model is not the only model available, and a thermodynamic approach was adopted by Benson et al. (114) to model the stability of the reacted interfacial carbon layer. This model shows that CO may form as a result of carbon oxidation, this can then diffuse to the interface between the SiC and carbon and gives an alternative interface reaction :-

$$SiC + 2CO \rightarrow SiO_2 + 3C \qquad (2.13).$$

From this CO diffusion may be rate limiting, not the Si + O diffusion as in the Cooper and Chyung (91) model. Benson et al (114), suggest that oxide additions such as nucleating agents which are multivalent may increase the CO activity level and so increase the kinetics of this reaction. However, since CO formation redox reactions partly consume the interfacial carbon layer, reactions can be suppressed by the formation of carbides such as NbC (39) and TiC (77). An attempt has been made to do quantitative studies on the interface, but experiments can be complicated by the number of interdependent variables. Interface thickening experiments in LAS were carried out and found parabolic kinetics of C layer increase and typical activation energies for diffusion of gases in amorphous materials.

Clearly the Cooper and Chyung (91) model for the oxidation of the SiC fibre is somewhat simplistic. During the composite fabrication the matrix constitution will change as the interface forms and hence a compromise for interface formation will be made with the temperature of composite fabrication and crystallisation of the matrix. It can be noted that a composite not having a C-rich or low τ interface exhibited brittle failure (91). Typical values for systems studied for both the debond energy of the interface Γ_i and the shear sliding resistance τ for GCMCs, are given in Table 2.5.

Since the role of the interface is critical to the determination of mechanical properties it is interesting to note the correlation of mechanical and interfacial micromechanical properties for composites in the thermally aged condition. As the development of GCMCs has progressed authors have begun high temperature aging in various environments to check the applicability of these composite systems for

Matrix System / Reinforcement Type.	Interfacial Micromechanics.		Ref.
	2Γ (Jm^{-2}).	τ (MPa).	
LAS / Nicalon	$2x10^{-4}$	2.8 - 3.5	(113)
BMAS / Nicalon	60.3	5.5	(113)
CAS / Nicalon	249		(113)
Corning 1723 / Nicalon	236		(113)
LAS III / Nicalon	$2x10^{-4}$	2.7 - 3.5	(116)
BMAS III / Nicalon		5.5	(116)
SiC / Nicalon		49 ± 15	(116)
(0.03μm Carbon)		25 ± 14	(116)
(0.07μm Carbon)		11 ± 5	(116)
(0.12μm Carbon)		0.6 ± 0.4	(116)
Mullite / SCS - 6	>200		(113)
Mullite / SCS - 6	85	30	(113)
Glass / SCS - 6	2.9	0.06	(113)
Glass / SCS - 6 (BN coated)	2.9	0.06	(113)
SiO_2 / SCS - 6	0.3	0	(113)
SiO_2 / SCS - 6 (BN coated)	0.3	0	(113)
SiN_x / SCS - 6		14.7	(116)
Borosilicate / SCS - 6		11.6 ± 1.3	(116)
SiN_x / SCS - 6		3.0	(116)
Mullite / SCS - 6		16.4	(116)
Zircon / SCS - 6		15.0	(116)
Soda - lime - silica / SCS - 6		13.9 ± 4.1	(116)
Borosilicate / SCS - 6		3.6 ± 0.7	(116)

Table 2.5. Measured interfacial properties for some GCMCs.

their intended applications. For composites aged in air for relatively short periods of time there can be considerable effects on the interfacial properties and this directly correlates with the mechanical properties (67) (80) (115) (116). The mechanism that is thought to operate is as follows :-

i). At low to intermediate temperatures (~ 600-800°C), the carbon interfacial layer is removed by oxidation to leave a gap or partial silica bridge.

ii). At higher temperatures the carbon rich layer is removed and replaced by a silica layer. If the formation of this silica layer is rapid a plug can form at the ends of the exposed fibres which effectively protects the composite from further degradation by oxygen ingress down the fibre's length. However, if the silica formation is slower the layer can extend down the fibre length. Studies have indicated that the onset of silica bridging occurs at temperatures >850°C and authors have shown that the silica bridge has resulted in an interface of high shear sliding resistance and hence degraded mechanical performance (38) (76) (80) (115).

It should be noted that for the fabrication of GCMCs as indicated earlier in this section there is a compromise between the composite densification, thermal stability of the fibre, crystallisation kinetics of the matrix and interface formation. A schematic of this is shown in Fig 2.7., in order to indicate the difficulty associated with composite fabrication.

The above review has indicated some of the GCMC systems already studied and their properties. The next section deals with the selection procedure for the composite system studied in this work.

2.4. Selection of Fibre and Matrix.

In selection of the composite matrix and fibre for use in this research a number of factors needed to be considered, many of which have been mentioned in the above discussion and Chapter 1. As indicated in Chapter 1., CMCs can offer

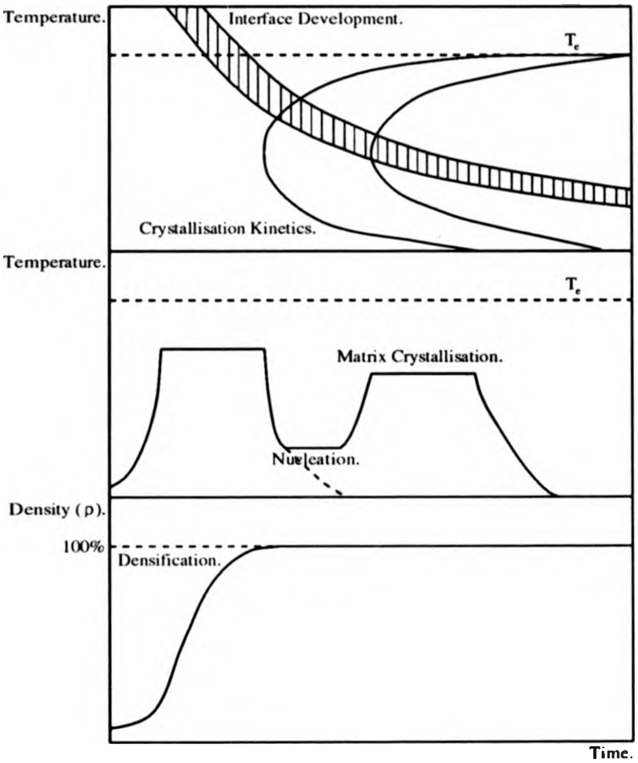
Temperature.
Interface Development.
T_c
Crystallisation Kinetics.
Temperature.
T_c
Matrix Crystallisation.
Nucleation.
Density (ρ).
100%
Densification.
Time.

Figure 2.7. Processing compromises in the fabrication of GCMCs.

considerable benefit to the gas turbine engine, but this requires the material to have high specific strength, good durability, creep resistance and complex shape capability.

These requirements and in particular those of creep resistance at high temperatures preclude the use of glass matrix composites. Complex shape capability indicates that a large diameter fibre such as Textron SCS-6 fibre is more difficult to utilise because of its maximum bend radius and so a small diameter fibre is preferable. From Table 2.1., it can be seen that a large number of fibres can be found with a small diameter, but other selection criteria for fibres need to be invoked. These criteria are :-

. Low density.

. High strength.

. High modulus.

. Oxidation resistance.

. Retention of properties to high temperatures (~ 1000-1200°C).

. Creep resistance.

. Thermal expansion coefficient close to that of the matrix material.

These further criteria allow many of the fibres to be eliminated. Carbon fibres cannot be used since their use temperature is limited by oxidation resistance to below ~ 500°C. As stated in Section 2.2.1., oxide fibres require precoating before incorporation in the matrix, in order to achieve a low shear sliding resistance interface and problems associated with high temperature creep deformation cause problems with their use.

The nitride / carbide fibres have properties which suit CMC application. The Fiberamic fibre retains its amorphous state to 1400°C before a 25% drop in strength occurs. However, these fibres are not readily available for use and hence, because of the scale of process development required in this study, were not used. Furthermore, studies have shown that pre-synthesised interfaces may be required with this type of fibre constitution, as fabrication with an MAS matrix / HPZ fibre resulted in a SiO_2 / C phase separated interface which, although not characterised mechanically, was thought not to have the required micromechanical response (77).

Hence the fibres which fulfil the selection criteria, and to which access is available in reasonable quantities, are the SiC fibres of Nicalon and Tyranno. Both fibres are very similar in composition and specification as seen in Table 2.1., with the Tyranno fibre having a higher oxygen content and a lower residual carbon content. The Nicalon SiC fibre was selected for this research since development has continued since its first manufacture in 1976 by Yajima et al (49) (81), and its properties and degradation are characterised. For both fibres studies have indicated that the free carbon is partly dispersed as graphite microcrystals and partly dissolved in the amorphous, mixed co-ordination tetrahedra (SiO_xC_{4-x} : $0 < x < 4$), with the oxygen accommodated in the network (85).

The degradation in properties of Nicalon with temperature was shown by Ko (75) and evaluation in more detail was undertaken by Bender et al (117). For the

Nicalon fibre, when heat treated in argon or nitrogen for 15 minutes, strength is retained to 1200°C before significant degradation. Under identical heat treatment conditions but in air, strength degradation is seen to occur at ~ 850°C (75). From Bender et al (117), a number of degradation mechanisms have been proposed including grain growth (originally ~ 2nm (117)), a change in Young's modulus, microporosity formation, crystallisation, growth of pre-existing flaws and the formation of surface flaws. Studies have suggested that the microstructure and chemistry are changed by high temperature exposure due to the evolution of SiO and CO from the fibre and hence thermochemical stability is critical. The evolution of CO from the fibre is critical to strength retention, and a study has shown that using CO heat treatments could increase the fabrication temperatures used currently (117).

For this research two types of Nicalon fibre were used. The type originally utilised is the NL-201 fibre, this being a standard ceramic grade Nicalon fibre with epoxy sizing designed for general use. The second Nicalon fibre utilised is the NL-607 fibre, which is a carbon coated ceramic grade fibre. This fibre was designed for use in CMCs and, apart from a 10-20nm pyrolytic carbon coating, shows the same properties as the standard ceramic grade fibre, and is supplied with PVA sizing.

For the selection of the matrix, as for the fibre, a number of criteria can be used and since a particular fibre has been identified the criteria relevant for this fibre need to be incorporated as well :-

. Composite use temperature.
. High strength.
. Good chemical durability.
. Matrix thermal expansion needs to be close to that of the fibre.
. Fibre / matrix interface formation.
. Creep resistance.
. Oxidation resistance.

Since Nicalon only exhibits thermal stability in nitrogen or argon to ~ 1200°C, a low temperature fabrication route is required for the composite. The way this was achieved in this work was to utilise a glass ceramic matrix.

By appropriate selection of the major phase in a glass ceramic, the composite matrix can fulfill all of the above criteria. Since a refractory matrix was required, a high temperature melting phase was selected, with a view to mechanical properties, thermal expansion, creep and oxidation resistance. The magnesium aluminosilicate ternary system was selected, with the major crystalline phase identified as cordierite. Cordierite in its high temperature polymorphic form has a thermal expansion coefficient of 2.6 x 10^{-6}°C^{-1} (very close to that of the fibre), a flexural strength of ~ 200MPa and, from Table 2.4., a use temperature of up to 1200°C, which is the point of thermal instability in the fibre for nitrogen or argon atmospheres. Within this study compositional issues, which are discussed more fully in Chapter 4., have allowed tailoring of the matrix thermal expansion by moving the composition along a tie line between cordierite and the higher thermal expansion coefficient phase enstatite (for enstatite $\alpha = 7.8 \times 10^{-6}$°$C^{-1}$).

Cordierite is a phase much used in the refractories industry and retains good high temperature strength with good thermal shock properties (51) (52). Since it is a silicate glass ceramic the fortuitous reaction described in Section 2.3. of this chapter enables the fabricated composite to have the desired interfacial micromechanical properties if the time and temperature process parameters are suitable (77).

2.5. Research Program Objectives.

In this chapter, CMCs and in particular GCMCs have been introduced. The last section, Section 2.4. has identified the reinforcement type, the composite matrix and the major crystalline phase required in that matrix. Further information on the matrix composition selection can be found in Chapter 4. The main objectives of this research program were :-

i). The identification of matrices suitable for potential composite application in the range 700-1200°C.

ii). Preliminary investigation into time and temperature HP conditions and their influence on the microstructure and interface structure.

iii). Development of a process to slurry infiltrate fibre yarn with glass ceramic frit and the construction of a laboratory scale filament winding system.

iv). Development of a hot press cycle to fabricate composites with the interface desired for appropriate micromechanical interfacial properties and appropriate matrix microstructure.

v). Evaluation of the general composite mechanical properties in the as-fabricated and thermally-aged conditions.

vi). Evaluation of composite mechanical properties at elevated temperature for short term exposure.

vii). Investigation of the micromechanical response of the interface and interface constitution for both the as-fabricated and thermally-aged composites, both by direct measurement and by microscopy.

Chapter 3. Experimental Techniques.

The composites produced in this study were characterised using a number of different techniques, with other techniques being used to modify and refine the processing routes used for fabrication. Microstructural characterisation involved the use of scanning electron microscopy (SEM) to identify phase distribution within the matrix, and x-ray diffraction for phase identification. The fibre / matrix interface constitution and composition were identified using transmission electron microscopy (TEM) and the interfacial parameters of debond energy (2Γ) and frictional sliding stress (τ) were measured using a fibre 'push-down' technique.

Macromechanical behaviour was evaluated at room temperature using 3 point flexure and tensile configurations, whereas for higher temperatures 4 point flexure and tension were used. Miscellaneous techniques were also used to evaluate density, thermal expansion coefficient and volume fraction of fibres within the composites. Glass powder characterisation used particle size analysis and differential thermal analysis (DTA).

3.1. Scanning Electron Microscopy.

3.1.1. Specimen Preparation.

During the course of this work two SEMs have been used for microstructural characterisation, a Cambridge Stereoscan S250 and a JEOL JSM 6100. Both microscopes are fitted with Link Analytical EDS detectors and analysers, the S250 being equipped with a Link Pentafet and AN10000 computer and the JSM 6100 with a Link Pentafet and e^{XL}II hardware / software. Samples were either coarse sliced using a Tyslide diamond saw, or were more accurately machined using a Capco annular diamond saw.

The samples were usually mounted in either MetSet polyester resin or Ciba Geigy plasticised liquid epoxy resin (Araldite MY753 with hardener HY956) which set cold and without applied pressure. The polishing was carried out both by hand and, by using a semi-automatic machine (Buehler MetaServ). For the hand prepared samples, SiC paper was used in the stages 320 (46μm), 600 (26μm), 800 (22μm), 1000 (18μm), 1200 (14μm), followed by diamond solution polishing of 6μm, 3μm, 1μm, and a final step of <¼μm. For samples polished automatically the series used was 70μm, 30μm, 6μm, 1μm with a final stage of <¼μm. The sample mounts were then painted with a carbon solution to prevent specimen charging within the microscope before carbon coating of specimen surfaces. If analysis involving light element identification was to be carried out the samples were given a gold sputter coating. Flexure samples were mounted and polished as indicated above, whereas for tensile fracture surfaces, the composites were attached to a stub using a conducting carbon glue and were then gold sputter coated.

3.1.2. SEM Imaging.

The main imaging modes used were those of secondary electron imaging (SE) and backscattered electron imaging (BS). Some x-ray mapping was used to try to identify the interface composition, but this had limited success. SE images were used mainly to check the topography of samples, since some of the fibres had a tendency to 'pop-out' from the surface of the sample. This is indicative of debonding of the fibre / matrix interface during sample preparation by the relief of thermal residual stresses within the composite. SE imaging was also used to view the fracture surfaces of the tensile loaded composites, since the large depth of field allows detailed imaging. The BS mode was used mostly for the microstructural characterisation of the composites. Contrast variations between the three main phases of cordierite, enstatite and silicon carbide are relatively small. However, areas containing the impurity element zirconia gave much higher contrast than the rest of the sample.

Phase identification was carried out where possible using EDS spectrometry, ensuring that the analysed area was within the x-ray excitation volume. Although both SEM systems used here had the capability of detecting light elements, no quantitative light element analysis was carried out because of the problems involved with this type of analysis (soft x-ray absorption, chemical shifts, matrix corrections and contamination). The light element capability of these systems was however used to try and detect the fibre / matrix interface in both the as-received and the thermally-aged composites. Two approaches were tried, linescanning and x-ray mapping. Both techniques met with limited success, as the interface region identified by TEM studies was too small, in comparison with the x-ray excitation volume for this technique.

3.2. Transmission Electron Microscopy.

3.2.1. Specimen Preparation.

The transmission electron microscope has been mainly used in this work for the characterisation of the fibre / matrix interface, with a limited amount of work carried out upon the matrix. The microscope used for this work is a JEOL JEM2000FX operated at 200kV, and EDS analysis, including a light element capability, was available via a Link e^{XL}II system coupled to two Pentafet detectors. A standard route was devised to prepare the TEM thin sections :-

i). Using a Capco annular diamond saw variable thickness sections were cut from the unidirectional composite perpendicular to the fibre direction.

ii). Sections were mounted on a glass slide using Crystal Bond or Lakeside wax (supplied by Testbourne).

iii). Mounted sections were ground / polished using 1000 / 1200 grit SiC paper to a thickness ~ 80μm before polishing with diamond slurry to a 1μm finish.

iv). Polished sections were then glued to copper slot grids (3mm diameter, with 2 x 1 mm slot) using epoxy resin (Araldite Rapid). Composite sections overhanging the copper ring were trimmed using either scalpel or razor blade.

v). The grid mounted sample was lightly dimpled on both sides, using a Southbay Technology Inc. Model 515 Dimpler.

vi). Dimpled samples were ion beam thinned using Ar ions at 5keV and angles < 30° until perforation of the sample occurred.

During preparation of the specimens a number of problems were encountered. Since the specimens were prepared from unidirectional composites, the relatively high concentration of fibres within the matrix meant that samples were relatively fragile, with cracking occurring even during the sectioning process. The fibre / matrix interface readily allows cracks formed to propagate through the sample, around the fibres. Early composites which exhibited poor mechanical behaviour were found to be extremely weak when sectioned and so, if the sections produced during stage i). were too narrow, they crumbled. During the grinding / polishing stage iii)., only the fine SiC papers were found to be suitable as coarser grades again introduced cracks into the specimens. During the final step of Ar ion beam thinning the fibres were seen to preferentially thin, although this effect could be reduced by using a shallower angle of incidence for the ion beam.

3.2.2. TEM Imaging.

The TEM was used mainly in absorption contrast mode, giving an image of the matrix and the fibre / matrix interface in high resolution. This form of contrast arises from the incoherent scattering of electrons from both the crystalline and the amorphous regions of the specimen. The intensity of the electron beam image can be related to the incident electron beam intensity using a simple power law. Tilting of the specimen allowed for the identification of amorphous regions within the sample.

High resolution imaging using the TEM allows the interface structure to be observed. Using the light element detection system available, the interface constitution was also determined. Quantitative analysis was not attempted, for the reasons given in Section 3.1., although studies of elemental presence and distribution in the interface region were carried out.

3.3. X - Ray Diffraction.

This technique was used to identify the phases present in the composite and the monolithic samples. Identification of the phases was carried out by the use of the J.C.P.D.S. files. For this study the main files used were (2-1057), (12-303), (14-249), and (19-768). The experiments were carried out using a Phillips PW 1130 / 00 X - ray machine, interfaced to a chart recorder for most of this work and then later to an Acorn Archimedes computer.

3.4. Differential Thermal Analysis (DTA).

This technique is mainly used in the study of the crystallisation of glasses and can be used to identify chemical and structural changes in the crystallisation of initially glassy matrices. Broad overviews of this subject can be found in McMillan (51) and Strnad (52). For the experiment glass powder is placed in one crucible and heated at the same time as standard (i.e. Al_2O_3 or SiO_2) with thermocouples connected to both. The standard can be inert, or gives a well defined event. An example DTA trace is shown in Fig 3.1., and gives the features by which information regarding the crystallisation of the powder can be found. Point 1. allows the approximate positioning of the glass transition temperature, T_g, which is indicated by an endothermic change in the curve, and the dilatometric softening point can be identified by point 2. The exothermic peaks, illustrated by points 3., and 4., are associated with the formation of crystalline phases. The shape of the peaks can give information on the crystallisation process. Finally, point 5., corresponds to the first melting of the crystalline phases within the sample, the endothermal minimum of fusion.

Because of the information that is attainable from the DTA curve, it is very useful for the determination of heat treatment schedules for glass ceramics and their ultimate use temperatures. The technique can also be used to study the kinetics and mechanisms of crystallisation by the variation of heating rates. However, for this study only one heating rate was used (10°Cmin^{-1}) and results were obtained using a

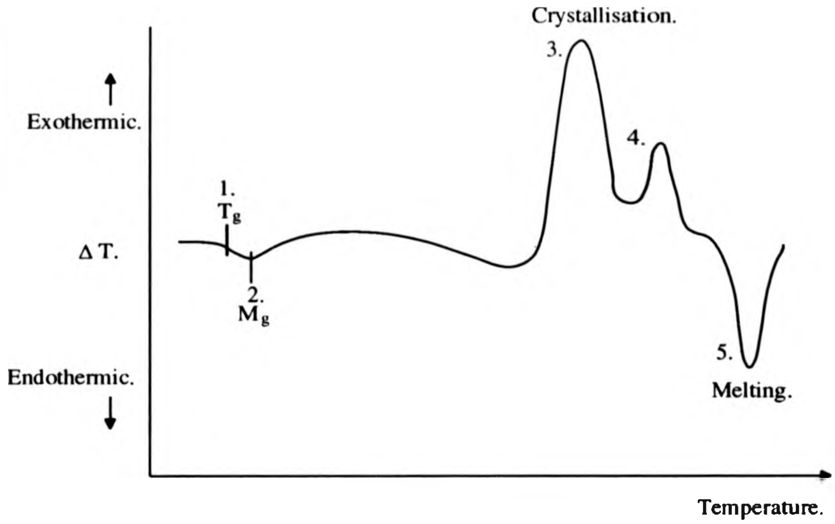

Figure 3.1. Schematic DTA trace illustrating the type of features obtained.

Stanton Redcroft DTA (Model DTA 673-4) with a maximum temperature of ~ 1250°C. From the results, crystallisation peaks were identified, as well as processing windows for the composites.

3.5. Mechanical Testing.

A number of different mechanical test methodologies were used in order to evaluate the mechanical behaviour of the composites, both at room and elevated temperatures. At the start of the program a simple 3 point flexure test was used in order to gauge the performance of the composites in the as-fabricated and thermally-aged conditions. This particular test methodology has the advantage of simplicity and small specimen size. However, care must be taken, when using this test, that the span to depth ratio is sufficiently large to avoid large shear delamination forces in the specimen (50). This test was used for the bulk of the study to rank processing routes, in order to provide some optimisation of the processing schedule for the composites. The thermal aging treatments carried out also employed this mechanical test methodology for consistency in the comparison of results. Towards the end of the program in-situ high temperature bend tests were carried out using a 4 point articulating jig. Larger specimens were fabricated using the process route developed in this study by Rolls-Royce, these allowed a limited amount of room and elevated temperature tensile testing and some tensile creep studies to be conducted.

It is important to realise that the different mechanical test methodologies used in this study have limitations as well as inherent advantages. Various authors have studied these methodologies to compare results (12) (43) (92) (118) (119). From the work of Evans (12), it has been identified that the matrix microcracking stress σ_{mm} can be satisfactorily evaluated in flexure or tensile tests, whereas the ultimate strength σ_{ULT} can only be evaluated correctly in tension. This is somewhat different to the work of Singh who found for a Zircon / SCS-6 composite that the Young's modulus E could be measured by either tension or flexure, but flexure testing gave higher values of σ_{mm}, σ_{ULT} (~ 70-75% of σ_{flex}) and ε_{mm} than for tensile tests (43). For this work the assumptions by Evans are used, Singh has however indicated empirically that both test methods give the same trends in composite behaviour with composite parameters (43). Other parameters such as WOF have also been found to depend on the test methodology (92).

Although both test methodologies are reviewed in more detail below, a few points regarding the applicability of each technique are indicated here. Flexure tests offer a number of advantages including simplicity of specimen geometry, small specimen size, and ease of technique adaption to high temperatures. However, a non-uniform stress distribution occurs in the sample, and the volume of the sample under test is smaller than for a tensile test. Because of this stress distribution, as the microcracking stress, σ_{mm}, is traversed, microcracks only occur in the tensile half of the specimen which destroys the macroscopic uniformity of the sample. Also, the failure mode in flexure needs to be identified, as failure can occur not only on the tensile face as required, but also by shear and compression (92).

Tensile tests do allow evaluation of all composite properties (WOF, σ_{mm}, ε_{mm}, σ_{ULT}, and ε_{ULT}), but problems are associated with a complex specimen geometry, specimen gripping and off-axis loading. As indicated in Chapter 2., failure for 0° / 90° laminate samples can be complicated (118). For tests carried out in this program relatively small numbers of samples have been used in each condition, hence statistical data treatments have not been used.

3.5.1. Room Temperature Mechanical Testing.

For the room temperature mechanical evaluation the majority of the testing work was carried out in three point flexure. As larger specimens became available toward the end of the program the room temperature evaluation was extended to include some tensile testing. For flexure testing in general, a number of sources of error can be identified, such as unequal moments, twisting, wedging stresses, pin to specimen friction, load mislocation and changes in the point of load application causing changes in moment (7) (120). The first four of these are first order errors, the first three tending to reduce the calculated stress, whereas the fourth increases the calculated stress. Frictional errors can be significant, but are difficult to remove and compensate for (120). Wedging stresses can be calculated and are usually the smallest of the first order errors, and are generally found to be negligible when the ratio of the specimen depth to its length is less than one (120). The errors can be minimised by careful sample alignment in the fixture, and the final error is not usually significant for short term tests such as those being discussed. Also, if the length of the specimen is increased relative to the other specimen dimensions, then the magnitude of the errors is decreased.

Errors may also occur if specimens deflect a large distance, and if the mode of failure in the test is not identified (119) (120). Several studies have proposed testing methodologies for high toughness CMCs, incorporating three and four point flexure as well as tensile tests. These tests recommend specific span to depth ratios for flexure tests :-

. For 3 point flexure : 15 - 17 : 1 (121).
3.91 ± 1.8 : 1 (119).
. For 4 point flexure : 30 - 34 : 1 (121).
42 : 1 (50).
21 - 23 : 1 (119).

This avoids high shear values in three point bending and the onset of matrix fragmentation for both (50). For the three point flexure testing carried out in this program the jig utilised hardened steel rollers in v-grooves in order to minimise frictional forces. The outer span was 44.5mm meaning that the span to depth ratio achieved was ~ 15:1. The samples were tested using a screw driven Instron 1122 tension / compression machine interfaced to a BBC microcomputer for automatic data logging. Samples also had an acoustic emission probe attached to monitor acoustic events and identify σ_{mm}. Acoustic events were processed by a Dunegan / Endevco system (modules 302A, 402, 920, and 922), which allowed calculation of the number of counts in a time envelope, but was not calibrated to measure the energy of the acoustic events. Acoustic jelly was used to couple the sample to the probe.

This data could be analysed using an Acorn Archimedes computer to evaluate the apparent stress via the equation for three point bend :-

$$\sigma = \frac{3PL}{2bd^2} \qquad (3.1).$$

where P = the overall applied load.

L = the span.

b = specimen width.

d = specimen depth.

Young's modulus was evaluated from the linear elastic region of the stress / deflection curve. All samples were prepared from the as fabricated composite by one of two approaches :-

i). For the in-house fabricated unidirectional plates (50x50mm), samples 3mm wide were cut using a Capco annular diamond saw.

ii). For the larger unidirectional fabricated tiles (100x100mm), samples were sectioned using a diamond dressed surface grinding wheel.

For both types of sample preparation the resulting bars were approximately 3x3mm in cross section and 50mm in length. Samples were then cleaned ultrasonically in methanol to remove wax from the mounting process. The samples were then tested as-cut, usually with a cut surface as a tensile surface in order to minimise the effects of the glass ceramic on the tensile surface as recommended by Evans (37). No surface grinding or polishing was carried out on the composite samples. For the limited amount of monolithic bend testing carried out in this study, samples were prepared from hot pressed matrix using the Capco annular diamond saw followed by progressive surface grinding to a 1μm finish. All samples were tested at a cross-head speed of 0.5mmmin^{-1}.

For the room temperature tensile testing, only the larger 100x100mm plate size could be used in a cross-ply orientation. Samples were gripped using a dovetail geometry shown schematically in Fig 3.2., along with the tensile specimen dimensions. This geometry was used since this apparatus was designed for tensile creep studies, for which edge loading is preferred over face loading (see Section 3.5.3.). Tensile tests were carried out using an Instron 1185, screw driven, tension / compression machine with a 100kN frame. The samples were diamond machined to the correct geometry using a CNC machine. As was the case for the flexure specimens, the samples were ultrasonically cleaned in methanol. Care was taken to ensure good sample alignment in the grips and that the sample was bedded in. Sample displacement was measured using a MTS contact extensometer with high temperature capability, and acoustic signals were monitored via a grip mounted acoustic probe. For this system,

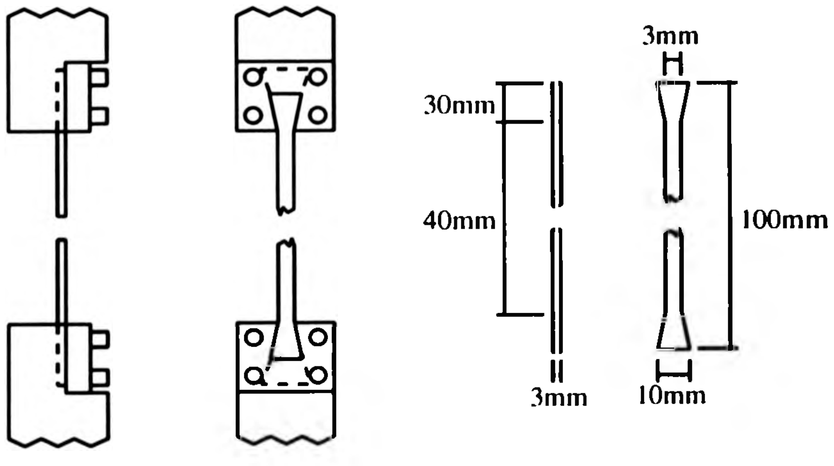

Side view. Face view. Specimen geometry.

Figure 3.2. Tensile gripping arrangement and specimen geometry.

test results were logged using an Acorn Archimedes computer. For this apparatus the acoustic signal was processed by an in-house amplifier system to give counts in a time envelope only. All samples were tested at a cross head speed of 0.2mmmin^{-1}.

Interpretation of tensile test results is easier than the flexure case since the whole of the sample is subjected to the tensile force and the stress is calculated simply by the force over the cross sectional area. As before, the composite elastic modulus can be calculated from the linear elastic portion of the curve. However, for this study, tensile tests were carried out on 0° / 90° laminate samples for which the interpretation of the tensile test curve is more difficult (72). The tensile response of these composites is reviewed in more detail in Chapter 6.

3.5.2. Elevated Temperature Mechanical Testing.

Most mechanical characterisation performed in this study was carried out at room temperature, although some short term high temperature tests were carried out both in tension and flexure. For high temperature flexure an articulating four point jig was constructed consisting of an alumina tube with SiC rollers, as shown in Fig 3.3. This enabled the same dimension samples as were utilised in the room temperature flexure evaluations to be used, although the span to depth ration is not in the range suggested (50) (121). From Marshall and Evans (92), it is suggested that the inner rod spacing is much less than the inner / outer rod spacing in order for the first damage to be matrix microcracking. There is not an obvious deviation from linearity and so for four point flexure either acoustic emission or direct observation should be used. This was not possible in this study. Care has been taken in the interpretation of σ_{ULT} as, if compressive matrix fragmentation occurs, the result is invalid. Samples were prepared as described in Section 3.5.1. The stress can be calculated for this test methodology from the following equation :-

$$\sigma = \frac{3P(L - l)}{2bd^2} \qquad (3.2).$$

where l = the inner loading span.

P = is the total load applied, half on each inner load point.

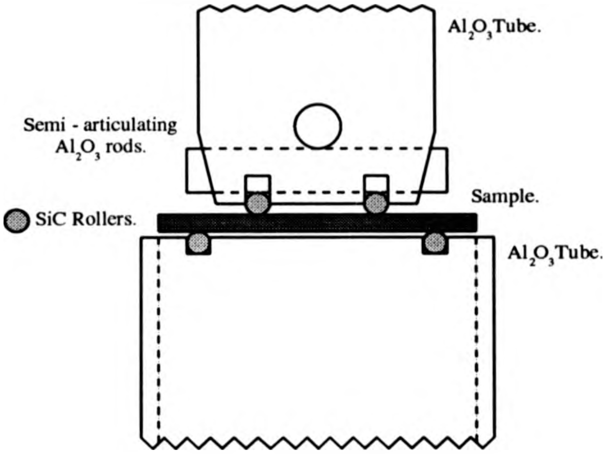

Figure 3.3. Schematic of four point high temperature flexure rig.

The alumina jig was heated by a split furnace at ~ 10°Cmin^{-1} with at least 30 minutes at temperature for the sample to stabilise. A slight preload, which was maintained below 40N, was used to keep the jig assembly in the correct orientation. Testing was carried out as above at 0.5mmmin^{-1} and data were recorded and analysed as above. However, acoustic emission could not be used since probe attachment to the sample was not possible.

For the tensile high temperature tests water cooled nimonic alloy grips were utilised, as for the room temperature tests, with the same configuration as shown in Fig 3.2. The furnace was used only to heat the gauge section of the sample and hence very fast heating rates can be attained (~ 15°Cmin^{-1}). Because of this, tensile samples were allowed to stabilise for ~ 1 hour at temperature. As for the bend testing, a small preload ~ 10MPa was used during heat up of the specimen to maintain its position within the grips. Again, computer data recording was used, with acoustic emission still possible since the grip mounted system was not affected by the furnace.

3.5.3. Creep Deformation Testing.

Utilising the large composite fabricated 100x100mm tiles allowed some tensile creep studies to be carried out. Samples were CNC machined as in the case for the tensile tests carried out (see Section 3.5.1., and 3.5.2.). The load frame and furnace used were as for the tensile high temperature tests. Extension could be very accurately monitored using the MTS contacting extensometer (100g edge load). For creep studies, the edge loading geometry was selected because of ease of specimen alignment and the lack of high contact forces as required by friction gripping (122). Other factors which can cause errors are kinking stresses introduced by specimen misalignment, temperature gradients in the furnace and transverse loadings (i.e. the extensometer).

For the tests carried out in this work, the high temperature tensile tests gave an indication of the creep conditions to be used, since these allowed for determination of the microcracking stress at temperature. Creep data was collected for a number of stress and temperature regimes, in order to gain information as to when the composite was characterised by plastic matrix and elastic fibres, plastic matrix and fibres, and when the composite was microcracked.

3.6. Micromechanical Measurement.

As noted previously, the interface plays a critical role in the determination of CMC mechanical properties. Changes in the interfacial micromechanical properties can cause large differences in the properties of composites, as demonstrated for the CAS / SiC system and the LAS / SiC system (67) (115). For quantitative evaluation of the shear sliding stress τ, the fibre pullout lengths, the saturation crack spacing, the unloading modulus and the hysteresis loop can all be used. The interfacial debond energy Γ, can be measured from the permanent strain ε_p, and the residual crack spacing. Only indentation tests allow calculation of both τ and Γ.

Indentation based techniques could be utilised within this study because of apparatus built at Warwick for the evaluation of interfacial micromechanics (123).

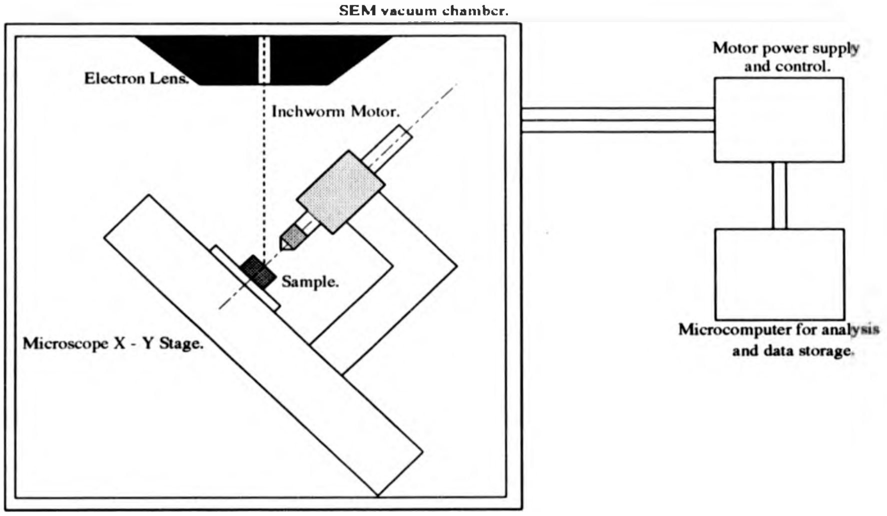
SEM vacuum chamber.
Electron Lens.
Inchworm Motor.
Sample.
Microscope X - Y Stage.
Motor power supply and control.
Microcomputer for analysis and data storage.

Figure 3.4. Schematic of the SEM based indenter system.

This system is a novel SEM based indenter as shown schematically in Fig 3.4., which utilises a piezo-electric motor to apply a load of up to 20N (this is in comparison to the nano-indent systems load capability of 0.1N). Load is measured by a piezo load cell to a resolution of 1mN. The apparatus is displacement controlled, a conical diamond of angle ~ 76° with a ~ 5μm radius tip is used to indent the fibre and allows the fibre to be pushed through a larger displacement than a Vickers or Berkovich geometry would allow. Displacement is measured via a capacitance gauge which permits a resolution of < 10nm over a 100μm range. Since the apparatus is SEM mounted the X-Y stage of the microscope is tilted to allow direct observation of the push down test. The whole apparatus is microcomputer controlled and this allows data logging of each test.

Analysis of data is also carried out via a microcomputer and uses the fibre push-down analysis developed by Marshall and Oliver (124). The analysis involves the subtraction of fibre reference hardness data from the actual push-down data, to compensate for the indentation depth of the diamond into the fibre. The model gives the fibre displacement in terms of applied load and material properties if stable crack growth occurs (124). :-

$$U = \frac{F^2}{4\pi r^3 \tau E_f} - \frac{2\Gamma}{\tau} \qquad (3.3).$$

where U = the fibre displacement.

F = the applied load.

Hence by plotting F^2 verses u, the gradient of the corresponding curve gives τ, and the y-axis intercept allows the calculation of the interfacial debond energy Γ. Specimens for push-down testing were prepared by bakelite hot mounting of 5mm deep sections followed by polishing as indicated in Section 3.1.1.

3.7. Miscellaneous Characterisation Techniques.

The composite samples were also characterised for volume fraction of fibres, density and thermal expansion. For fibre volume fraction determination in the composite, since small diameter fibres were being utilised, a computer based methodology was sought to avoid time intensive techniques such as paper cutting and weighing. For initial volume fraction measurements optical photographs scanned into the Link Analytical AN10000 system were studied using image contrast identification software. However, analysis features became available within the Link Analytical e^{XL}II system whereby a pre-programmed sequence could be written and used explicitly on different sections of the composite scanned directly from the SEM. Finally, a third system was available that could scan images as well as receive SEM images. The system is based around an IBM compatible 486PC and image analysis was carried out using a commercial package (Global Lab Image). This third facility allowed checking of the previous two analysis methods, based on its higher precision.

The density of the composites was measured for a number of test bars to give averaged results. The density was calculated from the samples weight in air and weight in water using the following equation :-

$$\rho = \frac{\text{Weight in air x Density of water}}{\text{Weight in air - Weight in water}} \qquad (3.4).$$

The variation of water density with temperature was accounted for in the evaluation. Prior to weighing in air all samples were cleaned in acetone, and prior to weighing in water samples were placed in a wetting agent. In some cases sample weight took ~ 10mins to stabilise in water indicating the presence of porosity.

Thermal expansion measurement was carried out using a fused quartz dilatometer and the temperature range 50°-900°C. The heating rate used was ~ $2°Cmin^{-1}$, and the apparatus was calibrated using a platinum standard. The extension of the composite was measured using a LVDT, and expansion calculated via the equation :-

$$\alpha = \frac{\Delta L}{L\Delta T} \qquad (3.5).$$

For the samples studied the thermal expansion coefficient was evaluated, over the range specified, as a linear quantity.

Finally, the glass powders were characterised for particle size. Analysis was carried out using a Malvern Mastersizer / E instrument utilising laser diffraction for the identification of particle size and distribution.

Chapter 4. Composition Selection and Composite Fabrication.

Within this study the approach to composition selection was first to investigate a number of compositions, based around the cordierite phase field, within the magnesium aluminosilicate ternary system, with additions of TiO_2 and P_2O_5. From these studies, and preliminary composite fabrication utilising chopped fibres, a composition was selected for further investigation and unidirectional composite fabrication. Composite fabrication involved the development of slurry infiltration for pre-impregnation of the fibre tow, fibre tow winding for a 'green' composite and the development, with refinement, of hot pressing schedules.

4.1. Composition Selection.

4.1.1. Silicate Ceramic Phases and the Glass Ceramic Process.

It has been previously noted that the MAS glass ceramic system was selected for the matrix within this study and that compositional issues were centred around the cordierite phase field with some inclusion of the higher thermal expansion phase enstatite. Cordierite has been studied extensively for use in a number of applications such as catalytic converter honeycombs, diesel particulate filters, spark plug insulators, refractories, electronic substrates, rotor vanes and heat exchangers in gas turbines.

Part of the MAS ternary diagram is shown in Fig 4.1., to illustrate the phases present and their melting temperatures. As cordierite melts incongruently at 1460°C the stoichiometric composition is outside the cordierite phase field and is in the mullite phase field. Cordierite as a phase is polymorphic giving, depending on the temperature of crystallisation :-

i). The high temperature stable or α form.

ii). The metastable lower temperature or μ form.

iii). A third stable form β-cordierite.

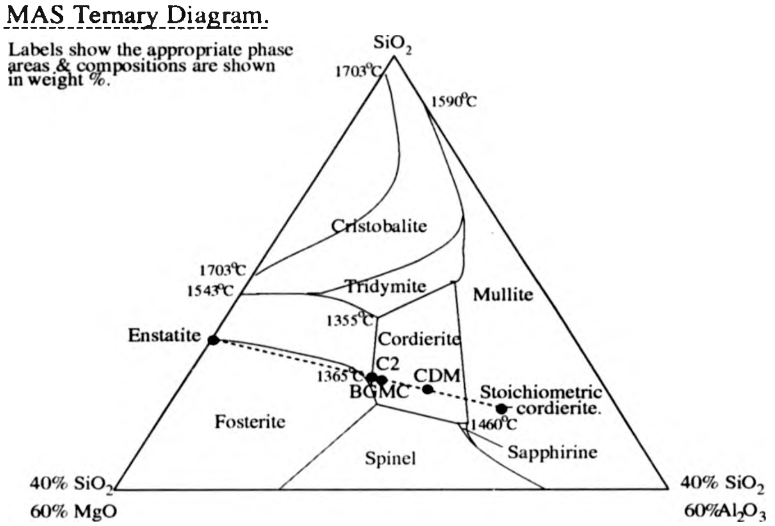
MAS Ternary Diagram.
Labels show the appropriate phase areas & compositions are shown in weight %.
SiO2
1703°C
1590°C
Cristobalite
1703°C
1543°C
Tridymite
Mullite
1355°C
Enstatite
Cordierite
C2
CDM
1365°C
BGMC
Stoichiometric cordierite.
1460°C
Fosterite
Spinel
Sapphirine
40% SiO2
60% MgO
40% SiO2
60%Al2O3

Figure 4.1. Part of the MAS ternary diagram.

The third form, β-cordierite, can be obtained from both the μ and α cordierites as well as from bulk glass and can be formed hydrothermally below 850°C (51) (125) (126). The two more widely used polymorphs of cordierite, the metastable form μ and the stable form α were discovered in a very early investigation into the MAS ternary system conducted by Rankin and Merwin (127). They identified these two polymorphs and noted that cordierites exhibited considerable solid solution. The naming of the metastable polymorph μ was left to Karkhanavala and Hummel (128).

The metastable μ-form has a structure related to that of β-quartz and, since it exhibits solid solutions between SiO_2 and $MgAl_2O_4$, is commonly referred to as a stuffed β-quartz solid solution (51) (52) (127) (129) - (134). Since the μ-form is metastable and transforms to the stable α-form at temperatures in excess of ~ 950°C, it can form first on crystallisation of the glass and the transformation can be sluggish to the α-form depending on whether nucleants are present in the glass (51) (127) (135). However for this study, since the potential application temperature is ~ 1000°C, μ-cordierite is not a desired phase and it also has a thermal expansion coefficient of $4.5\text{x}10^{-6\circ}\text{C}^{-1}$. Therefore it is undesirable as it would increase the matrix thermal expansion coefficient. The formation of the μ-cordierite phase has been studied by Roy (133) and is thought to occur by the precipitation of a silica rich solid solution with the isomorphous substitution of Si^{4+} tetrahedral sites by Al^{3+} ions, with Mg^{2+} ions occupying interstitial sites (129). The instability in the μ-phase may occur because of the lack of availability of small coordination number sites for the Mg^{2+} ions since, in the α-cordierite form, these ions occupy octahedral sites. The transformation of μ-cordierite to α-cordierite is non-reversible even for long heat treatments at high temperatures (136).

The stable high temperature α-cordierite polymorph can be formed from the bulk glass (μ-cordierite seems to form preferentially from powder surfaces (128)), or the μ and β polymorphs. A number of authors have carried out detailed investigations into its structure and have found that it is isostructural with beryl and is sometimes called indialite (137) - (141). It should be noted that, if α-cordierite is subjected to high temperature (~ 1200°C) treatments for extended times (~ 2000hrs), its structure evolves into a more thermodynamically stable form of orthorhombic symmetry. In this form it is known as 'low' cordierite, mineral cordierite or β-cordierite, as it contracts to the hexagonal 'high' cordierite. Many authors have characterised this cordierite structure and have found that the transition between the two forms may be categorised by order of the Si^{4+} and Al^{3+} ions within the nine tetrahedral sites and ranked by use of a distortion index Δ (142) - (147). Subsequent studies by Schreyer and Yoder indicated that compositional issues due to molecular water in the cordierite structure caused the transition form 'high' to 'low' symmetry and not polymorphism (148). However, the phases α and β cordierite are not easily differentiated via XRD, as the interplanar spacings for the two polymorphs are similar. A recent study has utilised TEM to identify the β-polymorph (126). All three polymorphs, μ, α and β, consist of Al and Si tetrahedra in six membered rings. However, for the metastable μ polymorph the tetrahedra form helices. Whereas, for the stable α and β polymorphs hexagonal rings are formed (126).

Before discussing the effects of nucleant additions to the crystallisation of cordierites, within this work a second phase within the MAS ternary system has been compositionally selected to be a desirable component in the final glass ceramic matrix. This phase is a higher thermal expansion phase enstatite, $\alpha = 7.8 \times 10^{-6}°C^{-1}$, with a melting point of 1557°C and hence is not expected to adversely affect the refractoriness of the final composite. As for cordierite, enstatite exhibits three polymorphs, ortho-enstatite (orthorhombic structure), proto-enstatite (orthorhombic structure), and clino-enstatite (monoclinic structure). Although the structures of the polymorphs are well understood stability is less well characterised, with clinoenstatite being the suggested low temperature polymorph (149). The polymorphs can be distinguished by the sequence of Mg atom planes in the a-axis direction but as stated by Lee (149) the use of XRD techniques to distinguish polymorphs is not easy. For this study no attempt to distinguish between polymorphs has been made, with enstatite presence in the composites being indicated by use of JCPDS (19-768).

For glass ceramic systems to be successful conversion of the glass into a crystalline form by devitrification must occur. A number of authors have discussed in detail the crystallisation mechanisms for glass ceramic matrices and so a detailed discussion will not be presented here (51) (52) (135) (150). It is important to realise that two processes need to occur for a glass ceramic matrix to be formed, those of nucleation and growth of crystals. For high strength glass ceramic materials, a small grain size is desirable and hence, before controlled growth of crystals occurs, it is important that a large number of crystal nuclei be formed. Nucleation within a glass occurs by two means :-

i). **Homogeneous Nucleation.** Because of brief structural fluctuations in the melt via thermal effects, nucleation with the same composition as the crystallising phase can occur. The nuclei are stable if they reach sufficient size such that the reduction in free energy equals or exceeds that of the interfacial surface energy, reducing the system's net free energy.

ii). **Heterogeneous Nucleation.** Here, the crystallising phase nucleates on a phase of different composition, which can range from a deliberate addition to the glass melt, free surfaces and impurity particles.

It is usual for heterogeneous nucleation to dominate since the activation energy required tends to be lower than that required for homogeneous nucleation. Also it is impossible to eliminate completely the presence of free surfaces and impurities within the glass melt. When these nuclei are formed, growth can occur by a reduction in the free energy for the system. In the above discussion it has been seen that phase separation occurs and hence nuclei are formed before growth of the glass ceramic crystals. For many glass ceramic systems phase separation can also occur via spinodal decomposition as described by McMillan (51) or Strnad (52). For spinodal decomposition the essential differences to the nucleation and growth mechanism can be described (51) : for spinodal decomposition, the composition changes continuously until equilibrium is reached, the interface between the two phases is diffuse to begin with but sharpens over time, and the two phases show high connectivity with regular spacing between regions, unlike the nucleation and growth.

If the nucleation rate is I and the crystal growth rate U, a schematic plot can be made to illustrate the temperature dependencies with time of these processes as shown in Fig 4.2. This figure also indicates heat treatment schedules that can be utilised to produce glass ceramics either as a two stage or single step heat treatment. Although very unlikely, if the temperatures T_2 and T_3 do not overlap, the nucleation and growth curves do not overlap, so the nucleation and growth processes can be controlled independently with full control over crystallisation. For the two stage heat treatment heating of the glass ceramic occurs to a temperature between T_1 and T_2 to allow for nucleation to occur, followed by a second heating step and isothermal hold to grow the formed nuclei. If nucleation in the glass ceramic is concurrent with crystallisation the

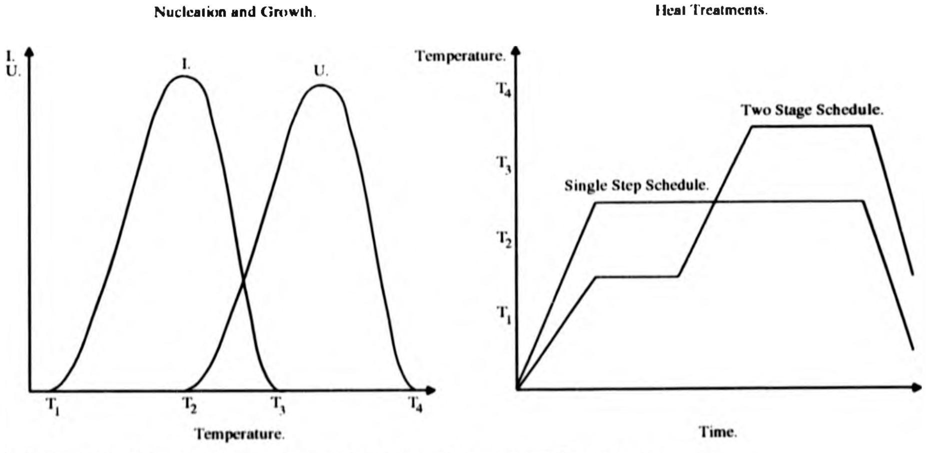

Figure 4.2. Nucleation and growth for a glass ceramic system.

single step heat treatment schedule may be utilised. A single step heat treatment can be used if T_2 and T_3 do not overlap. However, in this case, the nucleation rate must be high, in order to generate a fine grained microstructure as the nucleation curve is traversed during heating.

The nucleation and crystallisation kinetics of glass ceramics may be enhanced by the addition of nucleation catalysts to the glass melt. Detailed reviews on the roles of nucleants are given by McMillan (51) and Strnad (52). Generally nucleants can be divided into three categories, metals, halides acting by precipitation from the melt and metallic oxides. Within this study only limited work has been carried out on the addition of nucleation catalysts to MAS compositions and these additions have only been from the metallic oxides group, specifically being P_2O_5 and TiO_2. Because of this only these nucleants and their role will be discussed.

It should be noted that a number of authors have studied the role of nucleants in the MAS system and that the presence of impurities can significantly alter the crystallisation kinetics in this system, as can the thermal history (51) (52) (129) (131) (133) (150) - (152). The nucleant TiO_2 has been studied extensively and found to enhance kinetics in the range 2-20 wt% addition. It has been suggested that at higher temperatures the titanium ion forms part of the network as Ti^{4+}, but at lower temperatures promotes phase separation by destabilisation due to co-ordination effects as the ion goes to Ti^{6+}. Both Zdaniewski (129) and Barry (152) found that TiO_2 promoted μ-cordierite formation, although this may be due to a powder sample which can favour μ-cordierite formation. Barry et al. found that bulk crystallisation, which was poor, was effectively enhanced by the use of TiO_2, especially if a two stage heat treatment was used. As the amount of TiO_2 that was added was increased a lower crystallisation temperature was observed (152).

The role of P_2O_5 as a nucleant is somewhat different. The phosphorus ion is a network former but for electroneutrality requires an oxygen double bond and this network forming effect of the phosphorus destabilises the glass. Additions of P_2O_5 are not as large as for TiO_2, the P_2O_5 level being in the range 0.5-6 wt% with ~ 3 wt% being optimum in the MAS system (51). Hence P_2O_5 works by the promotion of amorphous phase separation, promotes surface nucleation and reduces melt viscosity (135).

For the study carried out here, although the effects of nucleants were investigated, for composite fabrication it must be considered that glass powder was used with a particle size in the range <20µm and so bulk nucleation characteristics are less important. The bulk nucleation efficiency of MAS is low. However, authors utilising powders have found that µ-cordierite may preferentially form suggesting that it may be surface nucleated as opposed to α-cordierite which is bulk nucleated (51) (133) (135). However, a fine grained microstructure can be produced by the crystallisation of a powder and if µ-cordierite is the first phase to form, then conversion to α-cordierite via a higher temperature heat treatment may be utilised (133) (135).

The MAS glass ceramic ternary system has been studied for use in composite systems previously as shown in Table 2.3. of Chapter 2. It is interesting to point out that Aveston, at the same time the A.C.K. theory was published, was experimenting with a cordierite based, glass ceramic matrix / SiC fibre composite (89). Considerable improvements for the composite properties were attained over the monolithic matrix material with toughening and pull-out observed. From this study Aveston also showed that composite properties were dependent on the polymorph of cordierite present in the matrix (89). When the matrix was the high thermal expansion coefficient µ-cordierite, brittle behaviour of the composite was experimentally observed. Whereas for the lower thermal expansion coefficient α-cordierite phase composite-like behaviour was observed. More recently Norman and Tilley have conducted an experimental program on cordierite-based, Nicalon fibre reinforced composites; the data for these systems is shown in Table 2.3., of Chapter 2 (53).

However, for the above studies the MAS composition used has been very close to, or that of, stoichiometric cordierite. During the initial study carried out in this work stoichiometric cordierite was used in order to compare with the compositions selected and to act as a benchmark for comparison with other studies. By movement away from stoichiometry a number of beneficial properties can be attained :-

i). Lower processing temperature to avoid fibre degradation.

ii). Tailoring of matrix thermal expansion to be above, below or equal to that of the fibre, allowing residual stress and interfacial characteristics to be altered by avoiding clamping stresses and interfacial decohesion.

iii). Availability of a process window for pressure.

The approach as indicated in Fig 4.1. has been to use a tie-line between stoichiometric cordierite and enstatite and to select compositions along this line up to the eutectic trough. Since the bulk nucleation efficiency of MAS glass is low nucleants were added, even though a powdered glass frit was being used, to see if their effect was important for these studies.

4.1.2. Glass Preparation and Crystallisation.

Initially glasses were based around the composition in weight percent as indicated in Table 4.1. The glasses were prepared via a standard technique as described below. Constituent powders were weighed and then mixed before glass melting (mixing time ~ 72 hrs). This charge was then melted in a platinum crucible at 1500°C (held at this isotherm for ~ 3 hrs) before pouring and quenching into deionised water. The glass was then dried and broken into small pieces (<<1mm) and remelted under the same conditions. This melt was then again quench cooled in deionised water and broken up into pieces (<<1mm) before ball milling in methanol with Al_2O_3 media for ~ 24 hrs and dried. Methanol was used since studies by Bridge had indicated that powders dry milled (i.e. no solvent) when sintered showed a strength decrease

Glass Designation.	MgO	Al_2O_3	SiO_2	Nucleants / Impurities.
Base glass.	24	22	54	
Base glass + P_2O_5.	24	22	54	2 P_2O_5
Base glass + TiO_2.	24	22	54	10 TiO_2
Composition to commercial manufacturers.	24.6	20.6	54.8	
EDS Analysis.				
CDM off eutectic.	18±1	27±4	53±3	3 ZrO_2, 1 CaO
BGMC eutectic.	24±0.2	21.5±0.4	54.7±0.3	

Table 4.1. Compositions of glasses the studied.

compared to the methanol milled powder (135).

By selection of glasses with these compositions, when ceramed, the phases of cordierite and enstatite should crystallise depending on the heat treatment schedule used. This allows not only the processing temperature to be lowered as the composition moves toward the eutectic trough, but allows a tailoring of the thermal expansion coefficient of the matrix via composition selection and heat treatment as indicated in Fig 4.3. From this plot it can be seen that for α-cordierite the thermal expansion coefficient of the matrix is below that of the fibre and, as the percentage of enstatite crystallised increases the fibre thermal expansion coefficient is traversed for ~ 9.6% enstatite. If the composition at the eutectic trough crystallised as indicated on the phase diagram a rule of mixtures calculation gives a thermal expansion coefficient of 4.8×10^{-6}°C^{-1}, which is close to the Corning CAS major phase anorthite.

From DTA traces given later it will be seen that the processing temperature of the CMC can be lowered, although an indication of this is available form the phase diagram. For stoichiometric cordierite it can be seen that melting occurs at 1460°C, whereas for the eutectic trough the melting temperature has fallen to 1365°C. Also movement from stoichiometry causes these compositions to show a 'processing-window' which is not apparent in the stoichiometric cordierite analysis.

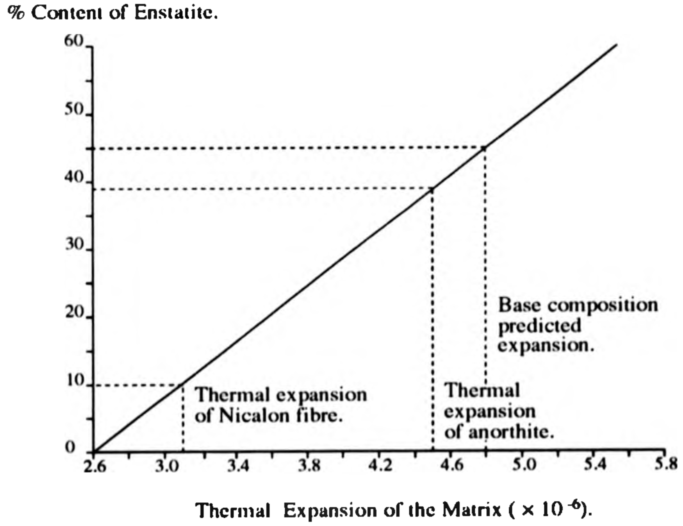

Figure 4.3. Predicted thermal expansion coefficient for the matrix with the percentage of enstatite present.

For the TiO_2 nucleant added glasses 10wt% was selected. During the melting process, and after the first quench, some of the glass exhibited brown discolouration instead of the nominally clear batch. This colouration was particularly noticeable in part of the melt and it was suspected that some rhodium (the crucible was platinum 10% rhodium) was leached from the crucible by the melt. The crucible was being used for its first melt and the remelt showed some discolouration as well. For the P_2O_5 nucleated system 2wt% was selected and no discolouration of the melt was observed.

For the base and P_2O_5 nucleant added glasses particle size analysis was performed and the results and those for the commercially sourced glass powders are shown in Table 4.2. For both powders a single particle size distribution is observed and, even though batches were prepared using nominally identical conditions, the distributions were found to be different. Table 4.2. also shows the results for two commercially sourced powders, which as explained later were manufactured to facilitate composite processing development. Differential thermal analysis experiments were carried out on all of the prepared powders to investigate the crystallisation characteristics of the powders and the effect of the added nucleants. The results compared to the stoichiometric glass batch, also prepared within this study, are shown in Fig 4.4.

For the stoichiometric cordierite composition it can be seen there is a slight endotherm at 824°C which is attributed to the glass transition temperature T_g. At higher temperatures two exothermic peaks are observed, one for the exothermic crystallisation of μ-cordierite at 939°C and the second the crystallisation of α-cordierite at 1044°C. Although the DTA apparatus could not exceed temperatures greater than ~

Glass Designation.	Particle Sizes (μm).		
	Average.	90%<.	10%<.
Base glass.	10.5	20.3	1.5
Base glass + P_2O_5.	4.7	9.6	1.0
CDM off eutectic.	9.2	21.3	0.9
BGMC eutectic.	15.9	40.0	1.4

Table 4.2. Particle size analysis results for the glasses studied.

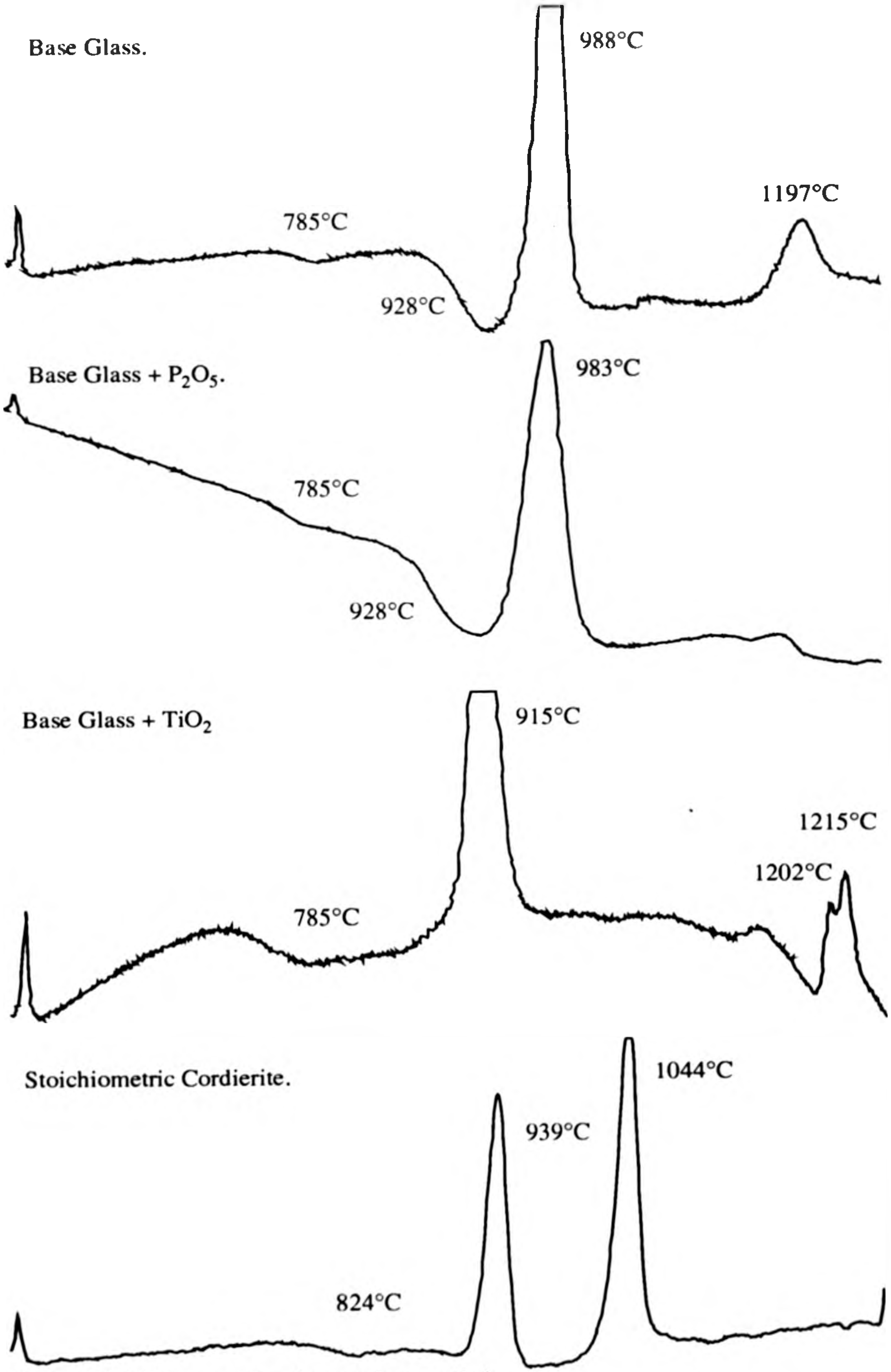

Figure 4.4. DTA traces for the powders studied.

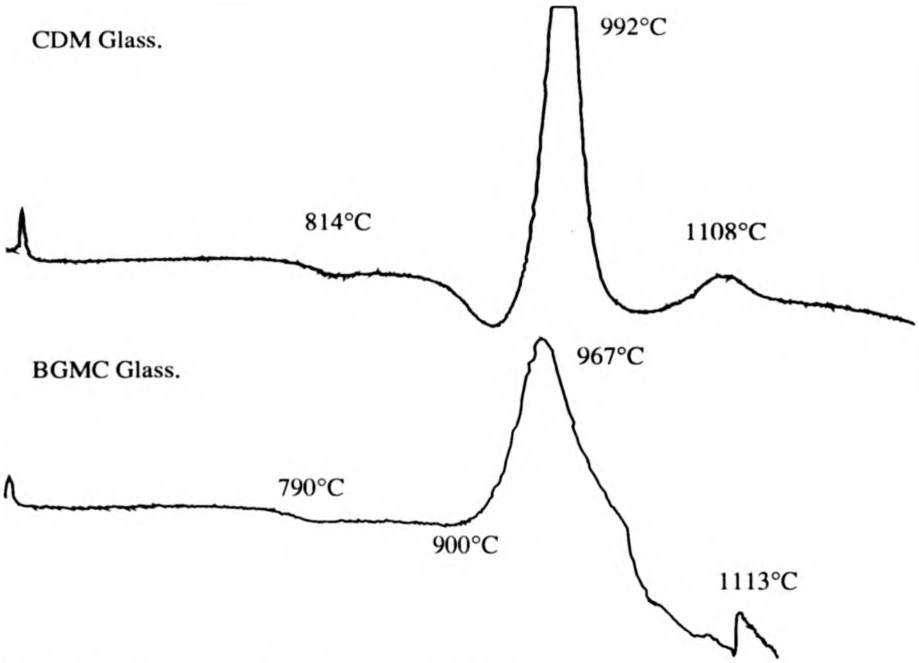

Figure 4.4., contd. DTA traces for the powders studied..

1250°C for stoichiometric cordierite, no endotherms can be seen relating to the melting of the glass. For the base (or eutectic trough) glass composition it can be seen that the crystallisation behaviour is very different. The glass transition temperature has fallen to $T_g \sim 785$°C and there is now an endotherm before the main crystallisation exotherm. This endotherm has its lowest value at 928°C where the exothermic reaction of crystallisation begins. The endotherm provides a 'processing-window' for composites as was discussed above and is one of the advantages of moving away from a stoichiometric cordierite composition. The endotherm is then followed by a major exotherm which is the result of the crystallisation of α-cordierite. At higher temperatures, because of the change in composition to the eutectic trough position, there is a smaller exotherm at 1197°C which is the enstatite crystallisation peak.

The two 'nucleant-added' base composition glasses exhibit the same glass transition temperature as the base glass, $T_g \sim 785$°C, but then show markedly different behaviour. For the 2wt% P_2O_5 nucleated glass there is a slightly broader processing window endotherm at the same minimum temperature, followed by an exothermic peak at a temperature very similar to the base glass for the crystallisation of α-cordierite. The crystallisation peak due to enstatite at higher temperatures is small, which may be due to the enhanced nucleation of α-cordierite. For the 10wt% TiO_2 nucleated base glass the processing window is broad, but the first exotherm is significantly shifted to lower temperatures. This exothermic peak corresponds to the crystallisation of μ-cordierite. Higher temperature behaviour is complex in this system, there being an endothermic drop before some crystallisation peaks. Following this endotherm there are two exothermic peaks at 1202°C and 1215°C, one due to the crystallisation or conversion of α-cordierite and one due to enstatite crystallisation.

The base glass composition was selected for further study as explained later in Section 4.2. Since the development of composite preparation technique was required the glass composition selected to be at the eutectic trough was prepared in reasonable quantities by two external glass manufacturers via Rolls-Royce. The first commercial supplier used was Ceramic Developments Midlands (CDM). Particle size analysis of this powder may be summarised as given in Table 4.2., and is of the same order of magnitude as the previous powders. A monolithic plate of this material was hot pressed under similar conditions as those utilised for composite fabrication, in order to check microstructural differences and to perform monolithic strength determination (the sequence used and the results of these experiments will be described later). However, the sample after hot pressing exhibited a different phase / microstructure to that found for the base composition glass. Subsequent phase analysis showed the bulk microstructure to have a composition as indicated in Table 4.1 The powder is slightly different in both magnesia and alumina content and close to that required for silica content, and from these figures has a position on the phase diagram as indicated in Fig 4.1. More importantly there is evidence of ZrO_2 contamination in the powder. This is believed to have arisen during the melting or milling processes, possibly by the use of zirconia milling media. It is difficult to evaluate fully the effect of the impurity zirconia on the microstructure, it has been used by authors as a nucleant although in quantities such as those used for TiO_2. Hence its nucleation efficiency may be very low for the quantity detected here, but may still affect the final microstructure. This was the powder used for the bulk of the study since the second powder supplied by an external source to the composition originally required was not available until near the end of the research.

This second powder, as with the CDM sourced powder, was supplied via Rolls-Royce. Because of the contamination problems encountered with the first commercially supplied powder, the second commercially supplied powder was only melted by the British Glass Manufacturers Federation (BGMC) and was returned in bulk frit pieces (3-10mm particle size). This bulk glass was then milled as for the base composition powder in methanol and with alumina media before being analysed both as a powder and as a hot pressed piece and found to have a composition as indicated in Table 4.1. Since this confirmed that the bulk glass (assuming only small levels of contamination form the alumina media) was of the required composition, the bulk glass was despatched to be milled separately by Particle Technology with subsequent particle size analysis as shown in Table 4.2. Following the return of this powder it was analysed as a hot pressed sample, the analysis giving the same composition as before. It can be seen that the powder has a higher average size than those previously analysed and that there is a considerable spread in the size distribution. It allowed for a useful comparison of composite processing and properties with a slight change in matrix composition. The DTA analyses for both of the commercially sourced powders are shown in Fig 4.4. For the CDM powder, which has the mid-cordierite phase field composition, T_g at ~ 814°C is followed by a processing window close to that of the base glass, an α-cordierite crystallisation peak at 992°C and a smaller enstatite peak shifted to a slightly lower temperature of 1108°C. For the eutectic trough BGMC powder T_g is again at 790°C as expected from the previous studies, with a broad processing window and the α-cordierite peak at ~ 970°C. Comparison after this is more difficult.

4.2. Composite Fabrication.

This section describes composite fabrication, from the chopped fibre systems studied at the beginning of the program through preliminary unidirectional composite fabrication to refined composite fabrication.

4.2.1. Chopped Fibre Systems.

Fabrication of samples within this system is relatively easily accomplished, with glass powder being mixed with fibre before consolidation. Fibres were desized, prior to consolidation into the composite, at 500°C for 10 minutes in air using an alumina crucible. For these samples consolidation was performed utilising a hot press apparatus, which is schematically shown in Fig 4.5. A r.f. induction coil is used to heat a graphite die to the required temperature via a Radyne r.f. generator operating at 450kHz. Pressure could be applied to the sample via an actuator ram driven by an independent hydraulic system. For the chopped fibre samples the die pressure used for consolidation was 10MPa. This pressure was selected since, on scale up of fabrication to unidirectional composites, the maximum pressure that could be used was

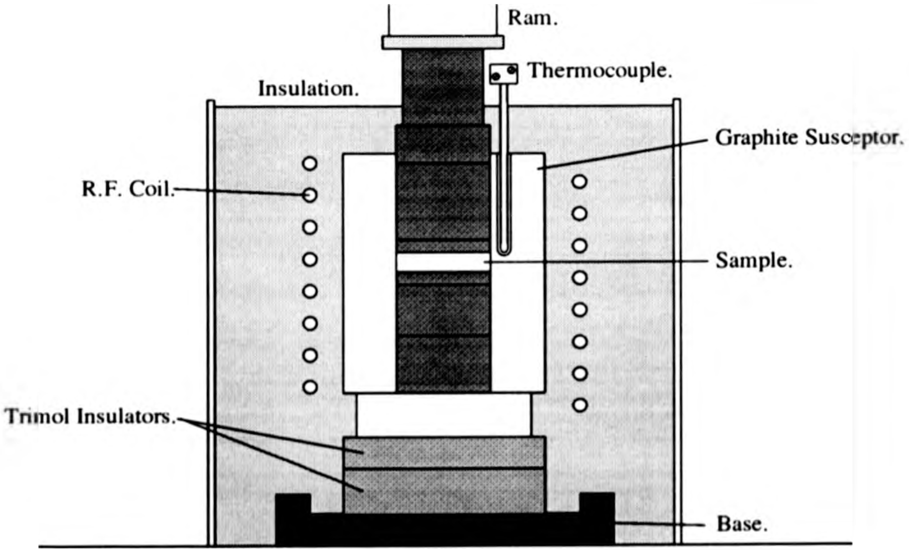

Figure 4.5. Schematic of the hot press system.

~ 20MPa before the burst pressure of the die was exceeded. The graphite die assembly was BN coated before loading with powder (~ 10g) and chopped fibres. A 10mm diameter round section die was used, with molybdenum discs on the top and lower ram surfaces which were in contact with the powder. This facilitated easier removal of the sample after hot pressing.

The chopped fibre samples studied and the corresponding heat treatments are indicated in Table 4.3. The heat treatment schedules were selected by the number of stages used (i.e. a one or two stage process) and the crystallisation temperatures of the powders as determined from DTA. The schedules can be divided into two groups, depending on the use of Window II or Window I pressings, as schematically illustrated in Fig. 4.6.

For the Window II pressings the approach is to heat the composite rapidly in order to miss the nose of the T-T-T curve and hence avoid crystallisation of the powdered glass before densification. For samples fabricated in this study a heat up

Designation.	Composition.	Heat Treatment. (°C, min).	Phase Structure (~%).		
			α	μ	ens.
CF1	Base Glass	1300, 5; ; 980, 30	80		20
CF2	Base Glass	1300, 5; ; 980, 90	71		29
CF3	+ 10 wt% TiO_2	1300, 5; ; 914, 30	69	31	
CF4	+ 2 wt% P_2O_5	1300, 5; ; 980, 30	74		26
CF5	+ 10 wt% TiO_2	1300, 5; 840; 60; 914, 30	71	29	
CF6	Base Glass	1300, 5;	78		22
CF7	+ 2 wt% P_2O_5	1300, 5; 880, 60; 980, 30			
CF8	Base Glass	1300, 5; 880, 60; 980, 90	83		17
CF9	+ 2 wt% P_2O_5	1300, 5; 880, 60; 980, 90	86		14
CF10	Stoichiometric Cordierite	1300, 5; ; 1044, 30	100		
CF11	Stoichiometric Cordierite	1300, 5; ; 1044, 90	100		
CF12	Base Glass	1200, 10; ; 980, 90	70		30
CF13	+ 2 wt% P_2O_5	1200, 10; ; 980, 90	75		25
CF14	Base Glass	1100, 10; ; 980, 90	15	63	22
CF15	+ 2 wt% P_2O_5	1100, 10; ; 980, 90	56	36	8
CF16	Base Glass	890, 10; ; 980, 90	12	69	19
CF17	+ 2 wt% P_2O_5	890, 10; ; 980, 90	14	67	19
CF18	Base Glass	890, 10; ; 980, 30		80	20
CF19	+ 2wt% P_2O_5	890, 10; ; 980, 30		72	28

Table 4.3. Chopped fibre pressings, the pressure used was 10MPa in all cases.

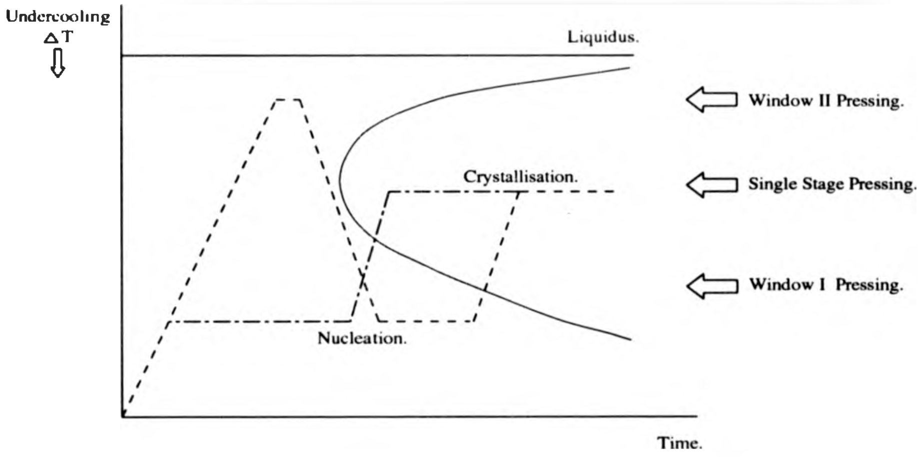

Figure 4.6. Schematic process routes for Window I and Window II schedules.

rate of ~ 40°min^{-1} could be achieved to heat the samples to a temperature of ~ 1300°C. Transient nucleation of the glass powder around T_g should also be minimised by a fast heat up. The temperature was selected since, by analysis of the DTA traces evidence of glass melting is apparent at temperatures ~ 1270°C (see Fig 4.4.), and hence at 1300°C the glass should be relatively easily densified but not flow readily enough to be displaced past the ram sections. The pressure is then applied to densify the composite by viscous flow and hence avoids imparting mechanical damage to the fibres via crystal impingement. The subsequent heat treatments are based on the more conventional one or two step glass ceramic process.

For the Window I Pressings again a fast heating rate was utilised, but temperature is held within the softening regime of the glass or 'processing-window'. Hence, viscous flow of the glass due to softening behaviour is used in order to densify the composite before subsequent heat treatment as described above.

For the samples CF1-11 window II pressing with an ultimate temperature of 1300°C was used. This temperature as stated above is near to the glass liquidus and hence densification is very good. The time for this densification step as indicated in Table 4.3. is kept as short as possible so that the thermal and chemical degradation of the fibres are minimised. From the table it can be seen that a number of different heat treatment schedules and times were used as well as the various glass powders. This was done in order to provide information on the microstructural and phase development with heat treatment. Microstructural development will be discussed later in Chapter 5., Section 1. However, some general comments can be made here. Shown in Table 4.3. are phase percentages for the composites, calculated using the ratio of peak heights from the XRD traces, in order to give an approximate indication of changes in phase structure with heat treatment. In order to calculate the correct phase ratio for the fabricated samples standards would need to be used. Comparison of the peak height ratios as used here ignores the differences in phase peak heights caused by differences in crystal symmetry and elemental composition of these phases. The crystal symmetry can effect the number of observed x-ray peaks and their intensities. Crystals with high degrees of symmetry (i.e. cubic), will have many equivalent planes for x-ray diffraction and so exhibit fewer, higher intensity peaks. For crystal symmetries with fewer equivalent planes more peaks are observed with differing intensities. Due to the differing symmetries of the phases studied here it can be realised that errors are associated with taking simple peak height ratios. The elemental composition of the phase can also alter the diffracted intensity observed, with light elements diffracting less than heavier elements. For the phases analysed here elemental composition is similar, although some errors may still occur because of this.

Both CF1 and CF2 showed good densification with low levels of porosity. Phase analysis by EDS showed the presence of cordierite and enstatite as expected, with XRD indicating phase percentages as shown in the table and Fig 4.7. gives an example XRD trace. The sample CF6 was produced as a densification trial and to evaluate the effects of no subsequent heat treatment. Although both the XRD and EDS analysis indicated the presence of α-cordierite and enstatite the microstructure was not as well developed, with larger amounts of glass present. Finally for the base composition glass a nucleation step of 60 minutes at 880°C was used for CF8, followed by a 90 minute crystallisation step, producing a very fine microstructure. For the base powder with P_2O_5 nucleant added, (CF4) the single step heat treatment showed a micron scale microstructure as for the above cases, with good fibre tow infill and very low levels of residual porosity. Near the fibres phosphorus rich specks (~ ¼µm) were

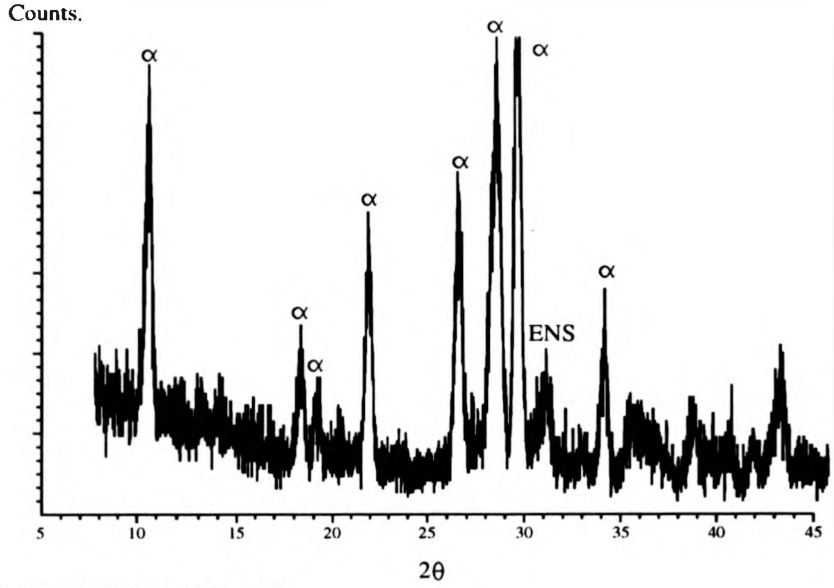

Figure 4.7. XRD trace for CF1.

seen which were not evident in the bulk matrix and some Al_2O_3 inclusions were also detected. The second two chopped fibres samples studied with this powder had a nucleation step followed by a crystallisation stage for a 30 or 90 minute duration. Again micron sized microstructures were observed with phosphorus rich nucleation specks near the fibres

For the TiO_2 nucleated base glass only two samples were fabricated, a single stage heat treatment sample CF3 which showed higher levels of porosity (pores up to 5μm) and a diffusion band of ~ 1μm into the fibres. The second sample utilised a nucleation step which considerably reduced the porosity and the fibre diffusion band (consisting of Mg and Al) remained at ~ 1μm. These two results confirm previous authors' work suggesting that this nucleant promotes the formation of μ-cordierite (see Section 4.1.).

Before a description is given of the lower maximum temperature window II pressings and the window I pressings a brief description will be given for CF10 and CF11, which were fabricated using stoichiometric cordierite powder. Both samples were fabricated using the window II densification regime. Since, as the DTA curve shows, there is no lower processing temperature window available. Good densification was achieved with an α-cordierite matrix with micron grain size. Some cracking of the matrix was observed and deflection of these cracks around the fibres occurred. There were Al_2O_3 micron sized particles dispersed within the matrix and a grain boundary phase which EDS analysis indicated to have a composition within the mullite phase field. Some in-diffusion of matrix elements into the fibre was observed to a depth of ~ 0.4μm.

The samples CF12-15 were all processed as window II pressings but with a lower maximum temperature before pressure application. For these samples only the base and P_2O_5 nucleated powders were utilised, with the lower densification temperature being followed by a single crystallisation step for 90 minutes. For the 1200°C maximum temperature pressings, CF12 and CF13, a submicron grain size matrix was formed, with a small level of residual porosity (pore size ~ 2μm). However, for both pressings tow infill was degraded. For CF14 and CF15 the maximum temperature was lowered to 1100°C and here the porosity (~ 1μm) was widespread with fibre bundle tow infill poor. The base composition glass exhibited a spherulitic growth morphology with a predominantly μ-cordierite matrix, unlike the P_2O_5 nucleated glass where a predominantly α-cordierite matrix was formed. Here it can be seen that the added nucleant can have a significant affect on the phase development in the glass ceramic for identical heat treatments. Bundle infill was thought to be poor as a result of the increased glass viscosity at the lower maximum temperature and possibly because crystallisation occurred during densification.

Window I composite fabrication was utilised for CF16-19. From the DTA trace a softening temperature for both the base and P_2O_5 nucleated glass was estimated at 890°C and hence for all samples this temperature was held for 10 minutes at 10MPa pressure. A single step crystallisation stage was then used at 980°C for either 30 or 90 minutes. For the 30 minute crystallisation samples, CF18 and CF19, porosity was widespread (up to ~ 10μm in size) and the fibre tow infill was poor. The base glass exhibited a spherulitic growth morphology with a phase structure of predominantly μ-cordierite, as did the nucleant-added glass. For samples crystallised for 90 minutes porosity was again widespread and ranged from ~ 3-10μm, the lower figure for the P_2O_5 nucleated glass and the higher for the base glass. Fibre tow infill was poor and both glass powders exhibited a predominantly μ-cordierite matrix.

The above chopped fibre studies allowed for the evaluation and determination of phase development for various different process routes. Hence, before unidirectional composite fabrication was carried out, a number of processing ideas had been evaluated. Significantly the TiO_2 nucleated powder was eliminated at an early stage because of its promotion of μ-cordierite. This argument may also be applied to the window I pressings coupled with the presence of porosity, which for potential applications for these composites is undesirable. The P_2O_5 addition glass powder gave very similar results to the base composition glass with some differences in phase structure, although fine-grained microstructures were developed for both powders. Hence, the necessity for a nucleant was negated and the base powder selected for further study. It was demonstrated that the lower maximum temperature pressings for the window II regime were less successful with slight porosity present and inferior bundle infill to the 1300°C pressings. However, bundle infill is an extreme test and the 1200°C pressings developed the desired fine grained microstructure with the advantage of less thermochemical damage to the fibres during processing.

4.2.2. Pre - Impregnation of the Fibre Tow.

To fabricate unidirectional composites the fibre tow and the glass frit matrix must be mixed sufficiently so that upon consolidation a composite of correct fibre volume fraction and fibre distribution is attained. As viscous flow of the glass is utilised fibre distribution cannot be controlled accurately. However, it is desirable to have infill of the fibre tow with matrix material and to eliminate large areas of monolithic matrix not reinforced with fibres. The way this is achieved is by pre-impregnation or pre-preg of the fibre tow as described by Prewo (39) or Norman and Tilley (53).

The system used in this study is based on the designs described by the above authors as well as some of the experience gained by Rolls-Royce utilising this

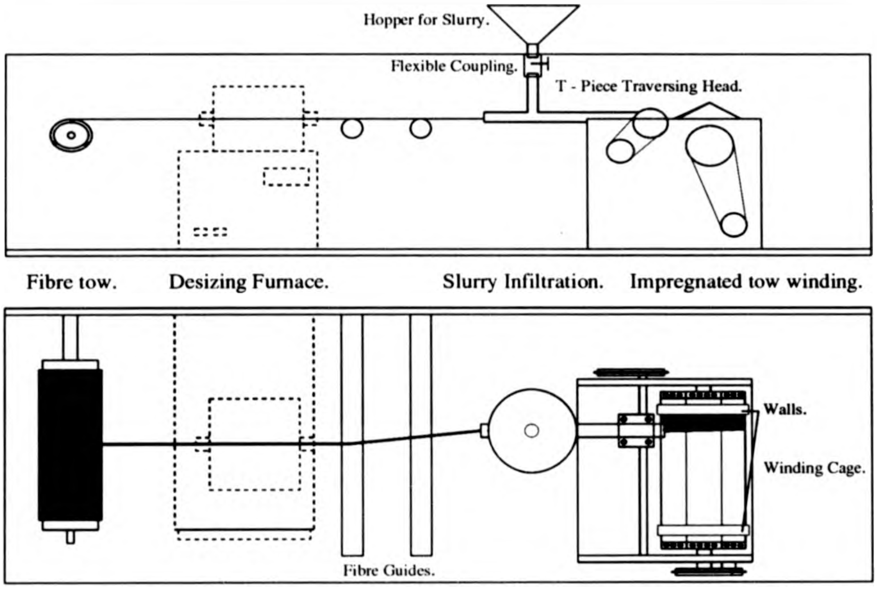
Hopper for Slurry.
Flexible Coupling.
T - Piece Traversing Head.
Fibre tow.
Desizing Furnace.
Slurry Infiltration.
Impregnated tow winding.
Walls.
Winding Cage.
Fibre Guides.

Figure 4.8. Schematic of the pre - preg apparatus developed in this program.

technique. However, a number of innovative steps have been developed during this work in order to produce consistent, handleable and high quality pre-preg. It should be realised that the pre-preg step is critical to the final composite properties. The apparatus was designed to infill the fibre tow with glass frit and then wind this tow onto a drum. Since, for both grades of Nicalon used in this study, the fibre tow consists of 500 fibres in a bundle which must be infilled with a powder of particle size ~ 10μm which is close to the fibre diameter, the problems associated with this technique can be realised.

A schematic of the apparatus developed in this study is shown in its final state in Fig 4.8. Some of the development process is indicated below, with the system required to give high quality and reproducible pre-preg, using the minimum of materials for maximum efficiency on a laboratory scale, allowing for the rapid evaluation of differing matrix chemistries and pre-preg or processing parameters. Since the hot press used in this study allowed for the fabrication of 50x50mm square unidirectional composite plates, the system designed here was to have the capability of producing enough pre-preg to fabricate three plates from a single run. In the following sections, a more detailed view of each section of the pre-preg apparatus and its development will be given.

Beginning at section 1 of the apparatus there is the Nicalon fibre spool. For this study initially Nicalon NL-201 grade fibre was used (the 201 represents a standard grade fibre, 1800 denier, 500 filament tow, with epoxy sizing) since studies at Rolls-Royce has indicated that this fibre had superior strength to the NL-202 and NL-222 grades. For later work the carbon coated Nicalon NL-607 grade fibre was utilised (the 607 referring the fibre to be used for GMC / CMC use, 1800 denier, 500 filament tow, with polyvinylalcohol (PVA) sizing). Fibre breakages during pre-preg runs did occur and one of the refinements adapted was to release the tension from the fibre as it left the spool before proceeding to the rest of the apparatus.

When the apparatus was first designed attempts were made to spread the fibre tow during fibre handling through the various stages of the pre-preg process. Various methods can be used to accomplish this including tapered rollers and air jets. In this work tapered PTFE rollers were used. However, problems were encountered since the fibre tow would slip off the taper and fibre breakages would occur on the surface of the rollers (not bundle breaks but significant enough numbers for the breaks to be seen). Hence, because of this problem most of the study utilised glass rods (diameter ~ 5mm) to guide the fibre tow.

Section 2 of the apparatus shows in dotted format a small furnace for fibre desizing. This is a conventional alumina tube furnace capable of running at 700°C with a 80mm hot zone. Early studies using the NL-201 fibre utilised this furnace to remove the epoxy size, with the conditions of removal adapted from previous Rolls-Royce work which showed by TGA that the above conditions were sufficient to remove the applied sizing. When the study began to use the NL-607 fibre, because of the pre-existing carbon coat and its susceptibility to oxidation, the desize furnace was not used.

The next two sections of the apparatus, 3 and 4, form the critical elements in pre preg production. These two sections are responsible for fibre tow infill and then the fibre winding. Section 3 of the apparatus is the slurry infiltration stage. As before at the outset a more conventional approach was adopted with an air-agitated slurry bath. It was found that slurry infill into the tow was poor and that large quantities of mixed slurry were needed. Hence an alternative method of pre-impregnation was devised with the T-piece head, comprising a small diameter glass tube attached to a hopper mechanism by a flexible coupling. The design has some elegance through simplicity as it can be attached directly to the winding mechanism and so avoids a separate fibre guide which can strip the fibre tow of slurry.

The slurry used with this apparatus was a mix of deionised water, $70gl^{-1}$ of polyethyleneoxide (PEO) and $600gl^{-1}$ of matrix frit. The PEO binder was mixed with the water and high shear blended for approximately 4hrs before any matrix powder was added. This subsequent mix was then further high shear blended for ~ 2hrs. Attempts were made to utilise previous mix ratios of binders and frit as for pyrex and CAS powders but this was unsuccessful, the differing powders giving slightly different pre-preg results. First attempts with lower PEO and glass frit loadings did not give the required matrix volume fraction. Through a series of experimental combinations, using varying combinations of PEO and glass frit loadings, the final combination stated above was reached. Problems with slurry viscosity were not encountered for the final combination, as the fibre tow passing through the T-piece 'pulled' the slurry through. Another binder system (PVA) was utilised in some experiments, but was not continued since it did not readily dissolve in water.

The final section of the apparatus, section 4, lays the impregnated fibre tow down on an octagonal winding drum so that after drying the pre-preg can be cut and stacked for composite fabrication. For the apparatus used here the traverse head and drum were driven separately to allow for fine control of the rotational speeds. Power supplies for the two motors were constructed in-house and were based on a constant current design so that the motors would run at constant speed. Preliminary calculations and set up procedures were used to give an indication of traverse head and winding cage speeds. For a single traverse run pre-preg quality was lowered due to the presence of gaps in the sheets and, upon removal from the winding drum, the sheets were found to be very fragile. Hence a double traverse run was used, the second reverse pass traversing at a slower speed. On this second run the pre-preg was rollered by a PTFE rod (Nylon was used, but found to be too light) which pushed the fibre tow into any gaps and evened pockets of slurry out within the sheets. This roller was left on after the finish of the run in order to maintain pre-preg quality.

The infilled tow was wound onto glass panels on the winding cage, the glass ensuring even slurry build up on the inside face of the pre-preg. A release coat of PTFE spray (Sprayflon) was applied directly to the glass panels to ease pre-preg removal. It was noticed that during PTFE rollering of the pre-preg an overspill band of slurry ~ 2cm either side of the pre-preg occurred. Hence, in order to retain this slurry within the pre-preg, masking tape 'walls' were wound around the cage to act as an overflow barrier. The pre-preg sheets were cut and removed from the apparatus using a scalpel and then cut to the appropriate size for fabrication. The higher strength of the two pass pre-preg sheets was useful at this stage for cutting and also for stacking in the hot press die.

The system developed in this study is novel due to a number of features. The release of fibre tow tension during pre-preg runs significantly reduced the possibility of fibre breakages, and the use of glass guide rods did not impart damage to the fibre tow. The T-piece and incorporated traverse arrangement is very economical with slurry, allows high frit loading within the tow and subsequent guide mechanisms for the fibre tow are not required. Finally the use of two passes and walls to prevent slurry overspill and rollering of the wound pre-preg produces high quality, strong and reproducible pre-preg.

4.2.3. Unidirectional Composite Fabrication.

Within this study a methodology has been developed for the fabrication of unidirectional or cross-ply composites via hot pressing. It has been found that the hot press schedule used is critical to the final composite properties and an attempt has been made to relate some of these changes to the hot press cycle employed. The composite samples were fabricated using the hot press apparatus as schematically shown in Fig 4.5. For composite tiles to be produced a 50x50mm square section die set was used. Before loading of the pre-preg sheets into the die all surfaces were BN coated and

Composite Designation.	Process Route.				
	Route.	Composition.	Temp. (°C).	Time. (min).	Pressure. (MPa).
UDM 1.	Pre - opt	Base Glass	950	30	3.5
UDM 2.	Pre - opt	Base Glass	1000	30	10
UDM3.	Pre - opt	Base Glass	1050		
UDM4.	Pre - opt	Base Glass	1100	60	7.4
UDM5.	Pre - opt	Base Glass	1050	30	10
UDM6.	Pre - opt	Base Glass	1100	30	10
CUDM5.	Opt	CDM Glass	1200	60	17.4
CUDM7.	Opt	CDM Glass	1200	60	17.4
CUDM12.	Opt	CDM Glass	1200	60	17.4
CUDM10.	Opt	CDM Glass	1200	120	17.4
CUDM11.	Opt	CDM Glass	1200	120	17.4
CUDM14.	Opt	CDM Glass	1200	180	17.4
CUDM15.	Opt	CDM Glass	1200	180	17.4
CUDM17.	Opt	BGMC Glass	1200	180	17.4
CUDM18.(RR UD/X ply).	Opt	CDM Glass	1200	60	10
CUDM19.(RR UD/X ply).	Opt	BGMC Glass	1200	60	10

Table 4.4. Identification of the composite samples fabricated.

molybdenum sheet was cut and placed on the top and bottom graphite pieces which were to be in contact with the sample. The molybdenum sheets allowed easy removal of the fabricated composites and provided a consistent as-pressed surface.

At the beginning of this study, some of the base composition glass was available from Rolls-Royce as pre-preg sheets utilising Nicalon NL-201 fibre. These were used as preliminary tests of fabrication routes available and were subjected to the hot press conditions given in Table 4.4. The samples UDM1-4 were hot pressed by Dr M. W. Pharaoh. It should be noted that for UDM3 a hot press failure occurred. For each of the samples the pressure was applied at 950°C. It can be seen that for samples UDM 2, 5, and 6, only the maximum temperature in the hot press cycle was altered. It was found that as the temperature increased the level of μ-cordierite within the sample decreased. Both the microstructural and mechanical behaviour of these samples will be discussed in more detail in Chapters 5., and 6., but it can be pointed out here that porosity was present in the samples and that the mechanical response was poor.

Hence, once consistent and high quality pre-preg was available, attempts were made at improving the fabrication cycle by use of the DTA traces. In order to

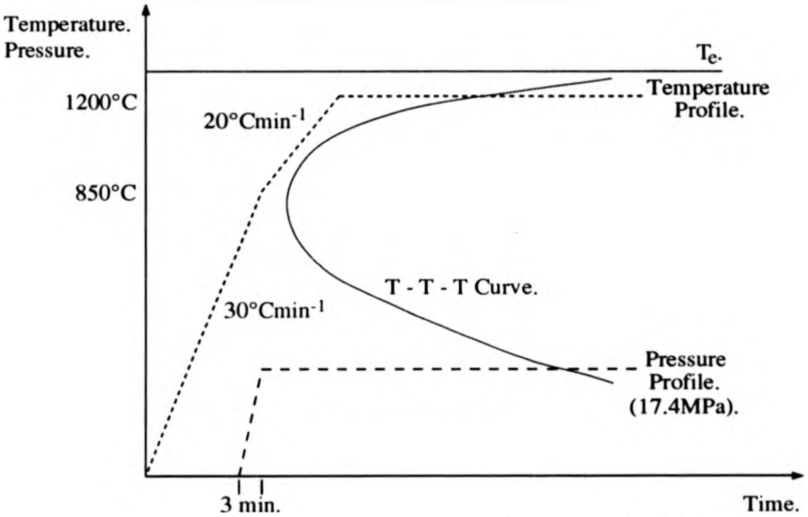

Figure 4.9. Schematic of the optimised process route for composite fabrication.

avoid high temperature fibre degradation, which may have been occurring in the above samples, a process schedule was designed to utilise the process window available. This route was first used on sample CUDM5 and was used with only minor modifications on all later samples. The route, which is illustrated schematically in Fig 4.9., produced a fine grained microstructure, good densification and good mechanical properties. The route, in general, is to use a fast heating rate, apply the pressure incrementally but quickly within the processing window as the temperature rises and to continue to heat to the desired temperature followed by a crystallisation isotherm. The isotherm selected is below the liquidus and so the crystallisation occurs as the interfacial reaction occurs, but at a temperature that does not degrade the fibres thermally (see Chapter 2., Section 4.). The final hold isotherm selected here is a compromise of many factors. The crystallisation peaks, as indicated by DTA, must be considered for the glass, as must the interface reaction kinetics, for the appropriate interfacial properties to be attained. The 1200°C isotherm temperature was selected since all DTA crystallisation peaks are below this temperature. The chopped fibre studies indicated that this temperature gave reasonable densification (bundle infill is not as much of an issue here), a fine grained microstructure of correct phase composition and interface constitution indicative of good interfacial properties.

The route applied more specifically here was first utilised for the commercially sourced CDM powder pre-preg. However, DTA traces for this, the base and the BGMC commercially sourced powder are very similar and so the process route developed is applicable to all these powders (Note : In Chapter 7., it will be demonstrated that this process route can also be applied to CAS CMCs). A fast heat up rate of ~ 30°Cmin^{-1} was used to reach the processing window of the glass (~ 850°C). Pressure was then applied before the minima of the first crystallisation peak was reached (here, 3 minutes for application of a 17.4MPa pressure), followed by heating at 20°Cmin^{-1} to the 1200°C isotherm.

For the samples fabricated α-cordierite was the major matrix phase with enstatite present. Estimates of phase content were hindered due to poorer quality XRD traces. All samples were fabricated with the hold isotherm at 1200°C, the only alteration being the hold time at this temperature which was varied for 1, 2, or 3 hours. The samples fabricated and conditions are given in Table 4.4. Differing heat treatment schedules would have been attempted if time had allowed, but this was not the case.

The composites CUDM18 and 19 were supplied as 100x100mm square plates by Rolls-Royce plc and were processed to the same schedule with a 1hr isotherm hold time at 1200°C and a lower consolidation pressure. Rolls-Rôyce also supplied 3 CDM $[\,0° / 90°\,]_{3s}$ and 2 BGMC $[\,0° / 90°\,]_{3s}$ 100x100mm square plates. A different pre-preg process is used by Rolls-Royce which is based on the more conventional process described previously with a single traverse run. Properties for these materials were not as good as the in-house prepared materials due to problems in the scale up of the process. The cross-ply $[\,0° / 90°\,]_{3s}$ 12 ply samples were used predominantly for tensile and creep testing, whereas the $[\,0°\,]_{10}$ unidirectional samples were used for flexure evaluation at room, elevated, and thermally aged conditions.

Chapter 5. Microstructure and Interfacial Properties of MAS Matrix Composites.

Within this chapter the microstructural and interfacial properties of the composites will be discussed. The chapter begins with the chopped fibre materials before describing in greater detail the microstructures of unidirectional composites and their interface structures. The micromechanical properties of the various interfaces are compared, followed by a more detailed correlation of the microstructural and interfacial properties.

5.1. Chopped Fibre Materials.

The chopped fibre systems were used within this study to evaluate both compositional and processing issues. The identification of possible glass compositions was stated in Chapter 4., and the subsequent processing routes utilising both window I and window II regimes lead to a diverse set of microstructures. Some details of the microstructures were identified in Chapter 4., with particular emphasis placed on the phase structure via XRD in order to illustrate the composition selection and process development ideas used within this study. This Section of Chapter 5. will illustrate the microstructures for these materials. From Chapter 4., Table 4.4. the phase content of these materials is given and so description here will be limited. Single stage process routes were utilised first followed by two stage routes.

Sample CF1 produced a fine micron scale microstructure as shown in Fig 5.1. Since the chopped fibre samples have a random dispersion of fibres within the material, it was found for CF1 that the microstructure near and ~ 500μm away from the fibres was very similar. This suggests that the nucleating effect of the fibres was not significant. The sample CF4 was processed as CF1 (see Table 4.3.), but utilised the P_2O_5 nucleated base glass. Again a micron scale microstructure was observed and ~ ¼μm P_2O_5 specks were seen near the fibres acting as nucleation sites. For the TiO_2 nucleated powder this process route produced a coarser ~ 5μm scale microstructure as shown in Fig 5.2. The inset in this figure shows evidence for a ~ 1μm diffusion band into the fibre (see below). Phase analysis of this sample indicated that the matrix was predominantly α-cordierite with μ-cordierite present (XRD showed a ~ 30% μ-cordierite matrix). The XRD analysis did not show evidence of a titanate phase as was found by EDS analysis. This analysis showed this titanate phase to contain magnesium, with a small amount of aluminium (~ 6wt%).

Samples CF5, 7, 8 and 9 used a nucleation as well as crystallisation step. The second TiO_2 nucleated sample, CF5, gave a finer microstructure than that of CF3, although, as with CF3, porosity was present. As before, the fibres exhibited a ~ 1μm diffusion band, with EDS analysis indicating the diffusion of Mg and Al into the fibre. The presence of μ-cordierite, in the samples utilising the TiO_2 nucleated glass, resulted in the powder not being pursued for further study. Sample CF7 used the P_2O_5 nucleant-added base glass with a nucleation and 30min crystallisation hold time. A smaller number of phosphorus rich specks are seen in the matrix compared to CF2 and CF4 (Fig 5.3.). As can be seen from this figure, some porosity is evident in the sample. The inset in the figure shows the phosphorus rich specks, as indicated both by their higher contrast in backscattered electron imaging and also by EDS analysis. These areas could be phosphates or phosphides as there is a reducing atmosphere present in the hot press during fabrication. However, this could not be confirmed. Samples CF8 and CF9 are base and nucleant added glasses, with the incorporation of a nucleation stage and 90min crystallisation hold. The base glass sample CF8 showed a micron scale microstructure with CF9, the nucleant-added glass sample, showing some porosity (less than CF7).

The next two samples in the chopped fibre series were fabricated to show differences in behaviour between stoichiometric cordierite and the glass compositions utilised within this study. Samples were densified in the same manner, the isotherm crystallisation time being extended from 30 minutes for CF10 to 90 minutes for CF11. In both cases Al_2O_3 contamination particles were observed in the α-cordierite matrix, with a grain boundary phase of mullite phase field composition. Porosity was present in the samples (for CF10 = 2.0 ± 0.5%) and matrix cracking, shown in Fig 5.4., did not however propagate into the fibre or the ~ 1/3μm diffusion band on the fibre surface.

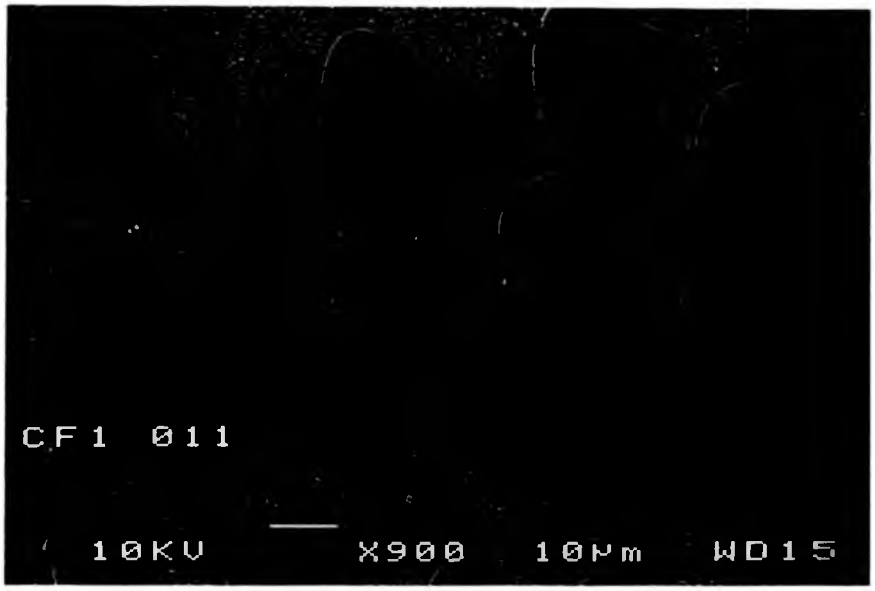
CF1 011
10KV
X900
10µm
WD15

Figure 5.1. SEM backscattered micrograph of CF1.

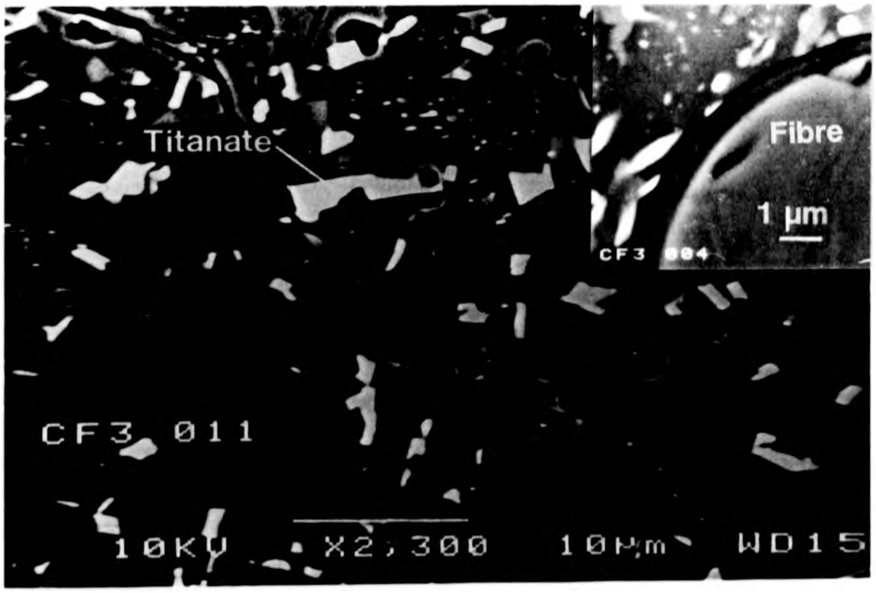
Titanate
Fibre
1 µm
CF3 004
CF3 011
10KV
X2,300
10µm
WD15

Figure 5.2. SEM backscattered micrograph of CF3.

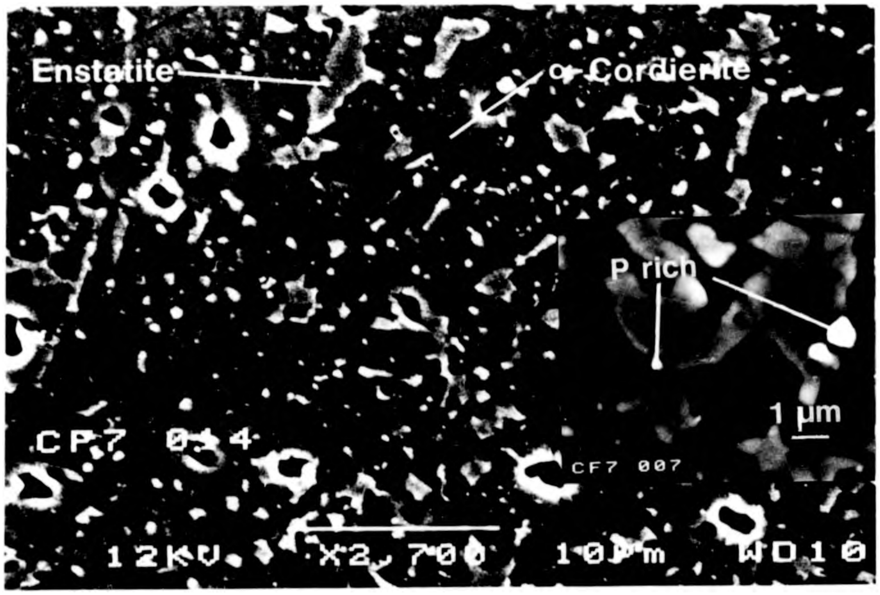
Enstatite
α-Cordierite
P rich
1 µm
CF7 014
CF7 007
12KV X2,700 10µm WD10

Figure 5.3. SEM backscattered micrograph of CF7.

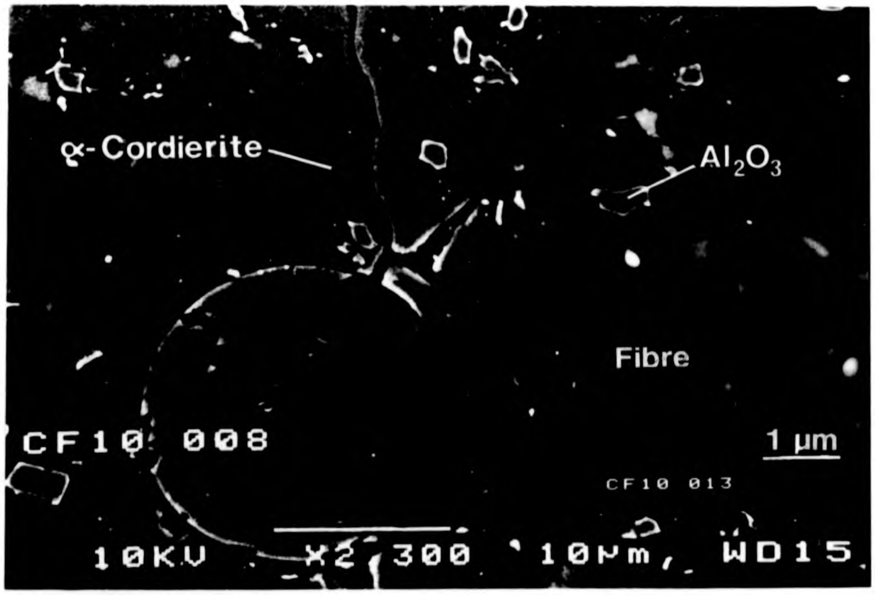
α-Cordierite
Al_2O_3
Fibre
CF10 008
1 µm
CF10 013
10KV X2,300 10µm WD15

Figure 5.4. SEM backscattered micrograph of CF10.

This is evident from the inset in this figure,which shows the diffusion band on the fibre surface and the crack impinging onto it. The fibre tow infill for these samples was found to be poor.

Window II pressings were investigated with lower minimum temperatures for samples CF12, 13, 14, and 15. For the 1200°C maximum consolidation temperature, the base and nucleant-added glasses are represented by CF12 and CF13. Porosity was present in both samples (lower for CF13) and bundle infill was degraded from the above higher temperature pressings. For the 1100°C maximum temperature pressings, CF14 and CF15, both samples exhibited porosity and poor bundle infill. The nucleant-added glass sample CF15 gave a fine, micron-scale microstructure as seen in Fig 5.5., which also shows evidence of crack deflection. For this sample μ-cordierite was present (~ 36%) and porosity on a ~ 1μm scale. For the base glass sample CF14 the matrix was predominantly μ-cordierite (~ 63%), which exhibited a spherulitic growth morphology (Fig 5.6.).

The final set of chopped fibre samples were used to investigate window I fabrication routes, with CF16 and 17 using a 30 minute crystallisation hold and CF18 and 19 using a 90 minute crystallisation hold. For all samples, porosity was observed, tow infill was poor and the predominant matrix phase was μ-cordierite. Specifically for the 90 minute crystallisation schedule, CF16 and 17, the base glass powder showed higher levels of porosity and the microstructure was spherulitic in morphology. The samples crystallised for 30 minutes showed porosity on a 10μm scale as opposed to the 3μm scale for the 90 minute samples. The base glass sample, CF18, exhibited a spherulitic growth morphology and matrix cracking.

Before a brief description of the interfacial characterisation carried out on these chopped fibre samples, it is appropriate to indicate that during this study a number of unreinforced glass ceramic samples were hot pressed for evaluation. The fabrication mimicked the composite schedule, with pressure application at the same temperature and a lower pressure, ~ 5-6MPa, used in order to avoid glass extrusion in the die set. Samples fabricated with the commercially sourced BGMC powder were cracked upon removal from the die body and a typical microstructure can be seen in Fig

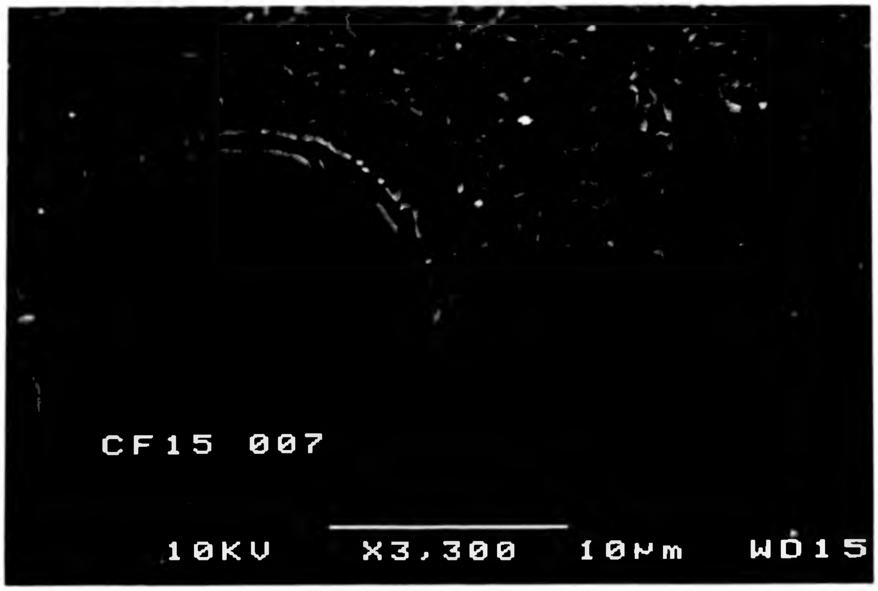
CF15 007
10KV
X3,300
10µm
WD15

Figure 5.5. SEM backscattered micrograph of CF15.

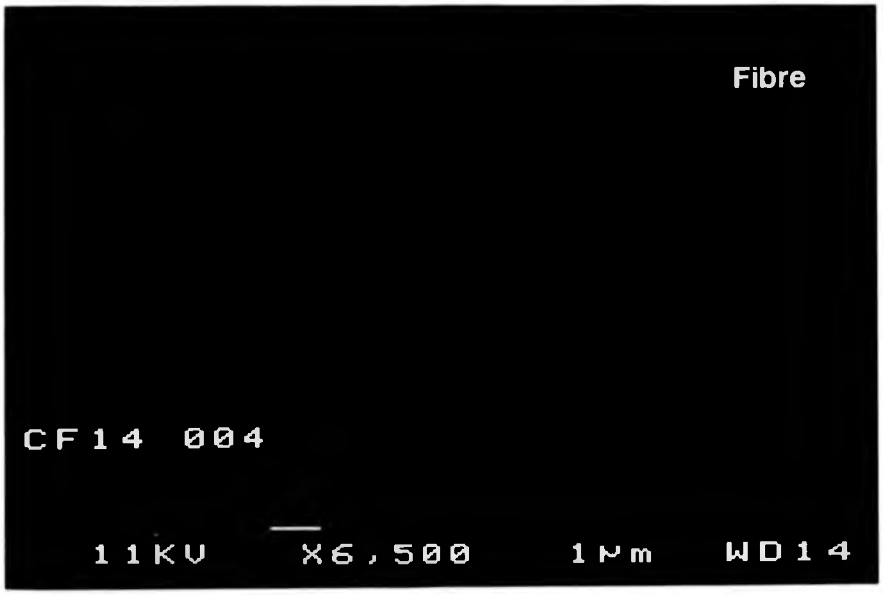
Fibre
CF14 004
11KV
X6,500
1µm
WD14

Figure 5.6. SEM backscattered micrograph of CF14.

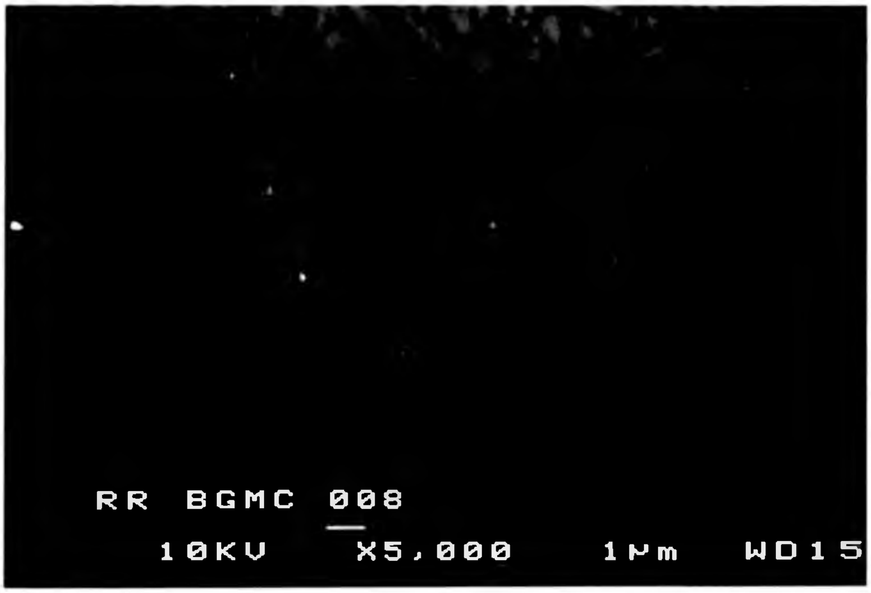
RR BGMC 008
10KV X5,000 1μm WD15

Figure 5.7. SEM backscattered micrograph of the BGMC glass ceramic.

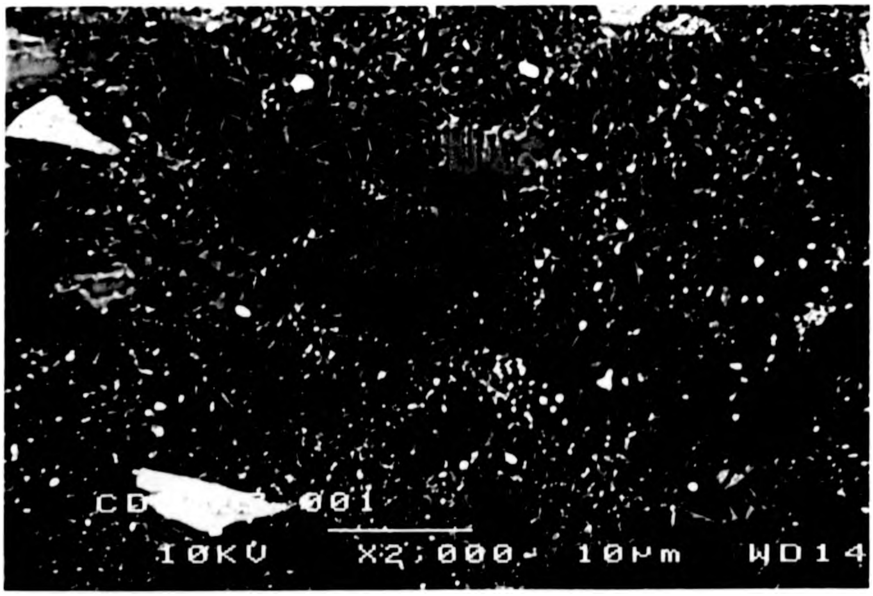
CD 001
10KV X2,000 10μm WD14

Figure 5.8. SEM backscattered micrograph of the CDM glass ceramic.

5.7. Some porosity is evident and EDS analysis indicated a diphasic structure, as did XRD, with an α-cordierite matrix and ~ 32% enstatite. As seen in the figure a fine micron sized grain structure is observable, although the structure is not as well developed as in the composite samples. The CDM sourced glass ceramic however, exhibits a very complicated microstructure as indicated in Fig 5.8. Again porosity is evident to ~ 2%, with EDS / XRD analysis indicating a predominant phase of α-cordierite, enstatite and the light grey and speckled regions containing concentrations of up to 10% ZrO_2 and the white dots up to 44% ZrO_2 (analysis is difficult due to small particle size, but indicates approximately 44% SiO_2, 3% MgO, and 6% Al_2O_3). Pressings of the base glass and P_2O_5 nucleated glass were also carried out, with the resultant microstructures similar to the BGMC sourced glass ceramic.

Some interface characterisation was carried out on the chopped fibre samples. Sample CF1 indicated, via EELS analysis, the presence of carbon enrichment at the interface, and the diffusion of Mg and Al into the fibre was also identified using EDS. This was also found for CF2 and the interface is shown in Fig 5.9. A number of points relating to this micrograph require further explanation. Within the matrix area on the micrograph light spots can be observed which are due to ion beam damage during specimen preparation. These areas are not seen in the matrix in general. Around the interface between the fibre and the matrix a dark band is present, particularly on the fibre side. This band is an artefact of the printing process and does not represent a sample related effect such as a diffusion band. Finally, toward the top right of the micrograph in the interface region a gap appears. This does not represent porosity at the interface but is again due to the ion beam thinning of the sample, the interface in this area has been beamed away. The micromechanical properties of the interface could not be measured for the chopped fibre samples. However, evidence for the suitability of the interface was gained from observation of deflected cracks at the interface in the TEM foils. Other chopped fibre samples were interfacially characterised during this study with similar results of carbon enrichment at the interface.

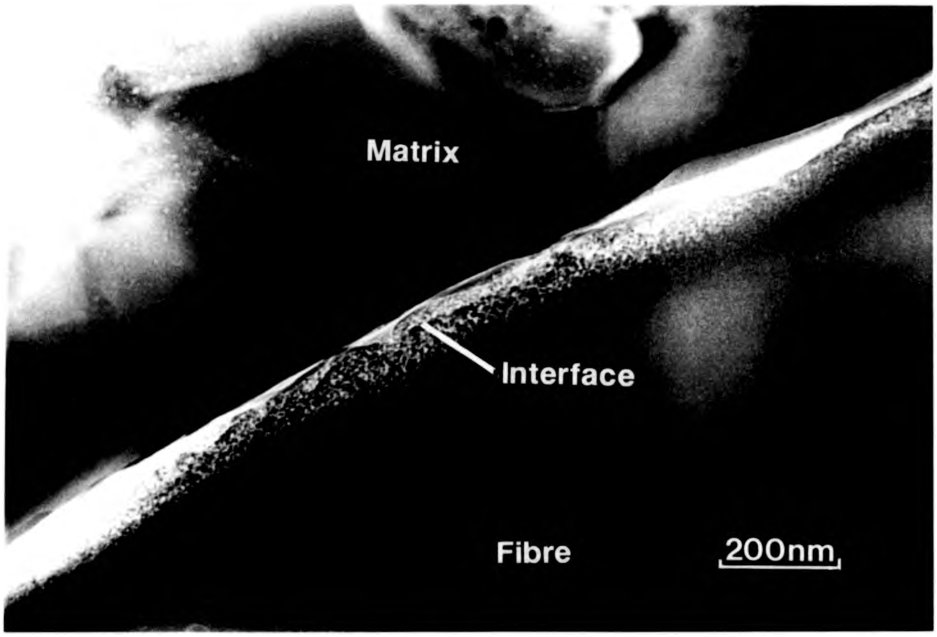
Matrix
Interface
Fibre
200nm

Figure 5.9. TEM micrograph showing the fibre / matrix interface in CF2.

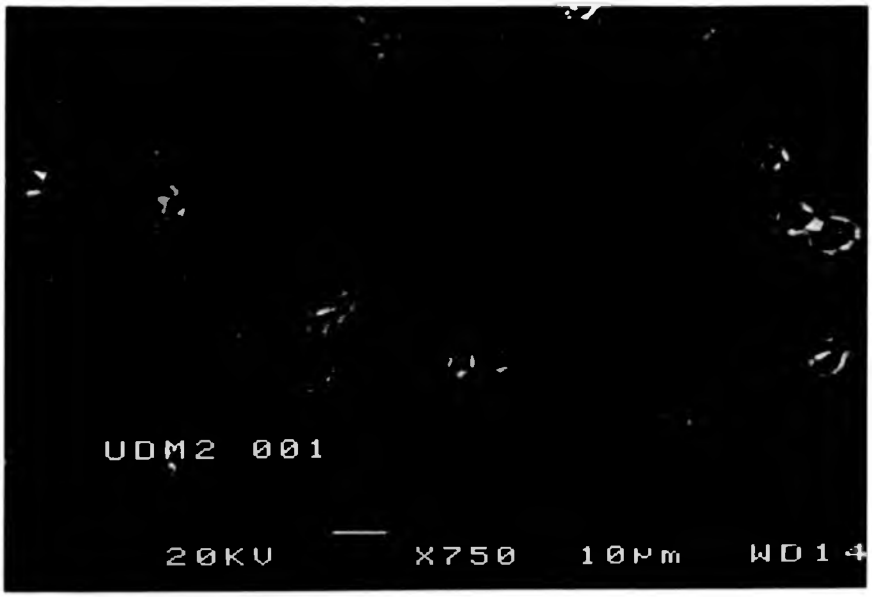
UDM2 001
20KV
X750
10µm
WD14

Figure 5.10. SEM backscattered micrograph indicating the structure of UDM2.

5.2. Unidirectional Composite Materials.

5.2.1. Microstructural Investigation.

Within this section the microstructures of the 'pre-refined processing' composites will be surveyed, before descriptions of the 'refined processing route' composites fabricated using the commercially sourced CDM and BGMC powders. The pre-preg for the pre-refined composite series was prepared by Rolls-Royce and, although the frit loading was high enough, porosity was present within the samples. The microstructure, as shown in Fig 5.10., is similar to that obtained for all of the UDM series samples. The micrograph shown in this figure shows that for these samples porosity is present and, in this particular case, damage to the fibres during the sample polishing has occurred. The fibre distribution within the sample is not ideal, with fibre tow clumping evident. For the series, XRD indicated an α-cordierite matrix with enstatite present, although approximate concentrations are difficult to ascertain as XRD traces from unidirectional composites are of poorer quality. EDS analysis confirmed this phase development. Optical photographs of these specimens allowed for volume fraction measurements as previously described and all composites fell within a band of 40 ± 4% volume fraction of fibres. It can be seen that some porosity is evident in the UDM series, although the level is low. The phase and microstructure attained validated the compositional selection philosophy. However, poor mechanical response indicated process development was required.

This led to the UDM series, mainly fabricated using the CDM powder. As will be described in Chapter 6., good mechanical behaviour was not achieved until CUDM5. This was attributed to too high a volume fraction of fibres within the composites and a non-optimised process schedule before this sample was reached. A typical microstructure for CUDM5 is shown in Fig 5.11a. The microstructure is complicated by the presence of the zirconia impurity and a small amount of porosity within the fibre bundles. A more detailed view of the microstructure is given in Fig 5.11b., where the complex nature of the microstructure can be seen. The samples

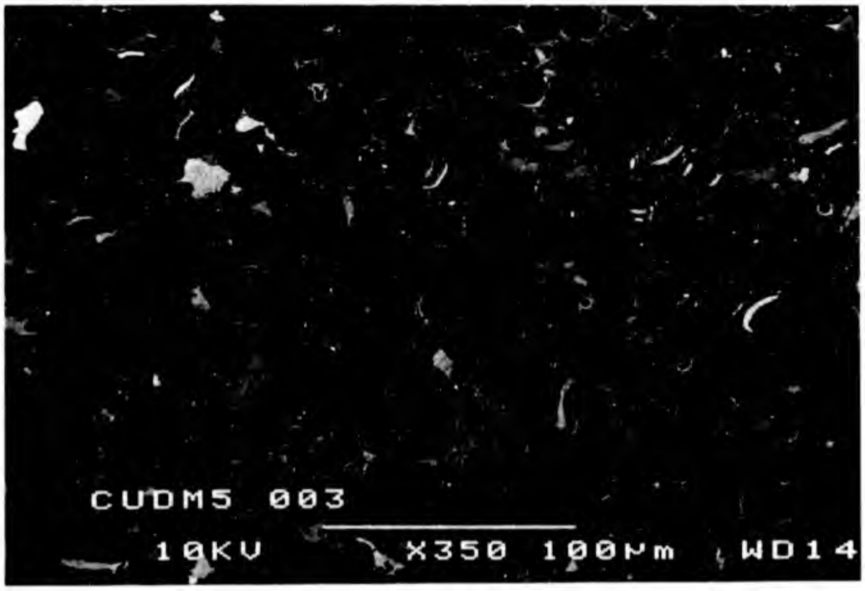
CUDM5 003
10KV X350 100µm WD14

Figure 5.11a. Low magnification SEM backscattered micrograph of CUDM5.

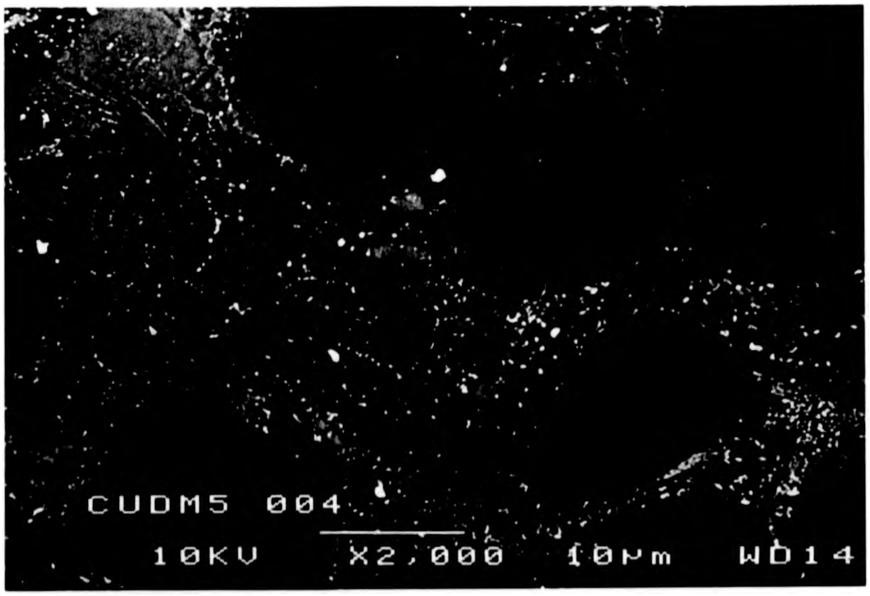
CUDM5 004
10KV X2,000 10µm WD14

Figure 5.11b. Higher magnification SEM backscattered micrograph of CUDM5.

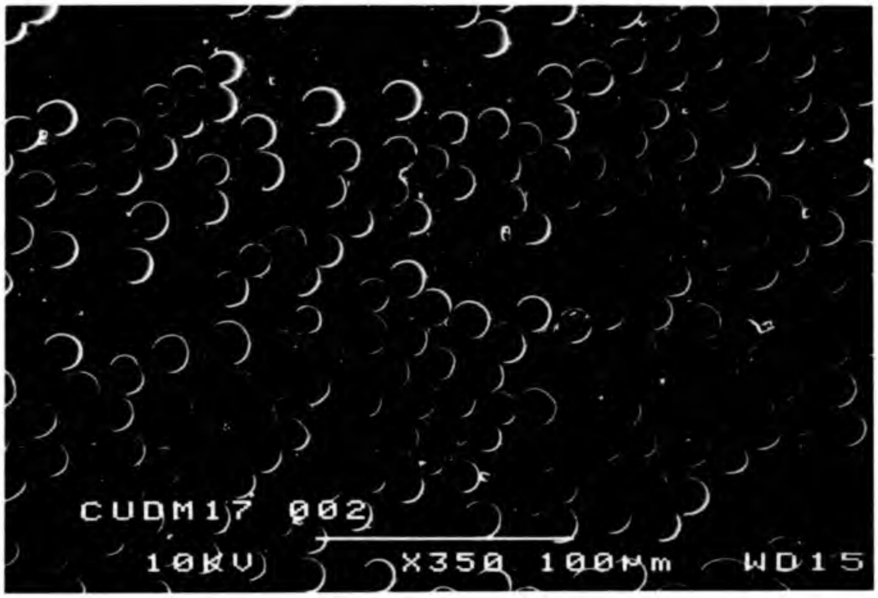
CUDM17 002
10KV X350 100μm WD15

Figure 5.12a. Lower magnification SEM secondary electron micrograph of CUDM17.

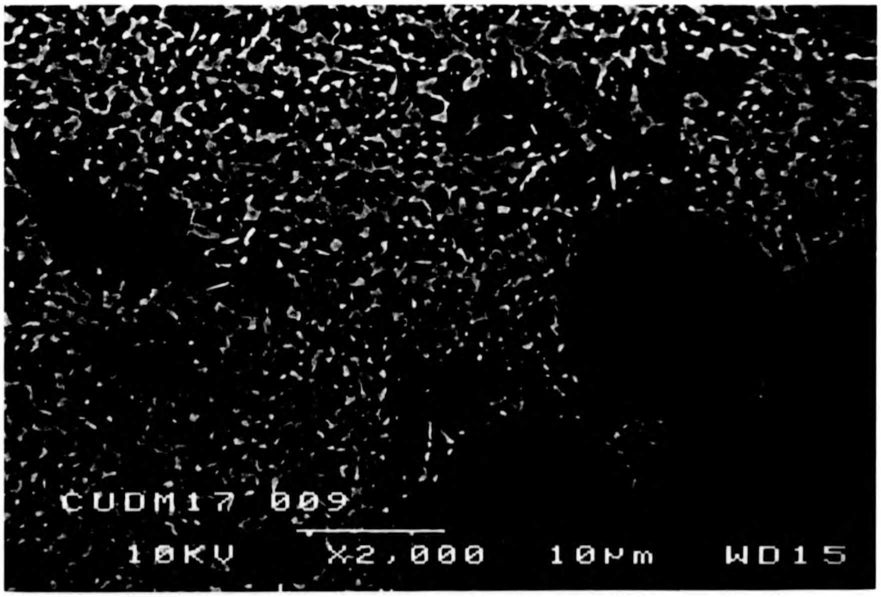
CUDM17 009
10KV X2,000 10μm WD15

Figure 5.12b. Higher magnification SEM backscattered micrograph of CUDM17.

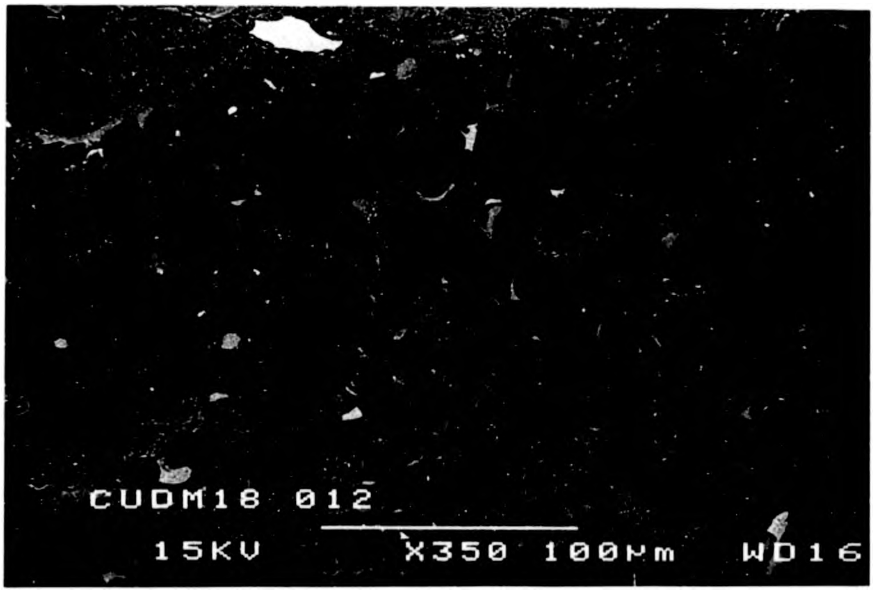
CUDM18 012
15KV X350 100µm WD16

Figure 5.13a. Lower magnification SEM backscattered micrograph of CUDM18 unidirectional.

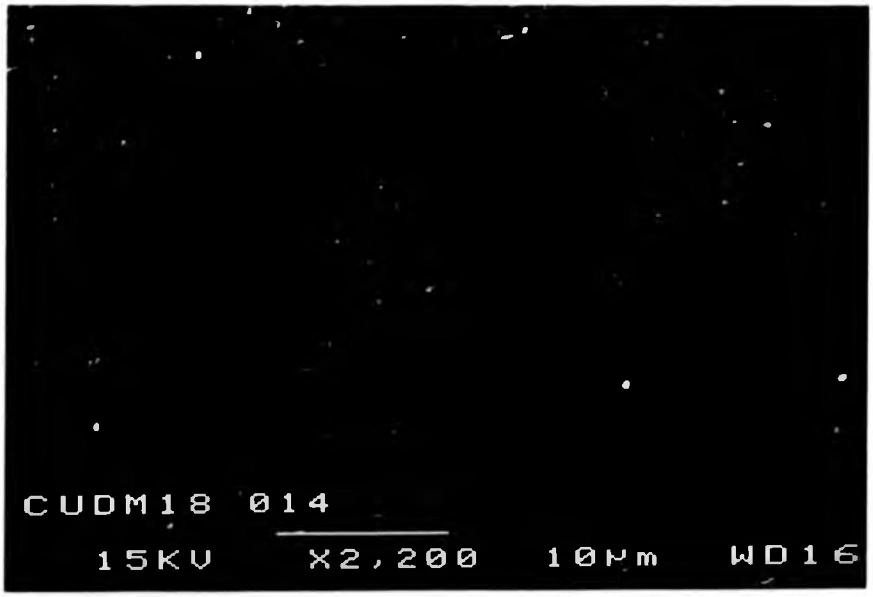
CUDM18 014
15KV X2,200 10µm WD16

Figure 5.13b. Higher magnification SEM backscattered micrograph of CUDM18 unidirectional.

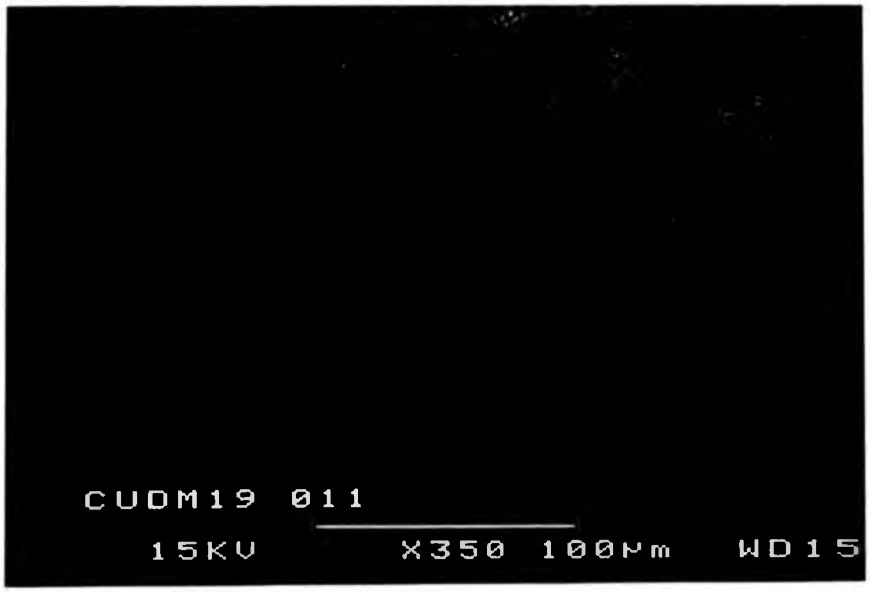
CUDM19 011
15KV X350 100µm WD15

Figure 5.14a. Lower magnification SEM backscattered micrograph of CUDM19 unidirectional.

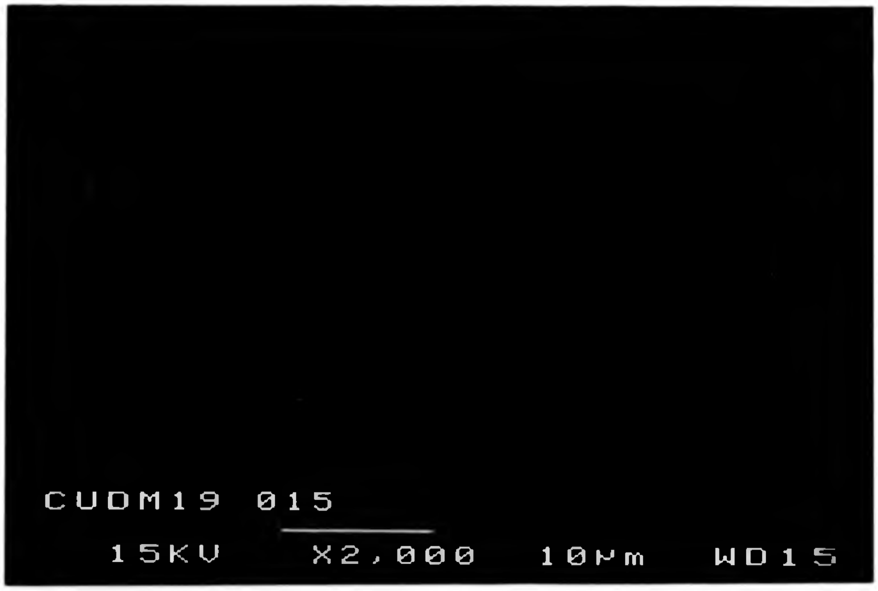
CUDM19 015
15KV X2,000 10µm WD15

Figure 5.14b. Higher magnification SEM backscattered micrograph of CUDM19 unidirectional.

CUDM7 and 12, as expected, exhibited the same structure as CUDM5. No obvious microstructural differences were observed between the 1hr, 2hr and 3hr isotherm composites. The matrix microstructure observed in these samples is similar to that observed for the CDM glass ceramic powder as shown in Fig 5.8. The only 'in-house' fabricated sample using the commercially sourced BGMC powder was CUDM17, microstructural views of this composite are given in Fig 5.12. The microstructure is now as for the CF base glass series without impurity additions present and the microstructure is fine grained. The micrograph shown in Fig 5.12a. shows evidence of polishing relief which causes the shadowing effect observed, as well as evidence of a small amount of residual porosity. The higher magnification micrograph presented in Fig 5.12b. indicates the fine grained diphasic microstructure achieved, with EDS and XRD indicating only α-cordierite and enstatite present in the matrix. For this composition, using the refined process schedule, good tow infill is achieved. However, there are matrix rich areas within the sample which would degrade the composite performance.

The materials supplied by Rolls-Royce utilising the process route described above are designated CUDM18 for the CDM powder composites and CUDM19 for the BGMC powder composites. Shown in Figs 5.13. and 5.14. are general and more detailed SEM micrographs for the unidirectional composites CUDM18 and 19. The micrographs presented in Fig 5.13. for CUDM18 show the differences between the Rolls-Royce fabricated materials and those fabricated in-house. Fig 5.13b. shows that the matrix microstructure for the CDM sourced glass ceramic materials is similar. However, differences can be seen from the lower magnification micrograph 5.13a. The fibre distribution in this sample is worse than the in-house composites, with more fibres touching and clumping more evident. The matrix has larger unreinforced areas with some large isolated pores (~ 10-15μm) present. Some of these comments are applicable to the CUDM19 composite. Again, the higher magnification image shown in Fig 5.14b. shows a similar scale microstructure as the in-house fabricated composites, with the lower magnification image indicating a non-optimised fibre distribution (Fig 5.14a.). Fibre tow clumping is evident, as are large bands of unreinforced glass ceramic between the fibre rich areas. These matrix rich areas would be detrimental to mechanical properties of the composite as would the porosity present in them (~ 5-10μm).

For the cross-ply samples a higher magnification image is presented for CUDM19, the BGMC powder composite in Fig 5.15. General features are similar for both cross-ply composites, with porosity more evident particularly on a fine scale. Fibre distribution was poor, with matrix rich areas existing within the plies and between the plies in some cases. The CUDM19 sample exhibited some debonding of the fibres from the matrix and crack deflection was evident. The matrices show a diphasic structure and, as indicated before, the CDM powder composite showed a more complex microstructure.

Within this study, a number of thermal aging treatments were conducted on the unidirectional samples. The aging temperatures selected were initially based upon work carried out within the research group utilising Corning CAS material (116). However, as more material became available, a sequence of aging treatments were carried out. Mechanical behavioural effects of the aging treatments will be discussed in Chapter 6. Optical micrographs were taken for CUDM18 and 19 in the as-fabricated and thermally-aged conditions (100hrs at temperature) for 450°C, 1000°C and 1200°C. Macroscale differences were not observed for the as-fabricated and 450°C aged composites. This was not true of the samples aged at higher temperatures. Here a white surface layer appears on the composite with the 1200°C showing greater degradation than the 1000°C case. For CUDM19 the surface layer was thicker for equivalent thermal aging to the CUDM18 composite.

The 450°C aging treatment showed no surface layer as can be seen by the SEM micrograph in Fig 5.16. and the composite microstructure is unaffected by the heat treatment. As will be described in the next section this is not true of the interfacial properties of the composites aged at 450°C. This surface layer is only evident in composites aged at temperatures of 1000°C or higher and evidence of this layer is shown in Fig 5.17. The surface layer is rich in the impurity element zirconium and contains voids indicative of gaseous evolution from within the composite. The layer

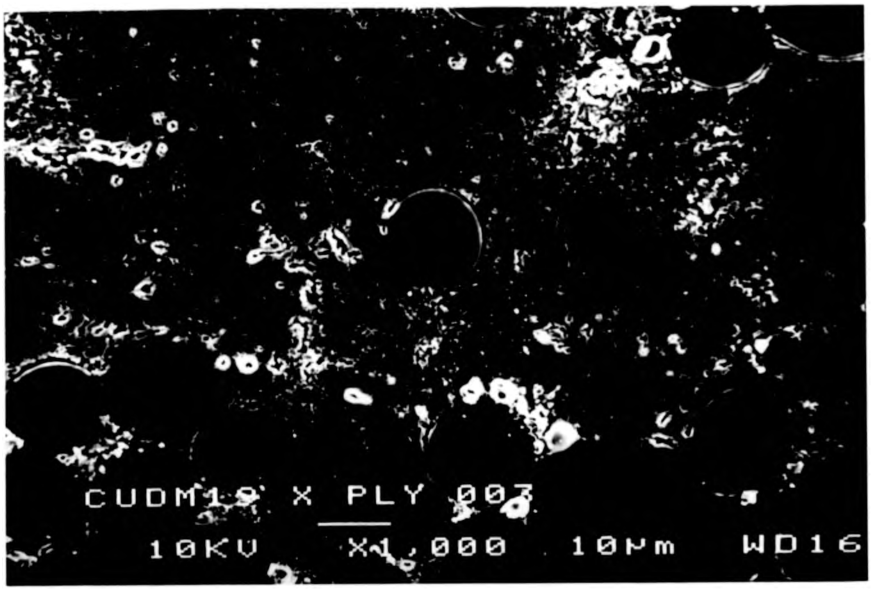
CUDM19 X PLY 007
10KV X1,000 10µm WD16

Figure 5.15. High magnification SEM secondary electron micrograph of CUDM19 cross-ply.

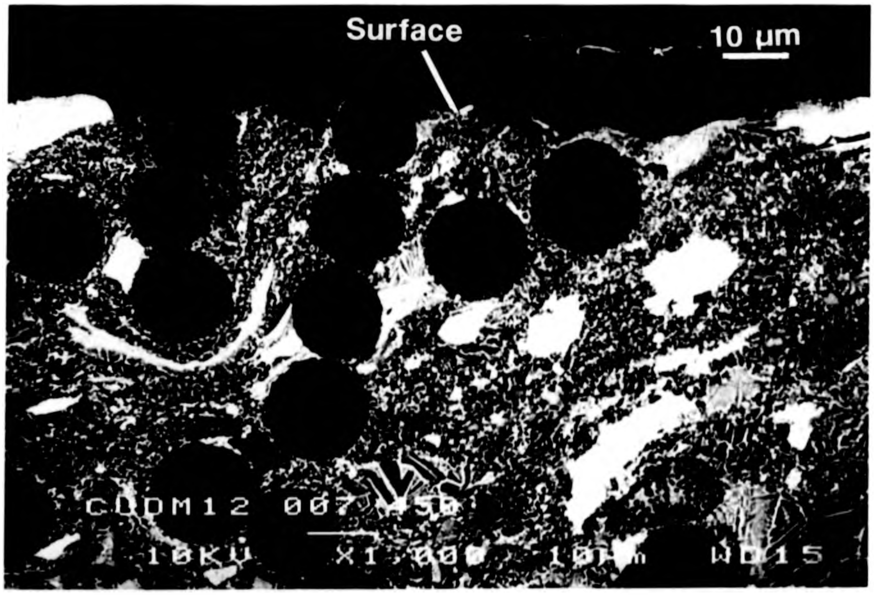
Surface
10 µm
CUDM12 007 450
10KV X1,000 10µm WD15

Figure 5.16. SEM backscattered micrograph for 450°C aging .

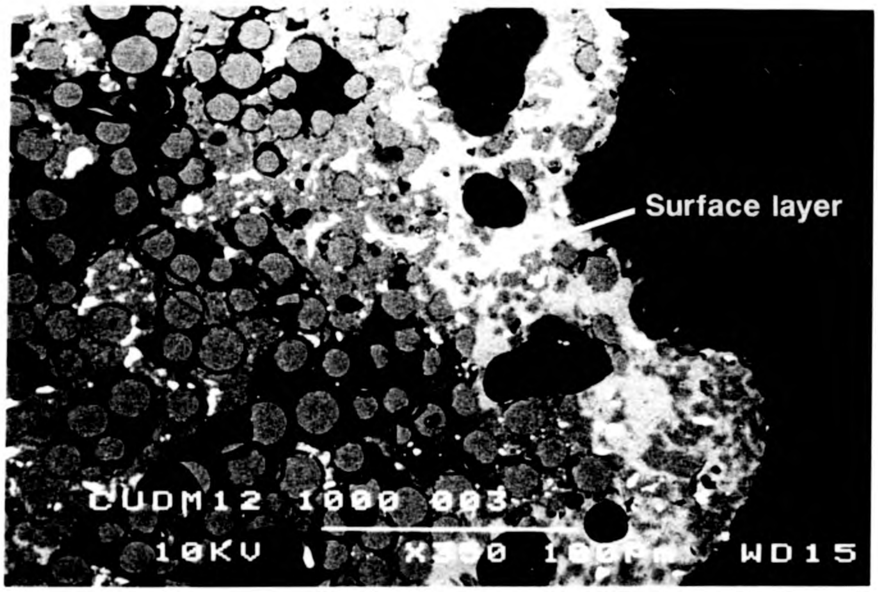
Surface layer
CUDM12 1000 003
10KV X300 100µm WD15

Figure 5.17. SEM backscattered micrograph for 1000°C aging of CUDM12.

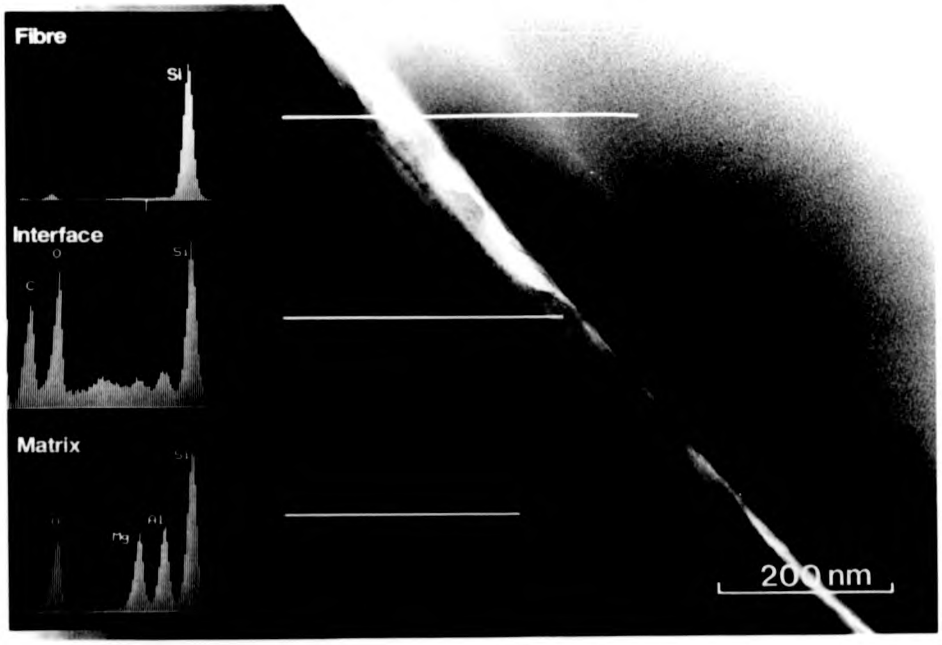
Fibre
Si
Interface
C
O
Si
Matrix
O
Mg
Al
Si
200 nm

Figure 5.18. TEM micrograph and light element analysis results for UDM4.

thickness varies between 60µm and 100µm, and the thermal aging treatment may affect the bulk of the composite if a suitable porosity path exists. If a porosity path from the surface does not exist, the oxygen ingress through the matrix is limited to a few fibre diameters (see the next section on interfacial characterisation of the composites).

Aging experiments carried out at higher temperatures show increased thickness of this surface layer. At 1200°C the reaction thickness varies from 80µm to 140µm. As for the 1000°C heat treatments, there are indications of gas bubble formation in the outer layer. The oxygen ingress depth is also increased as expected and porosity paths, if available, allow larger areas of the composite to be affected by the aging treatment. The composition of the surface layer was determined via EDS, with the main phase present having a composition of approximately 45% MgO, 23.5% Al_2O_3, 27.5 SiO_2 and 3% ZrO_2 (i.e. within the spinel phase field). Specific results given above relate to the 1hr isotherm hold time samples. Similar behaviour was observed for all the composites tested in this study.

5.2.2. Interfacial Structure and Micromechanical Behaviour.

TEM imaging and analysis is required to determine the structure of the interface. Fig 5.18. shows a TEM micrograph of UDM4, the smooth line being indicative of interface formation by reaction with the fibre as stated in Chapter 2. (Note : UDM4 contains NL-201 fibres). Using light element analysis the constitution of the interface can be investigated as presented in Fig 5.18. for UDM4. The presence of a carbon enriched interfacial layer is indicated by the light element traces, even though other elemental species (especially oxygen) exist in this layer. For the fibre analysis some matrix elements are present, representing diffusion of magnesium and aluminium into the fibre and this can be seen by the darker layer extending into the fibre ~ 110-180nm. As was the case in Fig 5.9. for CF2, ion beam damage of the matrix has occurred and can be seen in Fig 5.18.

For composites processed with a matrix from the commercially sourced CDM powder, as with the BGMC powder, similar results are attained, with the presence of the carbon interfacial layer being detected in all cases. This can be seen in Fig 5.19. which shows a micrograph and analysis results for CUDM7 (Note : CUDM7 contains NL-607 fibres). The analysis shown in this figure, as for Fig 5.18., shows that carbon enrichment occurs at the interface. It can also be seen that the diffusion of matrix elements into the fibre is lessened in this case. However, the analysed area is further into the fibre than for UDM4. As for UDM4, other elemental species are present at the interface. As was the case for the TEM micrograph of CF2, Fig 5.9., a band can be observed on the micrograph presented in Fig 5.19. around the interface region. This is an artefact of the printing process and does not represent a real specimen effect. Upon thermal aging treatment to 700°C the effect upon the interface is as indicated in Fig 5.20. Again on this micrograph a band is present around the interface region. This, as in the above case, is an artefact of the printing process. From the analysis results it can be seen that the carbon enrichment is no longer present at the interface. The interfacial structure is different form the non-aged specimens and analysis shows that silicon and oxygen are the major elements present in areas such as that shown, with smaller amounts of magnesium and aluminium. Hence, for this case, a silica bridge has formed across this part of the interface, although the bridging is not complete for this aging temperature. Further examination of the sample shows areas with carbon rich interfacial regions as is observed in the non-aged composite (Fig 5.19.). For this composite aged at 1000°C a silica plug is formed at the interface near the edges of the composite, and SEM x-ray linescans indicate no carbon at the interface with only silicon and oxygen present in major amounts with small residual amounts of magnesium and aluminium.

These results presented above relate directly to the 1hr crystallisation isotherm. However, similar results were obtained for the 2 and 3hr isotherm composites and hence they are believed to be generic. The longer processing times can not only affect the degree of crystallisation of the matrix, but can change the interfacial development also. For the 3hr isotherm analysis indicates a carbon rich interfacial layer, which has a thickness ~35-70nm, but the interface in some areas shows evidence of bubble formation, as will be discussed at the end of this chapter.

The above discussion has concentrated on the constitution and the scale

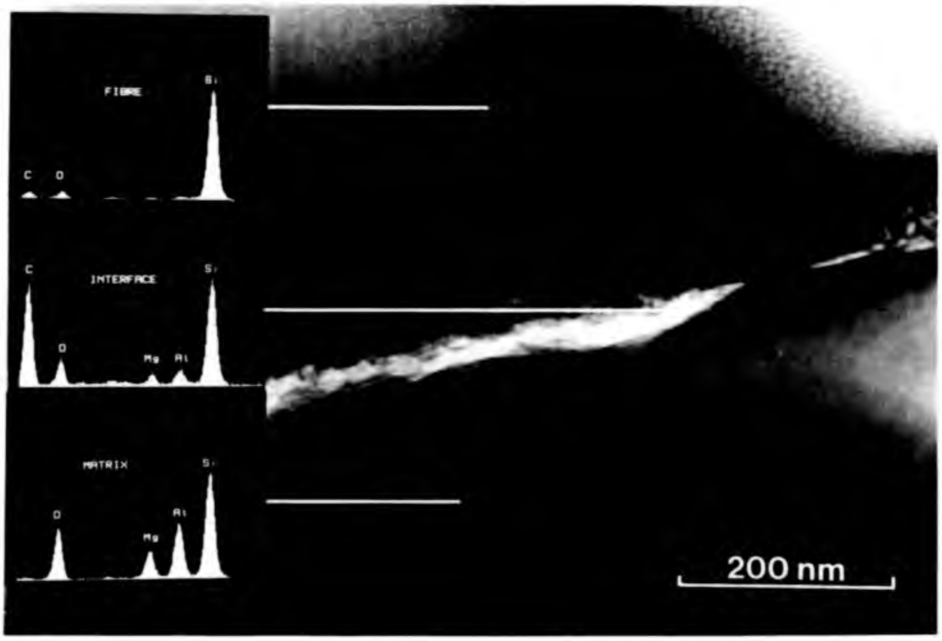
FIBRE
C
O
Si
INTERFACE
C
O
Mg
Al
Si
MATRIX
O
Mg
Al
Si
200 nm

Figure 5.19. TEM micrograph and light element analysis results for CUDM7.

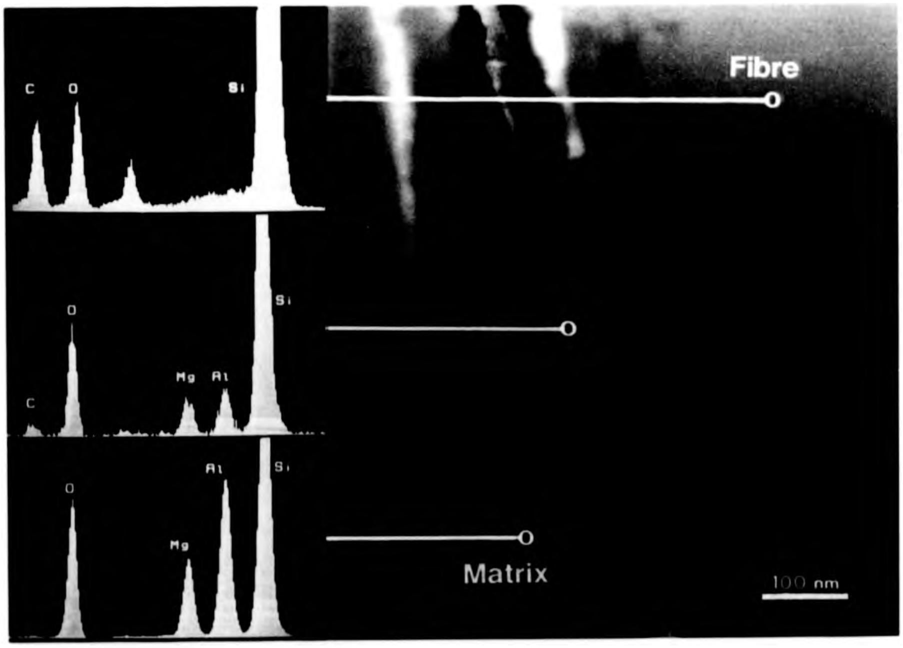
C
O
Si
Fibre
O
C
Mg
Al
Si
O
Mg
Al
Si
Matrix
100 nm

Figure 5.20. TEM micrograph and light element analysis results for CUDM7 after aging at 700°C for 100hrs.

of the interface. The remainder of this section concentrates on the micromechanical response of the interface. The micromechanical properties of the debond energy 2Γ and the shear sliding resistance τ, were measured as described in Chapter 3., Section 6., with an example of an indented fibre shown in Fig 5.21. This figure illustrates how accurately the indenter tip can be positioned on the fibre surface. Normally the fibre would not show any radial cracks and the test results are not used after cracking has occurred. The results of this evaluation are presented in Table 5.1., and are based on an average of ten indents per sample. For the sample aged at 1000°C it should be noted that indentations taken within a few fibre diameters from the sample edge produced very different results with 2Γ and τ much higher than those for the middle of the sample as presented in the table. This indicates that oxygen ingress into the sample causes a marked effect on the interfacial properties to within a few fibre diameters of the edge of the sample.

The table shows the marked difference between the NL-607 and NL-201 fibre types within the composite and this may be responsible for the differences in the mechanical response between these composites (see Chapter 6.). This difference can

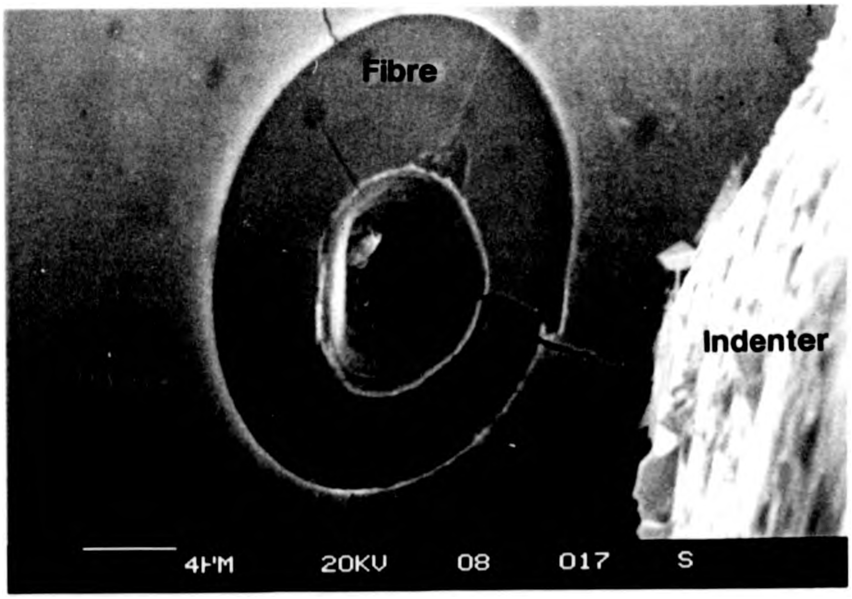

Figure 5.21. SEM micrograph showing an indented fibre.

Sample designation and state.	Micromechanical Properties.	
	2Γ (Jm^{-2})	τ (MPa).
MAS / NL - 201 as fabricated	30.4±7.2	239±150
MAS / NL - 607 as fabricated	12.4±5.4	48±15
aged 450°C	13.6±4.4	108±54
aged 700°C	35.6±29.2	248±120
aged 1000°C	14.2±8.4	42±7
CUDM18 unidirectional	2.6±1.6	45±9
CUDM19 unidirectional	8.2±3.8	70±16

Table 5.1. Micromechanical property measurements for composites in this study.

be further illustrated by the indenter load versus tip displacement plots shown in Fig 5.22. Results for the thermal aging experiments show the differences in the interfacial response due to exposure in air, and are shown graphically in Fig 5.23. This illustrates the rise in micromechanical properties at intermediate temperatures for composites fabricated with NL-607 fibre and the 3hr isotherm.

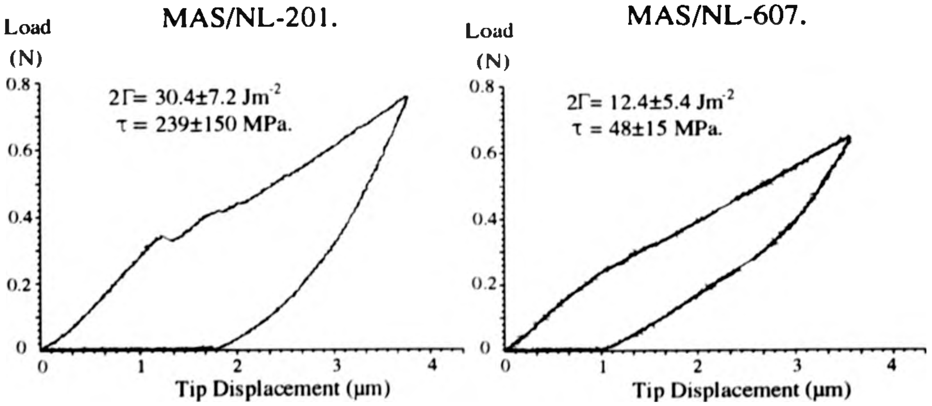

Figure 5.22. Load versus tip displacement plots for the NL-201 and NL-607 fibres.

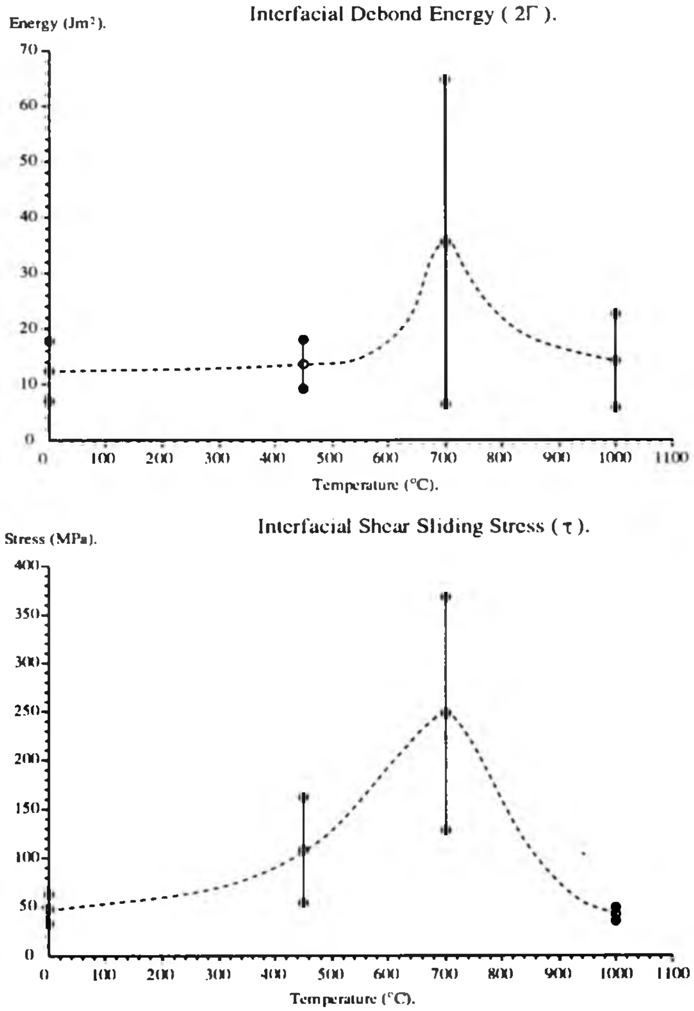

Figure 5.23. Graphical plot of the interfacial micromechanical properties 2Γ and τ, compared to thermal aging temperature.

5.3. Discussion of the Microstructure and Interfacial Properties of the Composites.

5.3.1. Matrix Densification and Crystallisation.

It should be remembered that the chopped fibre materials were studied in order to investigate powder compositions suitable for unidirectional composite fabrication, processing windows for composite fabrication and, in a preliminary manner, the interfacial structure of MAS matrix / Nicalon fibre composites. For the powder compositional selection criteria the use of chopped fibre material allowed for the selection of glass compositions not containing nucleants (as powder size was on a ~ 10µm scale). The role of TiO_2 added at 10wt% to the base glass composition was found to give phase evolution with the metastable µ-cordierite polymorph and hence, because of this phase's metastability and high thermal expansion, the powder was not pursued for further study. Titanates were found to segregate out from the glass and form relatively large facetted crystals within the bulk microstructure of the crystallised glass ceramic. The P_2O_5 nucleated base glass exhibited small ~ ¼µm phosphorus rich particles within the matrix.

Hence, for the bulk of the chopped fibre study, the P_2O_5 nucleated and base glass composition powders were utilised under a range of process conditions. Both powders were used in order to verify that the nucleant was not needed in any of these processing situations. For the window II pressings carried out at 1300°C with the single crystallisation and the nucleation and crystallisation steps involved, very little difference between the base and nucleant added glasses were observed. All samples were diphasic with α-cordierite as the major phase and variations in the percentage of enstatite as the minor phase. Hence not only can the composition alter the phase structure, but also the heat treatment used. All these samples exhibited good fibre tow infill under harsh conditions, with no prior tow infill before consolidation.

In order to evaluate whether the compositional selection concept of the tie line approach was valid, stoichiometric pressings were carried out for identical processing conditions. Differential thermal analysis of the stoichiometric glass indicated no obvious process windows and that glass softening was not occurring below 1300°C. Hence, by using a processing schedule with a maximum temperature of 1300°C, a microstructure containing porosity with residual cracking and having poor fibre bundle infill was produced.

Due to the thermal instability problems associated with Nicalon processing at high temperatures was to be avoided during composite fabrication. Although no damage to the fibre was observed by SEM or TEM due to the 1300°C short term processing exposure, if fabrication could be carried out at lower processing temperatures then this was considered desirable. Results, for the 1200°C maximum processing temperature, indicated that some residual porosity was present and that tow infill was degraded from the higher maximum temperatures. Utilising an even lower maximum temperature such as 1100°C porosity became far more evident, with the base glass exhibiting a predominantly μ-cordierite matrix. This indicates that 1100°C was too low for adequate consolidation. However, the 1200°C maximum temperature produced the correct scale microstructure and phase structure.

The final series of experiments utilising the chopped fibre route were used to investigate the window I pressing route that was available as a result of the change in composition away from stoichiometry. From the DTA traces of the base and P_2O_5 nucleated glasses a process window exists in the range of ~ 850°-930°C. Therefore pressure to consolidate was applied at 890°C. For these samples, much larger scale porosity was observed in the range 3-10μm dependent on the crystallisation isotherm hold time and all samples exhibited a predominantly μ-cordierite matrix. Hence this process window was unsuitable for use in composite fabrication.

5.3.2. Composite Interface, Microstructure and Properties.

Whilst the preliminary investigation was being carried out the availability of some pre-preg sheets allowed for a brief study of composite fabrication utilising a single step heat treatment process. These samples, designated UDM, used a range of pressures from 3.5-10MPa and temperatures from 950°-1100°C. The mechanical behaviour of these samples will be described in Chapter 6., but was poor in comparison to the optimised process route. These process schedules gave the correct phase structure and micron scale microstructure. However, porosity was present within the samples and some fibre bundles were poorly infilled. The temperature range employed in the fabrication of these composites and the heat treatment cycle used was believed to be a major contributory factor to the poor mechanical response. The application of pressure at the glass softening point could cause significant fibre damage due to thermal inertia. Pressure application was sudden, the whole load being applied at once, and was immediately followed by the crystallising heat treatment. The crystallisation step may have caused the porosity as the glass particles could no longer flow to close any pores and degraded bundle infill.

Analysis, using TEM, of the interfaces in these materials indicates the presence of a carbon rich interfacial layer. The presence of this carbon interfacial layer is desirable, but the interfacial properties of the composite can still be very different depending on the process route and fibre type used. Composites fabricated with the NL-607 fibre (i.e. CUDM7) showed very different interfacial properties in comparison to the NL-201 fibre (i.e. UDM4), as shown in Fig 5.22. The NL-201 composite has a very high debond energy and a high shear sliding resistance in comparison to the NL-607 fibre case. It must be remembered that the analysis of Marshall and Oliver used to calculate these results is not strictly applicable for the case of a sudden debond event as exhibited for the NL-201 fibre case (124). The analysis conditions apply to the case of a gradual debond, as exhibited by the NL-607 composites, and hence care must be used in the interpretation of the numerical data and its accuracy. However, the interfacial response of the two fibres is different, and the more gradual debond and lower values of 2Γ and τ exhibited by the NL-607 fibre composites would suggest a better mechanical response.

The combined information from the UDM and CF fabrication trials led to the development of the optimised fabrication schedule. It was decided, for consolidation reasons, to eliminate porosity and to provide for some glass flow into the tow bundles, that a temperature of 1200°C was required. This temperature was selected since both CF and UDM trials, carried out using 1100°C maximum temperatures, resulted in non-desirable properties. It is interesting to note that, for the UDM composites fabricated at 1100°C, the matrix predominantly consisted of α-cordierite. Whereas for the CF trials, with the non-nucleant added glasses, μ-cordierite matrices were predominant. This may be indicative of the effect of the fibres in promoting a transformation to the α-cordierite polymorph. Bundle infill problems utilising the chopped fibre route at 1200°C were considered to be less of a problem. Since, if correct pre-pregging was carried out, adequate frit would exist in the tow bundle and the temperature would allow some glass flow. Importantly, on a microstructural level, at 1200°C the base glass and nucleated glasses produced the desired micron scale microstructure and the appropriate phase structure.

The early processing attempts at unidirectional composite fabrication had used pressure application at a temperature of ~ 950°C. From analysis of the DTA traces this pressure application temperature is not in the process window available. Factors, such as the pressure application rate and the ~ 35°Cmin^{-1} heating rate, through this section of the fabrication procedure suggested that fibre damage and poor mechanical response would occur. This was confirmed, since the Young's modulus of the composite upon initial loading (the linear region of the stress / deflection curve) was degraded from a rule of mixtures calculation (see Chapter 6.). Hence, within the optimised process route, the pressure application was more gradual, starting after the glass softening point at 850°C. Pressure was applied smoothly over a 3 minute interval and the heating rate was 20°Cmin^{-1} through this part of the process. This approach allowed for fabrication of composites, in the CUDM series, which exhibited a Young's modulus very close to that predicted by a rule of mixtures.

The microstructures, exhibited by the CDM powder series of unidirectional composites, CUDM5-15 and 18, are complicated by the presence of ZrO_2 in the commercially sourced powder. The oxide impurity, ZrO_2, has been utilised as a nucleant in glass ceramic systems as described by Strnad (52) and McMillan (51). Other researchers have investigated the effect of this nucleant in the crystallisation of cordierite and cordierite containing systems (129) (152). Studies have utilised ~ 5-10wt% ZrO_2 as a nucleant and hence the impurity content, found in the powder utilised in this study, of ~ 3wt% may be too low to have any major effect. The above authors, in some cases, have used mixtures of ZrO_2 and P_2O_5, making it difficult to discern the effect of the ZrO_2. However, the studies show that ZrO_2 does have a definite effect as a nucleant and that the mechanism may have been by the precipitation of minor phases containing ZrO_2. The suggested nucleation mechanism is the liquid phase separation of ZrO_2-rich regions in a SiO_2 rich matrix followed by crystallisation of a β-quartz solid solution. This solid solution then transforms to μ-cordierite and then α-cordierite (158). This work has indicated an effect by the use of 5% ZrO_2 (stabilised with 3 mol% Y_2O_3) for nucleation catalysis. Although, for this study, P_2O_5 was added at 3wt% and so this addition may affect the role of the ZrO_2 (158).

Even though the microstructure is complicated by the impurity, XRD analysis indicates an α-cordierite and enstatite matrix mixture as required by the initial objectives of the program. It is not clear whether the ZrO_2 addition would significantly affect the viscosity of the glass or even its refractoriness. The powder was utilised for the bulk of the study because of its availability in reasonable quantities (i.e. ~ 5kg). Mechanical testing at room temperature for the as-fabricated condition, as described below and in Chapter 6., indicated good properties and hence, for this reason also, this powder composition was utilised. Due to the delay in the supply of the commercially sourced BGMC powder, a more limited amount of work was possible with this. The BGMC powder was the composition originally selected and did not contain significant impurity levels and results in a diphasic microstructure. The structure far more closely resembles that of the original base glass composition powders.

The microstructure of the Rolls-Royce fabricated materials reflects the difficulty in process scale up from the 50x50mm plate size used for the previous fabrication studies. The Rolls-Royce pre-preg process is different from the process developed in this study and so some differences are to be expected. However, the Rolls-Royce fabricated materials using the refined process route do show good mechanical properties. Although, as demonstrated in Chapter 6., the materials do not attain the levels set by the in-house materials. These materials show higher porosity levels and areas of matrix rich regions which are not as prominent in the in-house materials.

The interface within these composite systems is the key to good mechanical properties. Determination of both the interface constitution and micromechanical properties was made during this study. The linescanning technique could not resolve the interface. This is to be expected, since TEM studies subsequently revealed an interface width of <100nm and the calculated width of the x-ray excitation is ~ 1μm. As was previously mentioned in Chapter 3., Section 2.1., preparation of TEM foils required extreme care in order to produce useful results. The as-cut slices which were to be polished before ion beam thinning had poor mechanical properties and in some cases fibres were debonding from the matrix. This damage was probably occurring during the sectioning of these slices and as stated previously caused difficulty in the production of good TEM samples.

The constitution of the interface was analysed for a number of the composites. The analysis indicates that a C-rich interfacial layer exists, as would be expected from the matrix and fibre chemistries. For the UDM series, and in particular UDM4, the size of the interface for this processing route is 20-40nm with the Nicalon NL-201 fibre. For the refined processing route composites, the CUDM series, using the NL-607 fibre, then the interface thickness ranges from 25-70nm depending on the isothermal hold time. The thicknesses of the C-rich layer are augmented in the CUDM series by the presence of the 10-20nm pyrolytic carbon coat applied during the manufacture of the Nicalon NL-607 fibre. It should be noted that for the longer isotherm hold times at 1200°C, i.e. CUDM 14 / 15 using the NL-607 fibre, gas bubble formation may occur in the interface region. This phenomenon was also observed for MAS GCMCs fabricated with prolonged hold times by Murthy and Lewis who suggested that it is due to carbon oxidation products. These are produced as a result of locally enhanced SiO_2 activity since transport rates for CO and O_2 are reduced by the thickening of the interface layer (77).

The mechanism of formation for these carbon-rich interfaces is as described in Chapter 2., Section 3. The oxidation of the fibre surface to form a carbon layer and silica product is described by equation (2.12), and in detail by Cooper and Chyung (91). Within this study detailed characterisation of the interface has not been carried out. The constitution was evaluated, however the kinetics of interface formation have not been studied. The work has shown that a small increase in interface thickness occurred with increased isothermal hold time as would be expected. Further to this the diffusion of matrix elements into the fibre (Mg, Al) was noted.

As will be described later for the micromechanical properties of the interface, much of the interface characterisation work in the literature has centred on the

LAS / Nicalon system. Results indicate that for LASIII / Nicalon composites the interface consists of an amorphous or graphitic carbon layer (dependent on processing temperature and time) of thickness 50-150nm next to the fibre. This is surrounded by a polycrystalline NbC layer of thickness 20-200nm, with interfacial gaps present (near the NbC / C layer) of thickness ~ 40nm (159) (160). The interfaces observed in this work have a less complex structure and a smaller thickness. The work of Hommeny et al., reviews the interfacial studies conducted and also carried out a series of experiments using LAS / Nicalon composites to investigate the effects of processing time and temperature on the interface thickness (161). The research agreed with the models of Cooper and Chyung (91) and Benson et al. (114) and found that interface widths of 140-540nm of carbon were formed with processing time and temperature combinations ranging from 1000°C / 30min to 1100°C / 240min. They also found, as indicated in this work, that increased time at temperature led to increased interface thickness.

Other research into interface formation in CMC systems has shown that in-situ reacted interfaces, as formed by the MAS / Nicalon composites fabricated in this work, can exhibit a range of widths for the carbon-rich layer. Lewis and Murthy found that for borosilicate / Nicalon composites fabricated at 1100°C a 10-20nm carbon-rich layer could be observed with sodium diffusion into the fibre to a depth of 200nm. For GCMCs fabricated using temperatures in the range 1000°-1300°C, CAS / Nicalon had a carbon-rich layer of thickness 50-75nm, whereas for BAS / Nicalon the thickness increased to ~ 250nm (77). In their work, Cooper and Chyung observed a 80nm graphitic carbon interface layer in a Pyrex / Nicalon composite fabricated at 1300°C. For the same composite fabricated at 950°C no interface layer was observed and the composite exhibited a brittle mechanical response (91). The work of Chen et al. using MAS, dopant added glasses found carbon-rich interfaces in all cases for a 1300°C / 15min fabrication route, ranging from 22.5nm for a Nb doped glass to 58nm for a Li doped glass (diffusion of dopants into the fibres was observed) (97). Their results also indicated that the thicker the observed carbon rich layer, the higher the ultimate flexural strength of the composite. The work of Herron and Risbud on a Ba-Si-Al-O-N /

Nicalon composite showed a carbon-rich interfacial layer 10-20nm thick with Ba diffusion into the fibre (162). Finally, in this review of the literature, the work of Bonney and Cooper on the commercially available CAS / Nicalon Corning material indicated a graphitic interface of ~ 100nm thickness with Ca and Al diffusion into the fibres (112).

The above summary of some of the literature work on composite interfaces indicates that the interface widths observed in this work are small. For the NL-201 composites the carbon-rich region was 20-40nm in thickness. Whereas for NL-607 composites this thickness was increased to 25-70nm depending on the isothermal hold time. For the NL-607 fibre composites 10-20nm of this layer is the pre-applied pyrolytic coating. The interface widths observed in this work are similar to the widths seen in glass matrix composites fabricated by other researchers. Although, for the 3hr isothermal hold time, composites widths are approaching those of the LAS and CAS composite systems. It is interesting to note that the MAS composites fabricated by Chen et al., using doped MAS glasses also exhibit thinner interface widths with increased fabrication temperature but for a reduced time (97).

The differences in the indentation tests conducted for the NL-201 and NL-607 fibres in the MAS composites are quite dramatic. As stated above the analysis used to calculate the interfacial properties is not strictly applicable in the NL-201 case because of the sudden debond. In addition to this it must also be stated that the analysis does not in any way account for the Poisson effect upon the pushed fibre. However, for the NL-607 fibre case the analysis is valid, as gradual debond is observed on the load versus indenter depth trace. For the CUDM series, with the NL-607 fibre, the larger C-rich layer does show the desired debond and sliding properties. From Chapter 2., Table 2.5., the interfacial properties quoted here are somewhat greater than those given for other GCMC matrices. Part of this discrepancy is believed to be due to Poisson considerations and part due to the fact that, in many previous measurements, loads such as those used here could not be applied. Many of the GCMCs studied and evaluated previously have been the LAS matrix systems. Where, because the matrix has a linear thermal expansion coefficient lower than that of the fibre (for β-spodumene $\alpha = 0.9$ x

10^{-6}°C^{-1}), the matrix pulls away from the fibre during cool down from the fabrication temperature and hence low values of 2Γ and τ are to be expected.

The evaluation of the interfacial micromechanical properties τ, 2Γ depends critically on the fibre reference hardness that is subtracted from the actual push-down test data as explained in Chapter 3., Section 6. For this evaluation a number of fibre reference hardness traces were taken using a composite section polished parallel to the fibre direction (since Nicalon is nanocrystalline, there is thought to be no structural anisotropy). Using the same indenter tip as for the fibre push-down experiments the centre of the fibre was indented under increasing load until fibre fracture occurred. This gave a trace of the plastic deformation of the fibre dependent on the applied load assuming that the matrix deformation could be ignored. Since a number of reference traces were taken the results were averaged and a third order polynomial fitted to the average result. This fitted curve differed by ±0.008N from the actual results for all displacements. This reference curve then allows for the actual fibre displacement to be calculated, as required by the Marshall and Oliver analysis (124). Measurements of hardness for the Nicalon fibre taken with a Vickers indenter gave 20±1.5GPa for a 0.57N load, which is high when compared to Marshall's original work that indicated a fibre hardness of 13GPa for loads of 0.44 and 0.23N (163).

Since the interfacial sliding stress determined by push-down testing is sensitive to the fibre hardness, then small errors associated with the reference hardness of Nicalon could have considerable effects on the value of τ measured. This could explain the high values measured for τ in this work. For the conical indenter with its radiused tip the surface area is required in order to calculate the hardness of the material (H = Force / Area). The fibre hardness was not quantitatively evaluated for this geometry since it is not required for the Marshall and Oliver analysis (124). Hence it is difficult to comment on the fibre hardness effect for the measured τ values quoted here, except that the large values may be a consequence of errors associated with the reference hardness traces.

The use of the conical indenter geometry does, however, allow the fibres to be pushed large distances (up to 3μm) in comparison to the more obtuse Vickers or

Berkovich geometries. If the debond component of the interfacial analysis is ignored it is possible to calculate the debond length of the fibres (163). For the NL-607 fibres, calculation gives l=273±124µm and for the NL-201 fibres l=107±64µm. Hence, the criterion that the debond length is much greater than the fibre radius used in this analysis is satisfied and since the samples are 5mm deep the debond length does not approach the sample dimension.

As stated previously the Marshall and Oliver analysis provides only a simplified analysis, with no attempt to account for Poisson expansion, residual stress or interface roughness. Their model was tested experimentally on the LASIII / Nicalon system whose interface is described above. These interfaces, as indicated in Table 2.5., give micromechanical properties of $\tau \sim 3.5$MPa and $2\Gamma \sim 4\times10^{-2}$Jm^{-2}, which can be expected because of the thermal expansion coefficient of the matrix. The matrix pulls away form the fibres during the cool down from the fabrication temperature causing interfacial gaps and the low measured interfacial micromechanical properties. The Poisson effect of expansion of the fibres during push-down was thought to be negligible, since from Marshall and Oliver's work τ_{INDENT} agreed with $\tau_{TENSION}$ calculated from crack spacing measurements (124). Detailed analysis and study on the Poisson expansion effect was carried out by Weihs and Nix on the LASIII / Nicalon system (116). Their analysis suggested that τ would increase with Poisson expansion effects and that a compressive matrix strain would give an overestimate of τ using the push-down technique. Experimentally, using the LASIII / Nicalon system, their results were inconclusive. However, the system studied in this work does have a compressive matrix strain and so increases in τ might be expected.

On some of the push-down tests conducted an increasing gradient in the F^2 vs U plots was observed (these were not used for calculation of the micromechanical parameters). If this effect was only due to the Poisson expansion of the fibres (assuming for Nicalon $\nu = 0.2$, $r = 7.2\mu m$ and $2\Gamma = 0$Jm^{-2}) then the increase in radius is $\Delta r \sim 15$nm, which is of the same order of magnitude as the interface width in these composites (164). This may suggest that the smaller interface widths found for the MAS composites may not show enough compliance and hence the Poisson effect becomes noticeable. As this type of behaviour was only observed in a small number of cases the effect is thought to be small. Interface roughness may also effect the measured τ value and, since fibres are pushed relatively large distances by this technique, part of the increase in τ measured may be due to the increased sampling length and the roughness associated with this.

The measured values for τ given in Table 2.5., apart form the case of the LASIII / Nicalon system described above, show a considerable spread in results. All values are low in comparison to those given in this work. The SiC / Nicalon work of Lowden and Stinton shows the effect of changing the width of the carbon layer and shows that considerable decreases in τ are possible as the layer thickness is increased from 30nm to 120nm (103). For the composites studied in this research with interface widths ~ 35-70nm, relatively high τ values might be expected. This change in interfacial micromechanical properties was also noted by Singh, when Zircon SCS-6 composites showed improved mechanical behaviour with decreased τ values as BN interfacial coating were applied to the SCS-6 fibres (43). The other SCS-6 fibre composites listed in Table 2.5., show varied but lower values of τ than reported here. However, they will not be discussed further because of the differing fibre type.

The other micromechanical parameter of debond energy 2Γ, has fewer quoted results in the literature. Much of the work as with the interfacial sliding stress τ, has concentrated on the LAS / Nicalon system which exhibits very low debond energy. However, CAS / Nicalon material fabricated by Corning, using the same apparatus as used in this study, gives $2\Gamma = 5\pm1\mathrm{Jm}^{-2}$ and is of a similar magnitude to that given for the MAS / NL-607 material ($2\Gamma = 12\pm5\mathrm{Jm}^{-2}$) (164). Previously it has been suggested that for composite behaviour to occur, $2\Gamma_i/2\Gamma_f <¼$. Since, for oxidised fibres, $2\Gamma_f \sim 5\mathrm{Jm}^{-2}$ (this may be low), it can be realised that the measured debond energies do not satisfy this requirement (57). The composites fabricated in this work do show a graceful failure mode and hence there appears to be a discrepancy with this condition. Part of this problem may be due to the low measured value for the fibre fracture energy. However, the interfacial debond energy measured is for pure mode II loading. The crack deflection process at the interface is mixed mode and recent analysis has indicated that the measured values for mode II fracture energy may be 5-10x greater than the equivalent mode I fracture energy (165). Hence, if this model is correct, the debond criterion for composite graceful behaviour can be satisfied.

The behaviour of the interface in the thermally aged condition provides useful information for the application of this class of materials. Studies of the effect on mechanical properties after thermal aging are considered in Chapter 6. However, a number of authors have dealt with aging effects within the composite and the results given here validate these previous findings (67) (115) (153). The interface condition is unaffected by very low temperature heat treatments, i.e. those <400°C. However, as the intermediate temperature range is traversed, i.e. 400-800°C, the interface condition is affected, with both 2Γ and τ rising substantially and exhibiting increased data scatter.

The original Marshall and Oliver paper briefly examined the effects of thermal aging in an inert as well as air environment (124). Similar results were obtained for 950°C for 5min in air and 1000°C for 10min in air, with a strongly bonded interface occurring and no fibre movement during push-down testing. In fact it was these strongly bonded fibres that were used for the reference hardness indentations. They also found that aging at temperatures up to 1250°C in argon gave similar interfacial micromechanical properties to the as-fabricated material (124). Thouless et al., heat treated LAS / Nicalon at 800°C in air for 4, 8 and 16 hours, giving τ values of 30, 30 and 200MPa from the fibre pull-out distribution (67). Lewis et al., for the Corning CAS / Nicalon material evaluated the aging response at 700° and 1200°C for 100hours in air and found that for the as-received material $\tau = 25\pm3$MPa $2\Gamma = 9.6\pm1.2$Jm^{-2}, for aging at 700°C $\tau = 87\pm53$MPa $2\Gamma = 13.4\pm7.8$Jm^{-2} and for aging at 1200°C $\tau = 25\pm3$MPa $2\Gamma = 11.8\pm1.8$Jm^{-2} in the middle of the composite (153). All of these authors found that the interfacial micromechanical properties rise at intermediate temperatures, with a return at high temperatures in the composite bulk to the as-fabricated micromechanical response.

This is explained via the active oxidation of the interfacial carbon by the formation of CO or CO_2. The interfaces themselves act as pipe oxidation channels providing a route for gas transport along the longitudinal fibre directions from the exposed ends of the composite. This mechanism is expected to operate since O_2 diffusion through the matrix is slow (for the MAS matrix composites, ~ 0.3 μmhr^{-1} at 1000°C). As the temperature rises in this interval partial silica bridging may occur at the fibre / matrix interface. This was observed to occur for temperatures ~ 700°C or greater. This oxidation of the SiC fibre is a competitor reaction to that of the oxidation of carbon :-

$$SiC + 2O_2 \dashrightarrow SiO_2 + CO_2 \qquad (5.1).$$

$$C + O_2 \dashrightarrow CO_2 \qquad (5.2).$$

As silica bridging is only partial the interfacial micromechanical properties would exhibit large scatter as observed. For higher temperatures, i.e. 1000°C or greater, the oxidative loss of carbon from the interface is very rapid, leaving void space at the interface. However, oxidation of the SiC fibre is also rapid, causing the formation of a silica plug as described above. Hence, unlike the intermediate temperature range where some bridging of the interface may occur causing scatter in results, at higher temperatures plug formation stops the oxidative degradation of the interface ~ 30µm from the exposed fibre ends. This concept is schematically illustrated in Fig 5.24.

For these plugged interfaces 2Γ and τ values would be consistent with brittle composite fracture. However, as indicated in this work the fibres contained in the bulk of the material have interfacial micromechanical properties of the as-fabricated material. This is due to the low O_2 diffusion rates in the matrix and the effects of the silica plug blocking pipeline oxidation. It should be noted that if the change in the interfacial sliding resistance τ is only due to frictional effects from the silica bridge then, as the frictional sliding coefficient for carbon $\mu \sim 0.01$, to give appropriate results τ must increase by a factor of 10x and hence so should the frictional coefficient. This is comparable to the measured values for silica of $\mu \sim 0.3-0.8$ (67). The above discussion has concentrated on the change in the value of the interfacial sliding resistance τ. As shown in Table 5.1., the interfacial debond energy 2Γ also shows a similar dependence

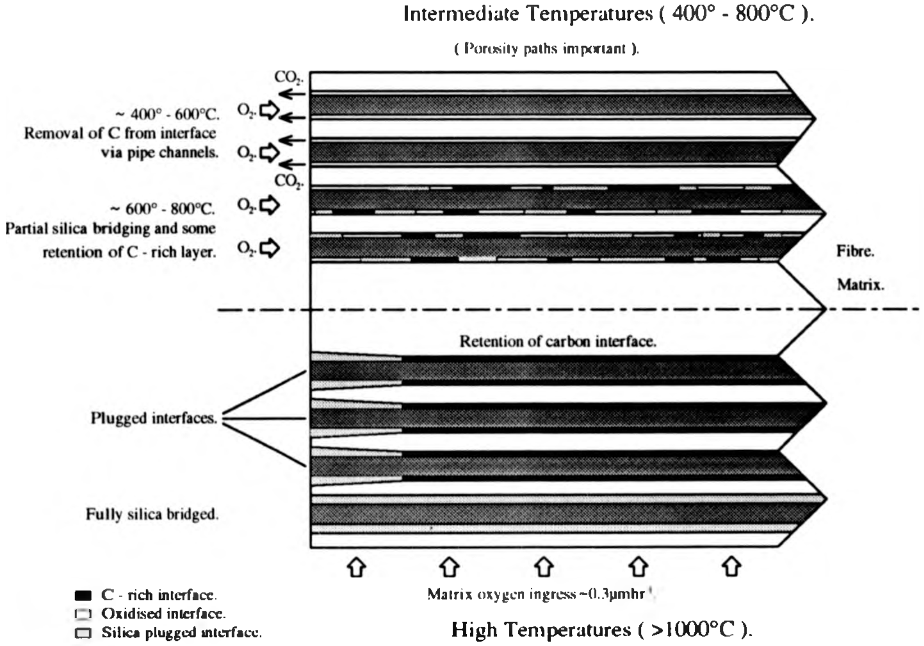
Intermediate Temperatures (400° - 800°C).
(Porosity paths important).
CO₂.
~ 400° - 600°C.
Removal of C from interface
via pipe channels.
O₂.
O₂.
CO₂.
~ 600° - 800°C.
Partial silica bridging and some
retention of C - rich layer.
O₂.
O₂.
Fibre.
Matrix.
Retention of carbon interface.
Plugged interfaces.
Fully silica bridged.
■ C - rich interface.
☐ Oxidised interface.
▨ Silica plugged interface.
Matrix oxygen ingress ~0.3μmhr⁻¹
High Temperatures (>1000°C).

Figure 5.24. Schematic diagram indicating the degradation of the composite at intermediate and high temperatures by 'pipe-line' oxidation.

with aging temperature to τ, which would be expected. Matrix degradation may be the limiting factor for temperatures in excess of 1000°C. The formation of a white surface layer, which increases in thickness for higher aging temperatures (60-80μm for 1000°C compared to 80-140 for 1200°C), indicates microstructural degradation.

It can be realised from the above discussion that investigation of microstructural and interfacial properties has led to a better understanding of the composite properties. Chopped fibre composite fabrication allowed for a broad investigation including selection of both processing route and glass composition, the elimination of the need for nucleants in the base glass and verification that C-rich interface formation occurred. From a microstructural perspective the goal was to achieve a diphasic, fully dense matrix and good fibre distribution within the final composite. It was realised that, by appropriate pressure application during fabrication, this could be achieved and a low residual glass content matrix formed. Fibre distribution, as indicated by low resolution SEM micrographs, was not ideal but, because of fabrication methodology, would be difficult to improve upon.

Interfaces formed in the composite series were shown by TEM light element analysis to be C-rich in all cases. However, micromechanical property measurements at the interface indicated that the carbon rich interface of 20-45nm, exhibited by the NL-201 composites, had very different and non-desirable properties compared with the C-rich interfaces exhibited by the NL-607 fibre composites. Evidence of gas bubble nucleation was found for prolonged fabrication times at elevated temperatures.

The investigation into the thermal aging of the composites in air validates current theories on the property degradation mechanism. Both TEM light element analysis and interfacial micromechanical property measurement indicated interface degradation at intermediate temperatures (400-800°C) and silica plugging at higher temperatures (~> 1000°C).

Chapter 6. Mechanical Behaviour of MAS Matrix Composites.

This chapter begins with a description of the elastic behaviour of the monolithic glass ceramic and the thermal expansion behaviour of the monolithic and CMC fabricated specimens. Following this a description is given of the mechanical properties of the composite in the as-fabricated condition during short term, high temperature testing, after thermal aging and under creep conditions.

6.1. Mechanical Response of Monolithic Glass Ceramics.

In order to characterise fully the benefits of the addition of fibrous reinforcements within the glass ceramic matrix and to assist in modelling the GCMC properties, an evaluation of the monolithic glass ceramic behaviour was required. Monolithic glass ceramic plates 50x50mm were fabricated, mimicking the composite hot press cycle but using a lower consolidation pressure to avoid glass extrusion within the graphite die. Microstructural characterisation of these samples is given in Chapter 5.

The test results are as shown in Table 6.1., for the base, P_2O_5, and CDM glasses with data also shown for 2 bars of the CDM glass ceramic aged for 100hrs at 1000°C. This data can be directly compared to the literature values for ultimate flexural strength as given in Chapter 1., Table 1.4. For the glass ceramic material used in this study and the process route utilised (which was developed for composite fabrication),

Sample Designation.	Density.	Flexure Data.		
	ρ (gcm^{-3}).	σ_{MOR} (MPa).	ε_{MOR} (x10^{-3})	E (GPa).
Base Glass	2.60±0.05	110±3	0.95±0.04	115±2
Base Glass + P_2O_5	2.61±0.01	137±2	1.13±0.02	121±2
CDM as fabricated	2.66±0.14	172±10	1.43±0.15	120±5
1000°C 100hrs	2.67±0.01	159±14	1.34±0.19	119±7

Table 6.1. Flexural test data for the glass ceramics fabricated in this study.

it can be seen that reasonable values for σ_{MOR} are attained. It should be realised that many of the materials (indicated in Table 1.4.), which possess higher strengths, contain additions of the nucleant TiO_2 (~ 10 wt%).

The glass ceramic density is as expected, with $\rho_{Cord} = 2.53$ gcm^{-3} and the remainder being taken up by the density of enstatite. The Young's modulus values are similar to typical glass ceramics as would be expected, since no optimisation has been attempted for the glass ceramic in isolation. Typically, the strain ε_{MOR} for these samples is ~ 0.001 or 0.1% as indicated in Table 6.1. The values for the 1000°C aged samples allow for comparison with the as-fabricated materials and show there is no degradation of the properties from the as-fabricated state within the error margins. Hence, the aging treatment does not significantly affect the glass ceramic, indicating that composites could be used at least up to this temperature with this system.

6.2. Thermal Expansion Characterisation.

As has been outlined in previous chapters thermal expansion mismatch between the fibre and the matrix is an important consideration when designing an appropriate CMC system. By the utilisation of chopped fibre materials it has been demonstrated that processing and matrix composition chemistry can alter the phase ratio and hence the thermal expansion of the composite system and the mismatch. From Chapter 2., a design requirement for a successful composite is a thermal expansion mismatch $\sim<3\times10^{-6}{}^{\circ}C^{-1}$ and this system, by theoretical prediction, is $0.5\times10^{-6}{}^{\circ}C^{-1}$ without additions of enstatite, which is a phase with a much higher thermal expansion coefficient (61).

The results of the thermal expansion measurement for both the monolithic and composite systems are shown in Table 6.2. It should be pointed out that the initial thermal expansion measurements for the base and P_2O_5 nucleated glass ceramics were carried out using a Netzch dilatometer system and not the apparatus used for all other measurements.

Sample Designation.	Temperature Range (°C).	Thermal Expansion Coefficient. ($\alpha \times 10^{-6}{}^{\circ}C^{-1}$).
Glass Ceramics.		
Hot Pressed Base GC	100 - 900	7.33
Hot Pressed Base GC + P_2O_5	100 - 900	6.00
Hot Pressed CDM GC	350 - 850	5.59
Composites.		
CUDM 1hr Isotherm Hold	100 - 750	3.40
CUDM 2hr Isotherm Hold	100 - 900	3.39
CUDM 3hr Isotherm Hold	100 - 900	4.12
CUDM18 Unidirectional	60 - 910	4.17
1000°C 100hrs	100 - 900	3.24
CUDM19 Unidirectional	50 - 910	3.76
1000°C 100hrs	100 - 915	4.53
CUDM19 X - Ply	100 - 900	3.24

Table 6.2. Thermal expansion coefficients for the materials fabricated in this study.

As with other measurements shown in Table 6.2., these values were taken over a 800°C temperature range, nominally through the 100° - 900°C region. For the initial two monolithic glass ceramic results the curves obtained were linear over this temperature range. The base glass has a higher thermal expansion coefficient than the P_2O_5 nucleated glass, this may be due to a higher crystallinity for the nucleated glass. It was previously stated that the base glass was selected since the nucleant added glass gave very similar results, with fine-grained microstructures developed for both glass powders. It is probable that the P_2O_5 addition to the glass causes a higher crystalline content and hence a lower thermal expansion coefficient. However, the effect of the added phosphorus content on the composite properties (such as diffusion into the fibre) is not known and hence the base glass was selected to avoid this complication.

For the composite behaviour description is more difficult. For the 1hr, 2hr and 3hr isotherm hold times, for materials fabricated in-house, differing behaviour was observed. For the 1hr isotherm hold time the expansion curve was linear with the 2hr and 3hr isotherm holds both exhibiting higher thermal expansion coefficients with increasing temperature. From the data in Table 6.2., both the 1hr and 2hr isotherm hold results are very similar, with a higher value recorded for the 3hr sample. The difference is suspected to be due to a higher enstatite phase content as residual glass is crystallised within the sample.

For the Rolls-Royce fabricated material CUDM18, the heat treatment at 1000°C for 100hrs decreases the thermal expansion coefficient. This material is subjected to a 1hr isotherm hold treatment and the high thermal expansion coefficient is possibly due to residual glass present in the matrix. Upon heat treatment it is possible that some of this glass is crystallised and hence lowers the thermal expansion coefficient for the composite (i.e. the 1000°C aging temperature is very close to the major crystallisation exotherm observed by DTA). This argument cannot however be applied to CUDM19, where an increase in thermal expansion coefficient is seen with the equivalent aging heat treatment. It is possible that this is due to an increase in the enstatite fraction, or possibly is due to the amorphous layer formed on the outer surface of the composite as shown in Chapter 5.

From Chapter 4., a thermal expansion coefficient could be predicted for the composite by assuming volume fractions of various phases. If these values are taken for the composite to be $V_f \sim 0.5$, with the matrix fraction split as 80% α - cordierite and 20% enstatite (i.e. for the composite 50% fibres, 40% α-cordierite, and 10% enstatite), then the predicted thermal expansion coefficient is $3.37 \times 10^{-6}{}^{\circ}C^{-1}$. Assuming a fully crystalline matrix the results are schematically plotted in Fig 6.1., for a range of matrix ratios. It is possible therefore to take the measured thermal expansion coefficient results and to indicate approximately the volume fraction of enstatite within the composite. However, the accuracy of this approach is difficult to validate experimentally due to the poorer quality of the XRD traces obtained for the composites. It should be remembered that microstructural phase analysis and subsequent volume fraction measurements are complicated by the presence of the ZrO_2 impurity and residual glass, again making accurate measurements difficult.

As indicated in Chapter 2., many theoretical models attempt to analyse for the effect of residual stresses within the composite. By the use of equation 2.7. and

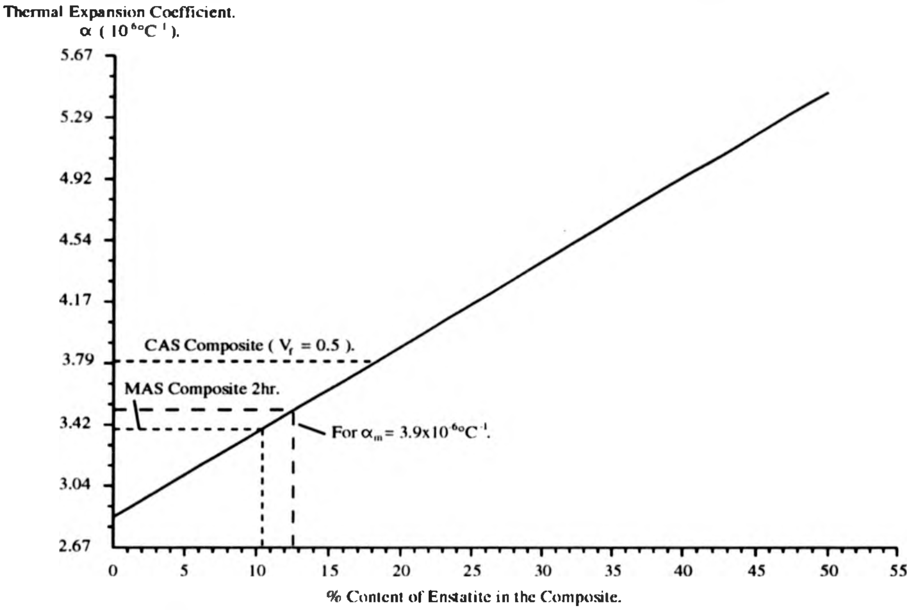

Figure 6.1. Thermal expansion coefficients for composites with $V_f = 0.5$ versus the percentage of enstatite.

taking values of $\alpha_m = 3.9 \times 10^{-6}$°$C^{-1}$ (giving a composite thermal expansion coefficient of 3.5×10^{-6}°C^{-1}), and $\Delta T = 1180$°C, then $\Omega = -9.44 \times 10^{-4}$. This is a relatively small Ω (mismatch strain) value and satisfies the requirement from Chapter 2., that the mismatch be small.

6.3. The Mechanical Behaviour of Composite Materials.

Within this section of Chapter 6. a number of subdivisions are made. Description and comment begins with samples tested in flexure and tension at **room temperature**. This work is then extended to show the results for samples tested in both flexure and tension at **elevated temperatures** for short term exposures. The effects of **thermal aging treatments** are then described, as are the **creep deformation** studies.

6.3.1. Room Temperature Testing in Flexure.

The mechanical evaluation work was predominantly carried out in flexure as, at the start of the study, a rapid ranking method was required to evaluate process routes. Once a suitable process route had been developed tensile studies were conducted. For this reason most of the data will be presented for flexure response, with a limited amount of tensile data being given for composites fabricated with the commercially sourced powders. The flexure tests carried out used a three point geometry with a span to depth ratio of ~ 15:1.

The discussion begins with the composites derived from non-optimised process routes, labelled the UDM series. The micro and phase structures of these composites were discussed in Chapter 5. The composites were found to give the correct phase but a non-optimised microstructure, since residual porosity was present. These composites were also processed using the Nicalon NL-201 grade fibre as indicated in Chapter 4. A summary of the mechanical properties is given in Table 6.3., and it should be noted that, for all tests in three point flexure carried out, the cross head speed used was 0.2mm/min. For UDM1, mode I cracking was observed on the tensile surface, but there was also compressive damage on the top surface, hence this data is strictly invalid. Tests on UDM2, 3, 4, 5, and 6 indicated mode I graceful failure as desired for the composite. For all samples except UDM5, σ_{mm} is close to σ_{MOR} and hence the behaviour, although 'composite-like', is approaching the monolithic brittle mechanical

Sample Designation.	Microcracking Stress. σ_{mm} (MPa).	Ultimate Stress. σ_{UBS} (MPa).	Ratio. σ_{mm}/σ_{UBS}	Modulus. (GPa).
UDM1	212±39	237±36	0.89±0.03	116±6
UDM2	203±40	247±30	0.82±0.07	123±12
UDM3	220±14	271±12	0.81±0.08	113±5
UDM5	251±7	504±52	0.50±0.06	-
UDM6	239±17	274±9	0.87±0.09	-

Table 6.3. Summary of the mechanical test data for the UDM series of composites.

response. For UDM5, microcracking occurs at a similar stress level to that observed for the other UDM series composites, but σ_{MOR} is well separated from this level being approximately double. Hence, UDM5 has the superior properties in the UDM series and this fabrication had pressure applied within the processing window when the process schedule was more carefully examined.

Mechanical data for the UDM series indicated that the composites were not attaining the levels predicted from a rule of mixtures calculation, nor the level of other glass ceramic systems. Of particular concern were the poor modulus values, suggesting mechanical and / or thermochemical damage to the fibres during processing. Utilising these results the optimised process schedule was developed, with pressure application during the process window, before the exothermic crystallisation peaks, and the use of the higher crystallisation temperature. Process time at temperature was also increased to facilitate better interface development. This issue also prompted the use of the NL-607 grade fibre with the 10-20nm pyrolytic carbon pre-coating.

In conjunction with this the development of the pre-preg process and the utilisation of the commercially sourced CDM glass powder allowed the CUDM (up to 15) series of composites to be fabricated. A summary of the mechanical response to three point flexure is shown in Table 6.4. for these composites and the BGMC sourced powder composite CUDM17. Also given in this table are the Rolls-Royce fabricated unidirectional composites CUDM 18 / 19. The composite density can be calculated to give ρ_{Comp} = 2.575gcm^{-3} and the CUDM series is very close to this calculated value. From the microstructural studies carried out in Chapter 5, this is reasonable, since only a very small amount of residual porosity was observed.

The mechanical data in Table 6.4. illustrate the excellent properties that can be attained for a reasonably optimised system. The table shows the results for individual pressings to confirm consistency in the results and also a summary for the isothermal hold times utilised. In order to calculate σ_{mm}, two approaches can be used. The first uses the initial deviation from linearity of the curve. However, this suffers from the necessity for there to be a perceptible change in the elastic modulus of the composite for the microcracking stress to be calculated. A number of authors have

Sample Desig.	Density. ρ (gcm^{-3}).	Microcracking Stress. σ_{mm} (MPa).	Ultimate Stress. σ_{UBS} (MPa).	Ratio. σ_{mm}/σ_{UBS}	Modulus. (GPa).
CUDM5	2.596±0.010	628±60	1074±124	0.58±0.11	
CUDM7	2.572±0.005	620±16	1043±40	0.59±0.03	
CUDM12	2.573±0.013	500±24	1092±10	0.46±0.03	
1hr Isotherm Summary		560±84	1068±65	0.52±0.10	153±15
CUDM10	2.580±0.042	682±12	1143±15	0.60±0.02	
CUDM11	2.577±0.011	647±59	1175±15	0.55±0.06	
2hr Isotherm Summary		665±78	1168±41	0.57±0.08	157±12
CUDM14	2.587±0.004	615±44	1081±45	0.57±0.06	
CUDM15	2.585±0.008	677±12	1105±40	0.61±0.03	
3hr Isotherm Summary		644±33	1093±53	0.59±0.06	148±9
CUDM17	2.578±0.011	591±62	1107±18	0.53±0.06	139±12
CUDM18	2.574±0.011	454±33	920±37	0.49±0.05	127±30
CUDM19	2.594±0.006	297±46	906±97	0.33±0.08	95±5
MAS / Nicalon NL -201		251±17	504±50	0.50±0.08	117±18

Table 6.4. Summary of the mechanical test data for the CUDM series of unidirectional composites.

indicated, by in-situ optical microscopy, that microcracking can occur before this initial deviation form linearity (61) (65) (66). Hence for this study, the onset of acoustic emission from the sample was used to detect the microcracking stress. However, again this method requires careful interpretation since local inhomogeneities such as matrix-rich regions within the composite can cause a locally reduced microcracking stress to be observed. For all data in Table 6.4. and in this study unless specifically indicated, it is the acoustic emission method that has been used to identify σ_{mm}.

For these composites a rule of mixtures calculation gives the composite elastic modulus to within experimental error, indicating that processing damage during fabrication can only be minimal. The matrix microcracking stress within these composites is also high giving a reasonable design stress for potential applications. Of importance in this respect is the separation between σ_{UBS} and σ_{mm}, which needs to be large if potential transient overstrains are to be tolerated without significant degradation in composite properties. It can be seen from Table 6.4, that for these composites σ_{mm} / σ_{UBS} = 0.5 - 0.6, indicating good separation of the two material properties.

Before a detailed review of the properties indicated in Table 6.4., it can be seen that the MAS / NL-201 composites have much reduced properties in comparison to the NL-607 containing systems. The elastic modulus is lower (~ 20 %) than indicated by a rule of mixtures, suggesting processing or thermochemical degradation of the fibres. The stresses σ_{UBS} and σ_{mm}, although indicating a similar level of separation to the CUDM series, have properties ~ 50% lower than those attained by the CUDM series. This can be attributed to the interface formation and fibre processing damage. Interface micromechanics as indicated in Chapter 5. for this composite and the CUDM series, indicate the importance of the interfacial response as well as the interface constitution.

The properties indicated in Table 6.4. for CUDM5-15 are for the NL-607 fibre reinforced CDM sourced powder for differing isotherm hold times. It can be seen that, for all of the results for the differing hold times, properties overlap and hence only trends can be indicated, as no drastic changes in room temperature flexure evaluation were observed. A typical stress / deflection curve is indicated, in Fig 6.2., for a 1hr isotherm hold time composite CUDM7. As can be seen graceful failure of the composite occurs and a nominal strain can be calculated to give $\varepsilon_{mm} \sim (4.12 \pm 0.06) \times 10^{-3}$ and $\varepsilon_{UBS} \sim (7.02 \pm 0.06) \times 10^{-3}$. Also shown in this figure is a backscattered electron micrograph of the tensile face of a flexure specimen. Although some damage has occurred during polishing, microcracking of the matrix is clearly evident, with microcracks bridged by unbroken fibres. The micrograph is of a composite tested beyond its ultimate flexure strength, σ_{MOR} and hence, saturation microcracking has

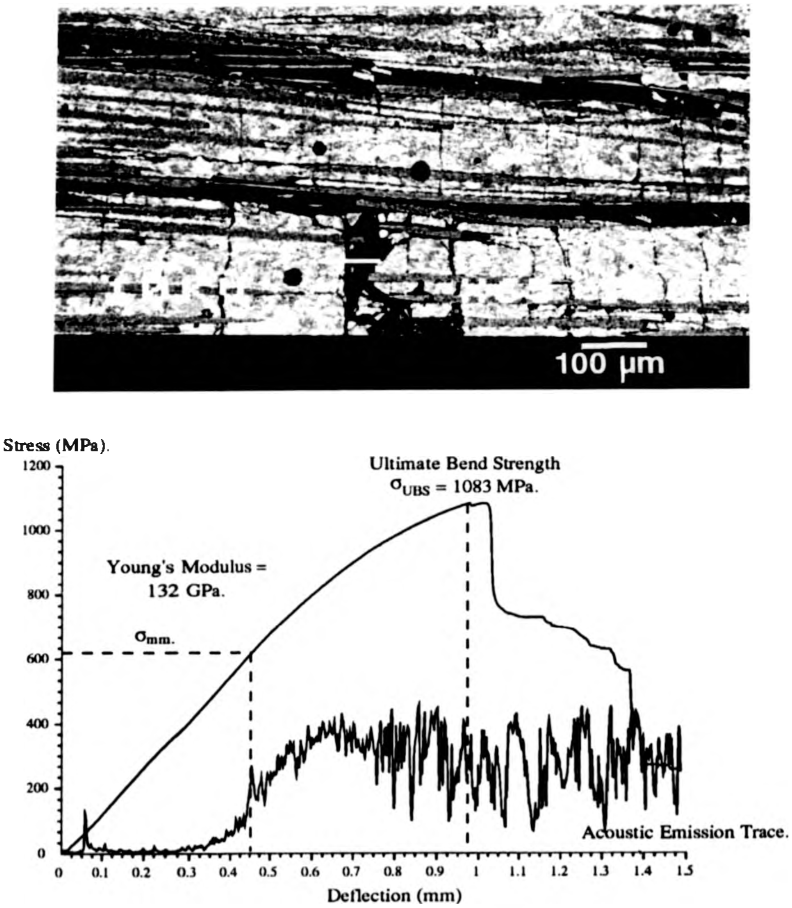

Figure 6.2. Stress / deflection curve for CUDM7, with a backscattered SEM micrograph of the tensile face of a composite specimen.

occurred.

For the 2hr isotherm, CUDM10 and 11, the measured properties are the highest for this system. Although time did not permit detailed studies of processing intervals around this, for matrix and interface development, this hold time would appear to give optimal results. A typical stress / deflection curve for this processing condition is given in Fig 6.3., with the nominal strain being ε_{mm} ~ (4.77 ± 0.40) x 10^{-3} and ε_{UBS} ~ (8.29 ± 0.63) x 10^{-3}. In this figure it can be seen that there is a region at the start of the test where virtually no load is applied, but the cross head of the test machine is moving (up to 0.1mm). This region preceding the linear elastic part of the composite

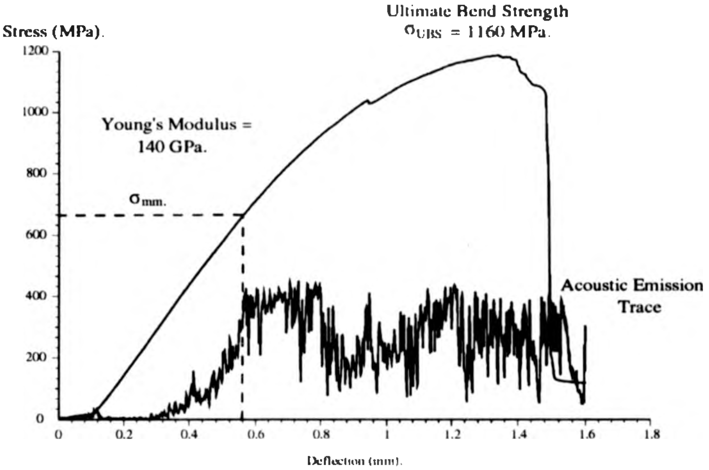

Figure 6.3. Stress / deflection curve for CUDM11.

response is caused by the flexure gig 'settling in' and is not a composite property.

The results for the 3hr isotherm hold time composites, CUDM14 and 15, show a decreasing trend, although the results are within experimental error of the 1 and 2hr samples. Since the matrix condition is similar following 1hr and 2hr isotherms this degradation may be due to interface effects as indicated in Chapter 5. The appearance of 'bubble-like' areas may be indicative of fibre damage due to carbon and or oxygen loss from the fibre surface although clearly this effect can only be small since properties are not significantly degraded.

The fabrication of CUDM17 was carried out to demonstrate the properties attainable with the originally selected tie line composition. From Chapter 5., the composite contains the desired phase and microstructure and from Table 6.4. the composite test data indicates good properties. Typically, the strain measured for this composite system is as for the above composites.

As stated in Chapter 5., CUDM18 and 19 contain some residual porosity within the composites. The interfacial behaviour of these composites is somewhat different to the in-house fabricated materials. For CUDM18 the interfacial sliding resistance τ is as for the in-house fabricated systems CUDM5-15. For CUDM19 the interfacial sliding stress τ value was higher than for CUDM18 and the in-house fabrications, but not as high as the case for the thermally aged materials, with the interfacial debond energy 2Γ similar to the as-fabricated materials. The changes in microstructure and interfacial response have an effect on the mechanical properties of these two composite systems, but processing damage during fabrication is also believed to have occurred. Elastic modulus values for CUDM18 show a small drop from the rule of mixtures calculation, with a large scatter indicating the material inhomogeneity. For CUDM19, the drop is significant, the measured value in this case being ~63% of the calculated prediction.

Hence, although values for CUDM18 should be comparable to CUDM5, 7 and 12, and values for CUDM19 comparable to CUDM17, this cannot be done with any reliability because of changes in processing, interface and microstructure. For CUDM18, values for ε_{mm}, ε_{UBS} are smaller but comparable with the in-house fabricated samples. It is possible that matrix rich regions lower the apparent microcracking stress in this system, although an attempt has been made to compensate for this by checking for the deviation from linearity. However, for CUDM19, ε_{mm} is much lower, with ε_{UBS} apparently higher. However, although care was taken to avoid this, compressive matrix fragmentation may have occurred invalidating the measured ε_{UBS}.

The composite properties described above can be compared to theoretical prediction as described below. For a simple rule of mixtures calculation, E ~ 150 GPa, and this falls within the observed scatter band for the in-house fabricated materials. From Chapter 2., equation 2.2. can be applied to calculate the matrix microcracking stress σ_{mm}. Using appropriate materials parameters and the measured values for τ, the predicted value for $\sigma_{mm} = 672\pm51$MPa (this assumes $\alpha_m = 3.9\times10^{-6}{}^{\circ}C^{-1}$, and hence the residual stress q= -85MPa). From Table 6.4., the measured values for matrix microcracking fall within this prediction and hence indicate the validity of modelling for this parameter. If the residual stress effects are not taken into account the predicted value for $\sigma_{mm} = 545\pm47$MPa. Therefore, the importance of residual stresses can be seen if accurate modelling predictions are to be obtained. The matrix saturation crack spacing can also be used to estimate the interfacial sliding resistance τ. Measurements taken on several composites gave the average crack spacing to be ~ 95µm. Using the analysis of Cao et al. and using the same materials parameters as used in the calculation of the matrix microcracking stress (σ_{mm}), this saturation crack spacing gives a calculated $\tau \sim 28$MPa (57). This value is smaller than the value measured by the push-down technique as described in Chapter 5. ($\tau = 48 \pm 15$MPa), but is of the same order of magnitude.

The measurement of σ_{mm} for this study used the onset of acoustic emission from the sample, as deviation from linearity requires an appreciable drop in modulus to occur before detection can take place. However, the acoustic emission approach can be inaccurate if a locally reduced matrix cracking stress occurs in the sample as a result of matrix rich regions or microstructural inhomogeneities. This is partly responsible for the spread of values given in Table 6.4., for σ_{mm}. It can be noted that for the composites σ_{mm}, ε_{mm} values are ~ 3x the σ_{MOR}, ε_{MOR} values recorded for the monolithic glass ceramic. Hence, considerable improvements over the base glass ceramic material are made by the addition of the Nicalon fibres.

The ultimate strength of the composite may also be predicted. Use of a simple bundle failure model predicts $\sigma_{ULT} \sim 1450$MPa, and the composites fabricated in this study approach this value. As discussed in Chapter 2. a number of models exist for the prediction of σ_{ULT} and take into account the in-situ materials properties and the interfacial properties. The models used here for predictions of the composite ultimate strength are those by Thouless, Sbaizero, Sigl and Evans (67) and Curtin (65). These models refer to tensile strength predictions only but are used here as a reference comparing typical GMC and GCMC flexure results. The results of these calculations are given in Fig 6.4. indicating the simple bundle failure and the two theoretical models. Also included are flexure results for some systems studied in the GMC and GCMC field and those of the composites fabricated in this study. The plot indicates that GMC materials approach the strength levels predicted by the simple bundle failure models. This is possibly due to the low temperature fabrication route used and viscous deformation of the glass avoiding mechanical damage to the fibres. The area marked for GCMC strengths is lower reflecting the change in processing conditions, with the NL-201 fibre composites fabricated within this work providing a bottom mark for this

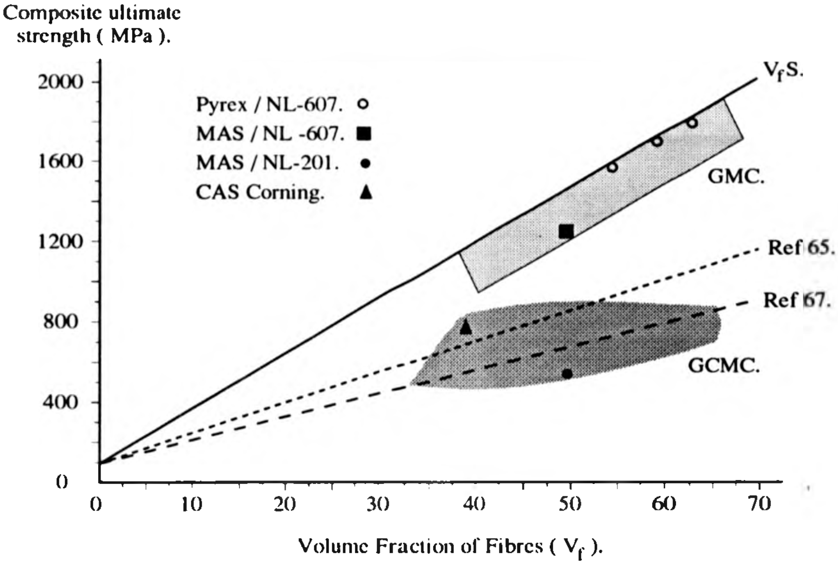

Figure 6.4. Plot of modelling strength verses V_f. The models used are the simple bundle failure, TSSE (67) and Curtin (65). Also plotted are literature values for comparison with the materials fabricated in this study.

range. The Corning CAS materials represent an upper bound for the GCMC systems. The optimised process route composites, utilising the NL-607 fibre composites fabricated in this study, move toward GMC strength levels, indicating that careful process development and fabrication are critical in achieving very high mechanical properties.

As stated above the theories used relate specifically to the prediction of the ultimate tensile strength of CMCs and not their flexure strength. Recent analysis by Steif and Trojnacki has attempted to relate these two measurements, since the ratio of flexure strength to tensile strength differs for different CMC systems (166). Their analysis indicated that this ratio was sensitive to the rate at which stress fell after the ultimate tensile strength was passed. Since the above plot is presented only to allow comparison of flexure strengths with other CMC systems no attempt to convert flexure data into tensile data has been attempted. Although this figure indicates that the materials fabricated in this study have very good as-fabricated properties in comparison to other CMC systems quoted in the literature, direct comparison can be made with the values given in Table 2.3. of Chapter 2. This table gives the measured flexure strengths for a number of CMC systems including glass ceramics, oxides, glasses, carbides and nitrides. As indicated in Fig 6.4. it is only the glass matrix composites that have strengths comparable to the composites fabricated in this work. The table contains a number of MAS based composites, with the work of Aveston in 1971 showing that high strength CMCs (σ_{MOR} ~ 600MPa) were obtainable using this system and that the polymorphic form of cordierite was important in achieving these high strengths (89). More recent work by Norman and Tilley using a cordierite nucleated with 11.5wt% TiO_2 gave good strengths (σ_{MOR} ~ 650MPa) with reasonable retention of strength to 1300°C (σ_{MOR} ~ 400MPa) (53). The work of Chen et al., although not producing high strength composites did indicate, as stated in Chapter 5., that thicker carbon rich interfaces gave improved strengths for the MAS doped glasses (97). The other glass ceramics listed in Table 2.3. show that the properties of the composites fabricated in this work are very good, with the commercially available LAS / Nicalon and CAS / Nicalon composites having properties similar to those of the composites fabricated in this study.

6.3.2. Room Temperature Tests in Tension.

Reservations as to the validity of flexure testing indicated the need for tensile evaluation of these materials. However, as indicated in the above section for the unidirectional fabrications, the Rolls-Royce materials show non-optimised microstructure and mechanical properties.

Initially, material availability only allowed for a limited study of test conditions and the requirement for creep deformation studies further restricted material availability. Higher temperature evaluation was restricted to tensile tests carried out after creep testing. Much of the creep deformation was carried out below the first matrix microcracking stress (associated with the 90° plies). The results of the tensile tests are summarised in Table 6.5., with a stress / strain plot exemplified in Fig 6.5 a). and a cyclic (hysteresis) curve shown in b). Two distinct regions on the stress / strain curve may be identified with a change in modulus. Microcracking in the 90° plies is

Temperature. (°C).	σ_{m1} (MPa)	ε_{m1} (x10^{-4})	E_1. (GPa).	σ_{m2} (MPa)	ε_{m2} (x10^{-4})	E_2. (GPa).	σ_{ULT} (MPa)	ε_{ULT} (x10^{-4})	E_{ULT}. (GPa).
Room Temp.	75	6.5	107	151	22	53	332	93	26
1000°C(crept)	-	-	-	100	9.5	85	125	15	55
1025°C(crept)	60	4.7	111	-	-	-	107	9.8	88
1050°C(crept)	50	4.0	116	96	9.0	90	136	16	46

Table 6.5. Tensile test data for room and higher temperature tests.

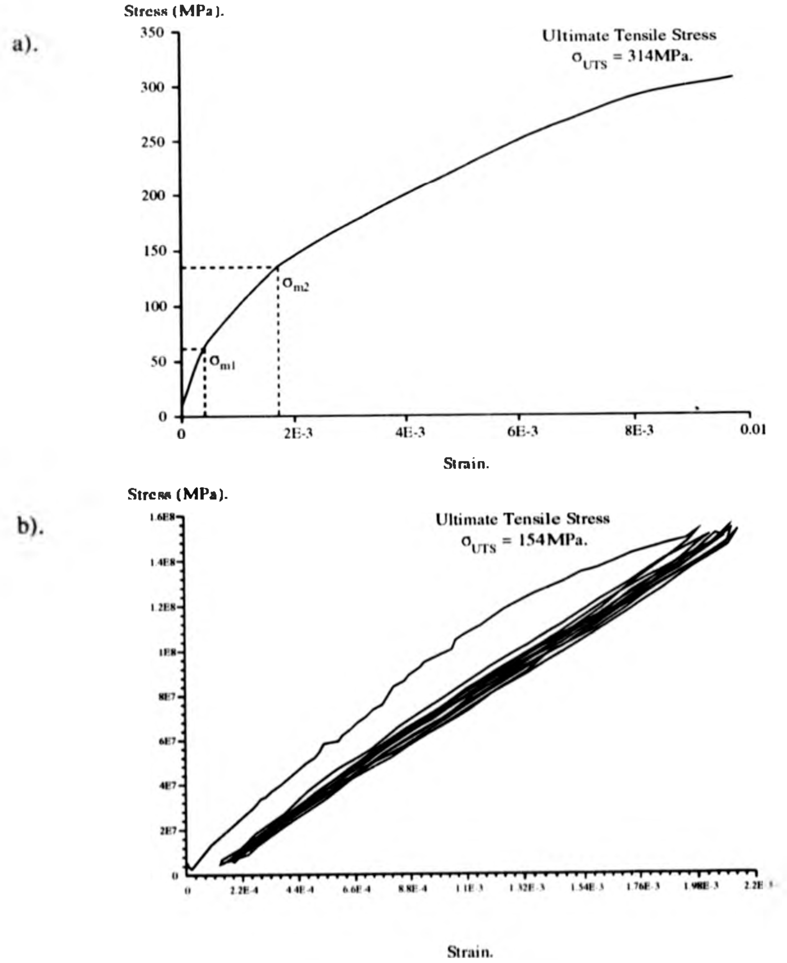

Figure 6.5. A typical tensile test curve for cross ply CUDM18 sample at room temperature is shown in a). and a hysteresis curve in b).

identified by the 'm1' subscript, and for this condition SEM imaging indicated that the microcracks did not traverse into the 0° plies. As the stress is increased microcracks form in the 0° plies as well as the 90° plies, identified by the 'm2' subscript. Acoustic emission and the change in modulus are used to identify these regions.

From the room temperature evaluation it can be seen that the tensile strength of the composite is reasonably high. These composites are layed up in a $[0°/90°]_{4s}$ configuration and hence, with a nominal $V_f \sim 40\%$ and using the contribution from the 0° fibres only, a bundle calculation gives $\sigma_{ULT} \sim 500$MPa and a rule of mixtures gives $E \sim 120$GPa. The composite properties do not attain these levels but show good properties in comparison to these predictions for an ideal system, bearing in mind the problems associated with process scale-up and the microstructural inhomogeneity observed in these materials. Using Fig 6.4. for the modelling predictions and assuming similar materials parameters, $\sigma_{ULT} \sim 305\text{-}395$MPa which is close to the observed values. This may indicate that materials properties used for the modelling calculation are low since the microstructure of these composites is poor. However, the models do allow us to predict the tensile strength reasonably accurately. Other researchers have found reasonable agreement with modelling predictions for the LAS / Nicalon and CAS / Nicalon systems when the appropriate in-situ composite properties are used (57) (63) (65) (71).

The tensile tests conducted indicate that the response of the materials fabricated in this study are similar to those described for other 0° / 90° composites (see Section 2.1.4., of Chapter 2.) (72). As previously stated SEM observation of the tested composites indicated microcracking in the 90° plies of the composite above σ_{m1} (Fig 6.5.), although these microcracks did not 'tunnel' into the 0° plies. This stress is lower than the matrix microcracking stress associated with an equivalent unidirectional composite material. However, the cracking in the 90° plies does not contribute significantly to the overall non-linear behaviour of the 0° / 90° composite. As the stress is increased to above the σ_{m2} level microcracks were observed in the 0° plies as well. This results in a behaviour which is similar to that of a unidirectional material (72).

The hysteresis curve shows the effect of repeated cycling (to above the second microcracking level) upon the composite response for a sample which had already been taken to above the first microcracking level for the first cycle. It is observed that a residual strain level is reached. This is indicative of microcracks not closing up within the composite after the first loading cycle. The ε_p value can be used to calculate the misfit strain and the interfacial debond energy, whereas the hysteresis loop width can be used to evaluate the shear sliding resistance. However, when the experimental curve is compared to the idealised curve given in Fig 2.4. of Chapter 2., it can be realised that accurate measurements of these parameters is difficult. From the experimental curve the permanent strain does not increase significantly with increased number of cycles, indicating that any subsequent damage closes upon load removal. The narrow width of the hysteresis loop indicates a high τ value which correlates with the measured indentation value.

6.3.3. The Mechanical Behaviour of Composite Materials at Elevated Temperature.

For the flexure tests a number of authors recommend minimum span to depth ratios for valid property measurements. Since, within this study, the four point flexure specimens were identical to the three point specimens, it is clear that even the lowest recommended ratio of 21-23:1 cannot be realised (119). However, the specimens tested did not show signs of matrix fragmentation on the top surface and only a limited number of tests were carried out in order to evaluate the effect of short term, environmental exposure under load. For the in-house fabricated composites the temperature selected was 450°C. Whereas, for the Rolls-Royce fabricated unidirectional tiles the temperatures used were 550°C and 1000°C. Figure 6.6., is the result of the 450°C test on CUDM15, (a 3hr isothermal hold time sample). As indicated in this figure, unlike the room temperature flexure tests, no 'settling in' of the flexure gig is observed. Because, as stated in Section 3.5.2. of Chapter 3., a preload is applied to the gig to ensure that the correct alignment of the sample and fixture is maintained.

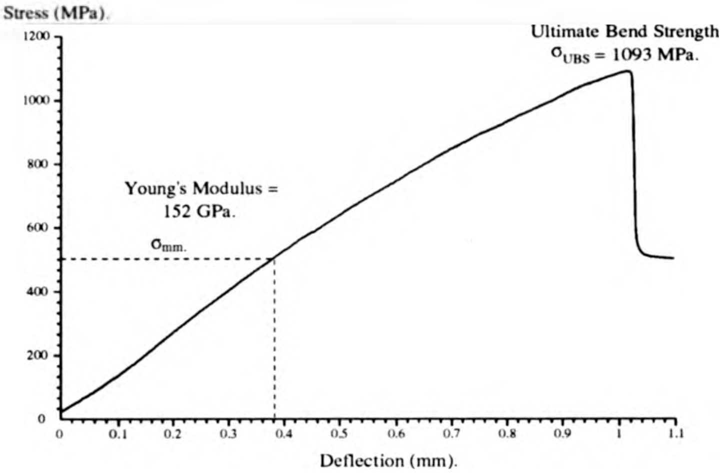

Figure 6.6. Stress / deflection curve for CUDM15 tested in four point flexure at 450°C during a short term exposure.

Due to the elevated temperature conditions the acoustic emission probe could not be attached to the specimen and hence the determination of σ_{mm} is less accurate for this and other results presented for the flexure samples. However, as the figure shows, there is no reduction in the ultimate flexure strength, with a small fall in the matrix microcracking stress. The measured modulus is within the as-fabricated value, as is the calculated strain. For the Rolls-Royce fabricated composites short term tests at 550°C indicated the same trend. The short term exposure at this intermediate temperature caused no significant degradation in properties.

For the tests carried out at 1000°C degradation was observed. As shown in Figure 6.7. for CUDM19, properties were not retained during short term exposure under mechanical loading. The ultimate strength is severely degraded (~ 40-50% of the as-fabricated materials). The modulus of the materials is similar to that measured for the as-fabricated case.

The degradation is possibly due to the exposure of interfaces to the environment directly after microcracking has occurred. For the lower intermediate temperature tests oxidation of the interface as previously described is slow and hence the materials properties can be retained for the test interval. However, for the higher temperature tests the oxidation of the interface is rapid and hence degradation can occur within the timescale of the experiment. Therefore the plugging of the interface and the

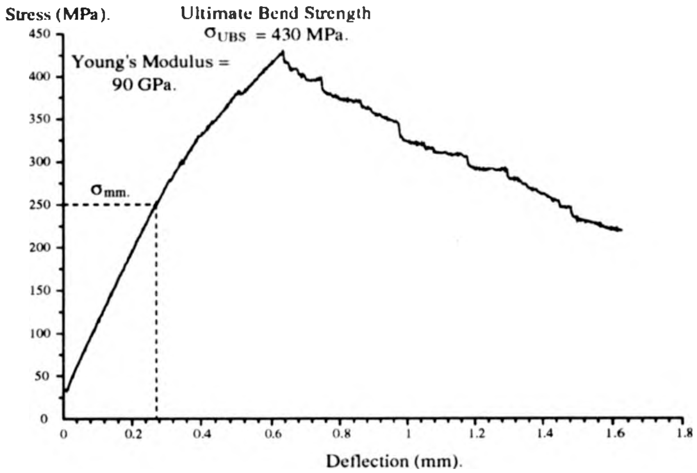

Figure 6.7. Stress / deflection curve for CUDM19 tested in four point flexure at 1000°C during a short term exposure.

protection of the bulk of the composite cannot occur, causing the degradation in the performance as indicated above.

The short term tensile tests gave the results indicated in Table 6.5. Because of the varied creep pre-history applicable to these materials interpretation of the data is difficult. The tests show property degradation from the as-fabricated materials for the higher temperature tests conducted. However, the degradation mechanism may be coupled to the previous creep characterisation as well as the elevated mechanical test.

6.3.4. The Mechanical Behaviour of Composite Materials Subjected to Thermal Aging Treatments in Air.

The previous section described the behaviour of composite materials after short term exposure to elevated temperatures in an oxidising environment. Clearly this is an important aspect of behaviour for the potential applications for this type of material. Also of critical importance is the longer term stability of the composite after exposure to an oxidising environment at elevated temperatures. The microstructural effects of these heat treatments have been previously described in Chapter 5., as well as the change in interfacial constitution and micromechanical response. Hence, in this section only the mechanical response will be considered.

All samples were tested in three point flexure for consistency with the as-fabricated samples, following exposure to various heat treatments at a range of temperatures for 100hrs (see Chapter 5.). Mechanical test specimens (i.e. ~ 3x3x50mm) were placed in a furnace at temperature and removed to air cool outside the furnace (hence avoiding transient temperature effects). Initially, studies were carried out using CUDM5-17 at a smaller range of temperatures, with a more detailed study being conducted on the unidirectional CUDM18 and 19 plates where there was greater material availability.

Results will be described for the CUDM 5-17 series first, since these represent the in-house fabricated materials displaying the optimised mechanical response. A smaller temperature variation was selected initially in order to investigate the low, intermediate and high temperature response of the composites to thermal aging. The results of density measurements indicate, that for all treatments up to and including 1000°C for 100hrs, the aging treatment has no significant effect on the composite density (i.e. all densities are within ~ 1% of the as fabricated density). However, for aging at 1200°C there is a marked effect upon density with a reduction of ~ 10-13% from the as-fabricated condition. This is to be expected from the microstructural information displayed in Chapter 5., which showed a reaction layer at the surface of these samples. This reaction layer indicated bubble formation, implying that during the aging treatment gases were driven off the sample.

The trend indicated by the mechanical property data is illustrated in Fig 6.8., which plots both σ_{UBS} and σ_{mm} for the 3hr isotherm (CUDM14 and 15). Results for the other isothermal hold time composites exhibit a very similar behaviour, but are not plotted in the figure for reasons of clarity.

For 450°C aging the degradation in mechanical properties is most severe for σ_{UBS} but not σ_{mm}. An example stress / deflection curve is given in Fig 6.9., indicating that behaviour is still composite-like, even though the properties are degraded. As can be seen form this figure the initial region of the test shows an upturn

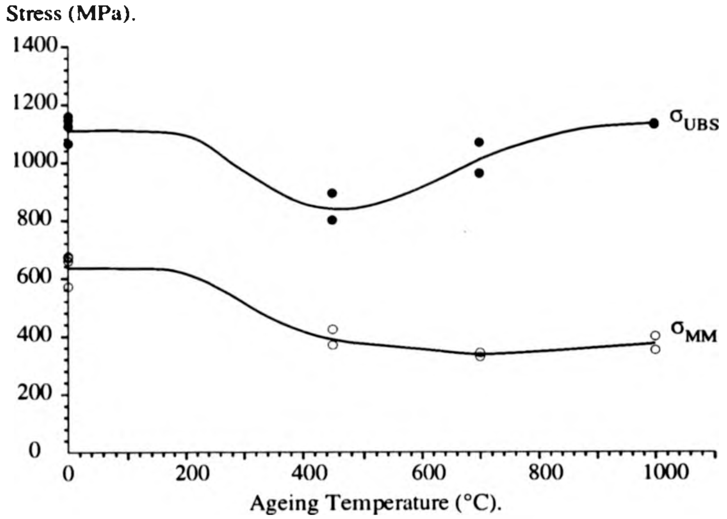

Figure 6.8. Summary plot for the aged 3hr isotherm composites indicating the trends in σ_{mm} and σ_{UBS}.

in the stress / deflection behaviour of the composite. This, as was stated for the room temperature flexure tests, represents the fixture 'settling in' and so is not a composite property. The sample can be imaged using SEM showing that little pullout of the fibres is observed. For the sample both ε_{mm} and ε_{UBS} are smaller by 40-45% with a drop in elastic modulus of ~ 14% from the as-fabricated condition. Hence, aging at this temperature affects all composite properties.

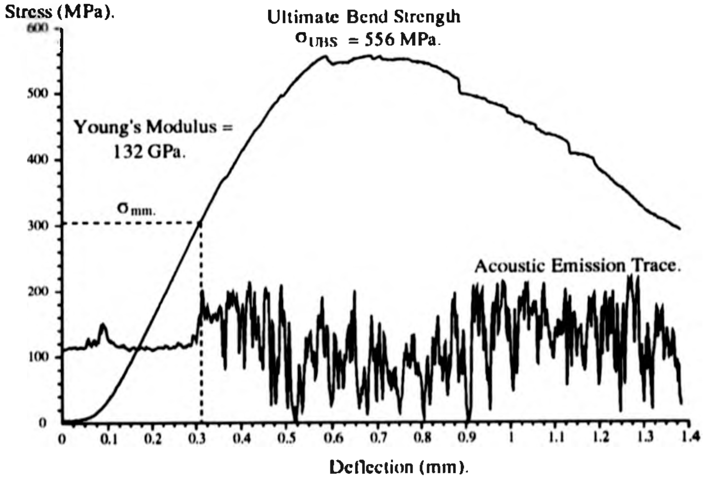

Figure 6.9. Stress / deflection curve for CUDM12 aged at 450°C.

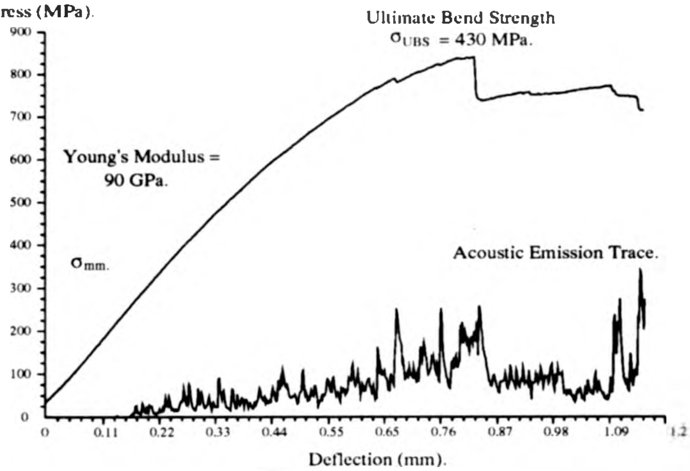

Figure 6.10. Stress / deflection curve for CUDM11 aged at 700°C.

For the 700°C aged sample the example curve is given for CUDM11 in Fig 6.10. with properties degraded from the as-fabricated material, although degradation is not as severe as the 450°C aged composites except for the modulus E. For this result, in comparison to the as-fabricated composite, a drop in ε_{mm} by ~ 40%, ε_{UBS} by ~ 5% and E by ~ 20% occurs. It can be realised that, although σ_{UBS} is only degraded slightly, σ_{mm} continues to exhibit degradation, as does the modulus, from the 450°C aged condition.

At 1000°C the properties of the composite are unaffected for σ_{UBS}, with σ_{mm} reaching similar values to the 450°C aged condition. For this condition an example curve is shown in Fig 6.11., for CUDM14. From the figure it can be seen that acoustic emission occurs at very low stresses and hence strains (i.e. ~ 300MPa). However, deviation from linearity occurs at much higher stresses (i.e. ~ 570MPa). This is a large discrepancy and may be occurring as a result of the oxidised surface layer previously described in Chapter 5. This layer, if glassy, could fail at very low stresses and hence would cause acoustic events to occur and be registered which were not associated with matrix microcracking within the composite. However, a comparison with the as-fabricated material can be made for ε_{UBS} and E, indicating that material properties are very similar. From SEM examination of the tensile fracture face microcracking is observed with fibres bridging intact across cracks. There is also evidence of pullout

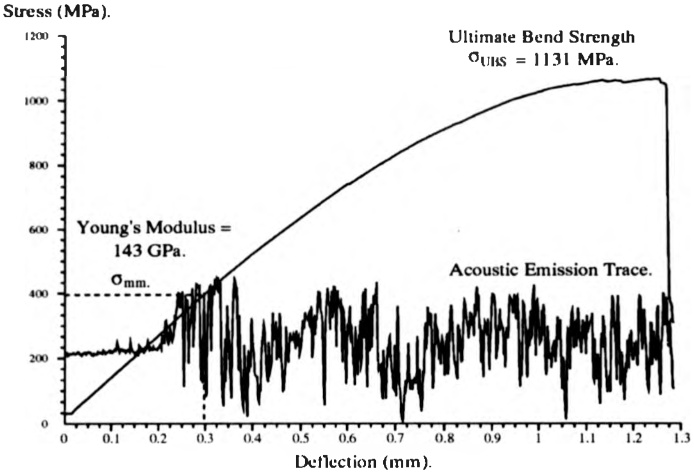

Figure 6.11. Stress / deflection curve for CUDM14 aged at 1000°C.

from the faces.

The results for 1200°C show a severe drop from the as-fabricated composite condition and do not exhibit a classical 'composite-like' response. The illustrative trace shown in Fig 6.12., for CUDM14 indicates a typical result from this aging regime. Acoustic events occur at all stresses during the test due to the now large glassy surface layer on the composite. As before for 1000°C this layer will fail at low stresses, especially where bubble formation within this layer has occurred. The composite shows linear elastic behaviour to virtually full load before continuing to

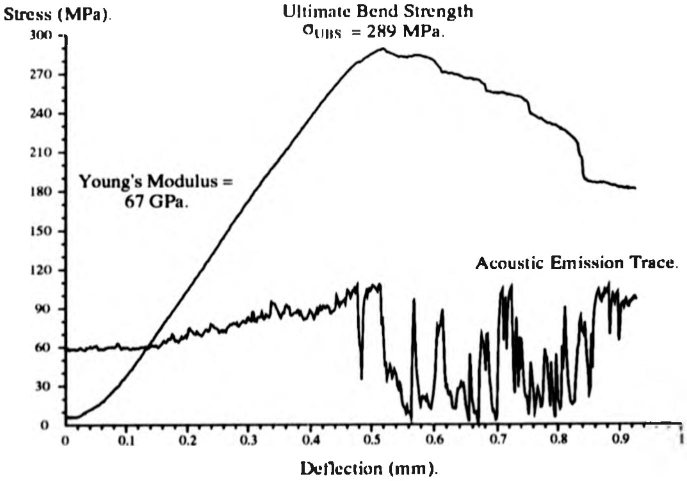

Figure 6.12. Stress / deflection curve for CUDM14 aged at 1200°C.

carry load beyond this point. Composites tested aged at 1200°C showed compressive matrix damage on the top surface and the effect of this upon the test result is difficult to calculate. If the test result is valid, $\varepsilon_{UBS} \sim 4.33 \times 10^{-3}$ which is very close to the ε_{mm} for the as-fabricated composite, however σ_{UBS} is $\sim 0.68\sigma_{mm}$ for the as-fabricated system. The composite then retains approximately 62% of its strength to $\varepsilon \sim 2.69 \times 10^{-3}$ (assuming a constant E). As can be seen from this trace, identification of σ_{mm} is not possible, even though 'composite-like' properties are seen, as failure is not brittle. The degradation of the materials properties at 1200°C is attributable to the microstructural degradation of the composite as stated in Chapter 5. From Table 2.4. of Chapter 2. the maximum use temperature of cordierite was 1200°C. This has not been achieved in this work, with composite properties at 1200°C degraded from those at 1000°C probably due to residual glass in the matrix.

Only a small amount of thermal aging was carried out on the BGMC sourced powder composite CUDM17. At 1000°C properties were marginally degraded from the as-fabricated case (by ~ 15%) which may be due to the glassy region on the sample surface, and the non-optimised route to fabricate this composite (i.e. as the same route was used for the CDM sourced powder composites). Interestingly, aging at 1000°C for 100hrs followed by aging at 450°C for 100hrs produces degradation which would not be expected due to plugging. The effect is not as great as for the single 450°C aging treatment but properties are below that of the as-fabricated material. However, microstructurally the sample contained porosity and hence ingress of oxygen to the interfaces may have occurred.

The above indicated some of the aging work carried out on materials fabricated in-house. A larger aging matrix was carried out for both commercially sourced powders, utilising the larger Rolls-Royce fabricated unidirectional plates. However, due to the non-optimal microstructure and room temperature properties of these materials, compared to the in-house fabricated materials, the data for these aging treatments requires careful interpretation. Aging treatments were carried out between 300°-1200°C and the results are indicated in Fig 6.13. for both powder systems. The figures also include the results for pre-aged specimens (aged at 1000°C) followed by

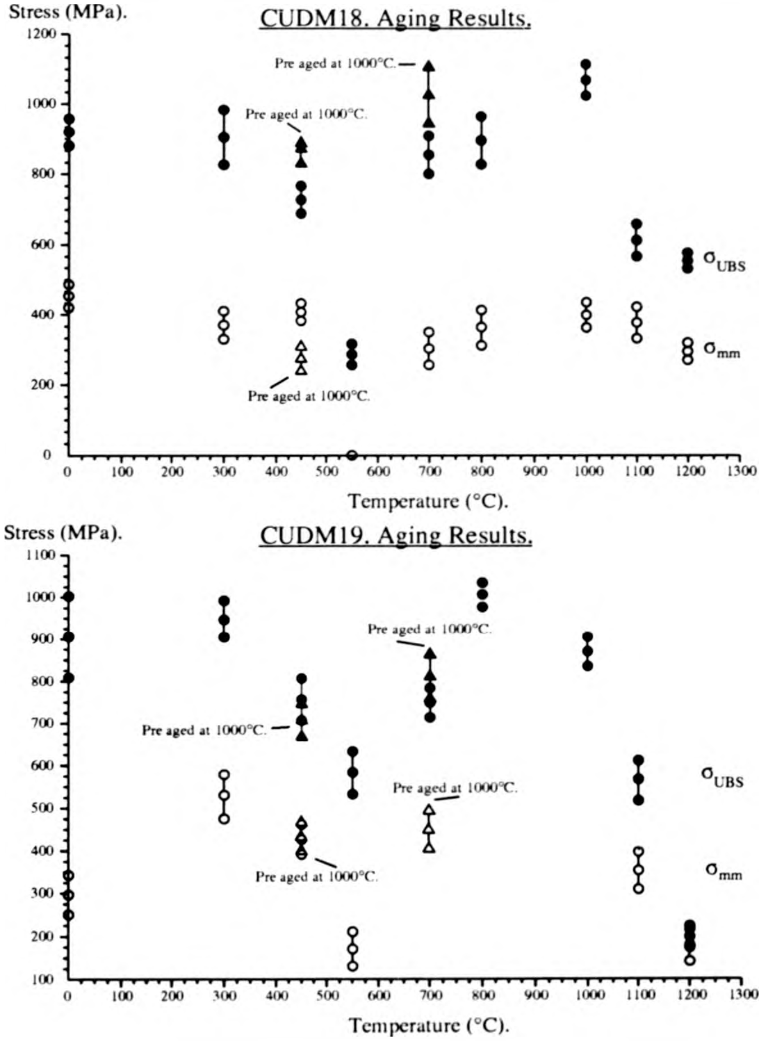

Figure 6.13. Summary plots for the Rolls-Royce fabricated composites indicating the trends in σ_{mm} and σ_{UBS}.

aging treatment at an intermediate temperature.

The figure indicates that the same trends in behaviour are observed for CUDM18 and 19, as for the in-house fabricated materials. No degradation in properties was observed below 300°C, with a fall observed at intermediate temperatures and a recovery in measured properties as higher temperatures are used. The fall off at temperatures >1000°C is again attributed to microstructural degradation. The pre-aged composites give inconclusive results, the recorded properties being very close to the single heat treatment values and showing similar scatter. Residual porosity in the CUDM18 and 19 composites allows oxygen ingress via the matrix to the interface for all aging treatments. The effect this has on the recorded mechanical properties is difficult to ascertain as the composites do exhibit the expected trend with increased scatter in the results.

The aging mechanisms and interfacial response were discussed in detail in Chapter 5. However, this mechanical property study indicates the critical role of the interface in the composite for the retention of good mechanical properties. The increase of the interfacial micromechanical properties due to intermediate temperature aging corresponds to a fall in the macromechanical properties. The increase in interfacial shear sliding resistance causes the stress transfer lengths in the composite to be decreased and so composite properties are degraded. For aging at 700°C both debond energy and shear sliding resistance are increased substantially. The interface does not debond as readily, causing the crack deflection properties of the interface to be reduced and, as for the intermediate temperature aging, the increase in τ causes a fall in mechanical properties. Due to the considerable scatter measured for the 700°C aging treatment and the partial nature of the silica bridge, areas of the composite exhibit good mechanical response. Finally at 1000°C aging causes the formation of plugs in the composites and protects the bulk of the composite from 'pipeline-oxidation'. The as-fabricated mechanical response is retained because of this mechanism, as are the micromechanical properties for the bulk material. However, fibres within ~ 30µm of the edge of the aged bar showed much increased micromechanical properties due to full silica bridging of the interfaces. For these fibres crack deflection at the interface does not occur.

The thermal aging work carried out on the composites fabricated in this study shows that the composites behave in a similar manner to other GCMC systems. Increased debond energy and shear sliding resistance at the interface has been noted for causing degraded macromechanical properties (38) (67) (76) (80) (115). Work by Thouless et al., on the LAS / Nicalon system indicated large changes in τ for aging at 800°C for 4, 8, 16 and 100hrs (67). Their results showed that a silica bridge formed across the fibre / matrix interface and caused a change in fracture behaviour of the composite to brittle fracture after 4hrs at this temperature (67). The work of Pharaoh et al. on the CAS / Nicalon system again showed silica bridge formation at the fibre / matrix interface at these intermediate temperatures (115). As was found in this study the greatest fall in macromechanical properties was observed around the 500°C temperature region by these workers, with aging at temperatures > 900°C forming a full silica bridge at the edge of the composite and so protecting the bulk of the material from 'pipeline-oxidation' of the interface. Hence, for the CAS / Nicalon system, the as-fabricated properties were retained after thermal aging in air at temperatures > 900°C (115).

6.3.5. The Creep Deformation of Composite Materials in Air.

The above sections have illustrated composite mechanical behaviour for a variety of test conditions in order to evaluate composite performance with respect to potential applications. The evaluation would not be complete without some investigation of the effects of longer term exposure to high temperature oxidising environments under load. The evaluation was conducted for. the CDM powder composite CUDM18 only, as the grip design for the creep apparatus was unsuitable, due to width problems, for the thicker plates of the BGMC powder composites. In an attempt to characterise the material's behaviour a number of temperature and stress combinations were utilised covering 1000°-1150°C and 50-90MPa. These temperatures were selected in an attempt to give conditions of both matrix creep, coupled with no creep of the fibre (elastic fibres) and matrix creep plus fibre creep. The stress selected also allowed investigation of composite response above the matrix microcracking stress σ_{ml}, in order that the effect of oxygen ingress into the composite during loading at temperature could be investigated.

Initial studies were carried out using temperatures of 1000°C and 1025°C, with the results given in Table 6.6. for the minimum creep rate from each experiment. Studies show that the observed creep deformation curves were very similar

Temperature (°C).	Applied Stress (MPa).	Min Creep Rate ($x10^{-8}s^{-1}$).
1000	80	0.23
1025	80	1.36
1050	80	0.65
1050	90	0.53
1100	70	2.20
1150	50	1.33
1150	70	2.06

Table 6.6. Summary of the creep experimental conditions and the creep rates observed.

in shape for all the conditions investigated, with an initial transient region followed by a region of continuously decreasing creep rate with time. For all the cases studied a steady state regime was not observed. The results all indicate the expected trend, with an increasing creep rate observed with increasing temperature.

The second series of creep tests conducted are indicated in Table 6.6. and extend the range of temperature and the stress applied. A typical creep characterisation curve is shown in Fig 6.14. for the 1150°C temperature condition. Because of material availability problems these curves were taken from the same sample. The applied stress increased from 50MPa to 70MPa after the 50MPa curve was obtained.

The tests reveal interesting results and indicate that the composites can sustain high loads at high temperatures. For example the 1150°C test for 70MPa

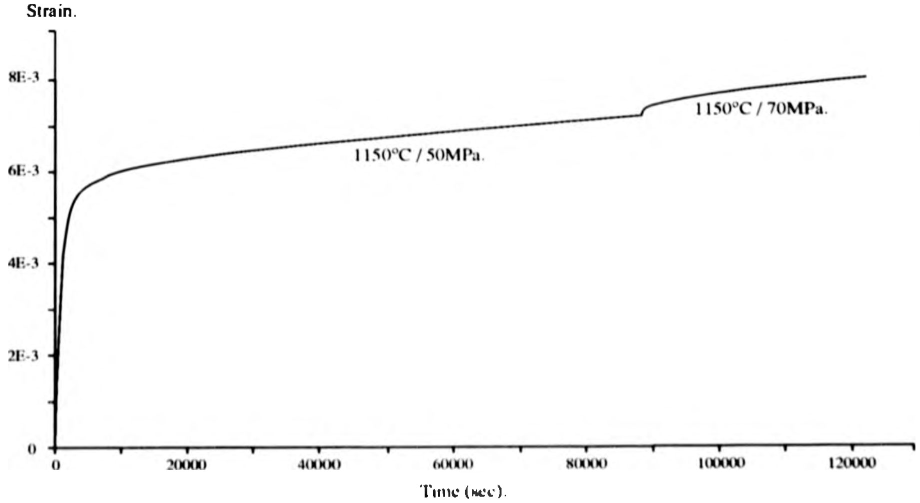

Figure 6.14. Typical creep deformation curves.

showed the life of the sample for these conditions was ~ 10hrs. It can be seen that the creep evaluation conducted in this work has not allowed for a complete set of results to be attained and hence conclusions are difficult to draw.

For the limited studies conducted here the observed minimum creep rates suggest that fibre creep dominated the test results. At lower temperatures the fibres behave elastically and hence, although the strain on the fibres and the matrix is identical, it is the matrix which creeps. Thus the initial transient region is indicative of stress transfer from the matrix (creeping viscoelastically or by a diffusion mechanism if fully crystalline) to the fibre which gives a near zero creep rate as the fibres behave elastically. This type of behaviour has been modelled for metal matrix composites by McLean (154).

At higher temperatures the fibre can creep as well as the matrix and hence composite creep is a combination, in parallel, of these two effects. This type of behaviour can be modelled as parallel spring and dash-pot elements, as recently demonstrated by Xu and Holmes (155). Other work on CMC creep has indicated the possibility of creep strain recovery in these systems, although this was not investigated in this work (156) (157).

6.4. Summary.

This chapter has presented the mechanical behaviour of the composites for a variety of conditions. The behaviour of the monolithic glass ceramic and the thermal expansion characterisation of the materials have also been presented. Within this summary these properties will be reviewed.

In order to demonstrate the benefit of the reinforcement upon all the composite mechanical properties, an investigation of the monolithic glass ceramic properties was conducted. Processing was chosen to mimic the composite fabrication schedules and hence the optimisation of the glass ceramic properties with respect to mechanical response and crystallisation was not carried out. The results show reasonable but not high figures for the mechanical properties. Microstructural and phase analysis indicated the desired matrix structure. The thermal expansion characterisation indicates high values for monolithic samples. However, the addition of fibres would lower these values.

The extension of the thermal expansion coefficient characterisation to the as-fabricated and the aged composites was then carried out. For the observed composites (in the CUDM series) $V_f \sim 0.5$, and a matrix of 80% α-cordierite and 20% enstatite, the predicted thermal expansion coefficient is $3.37 \times 10^{-6}{}^{\circ}C^{-1}$. This is close to the measured values and gives an indication of the enstatite content in the final fabricated composites. The results for CUDM18 and 19 show higher measured thermal expansion coefficients. For CUDM19 cross ply with a $V_f \sim 0.4$ and the matrix split as above, the predicted coefficient is $2.44 \times 10^{-6}{}^{\circ}C^{-1}$, negating the effect of the fibres in the 90° plies. The expansion coefficient measured is higher than this, suggesting an increased enstatite content or increased residual glass content.

Early composite fabrication studies resulted in the UDM series. This series validated the use of the compositional selection criteria but produced composites with poor mechanical response. Although improvements over the monolithic glass ceramic were attained, the lack of separation between the microcracking and ultimate stresses coupled with the low levels attained by these parameters indicated processing difficulties. Part of this was attributed to the pre-preg quality and part to the process schedule utilised as explained previously.

The results for the CUDM series of fabrications indicate the excellent property levels attainable using GCMCs via flexural testing. A rule of mixtures calculation for these composites falls within the observed scatter for the fabricated materials, and composite strength approaches a simple bundle calculation value. The composites fabricated in this study move toward mechanical property levels reached by GMC composites. The trend indicated by the fabricated materials in this study suggests that a 2hr isotherm hold time provides some optimisation of the process parameters with respect to microstructure and interface development. The matrix microcracking stress as measured experimentally by the occurrence of acoustic emission correlates well with theoretical prediction when matrix residual stress effects were taken into account.

It is interesting to note that CUDM17, which represents a different MAS composition form the CUDM5-15 series, also displays very high mechanical properties. This validates the process methodology and in particular the pressure application interval ideology developed in this work. The results for the MAS / NL-201 composites indicated properties approximately half as good as those of the NL-607 fibre composites. The separation between the ultimate strength and the microcracking stress is similar to that for the NL-607 fibre composites, however the modulus is slightly degraded from the rule of mixtures prediction. The interfacial micromechanical response for the two fibre types is very different and would contribute significantly to the difference in the mechanical properties.

The larger unidirectional and cross-ply plates fabricated by Rolls-Royce did not exhibit the same high properties achieved by the in-house fabrications, as a result of scale-up problems associated with the composite fabrication process. However, the larger material availability allowed for thermal aging treatments to be carried out on the unidirectional plates for both MAS compositions and the tensile testing of these composites. The mechanical property measurements for flexural testing of CUDM18 and 19 indicated a small drop in the elastic modulus with considerable scatter for CUDM18 and a fall in the modulus for CUDM19. Process damage to the fibres is indicated by this modulus fall, however a contribution would also be expected from the non-optimised microstructure and the change in the interfacial response as compared to the in-house fabricated composites.

The tensile evaluation was only conducted on CUDM18 and indicated that material performance was degraded from the optimal properties displayed by the in-house materials. However, the tests allowed for the identification of two regions by a modulus drop associated with cracking in the 90° and then 0° plies, as described by Evans (72). A cyclic test on the composite showed a small permanent strain after the first cycle that was not significantly increased by subsequent cycling. The width of the hysteresis curve was narrow, indicating a high τ value and shows that this method of determining τ is only accurate for composites with low τ value interfaces.

The results for the short term, elevated temperature tests indicate the differences in timescales applicable for the flexural evaluation. Degradation was not apparent in the short term tests at intermediate temperatures (450°-550°C) due to the timescale of the experiment. In tests conducted at 1000°C mechanical property degradation was observed indicating rapid oxidation of the interface. The short term tensile tests indicated that material behaviour was degraded at the higher temperatures, but the varied creep pre-history of the samples means data interpretation is difficult.

For the thermal aging experiments the smaller aging matrix (450°-1200°C) carried out, utilising in-house fabricated materials, indicated that density was unaffected up to 1000°C, with a fall of ~ 10-13% at 1200°C. The mechanical response does not show this lack of degradation up to 1000°C, with aging treatments indicating the largest degradation in properties at 450°C for the ultimate strength with a slight recovery at 700°C and a return to the as-fabricated properties at 1000°C. The silica plugging and oxidative carbon loss model accounts for this behaviour. After the 1200°C aging, a degradation in composite properties due to microstructural degradation and exposure of the interfaces occurs. The larger aging matrix was carried out using the unidirectional Rolls-Royce fabricated tiles. Due to the microstructural porosity and inhomogeneity of these materials the results obtained are less reliable than for the in-house materials. Both CUDM18 and 19 exhibited the same trends in behaviour as the in-house fabricated composites, however pre-aging at 1000°C gave inconclusive results.

Finally, the creep characterisation of these materials indicates that, for the test conditions used, the properties are dominated by the fibre creep. The small number of evaluations conducted does not allow for accurate conclusions to be drawn. The composites exhibit non-steady state creep, the curves always decreasing in slope over the test period as the stress is transferred form the matrix to the fibres. Hence the results are for the minimum creep rates observed and indicate that the creep rate is similar to other GCMC systems.

Chapter 7. Comparative Studies on CAS Matrix Composites.

In parallel to the above work the research has also included a small amount of work utilising the CAS ternary system as a potential glass ceramic matrix for CMC materials. This has utilised the compositional selection and processing criteria developed within the MAS program in order to evaluate the general suitability for glass ceramic matrix systems. Hence the results presented below indicate a non-optimised system for composition selection and to some extent hot press schedule.

7.1. Composition Selection and Composite Fabrication.

The CAS system has been used extensively for GCMC fabrication and is available as a commercial product from Corning. In Chapter 1. a number of features of the CAS system were indicated in tabular form. The anorthite matrix is selected for composite systems since it offers a refractory phase (up to 1553°C) and can be processed via the conventional glass ceramic routes. From Table 1.4. and Table 1.5. in Chapter 1., CAS glass ceramics have similar strengths to MAS systems and anorthite has a thermal expansion coefficient of 4.5×10^{-6} C^{-1} which is above, but not greatly dissimilar to that of the fibre. Density of CAS glass ceramic is similar to that of MAS glass ceramic and as is the case for MAS, bulk crystallisation is difficult (51) (52).

Hence, a large number of similarities exist for both systems as a base for for matrices in composite materials. In order to utilise the processing methodology developed within the above study a tie-line was taken from stoichiometric anorthite to wollastonite for compositional selection. The wollastonite phase is refractory (up to 1554°C), but has a high thermal expansion coefficient of 9.4×10^{-6}°C^{-1}. Three compositions were selected for study along this tie-line to develop diphasic matrices and utilise the possibility of lowered processing temperatures due to the eutectic trough between the two phases at 1307°C. The compositions selected are indicated in Fig 7.1., which is a part of the CAS ternary diagram. As with the MAS ternary system studied

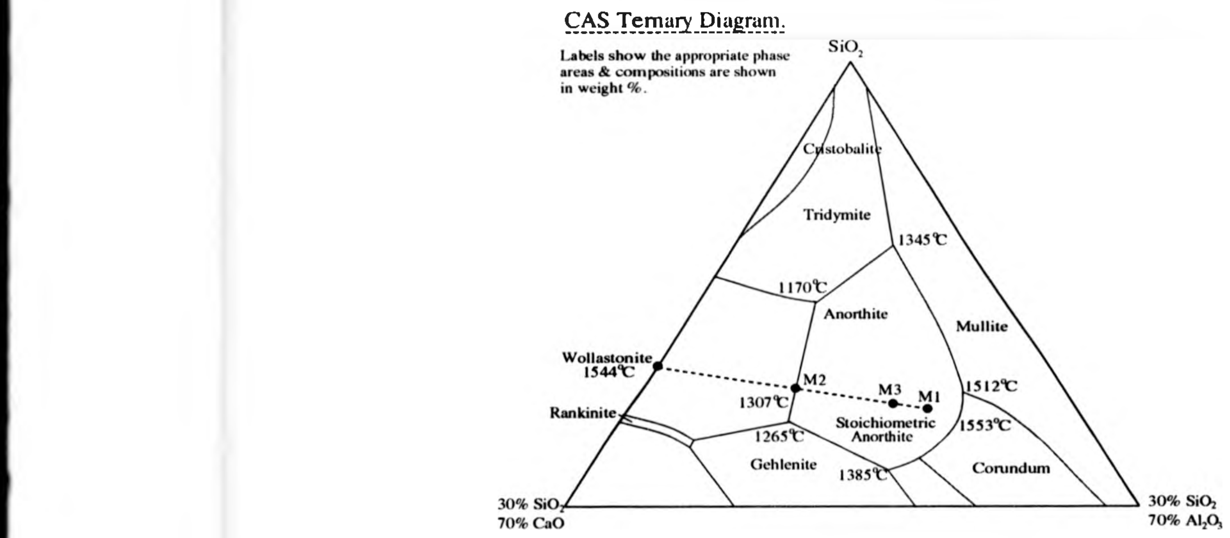
CAS Ternary Diagram.
Labels show the appropriate phase areas & compositions are shown in weight %.
SiO$_2$
Cristobalite
Tridymite
1345°C
1170°C
Anorthite
Mullite
Wollastonite
1544°C
M2
M3
M1
1512°C
1307°C
Rankinite
Stoichiometric Anorthite
1553°C
1265°C
Gehlenite
1385°C
Corundum
30% SiO$_2$
70% CaO
30% SiO$_2$
70% Al$_2$O$_3$

Figure 7.1. Part of the CAS ternary system.

above compositions were studied at stoichiometry (M1), within the phase field (M3) and at the eutectic trough (M2). These off-stoichiometric compositions were selected on the basis that composition M2 would give 50% anorthite and 50% wollastonite, so giving a thermal expansion coefficient of 6.95x10^{-6}°C^{-1}. Composition M3 would give 80% anorthite and 20% wollastonite giving a thermal expansion coefficient of 5.48x10^{-6}°C^{-1}. The differential thermal analysis traces for two of these powder compositions are shown in Fig 7.2. Due to thermal expansion considerations descriptions will be based on the differences between stoichiometric anorthite and M3, the mid-phase field composition powder. For the stoichiometric anorthite powder composition, as was the case for the stoichiometric cordierite powder, the DTA curve does not indicate any processing windows or melting below ~ 1275°C, with a T_g ~ 840°C.

For the modified compositions, M2 and M3 (M3 is not shown in the figure), the DTA curve is altered considerably. Glass softening occurs at a much lower temperature for M2 (T_g ~ 780°C), although it is similar for M3 (T_g ~ 835°C). Importantly however, both modified compositions show softening behaviour, for M2 this occurs at ~ 924°C and for M3 again the value is higher at ~ 937°C. Because of the move of composition away from stoichiometry both modified compositions show two exothermic maxima of crystallisation, the wollastonite peak appearing first at ~ 980°C

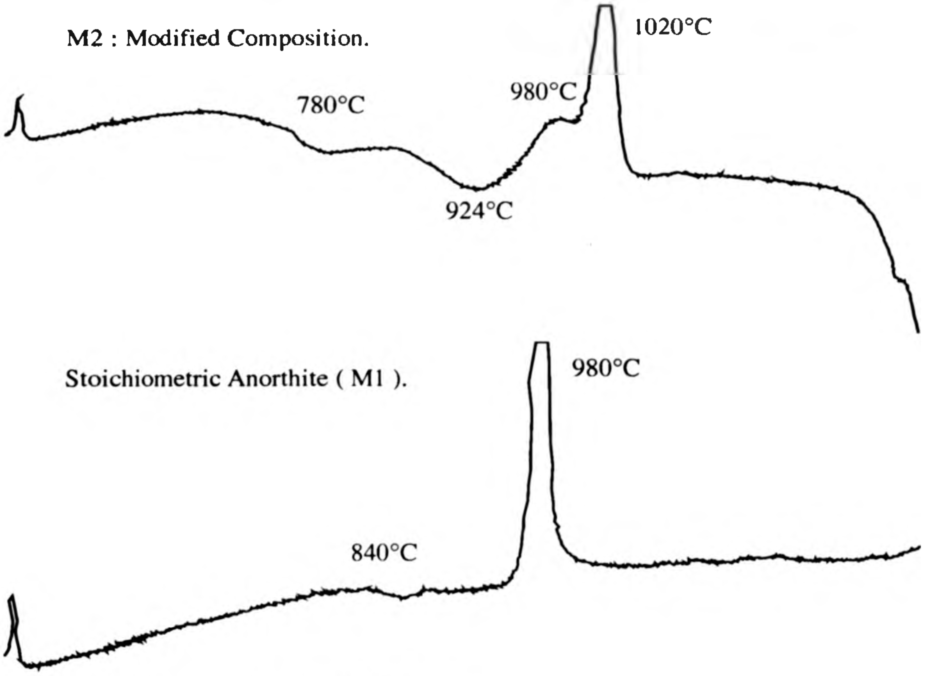

Figure 7.2. DTA traces for the CAS glasses.

for both powders followed by the larger anorthite crystallisation peak at ~ 1020°C for both powders.

As with the MAS system nucleants were not added because of the use of powders and not bulk glasses for the fabrication of the composites. Composite fabrication followed the route developed for the MAS system and studies utilising the stoichiometric powder gave poor tow infill, and ~ 5μm voids dispersed relatively evenly in the matrix, with XRD and EDS confirming an anorthite matrix. For the modified powder composites infill was improved and porosity less evident, however microstructures showed grain sizes ~ 2-3μm. For these composites the desired phase structure of anorthite and wollastonite was produced, however the poor quality of the XRD traces did not allow for approximate phase concentrations to be calculated. It should be realised that with these compositions, as with the MAS system, the isotherm hold temperature was 1200°C, since all crystallisation peaks occurred below this temperature and (unlike the MAS system) the hold time was limited to 1hr. The pressure was applied incrementally during the appropriate softening region, as developed for the MAS system. However, the pressure and temperature cycle has not been optimised for the compositions used.

7.2. Mechanical Properties of CAS Composite Materials.

A number of hot press fabrication runs were carried out using the compositions above in order to evaluate, to a limited extent, the mechanical behaviour and performance of this system. All tests were conducted at room temperature and in three point flexure in order to provide a ranking and to facilitate comparison with MAS composite fabrications. To act as a base a stoichiometric system was pressed as indicated above at 10MPa, which gave reasonable strength ($\sigma_{UBS} \sim 517$MPa) although many samples failed in shear and not in a tensile manner.

This problem was encountered for the CAS M3 CMCs fabricated using the standard hot press route, although using a higher pressure of 15MPa did improve the composite properties. A typical stress / deflection plot for a CAS M3 / NL-607 composite is given in Fig 7.3. It can be realised that, by the application of this process route, σ_{UBS} is high, with a good separation (~ 54%) from σ_{mm}, and the modulus is retained to within the rule of mixtures value. For these CAS M3/ NL-607 composites

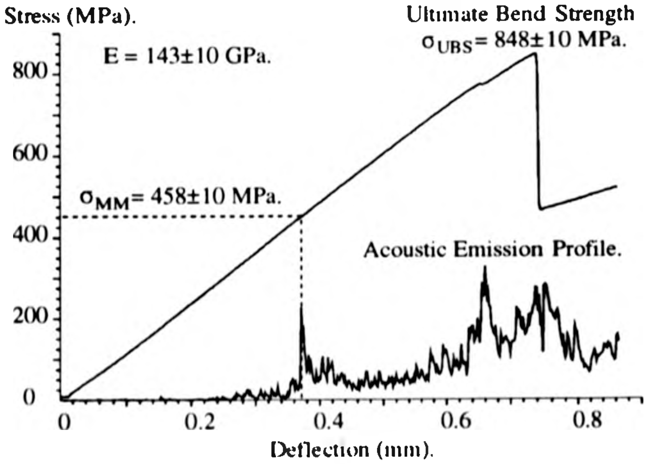

Figure 7.3. Typical stress / deflection curve for a CAS / NL - 607 composite.

the mechanical data can be summarised as follows : σ_{mm} = 530 ± 51MPa, σ_{UBS} = 827 ± 25MPa, and E_c = 146 ± 6GPa.

For the sample shown in Fig 7.4., $\varepsilon_{mm} \sim 3.2 \times 10^{-3} \pm 0.3 \times 10^{-3}$ and $\varepsilon_{UBS} \sim 5.9 \times 10^{-3} \pm 0.5 \times 10^{-3}$. These are somewhat smaller than the values for the MAS mid - phase field powder with ε_{mm} being ~ 78% and ε_{UBS} ~ 84%. Hence properties show the non-optimised state of the process route. The M2 powder was not utilised in CMC fabrication trials due to its high predicted thermal expansion coefficient with respect to the fibres.

7.3. Conclusions from the Comparative Study.

The comparative study was carried out in order to test the applicability of the compositional selection criteria and fabrication route developed for other systems in comparison to that of MAS. The CAS system was selected since a commercially available system utilising this ternary was available for comparative results as well as the data generated by this study for the MAS GCMCs.

Identical matrix selection criteria were applied to composition selection within this system, resulting in a tie-line between stoichiometric anorthite and wollastonite. Both the eutectic trough and the mid-anorthite-phase-field powder composition powders indicated process windows via DTA, although the eutectic trough powder was not utilised in CMC fabrication due to thermal expansion considerations. Mid-phase field powder (M3) composites were fabricated mimicking the MAS hot press schedule for pressure application with the same 1200°C isotherm hold. This produced composites with the desired diphasic matrix structure between anorthite and wollastonite.

This route produced CAS / NL-607 composites of strengths near to those of the MAS material (~ 95% σ_{mm} and ~ 77% σ_{UBS}), with a modulus as predicted from the rule of mixtures. This, to a degree, validates the process route developed within this work. No attempt has been made to optimise the process schedule for these CAS composites beyond the pressure application window for fabrication and hence these results do represent a non-optimised system. From tests carried out by Dr. M. W. Pharaoh at Warwick University, on the commercially available CAS material, this has $\sigma_{mm} = 330 \pm 42$MPa, $\sigma_{UBS} = 767 \pm 21$MPa and $E = 99 \pm 7.8$GPa for three point flexure specimens. It should be pointed out that ε_{mm} and ε_{UBS} are higher for the Corning material (this study $\varepsilon_{mm} \sim 74\%$ and $\varepsilon_{UBS} \sim 49\%$). Clearly, properties such as effects of aging and thermal expansion would need to be measured in order to give a better evaluation of this material, but initial properties measured are good for a non-optimised system.

Chapter 8. Overview, Conclusions and Future Work.

8.1. Overview.

As indicated by the considerable amount of research work conducted into the development and testing of CMCs, it can be realised that this class of material offers damage tolerance, with the possibility of oxidation resistance and a high temperature, high specific strength for potential application in a wide range of high risk thermostructural components. Within this work the primary interest was in application to the gas turbine environment where ceramics offer considerable weight and operational temperature advantages over the currently used superalloys. Previous researchers have utilised the glass ceramic route in the fabrication of CMCs, with Aveston in the early 1970s producing cordierite matrix composites (89). The glass ceramic route was utilised because of its potential to offer lower processing temperatures, hence avoiding thermochemical degradation of the fibre and the fortuitous interfacial reaction between this aluminosilicate matrix and the SiC fibres. Within this work the approach has been to use a diphasic matrix with phases selected from the MAS glass ceramic ternary system. The differing thermal expansion of these phases allows tailoring of the matrix thermal expansion and the mismatch strain within the composite system.

The study began by initial composition selection on a tie line between cordierite and enstatite at the eutectic trough. The effect of the nucleants P_2O_5 and TiO_2 added at 2wt% and 10wt% respectively to this composition were investigated for identical processing conditions for chopped fibre systems. It was found that the nucleant could have a significant effect on the phase development within the matrix, the incorporation of TiO_2 causing the preferential formation of the μ-cordierite polymorph. This polymorph's metastability and high thermal expansion coefficient led to the elimination of the TiO_2 nucleant from the study. The base glass powder and P_2O_5 nucleant added powder were found to give similar results both for process conditions utilising window I and window II regimes. Hence, the use of the nucleant was negated in this work. The availability of a small amount of pre-preg at the beginning of the project allowed some initial unidirectional composite fabrication trials to be carried out. These achieved limited success. The results of these fabrications highlighted the presence of fibre damage causing a drop from the calculated elastic modulus values and indicated the importance of pressure application within the fabrication regime.

Whilst the chopped fibre trials were being carried out in order to investigate process-variables, parallel development was occurring on fibre tow infill and subsequent winding. The development of a pre-preg process was required to allow for rapid evaluation of matrix compositional changes and to evaluate novel pre-preg ideas. Apparatus development led to the use of a T-piece traverse head allowing fibre tow infill and winding without the need for a separate traverse arrangement. The use of rollered pre-preg and 'walls' on the edge of the pre-preg section gave consistent quality. Alleviation of the fibre tow tension before slurry infill minimised tow breakages.

For the purposes of producing a reasonable amount of composite material the glass composition selected for further study was passed to a commercial glass manufacturer for supply. The resultant batch was within the cordierite phase field, not on the eutectic trough and contained ~ 2wt% ZrO_2 impurity. Due to time constraints and the necessity of process development this powder was utilised for the bulk of the study. Towards the end of the study the use of a second glass manufacturer led to the supply of glass powder of the required composition without significant impurity addition. Brief studies carried out on the this powder in composite form showed very similar results to the mid-cordierite phase field powder.

The availability of high quality pre-preg allowed for the development of the refined composite processing schedule. This route utilises a rapid heat up followed by controlled pressure application within a process window before crystallisation of the glass ceramic begins. The composite is then further heated to an isotherm hold temperature (for this work 1200°C) in order to crystallise the matrix and develop the correct phase and interface structure. Mechanical evaluation of the unidirectional composites prepared via this route with differing isotherm hold times gave ultimate flexural strengths >1GPa, with $\sigma_{mm} / \sigma_{UBS} \sim 0.5\text{-}0.6$. Hence composites with very high strengths and good separation between microcracking and ultimate load capacity were produced. It was found, for the small investigation into isothermal hold time, that, for this composite system, a 2hr hold at 1200°C gave the highest attained properties. However, the statistical spread in data for all hold times overlap. Due to the reservations as to the validity of flexural evaluation of CMCs a limited tensile evaluation study was carried out with cross-plied composites being tested at room and elevated temperatures and under creep conditions. The results of these evaluations can be summarised, realising that the material used for these tests was degraded in properties from the in-house fabricated samples due to difficulties in process scale up. The room temperature tensile evaluation indicated two regions that could be identified, microcracking in the 90° plies and then the 0° plies. Creep evaluation was conducted before the short term high temperature tests and hence the microcracking stress may have been exceeded, allowing oxygen ingress into the sample. Due to the time required for the creep evaluations the results of the tensile tests at elevated temperatures may not accurately reflect the short term response of the materials at high temperatures, although, as for the bend results, degradation is observed. The creep test regime indicated that for 50-80MPa applied stress, for temperatures 1000°-1150°C, the composite was dominated by fibre creep. The observed creep rates were ~ $\dot{}$ 1.6 x $10^{-8}s^{-1}$ and a steady state creep was not attained for the test conditions.

In order to evaluate the effect of prolonged high temperature exposure in air a series of aging experiments were carried out. Studies using both in-house and Rolls-Royce fabricated unidirectional composites were undertaken. A reduction in mechanical properties was observed for composites aged at intermediate temperatures (450°-800°C) whereas composites aged at 1000°C retained properties similar to the as-fabricated materials. For temperatures in excess of 1000°C microstructural degradation was observed and a surface layer was evident. The layer had a composition within the spinel phase field and contained bubble like voids indicative of gaseous evolution. As the aging temperature was increased the thickness of this layer increased (60-80 µm at 1000°C to 80-140 µm at 1200°C). Pre-aging at 1000°C followed by aging at intermediate temperatures did compensate for some of the mechanical property degradation.

In order to investigate the degradation mechanism operating at intermediate temperatures, since no obvious microstructural changes were occurring, the fibre / matrix interface was examined. Degradation was seen to occur via the oxidation of the carbon-rich, interfacial layer during the aging at intermediate temperatures. Removal of the carbon layer via pipe oxidation channels down the fibre lengths within the composite led to a change in the interfacial micromechanics and subsequent degradation of the observed mechanical properties. At aging temperatures 450°C-700°C, oxidative loss of the carbon layer occurred with partial silica bridging of the interface at the higher end of the temperature range. At higher temperatures, (i.e. 1000°C) the silica bridge formation was rapid enough to cause a plugging effect, sealing the ends of the composite from pipeline oxidation. From the 1000°C aging treatments the oxygen ingress via the matrix was ~ $0.3\mu m hr^{-1}$ and hence, for the 100hr time interval used in this work, the bulk of the composite retained the as-fabricated material properties.

This model for interfacial degradation is validated by the interfacial micromechanical measurements taken on the aged specimens. The use of a novel, SEM based indenter system allowed for evaluation of the interfacial micromechanical response for 2Γ, (the debond energy) and τ (the shear sliding resistance). This analysis showed that for 450°C aging, although the debond energy 2Γ was similar to the as-fabricated material, the shear sliding resistance was doubled and exhibited far greater scatter. At 700°C the debond energy increased by three times and the shear sliding resistance five times with both parameters exhibiting considerable scatter. This is indicative of the partially silica bridged interface observed via TEM, as opposed to an oxidative loss of carbon from the interface. At 1000°C the bulk micromechanical properties are very close to the values measured for the as-fabricated composites. However, indentation tests carried out within a few fibre diameters (~ 30μm) from the composite surface indicated very high values for both 2Γ and τ, consistent with the fully, silica bridged interface observed by SEM.

8.2. Conclusions.

1. The composition selection principle used to move away from stoichiometry and toward a diphasic silicate matrix offers the advantages of a lower processing temperature, the development of a process window and tailoring of the matrix thermal expansion coefficient.
2. Within this work, a novel pre-preg methodology has been developed. The use of a T -piece traverse head, 'walls' on the pre-preg sides and rollered output gives high quality and reproducible pre-preg.
3. The hot press schedule developed minimised process damage to the fibres and was applicable to more than one glass ceramic system (CAS in addition to MAS).
4. Microstructural analysis of the fabricated MAS composites indicated the desired diphasic α-cordierite and enstatite matrix, containing virtually no residual porosity.
5. Interfacial analysis using TEM indicated the presence of a carbon rich layer ranging in thickness from 25 to 65nm for a 1hr isotherm to 35 to 70nm for a 3hr isotherm using the NL-607 fibre. For the NL-201 fibre type a carbon rich interface with a 20 to 45nm thickness was also observed.
6. MAS / NL-607 composite properties exceed those of other GCMC systems in flexure ; $\sigma_{mm} = 665\pm75$MPa, $\sigma_{UBS} = 1168\pm41$MPa and $E = 157\pm12$GPa. Tensile studies indicated successive microcracking in the 90° and 0° plies identified by a modulus drop and acoustic emission.
7. Short term high temperature testing of MAS / NL-607 composites in flexure indicated that at intermediate temperatures (i.e. 450°-700°C) degradation did not occur. However, at higher test temperatures (i.e. 1000°C) rapid oxidation of the interface could occur resulting in degradation.
8. The oxidative behaviour of the MAS / NL-607 composites indicated, at intermediate temperatures (450°-800°C), oxidative carbon removal form the interface occurred. At higher temperatures in this interval, partial silica bridge formation was observed as well as carbon removal. At 1000°C, a silica plug can form, protecting the interface from pipeline oxidation. For temperatures greater than 1000°C microstructural

degradation occurs.

9. The micromechanical behaviour of the MAS / NL-607 composite fibre / matrix interface was investigated, with 2Γ and τ increasing from the as-fabricated values of $12.4\pm5.4Jm^{-2}$, 48±15MPa to $13.6\pm4.4Jm^{-2}$ for 450°C and $35.6\pm29.2Jm^{-2}$, 248±120MPa for 700°C. At 1000°C the values return to those of the as-fabricated composite for fibres within the bulk. Fibres up to ~ 30μm from the edge exhibited very high values indicative of fully silica bridged interfaces.
10. The creep properties of the MAS composites have been investigated in tension. For all conditions investigated a steady state creep regime was not reached and the composite creep rate was ~ $1.6 \times 10^{-8}s^{-1}$. The creep behaviour was dominated by fibre creep.

For the materials fabricated in this work the matrix microcracking stress is above that of the typical in-service stress required in the gas turbine (100-300MPa). However, a number of problems need to be addressed before application of these materials occurs. Attachment stresses, localised stresses and overstress may exceed the matrix microcracking stress and hence allow environmental access to the fibre matrix interface. This would be followed by degradation of the materials properties. Composite application temperatures of ~ 700°-1200°C were suggested for this type of material at the beginning of the program. This research has indicated that at 700°C property degradation occurs due to oxidation of the carbon-rich interface and partial silica bridging. Hence, unless the interface can be protected by silica plugging or by an external surface layer, application at this temperature could not occur. Above 1000°C, microstructural degradation in the above system was observed. Therefore, the upper temperature limit of application is too high for the material fabricated in this study.

In conclusion, although in this research, composite materials possessing very high mechanical strengths and overstress tolerance have been fabricated, potential application as thermostructural components still requires development to be carried out.

8.3. Future Work.

Within this work a composite system with good mechanical response has been identified. However, the development of the pre-preg and fabrication schedule has only allowed for limited characterisation of microstructure, interface structure and mechanical response in the as-fabricated, thermally aged and crept states. Therefore, there are a number of areas that can be identified for future work :-

1. A more detailed study of pre-preg conditions to gain a better fibre distribution and to vary V_f in the final composite.
2. A more complete study of process schedule with respect to the optimisation of mechanical response, aging response and the elimination of residual glass.
3. A further detailed study of the microstructure of the composites for both MAS powder compositions and an estimation of the residual glass content.
4. The extension of the tensile studies for all conditions to validate the mechanical response data.
5. Extension of the creep characterisation of the materials to simulate more realistic potential application conditions and more fully investigate the material properties outside the fibre dominated region.
6. The extension of the processing methodology and the compositional selection ideology to other glass ceramic systems.

References.

1. Kingery W.D., Bowen H.K. and Uhlmann D.R., "Introduction to Ceramics." 2nd Edition. Wiley. New York 1976.
2. Richerson D.W., "Modern Ceramic Engineering : Properties, Processing, and Use in Design." 2nd edition, Marcel Dekker Inc (1992).
3. French C. C. J., "Future prospects for Engineering with Ceramics." Brit. Ceram. Proc No. 46 April 1990. "Advanced Engineering with Ceramics" Ed Morrell.
4. Butler E. G. and Lewis M.H., Proc. 4th. Int. Symp. on Ceram. Mat. and Components for Engines, Gothenberg, Sweden, 1991.
5. Dryell D.R. and Freeman C.W., "Materials Development for Turbomachinery Design." 38 - 45, 2nd Parsons Int. Turbine Conf. Ed. Taplin D.M.R, Knott J.F. and Lewis M.H., Inst. of Metals. London.
6. Meethan G.W., J. Mat. Sci. 26, 853 - 860 (1991).
7. Tuersley I. P., PhD Thesis, University of Warwick, 1990 .
8. Devendra K. and Syers G., "Advanced Engineering with Ceramics." 93 - 112, British Ceram. Proc. 46, Ed Morrell (1990).
9. Davidge R.W., "Mechanical Behaviour of Ceramics." Cambridge University Press (1979).
10. Ingliss C. E., Trans. Inst. Naval. Archit. 55, 219 - 230 (1913).
11. Griffith A.A., Philos. Trans. R. Soc. London. A221, 163 - 198 (1920).
12. Evans A. G., Mat. Sci. and Eng. 71, 3 - 21 (1985).
13. Hillig W. B., Ann. Rev. Mater. Sci. 17, 341 383 (1987).
14. Lange F. F., J. Amer. Ceram. Soc. 61 [5-6], 270 - 271 (1978).
15. Lewis M. H., Powell B.D., Drew P., Lumby R.J., North B. and Talyor A.J., J. Mat. Sci. 12, 61 (1977).
16. Lewis M. H., Bhatti A.R., Lumby R.J. and North B., J. Mat. Sci. 15, 103 (1980).
17. Karunaratne B.S.B. and Lewis M.H., J. Mat. Sci. 15, 1781 (1980).
18. Karunaratne B.S.B. and Lewis M.H., J. Mat. Sci 15, 449 (1980).
19. "Ceramic Materials and Components for Engines.". p 1480 - 1494, Ed.

Tennery V. J., The American Ceramic Society (1989).

20. Advances in Ceramics Vol. 26, 19 - 54. Ed. Yam M. F., Niwa K., O'Bryan H. M., and Young W. S., The American Ceramic Society (1989).
21. "Ceramic Materials and Components for Engines.". p 831 - 840, Ed. Tennery V. J., The American Ceramic Society (1989).
22. Rungdren K. and Elfving P., p 1043 - 1052, Advances in Ceramics Vol. 24B. Ed. Somiya S., Yamamoto M., et al. The American Ceramic Society (1988).
23. Okamoto Y., Leuji J., et al., p 565 - 571, Advances in Ceramics Vol. 24B. Ed. Somiya S., Yamamoto M., et al. The American Ceramic Society (1988).
24. Yen T. and Guo J., p 573 - 582, Advances in Ceramics Vol. 24B. Ed. Somiya S., Yamamoto M., et al. The American Ceramic Society (1988).
25. Becher P.F., J. Amer. Ceram. Soc. 74[2], 255 - 269 (1991).
26. Rice R. W., Ceram. Eng. Sci. Proc. 7 - 8[II], 667 - 694 (1990).
27. Lewis D., Amer. Ceram. Soc. Bull. 67[8], 1349 - 1356 (1988).
28. Mah T., Mendiratta M.G., Katz A.P. and Khodabakhsh S.M., Amer. Ceram. Soc. Bull. 66[2], 304 - 307 (1987).
29. Evans A. G., Mat. Sci. and Eng. A105/106, 65 - 75 (1988).
30. Weiderhorn S.M., Ann. Rev. Mater. Sci. 14, 373 - 403 (1984).
31. Faber K.T. and Evans A.G., Acta. Met. 31[4], 565 - 584 (1983).
32. Razzell A.G., "Silicon Carbide Fibre Silicon Nitride Matrix Composites." PhD Thesis, University of Warwick (1992).
33. Lange F. F., J. Amer. Ceram. Soc. 56[10], 518 - 525 (1973).
34. Tani E., Umebayashi S., Kishi K., Kobayishi K. and Nishijima M., Amer. Ceram. Soc. Bull. 65[9], 1311 - 1315 (1986).
35. Stevens R., "ZrO_2." Magnesium Elektron Public No. 113.
36. Schioler L.J. and Stiglich J.J. Amer. Ceram. Soc. Bull. 65[2], 289 - 292 (1986).
37. Marshall D.B. and Ritter J.E., Amer. Ceram. Soc. Bull. 66[2], 309 - 317 (1987).
38. Evans A. G., J. Amer. Ceram. Soc. 73[2], 187 - 206 (1990).
39. Prewo K. M., "Glasses and Glass Ceramics." Chapter 10., 336 - 368. Ed. Lewis M.H., Chapman and Hall (1988).

40. Cornie J.A., Chiang Y.M., Uhlmann D.R., Mortensen A. and Collins J.M., Amer. Ceram. Soc. Bull. 65[2], 293 - 304 (1986).

41. Becher P.F., Hsueh C-H., Angelini P. and Tiegs T.N., J. Amer. Ceram. Soc. 71[12], 1050 - 1061 (1988).

42. Li J., MSc Thesis, University of Warwick (1988).

43. Singh R. N., J. Amer. Ceram. Soc. 73[10], 2930 - 2937 (1990).

44. Chaim R., Baum L., and Brandon D. G., J. Amer. Ceram. Soc. 72[9], 1636 - 1642 (1989).

45. "Ceramic Materials and Components for Engines.". p 260 - 272, Ed. Tennery V. J., The American Ceramic Society (1989).

46. Liu H., Weisskopf K.L. and Petzow G., J. Amer. Ceram. Soc. 72[4], 559 - 563 (1989).

47. Shalek P.D., Petrovic J.J., Hurley G.F. and Gac F.D., Amer. Ceram. Soc. Bull. 65[2], 351 - 356 (1986).

48. Tiegs T.N. and Becher P.F., Amer. Ceram. Soc. Bull. 66[2], 239 - 242 (1987).£

49. Yajima S., Okamura K., Hayashi J. and Omuri M., J. Amer. Ceram. Soc. 59, 234 (1976).

50. Mecholsky J.J., Amer. Ceram. Soc. Bull. 65[2], 315 - 322 (1986).

51. McMillan P.W., "Glass Ceramics." Academic Press London (1979).

52. Strnad Z., "Glass Ceramic Materials." Elsevier (1986).

53. Norman B.J. and Tilley B.P., "Advanced Engineering with Ceramics." 127 - 140, British Ceram. Soc. Proc. 46, Ed. Morrell R., (1990).

54. Hillig W., Ceram. Eng Sci. Proc. 9[7-8], 755 - 758 (1988).

55. Aveston J., Cooper G.A. and Kelly A. "The Properties of Fibre Composites." NPL Proc. Conf. Nov. 1971. IPC Science and Technology Press Surrey (1971).

56. Knowles K.M. and Yang X.F., Ceram. Eng. Sci. Proc. 12[7-8], 1375 - 1388 (1991).

57. Cao H.C., Bischoff E., Sbaizero O., Ruhle M., Evans A.G., Marshall D.B. and Brennan J.J., J. Amer. Ceram. Soc. 73[6], 1691 - 99 (1990).

58. Yang X.F. and Knowles K.M., J. Amer. Ceram. Soc. 75[1], 141 - 147 (1992).

59. Danchaivijit S. and Shetty D.K., J. Amer. Ceram. Soc. 76[10], 2497 - 2504 (1993).

60. Sutcu M., J. Mat. Sci. 23, 928 - 933 (1988).

61. Evans A.G. and Marshall D.B., Acta. Met. 10, 2567 - 2583 (1989).

62. Budhiansky B., Hutchinson J.W. and Evans A.G., J. Mech. Phys. Sol. 34[2], 167 - 189 (1986).

63. Beyerle D.S., Spearing S.M,. Zok F.W. and Evans A.G., J. Amer. Ceram. Soc. 75[10], 2719 - 2725 (1992).

64. Thouless M.D. and Evans A.G., Acta Met. 36[3], 517 - 522 (1988).

65. Curtin W.A., J. Amer. Ceram. Soc. 74[11], 2837 - 2845 (1991).

66. Curtin W.A., Acta. Met. Mater. 41[5], 1369 - 1377 (1993).

67. Thouless M.D., Sbaizero O., Sigl L.S. and Evans A.G., J. Amer. Ceram. Soc. 72[4], 525 - 532 (1989).

68. Marshall D.B., Cox B.N. and Evans A.G., Acta. Metall. 33, 2013 (1985).

69. McCartney L.N., Proc. R. Soc. Lond. A409, 329 - 350 (1987).

70. He M. and Hutchisnsion J.W., Int. J. Solids. Struct. 25[9], 1053 - 1067 (1989).

71. Sutcu M., Acta. Met. 37[2], 651 - 661 (1989).

72. Evans A.G., Ref 2. AGARD - R - 795. "Introduction of Ceramics into Aerospace Structural Composites.". Antalya Turkey 1993.

73. Heredia F.E., Spearing S.M., Evans A.G., Mosher P. and Curtin W.A., J. Amer. Ceram. Soc. 75[11], 3017 - 3025 (1992).

74. Hayhusrt D.R., Leckie F.A. and Evans A.G., Proc. R. Soc. London A434, 369 - 381 (1991).

75. Ko F. K., Amer. Ceram. Soc. Bull. 68[2], 401 - 413 (1989).

76. Prewo K.M., Amer. Ceram. Soc. Bull. 68[2], 395 - 400 (1989).

77. Murthy V.S.R. and Lewis M.H., Compos. Sci. and Tech. 42, 221 -249 (1991).

78. Prewo K.M., J. Mat. Sci. 21, 3590 - 3600 (1986).

79. Bunsell A.R., J. App. Polymer Sci. : App. Polymer Symposium 47, 87 - 98 (1991).

80. Stohr J.F., Ref 1. AGARD - R - 795. "Introduction of Ceramics into Aerospace Structural Composites.". Antalya Turkey 1993.

81. Yajima S., Hayashi j., Emery M., and Okamura K., Nature (London) 261, 683 (1976).

82. Mah T., Hecht N.L., McCullum D.E.,Hoenigman J.R., Kim H.M., Katz A.P. and Lipsitt H.A., J. Mat. Sci. 19, 1191 - 1201 (1984).

83. Chaim R.D., Brandom D.G. and Baum L., Ceram. Eng. Sci. Proc 9[7-8], 695 - 704 (1988).

84. Lipowitz J., LeGrow G.E., Lim T.F. and Langley N., Ceram. Eng. Sci. Proc. 9[7-8], 931 - 942 (1988).

85. Murthy V.S.R. and Lewis M.H., Mat. Letters 20, 263 - 268 (1989).

86. Foltz T.F., Ceram. Eng. Sci. Proc. 6[9-10], 1206 - 1220 (1985).

87. Mackin T.J., Yang J. and Warren P.D., J. Amer. Ceram. Soc. 75[12], 3358 - 3362 (1992).

88. Stinton D.P., Caputo A.J. and Lowden R.A., Amer. Ceram. Soc. Bull. 65[2], 347 - 350 (1986).

89. Aveston J., Paper 5, 63 - 87, The Properties of Fibre Composites Conf Proc NPL Nov 1971, IPC Science and Technology Press Ltd.

90. Brennan J.J. and Prewo K.M., J. Mat. Sci. 17, 2371 - 2383 (1982).

91. Cooper R.F. and Chyung K., J. Mat. Sci. 22, 3148 - 3160 (1987).

92. Marshall D.B. and Evans A.G., J. Amer. Ceram. Soc. 68[5], 225 - 231 (1985).

93. Rolls - Royce GCMC Review Meeting, Rolls - Royce Bristol March (1991).

94. Prewo K.M., Brennan J.J. and Layden G.K., Amer. Ceram. Soc. Bull. 65[2], 305 - 313 (1986).

95. Brennan J.J., External Report UTRC R84 - 916018 - 4 (1984).

96. Kim R.Y. and Katz A.P., Ceram. Eng. Sci. Proc. 9[7-8], 853 - 860 (1988).

97. Chen M.Y., Battison J.M. and Mah T.I., J. Mat. Sci. 24, 3213 - 3220 (1989).

98. Ritter J.E., Genarri P.A., Nair S.V., Haggerty J.S. and Lightfoot A., Ceram. Eng. Sci. Proc. 10[7-8], 625 - 631 (1989).

99. Prewo K.M. and Brennan J.J., J. Mater. Sci. 15[2], 463 - 468 (1980).

100. Prewo K.M. and brennan J.J., J. mat. Sci. 17, 1201 - 1206 (1982).

101. Chamberlain A., Pharaoh M.W. and Lewis M.H., p 321 - 328, HTCMC1 Ed. Naslain R., Lamon J. and Doumeingts D. ECCM6 Bordeaux 1993. Woodhead Publishing.

102. Rahaman M.N. and Moulson A.J., J. Mat. Sci. 19, 189 - 194 (1984).

103. Lowden R.A. and Stinton D.P., Ceram. Eng. Sci. Proc. 9[7-8], 705 - 722 (1988).

104. Sygulla D., Muhlratzer. and Agatonovic P., Ref14. AGARD - R - 795. "Introduction of Ceramics into Aerospace Structural Composites.". Antalya Turkey 1993.

105. Krenkel W., Ref 13. AGARD - R - 795. "Introduction of Ceramics into Aerospace Structural Composites.". Antalya Turkey 1993.

106. Bhatt H., Donaldson K.Y., Hasselman D.P.H. and Bhatt R.T., J. Amer. Ceram. Soc. 73[2], 312 - 316 (1990).

107. Giffen C.W., Limaye S.Y., Richerson D.W. and Shetty D.K., Ceram. Sci. Eng. Proc. 9[7-8], 671 - 678 (1988).

108. Miyoshi Y., Kodama H., Sakamoto H., Gotoh A. and Iijima S., Conf. Proc. Oak Ridge, Tennessee, USA, 7 -9 June (1988).

109. Lamicq P.J., Bernhart G.A., Dauchier M.M. and Mace J.G., Amer. Ceram. Soc. Bull. 65[2], 336 - 338 (1986).

110. Fitzer E. and Gadow R., Amer. Ceram. Soc. Bull. 65[2], 326 - 335 (1986).

111. Mouchon E. and Colomban Ph., Euromat 1993, 3rd European Conf. on Adv. Mat. and Processes., Paris 1993. in Journal of Physics IV.

112. Bonney L.A. and Copper R.F., J. Amer. Ceram. Soc. 73[10], 2916 - 2921 (1990).

113. Kerans K., Randall S.H., Pagano N.J. and Parthasarathy T.A., Amer. Ceram. Soc. Bull. 68[2], 429 - 442 (1986).

114. Benson P.M., Spear K.E. and Pantano G.C., Ceram Eng Sci Proc 9[7-8], 663 - 670 (1988).

115. Pharaoh M.W., Daniel A.M. and Lewis M.H., J. Mat. Sci. Lett. 12[13], 998 - 1001 (1993).

116. Weihs T.P. and Nix W.D., J. Amer. Ceram. Soc. 74[3], 523 - 534 (1991).

117. Bender B.A., Wallace J.S. and Schrodt D.J., J. Mat. Sci. 26, 970 - 976 (1991).

118. Sbaizero O. and Evans A.G., J. Amer. Ceram. Soc. 69[6], 481 - 486 (1986).

119. Lewis D., Bulik C. and Shadwell D., Ceram. Eng. Sci. Proc. 6[7-8], 507 - 523 (1985).

120. Hoagland R.G., Marschall C.W. and Duckworth W.H., J. Amer. Ceram. Soc. 59 [5-6], 189 - 192 (1976).
121. Larsen D.C., DoD / NASA Advanced Composites Working Group 9th Conf. Comp. Mat. (1985).
122. Holmes J.W., J. Comp. Mat. 26[6], 916 - 933 (1992).
123. Daniel A.M. and Lewis M.H., Ceram. Eng. Sci. Proc. 14[7-8], 131 - 138 (1993).
124. Marshall D.B. and Oliver W.C., J. Amer. Ceram. Soc. 70[8], 542 - 48 (1987).
125. Yoder H.S., Amer. J. Sci. 250, 569 (1952).
126. Chaim R. and Heuer A.H., J. Amer. Ceram. Soc. 75[6], 1512 - 1521 (1992).
127. Rankin G.A. and Merwin H.E., Amer. J. Sci. 45, 301 (1918).
128. Karkhanavala M.D. and Hummel F.A., J. Amer. Ceram. Soc. 36(12), 389 (1953).
129. Zdaniewski W., J. Amer Ceram. Soc. 58[5-6], 163 (1975).
130. Predecki P., Haas J., Faber JR J. and Hitterman R.L., J. Amer. Ceram. Soc. 70[3], 175 - 182 (1987).
131. Hochella JR M.F. and Brown JR G.E., J. Amer. Ceram. Soc. 69[1], 13 - 18 (1986).
132. Schreyer W. and Schairer J.F., Carn. Inst. Wash. Year Book 197 (1958).
133. Roy R., Z. Kristollogr. 111, 185 (1959).
134. Schreyer W. and Schairer J.F., Z. Kristallogr. 116, 60 (1961).
135. Bridge D.R., "Aspects of Electronic Device Packaging." PhD Thesis. University of Warwick 1986.
136. Toropov M.A. and Barazokovski V.P., "High Temperature Chemistry of Silicates." p32. Invest. A. Kad. Nauk. Moscow (1963).
137. Bragg W.L., Z. Kristallogr. 74, 237 (1930).
138. Bystrom A., Arkiv. Kemi. Mineral. Geol. 15B[12], 1 (1941).
139. Gibbs G.V., Amer Mineral. 51[7], 1068 (1966).
140. Meagher E.P. and Gibbs G.V., Can. Mineral. 15[1], 43 (1977).
141. Cohen J.P., Koss F.K. and Gibbs G.V., Can. Mineral. 62[1-2], 67 (1977).
142. Sorrel C.A., J. Amer. Ceram. Soc. 43[7], 337 (1960).
143. Carpenter M.A., Putnis A., Navrotsky A. and McConnell J.D.C., Geochim. Cosmochim. Acta. 47, 899 (1983).

144. Putnis A., Nature. 287, 128 (1980).

145. Toropov N.A., Zhukauskas R.S.M. and Alienikov F.K., Inorg. Mat. 2[2], 307 (1966).

146. Putnis A. and Bish D.L., Amer. Mineral. 68[1-2], 60 (1983).

147. McMillan P., Putnis A., and Carpenter M.A., Phys. Chem. Min. 10(6), 256 (1984).

148. Schreyer W. and Yoder H.S., Neues. Jahrb. Mineral. Akstr. 101, 271 (1964).

149. Lee W.E. and Heuer A.H., J. Amer. Ceram. Soc. 70[5], 349 - 360 (1987).

150. James P.F., "Glasses and Glass Ceramics." Chapter 3., p 59 - 103. Ed. Lewis M.H., Chapman and Hall (1988).

151. Watanabe K., Geiss E.A. and Shafer M.W., J. Mat. Sci. 20, 508 - 515 (1985).

152. Barry T.I., Cox J.M. and Morrel R., J. Mat. Sci. 13, 594 - 610 (1978).

153. Lewis M.H., Chamberlain A., Daniel A.M., Pharaoh M.W., Razzell A.G. and Sutherland S. Ref 10. AGARD - R - 795. "Introduction of Ceramics into Aerospace Structural Composites.". Antalya Turkey 1993.

154. McLean M., Mat. Res. Soc. Symp. Proc. 120, 67 - 79 (1988).

155. Wu X. and Holmes J.W., Shanghai Engine Conference 1994, in press.

156. Park Y.H. and Holmes J.W., J. Mat. Sci. 27, 6341 - 6351 (1992).

157. Wu X. and Homes J.W., J. Amer. Ceram. Soc. 76[10], 2695 - 2700 (1993).

158. Sue Y.J., Chen S-Y., Lu H-Y. and Shen P., J. Mat. Sci. 26, 1699 - 1704 (1991).

159. Weihs T.P., Sbaizero O., Luh E.Y. and Nix W.D., J. Amer. Ceram. Soc. 74[3], 535 - 540 (1991).

160. Chaim R. and Heuer A.H., Advanced Ceram. Mat. 2[2], 154 - 158 (1987).

161. Hommeny J., Vanvazah J.R. and Kelly M.A., J. Amer. Ceram. Soc. 73[7], 2054 - 2059 (1990).

162. Herron M.A. and Risbid S.H. Amer. Ceram. Soc. Bull. 65[2], 342 - 346 (1986).

163. Marshall D.B., J. Amer. Ceram. Soc. 67[12], C259 - C260 (1984).

164. Daniel A.M., " Interfacial Properties of Fibre Reinforced Ceramic Matrix Composites. ". PhD Thesis, University of Warwick (1995).

165. Jensen H.M., Acta Metall. Mater. 38[12], 2637 (1990).

166. Steif P.S. and Trojnacki A., J. Amer. Ceram. Soc. 77[1], 221 - 229 (1994).

THE BRITISH LIBRARY
BRITISH THESIS SERVICE

TITLE	NOVEL SILICATE MATRIX COMPOSITES .
AUTHOR	A. CHAMBERLAIN
DEGREE	Ph.D
AWARDING BODY	Warwick University
DATE	1994
THESIS NUMBER	DX198224

THIS THESIS HAS BEEN MICROFILMED EXACTLY AS RECEIVED

The quality of this reproduction is dependent upon the quality of the original thesis submitted for microfilming. Every effort has been made to ensure the highest quality of reproduction. Some pages may have indistinct print, especially if the original papers were poorly produced or if the awarding body sent an inferior copy. If pages are missing, please contact the awarding body which granted the degree.

Previously copyrighted materials (journal articles, published texts, etc.) are not filmed.

This copy of the thesis has been supplied on condition that anyone who consults it is understood to recognise that its copyright rests with its author and that no information derived from it may be published without the author's prior written consent.

Reproduction of this thesis, other than as permitted under the United Kingdom Copyright Designs and Patents Act 1988, or under specific agreement with the copyright holder, is prohibited.

DX
198224